

# Multijet Background Estimation for Supersymmetry Searches and Radiation Damage Studies with the ATLAS Detector



**Harry James Moss**

Department of Physics and Astronomy  
University of Sheffield

A thesis submitted in partial fulfilment of the requirements for the  
degree of  
*Doctor of Philosophy*

July 2018



In memory of Alban Derek Moss.



# Abstract

This thesis documents a data-driven methodology for the estimation of the multijet background in fully hadronic final states with high missing transverse momentum within the ATLAS detector at the Large Hadron Collider. The implementation of this methodology within two analyses searching for evidence of supersymmetric particle production using  $36.1 \text{ fb}^{-1}$  of  $\sqrt{s} = 13 \text{ TeV}$  proton-proton collision data is described.

The two analyses described in this thesis investigate supersymmetric particle production via the strong interaction both inclusively via the superpartners of the first and second generation quarks and exclusively via the superpartners of the third generation  $t$  and  $b$  quarks. Both analyses consider the eventual decay of any produced supersymmetric particles to standard model particles and the lightest neutralino  $\tilde{\chi}_1^0$ , which escapes without detection and is observed as missing momentum in the transverse plane of the detector.

Additionally, an investigation into the level of radiation damage received by the ATLAS silicon Semiconductor Tracker is presented with predictions of the level of radiation damage faced over the course of the planned lifetime of the detector.



## Acknowledgements

Thanks must go first and foremost to my supervisor, Dan Tovey. This thesis and the preceding four years would not have been possible without his continual help and advice. Thanks must also go to Davide Costanzo, who provided a fantastic academic example to follow, Gary Fletcher for his help during the first year of my PhD and Mark Hodgkinson for his consistent guidance over the years.

I would like to thank friends and colleagues who I shared my time in Sheffield with. Joe, Ellie and Ross must receive special mention, if not only for coping with any complaining from my end for four years. The Sheffield ATLAS group have provided an excellent working environment over the last few years, whether physically at Sheffield or in our uncomfortably warm office at CERN. I'm very grateful to have shared my time with Calum, Vangelis and Guillermo who have consistently provided great advice within my work as well as fantastic distractions from it.

At CERN, I'd like to thank everyone who made my two year long term attachment as enjoyable as it was. Thanks to those I have been lucky enough to work with during my time there — particularly Chris Young, Taka Kondo, Martin Tripiana and the members of the sbottom and strong0L analyses. Thanks also to the LTA 2015-2017 collective who made my time at CERN immensely more enjoyable than it had any right to be. Particular thanks must go to Adam Parker, Michael Fenton, Xanthe Hoad, Matt Buckland, John Anders, Kārlis Dreimanis, Johnny Raine and the “Department of Mysteries” as a whole.

Thank you to my family, particularly my parents Hilary and Nigel, who have supported me throughout my education and have provided an endless supply of support, kind words and encouragement over the years. It is truly appreciated and I certainly would not have found myself completing this thesis if it weren't for them. Finally, to Angs, thank you for proof-reading this thesis. Thank you for putting up with the stress, the

---

countless late nights of work, and my moving to Geneva for two years. Thank you for being there every day to unfailingly brighten my mood.

# Author's Contribution

This thesis is dependent on work performed by members of the ATLAS collaboration. Contributions made specifically by the author are highlighted in this section.

## **Estimating Radiation Damage in the ATLAS SCT**

Chapter 4 describes an analysis undertaken by the author in which the effect of radiation damage within silicon ATLAS SCT barrel modules is investigated. The strong temperature dependence of the radiation damage lead to the analysis of several cooling plans for the SCT over the coming years. The results of this study were used by the SCT working group to inform the cooling strategy of the detector. The author also undertook measurements of SCT module currents under increasing applied voltages at regular intervals throughout the course of the PhD.

## **The *Jet Smearing* Method**

Chapter 6 details a data-driven methodology for the estimation of the QCD multijet background within ATLAS analyses. This method was developed during Run 1 for  $\sqrt{s} = 7$  TeV and  $\sqrt{s} = 8$  TeV data and is well documented. The author was responsible for performing all necessary calibrations of the jet response to data for all aspects of the method during the  $\sqrt{s} = 13$  TeV data taking campaign, which forms the main contribution within this thesis.

The author was responsible for the first inclusion of calibrations for the  $\phi$ -smearing of  $b$ -tagged jets. Additionally, a short study is presented in which the author confirms a central assumption of the methodology for the first time.

---

## **Implementation of Jet Smearing in ATLAS SUSY Searches**

Chapter 7 details the implementation of the data-driven methodology described in chapter 6 within two ATLAS SUSY searches, both of which feature the author as an analysis member. The first analysis discussed is often regarded as one of the flagship SUSY analyses within ATLAS, and so calibration of the Jet Smearing software was performed with this analysis in mind while working closely with fellow analysers. The author was involved with providing alternative systematic uncertainties to the second analysis presented in chapter 7 in addition to generating the estimate of the multijet background for the analysis. The chapter closes with a study, performed by the author, investigating the impact of the fully calibrated Jet Smearing software tool including all associated systematic and statistical uncertainties on the multijet estimate in one of the signal regions of the analysis.

# Table of contents

List of Abbreviations	xv
<b>1 Introduction</b>	<b>1</b>
<b>2 Theoretical Background</b>	<b>3</b>
2.1 Introduction . . . . .	3
2.2 The Standard Model . . . . .	4
2.2.1 Quantum Electrodynamics (QED) . . . . .	6
2.2.2 Quantum Chromodynamics (QCD) . . . . .	7
2.2.3 Electroweak Interaction . . . . .	8
2.2.4 Symmetry Breaking and the Higgs Mechanism . . . . .	10
2.2.5 Jet Physics at Hadron Colliders . . . . .	15
2.3 Limitations of the Standard Model . . . . .	22
2.3.1 Hierarchy Problem . . . . .	23
2.4 Supersymmetry . . . . .	25
2.4.1 R-parity . . . . .	26
2.4.2 Soft Supersymmetry Breaking . . . . .	27
2.4.3 Minimal Supersymmetric Standard Model . . . . .	28
2.5 SUSY Production at the LHC . . . . .	29
2.5.1 Previous Inclusive SUSY Searches at the LHC . . . . .	32
<b>3 The ATLAS Detector at the LHC</b>	<b>37</b>
3.1 Physics with Hadron Colliders . . . . .	37
3.1.1 Luminosity . . . . .	38
3.2 The Large Hadron Collider . . . . .	40
3.3 The ATLAS Detector . . . . .	42
3.3.1 Overview . . . . .	43

## Table of contents

---

3.3.2	Inner Detector . . . . .	45
3.3.3	Calorimetry . . . . .	53
3.3.4	Muon Spectrometer (MS) . . . . .	58
3.3.5	Magnet System . . . . .	59
3.3.6	Trigger and Data Acquisition (TDAQ) System . . . . .	59
3.4	Data Processing and Simulation . . . . .	61
3.4.1	ATLAS Events . . . . .	62
3.4.2	Event Simulation for ATLAS Analyses . . . . .	64
<b>4</b>	<b>Estimating Radiation Damage in the ATLAS SCT</b>	<b>65</b>
4.1	Introduction . . . . .	65
4.2	Radiation Damage in SCT Silicon Sensors . . . . .	67
4.2.1	Annealing . . . . .	69
4.3	Assumptions Used in Model Predictions . . . . .	70
4.4	Leakage Current Predictions . . . . .	72
4.5	Depletion Voltage . . . . .	78
4.6	Current-Voltage Profiling . . . . .	84
4.7	Conclusions . . . . .	87
<b>5</b>	<b>Analysis Tools</b>	<b>91</b>
5.1	Physics Object Reconstruction . . . . .	91
5.1.1	Tracks and Vertices . . . . .	92
5.1.2	Jets . . . . .	93
5.1.3	$b$ -tagged Jets . . . . .	102
5.1.4	Electrons and Photons . . . . .	107
5.1.5	Muons . . . . .	110
5.1.6	Missing Transverse Momentum . . . . .	111
5.1.7	Resolving Overlapping Objects . . . . .	114
5.2	Object Uncertainties . . . . .	115
5.2.1	Jet Energy Scale (JES) . . . . .	115
5.2.2	Jet Energy Resolution (JER) . . . . .	117
5.2.3	Jet Vertex Tagger (JVT) . . . . .	117
5.2.4	$b$ -jet Identification Efficiencies . . . . .	118
5.2.5	Lepton Efficiencies . . . . .	118
5.2.6	$E_T^{\text{miss}}$ . . . . .	118
5.2.7	Luminosity . . . . .	119

<b>6</b>	<b>The <i>Jet Smearing</i> Method</b>	<b>121</b>
6.1	Jet Smearing Overview . . . . .	121
6.2	Determination of the Jet Response . . . . .	127
6.2.1	Response Map Construction Method . . . . .	127
6.2.2	Response Maps for 2015 and 2016 Data . . . . .	129
6.2.3	Response Maps Constructed for 2017 Data . . . . .	132
6.3	Determination of Seed Selection . . . . .	135
6.4	Correcting the Initial Response . . . . .	138
6.4.1	Dijet Balance Analysis . . . . .	139
6.4.2	Dijet $\phi$ Smearing . . . . .	148
6.4.3	Tail correction via the Mercedes analysis . . . . .	160
6.5	Jet Smearing Uncertainties . . . . .	176
6.5.1	Seed Statistics . . . . .	176
6.5.2	Smearing Statistics . . . . .	177
6.5.3	Total Statistical Uncertainty . . . . .	178
6.5.4	Seed Selection . . . . .	178
6.5.5	Low-side Tail Shape Selection . . . . .	179
6.5.6	Gaussian Core Correction . . . . .	179
6.6	Origin of $E_T^{\text{miss}}$ in 0-lepton SUSY analyses . . . . .	179
6.6.1	Alternative $E_T^{\text{miss}}$ definitions . . . . .	180
6.6.2	Kinematic regions investigated . . . . .	182
6.6.3	Results . . . . .	183
6.6.4	Conclusion . . . . .	187
6.7	Summary . . . . .	187
<b>7</b>	<b>Implementation of Jet Smearing in ATLAS SUSY Searches</b>	<b>189</b>
7.1	Analysis Motivation . . . . .	190
7.2	Discriminating Variables . . . . .	190
7.2.1	Simple Variables . . . . .	191
7.2.2	Leading Dijet Invariant Mass $m_{jj}$ . . . . .	191
7.2.3	Effective Mass $m_{\text{eff}}$ . . . . .	192
7.2.4	$\frac{E_T^{\text{miss}}}{m_{\text{eff}}(N_j)}$ and $\frac{E_T^{\text{miss}}}{\sqrt{H_T}}$ . . . . .	192
7.2.5	Azimuthal Separation Between Jets and $E_T^{\text{miss}}$ . . . . .	193
7.2.6	Aplanarity . . . . .	193
7.2.7	Leading Dijet $p_T$ Asymmetry $\mathcal{A}$ . . . . .	194
7.2.8	Minimum Mass of a Lepton and $b$ -Jet Pair, $m_{bl}^{\text{min}}$ . . . . .	194

## Table of contents

---

7.2.9	Transverse Mass $m_T$ . . . . .	194
7.2.10	Contransverse Mass $m_{CT}$ . . . . .	194
7.2.11	$m_T^{\min}(\text{jet}_{1-4}, E_T^{\text{miss}})$ . . . . .	195
7.3	General SUSY Analysis Strategy . . . . .	195
7.3.1	Statistical Interpretation . . . . .	197
7.4	Strong SUSY Production Resulting in 2-6 Jets and $E_T^{\text{miss}}$ . . . . .	198
7.4.1	Event Selection and Signal Regions . . . . .	200
7.4.2	Background Estimation . . . . .	202
7.4.3	Results . . . . .	208
7.5	Third Generation SUSY Production Resulting in $b$ -Jets and $E_T^{\text{miss}}$ . . . . .	213
7.5.1	Event Selection and Signal Regions . . . . .	214
7.5.2	Background Estimation . . . . .	219
7.5.3	Results . . . . .	229
7.6	Revised Multijet Estimate Uncertainty . . . . .	236
7.6.1	Multijet Contribution in SRC CRs . . . . .	237
7.6.2	Event Yields in SRC . . . . .	243
7.7	Summary . . . . .	248
<b>8</b>	<b>Conclusions</b>	<b>249</b>
	<b>References</b>	<b>251</b>
	<b>Appendix A Radiation Damage Estimation</b>	<b>263</b>
	<b>Appendix B Strong SUSY Production Analysis Signal Regions</b>	<b>269</b>
	<b>Appendix C Sbottom SUSY Analysis Kinematic Regions</b>	<b>273</b>

# List of Abbreviations

ALICE	A Large Ion Collider Experiment
ATLAS	A Toroidal LHC ApparatuS
ADC	Analogue to Digital Converter
BIB	Beam Induced Background
BSM	Beyond the Standard Model
CERN	Organisation Européen pour la Recherche Nucléaire
CL	Confidence Level
CMS	Compact Muon Solenoid
CPU	Central Processing Unit
CR	Control Region
CSC	Cathode Strip Chamber
CST	Cell-based Soft Term
DGLAP	Dokshitzer–Gribov–Lipatov–Altarelli–Parisi
DM	Dark Matter
ECAL	Electromagnetic Calorimeter
EM	Electromagnetic
eV	Electron volt
EW	Electroweak
FCAL	Forward Calorimeter
FLUKA	FLUktuierende KAskade
FSR	Final State Radiation
GSC	Global Sequential Calibration
HCAL	Hadronic Calorimeter
HEC	Hadronic Calorimeter Endcap Cell
HLT	High Level Trigger
HV	High Voltage

## List of Abbreviations

---

IBL	Insertable B-Layer
ICHEP	International Conference on High Energy Physics
ID	Inner Detector
IRC	Infrared and Collinear
ISR	Initial State Radiation
JER	Jet Energy Resolution
JES	Jet Energy Scale
JVT	Jet Vertex Tagger
LEP	Large Electron-Positron Collider
LHC	Large Hadron Collider
LO	Leading Order
LSP	Lightest Supersymmetric Particle
MC	Monte Carlo
MDT	Monitored Drift Tube
ME	Matrix Element
MET	Missing Transverse Energy
MJB	Multijet Balance
MS	Muon Spectrometer
MSSM	Minimal Supersymmetric Standard Model
MSTW	Martin-Stirling-Thorne-Watt
NIEL	Non-Ionising Energy Loss
NLO	Next-to-Leading-Order
PDF	Parton Distribution Function
PIX	ATLAS Pixel Detector
PKA	Primary Knock-On Atom
PS	Proton Synchrotron
PV	Primary Vertex
QCD	Quantum Chromodynamics
QED	Quantum Electrodynamics
QFT	Quantum Field Theory
RF	Radio Frequency
ROI	Region Of Interest
RPC	Resistive Plate Chamber
SCT	SemiConductor Tracker
SF	Scale Factor

---

SFOS	Same Flavour Opposite Sign
SHERPA	Simulation of High-Energy Reactions of PArticles
SM	Standard Model
SPS	Super Proton Synchrotron
SR	Signal Region
SSB	Spontaneous Symmetry Breaking
SU( $N$ )	Special Unitary group of degree $N$
SUSY	Supersymmetry
SV	Secondary Vertex
TDAQ	Trigger and Data Acquisition
TDR	Technical Design Report
TEEC	Transverse Energy-Energy Correlation Transfer Fac-
TF	tor
TRT	Transmission Radiation Tracker
TST	Track-based Soft Term
UE	Underlying Event
UV	Ultraviolet
VBF	Vector Boson Fusion
VEV	Vacuum Expectation Value
VR	Validation Region
WIMP	Weakly Interacting Massive Particle



# Chapter 1

## Introduction

Particle physics attempts to describe the elementary components of visible matter and the fundamental forces through which it interacts. The Standard Model of particle physics is a theoretical framework that encapsulates the sum of experimentally verified theories which, for the most part, accurately describes a range of phenomena observed in our universe and is reviewed in chapter 2. Crucially, some questions are left unanswered, motivating theoretical extensions to the model, some of which introduce new particles that are often more massive than those observed to date. One such proposed extension to the Standard Model is supersymmetry, a boson-fermion symmetry which introduces *superpartner* particles for the observed Standard Model particles. Supersymmetry is motivated by a desire to explain why the mass of the recently discovered Higgs boson is approximately  $125 \text{ GeV}/c^2$  and may offer an explanation for the composition of the abundant ‘dark matter’ in our universe. Supersymmetry and its motivations are explored in chapter 2.

The advent of the Large Hadron Collider at CERN affords physicists the opportunity to explore the high-energy frontier of particle physics as it operates at the highest centre-of-mass collision energy of any particle collider to date. The LHC has already been successful in one of its design goals — discovery of the Higgs boson. The Standard Model is often thought of as analogous to a puzzle, with the Higgs boson representing the final piece. Nevertheless, the Standard Model is not the complete picture. Physicists at the LHC continue to search for the missing pieces of the overall puzzle that describes our universe.

## Introduction

---

After discussing the theoretical motivations for supersymmetry, chapter 3 discusses the components of the **A Toroidal LHC ApparatuS** (ATLAS) detector [1] located on the LHC beam-line where counter-rotating beams of protons are brought together and collided. Particular attention is paid to the silicon strip Semiconductor Tracker, on which the author performed diagnostic measurements over the course of the  $\sqrt{s} = 13$  TeV data taking campaign. Chapter 4 details a study performed by the author exploring the effects of damage to the Semiconductor Tracker due to the radiation induced by particle collisions and uses existing theoretical models to predict the effects of this damage over the expected operating time of the detector.

An overview of the ATLAS physics analysis toolkit is given in chapter 5 and explores the procedure of identifying detector signals as particles for use in physics analyses.

A data-driven methodology for the estimation of a potentially large QCD multijet background in searches for supersymmetry is introduced in chapter 6, first developed prior the initial ATLAS data taking campaign at  $\sqrt{s} = 7$  TeV. The software implementation of this methodology was developed and updated for data recorded during 2015 and 2016 at a centre-of-mass energy of  $\sqrt{s} = 13$  TeV by the author. Two ATLAS analyses searching for supersymmetry are introduced in chapter 7, which both use the methodology described in chapter 6. The author was a member of the analysis team for both analyses, with the aim of optimising the multijet background estimation for the analyses and, for one analysis, implementing the method to generate an estimate of the QCD multijet background.

Finally, a summary of the items explored in this thesis and the impact of the results obtained in the two analyses in chapter 7 are considered in chapter 8.

# Chapter 2

## Theoretical Background

### 2.1 Introduction

This chapter introduces the Standard Model (SM). A brief summary of the content of the SM is given, with an exploration of its failings and subsequent theoretical motivation for extensions to the model. Particular focus is given to one of the classes of supersymmetric (SUSY) extensions to the SM, the Minimal Supersymmetric Standard Model (MSSM).

The SM is a theoretical framework constructed in the language of quantum field theory (QFT) and informed by experimental observation that describes all known fundamental particles and interactions, excluding the gravitational interaction. It is one of the most successfully experimentally verified theories in physics to date. The observation of all particles predicted by the SM was achieved in 2012 by the ATLAS and CMS [2] experiments with the discovery of a Higgs boson [3, 4].

Not all observed phenomena are described by the SM. No SM particle is an adequate candidate for dark matter (DM), which may account for approximately 25% of the energy density of the universe. The *hierarchy problem* within the SM, caused by the high sensitivity of the Higgs mass to new physics in the vast energy range between the weak scale and the Planck scale, is explained in detail in section 2.3. Solving the hierarchy problem remains one of the key motivations of extensions to the SM.

## 2.2 The Standard Model

A brief overview of the components of the Standard Model is provided in this section before exploring potential theoretical extensions to the model. The SM classifies fundamental particles by their internal angular momentum, the quantum number *spin*. Particles with half-integer spin are termed *fermions* and form the constituents of matter. Particles with integer spin are termed *bosons* and are the mediators of the interactions in the SM. The particle content of the SM is shown in tables 2.1 and 2.2.

Table 2.1 SM bosons (interaction mediators) and their properties. The eight copies of the gluon are not displayed. Masses are taken from [5] and arise due to the Higgs mechanism.

Particle	Charge	Mass	Spin
$\gamma$	0	—	1
$W^\pm$	$\pm 1e$	$80.379 \pm 0.012$ GeV	1
$Z$	0	$91.1876 \pm 0.0021$ GeV	1
$g$	0	—	1
$H$	0	$125.18 \pm 0.16$ GeV	0

Table 2.2 Spin- $\frac{1}{2}$  Fermions and their properties. Copies of quarks corresponding to differences in their colour quantum number are not shown. Masses (or mass constraints where measurements are not available) are taken from [5]. The quoted mass for the  $t$  quark is taken from direct measurements.

Quarks			Leptons		
Particle	Charge	Mass	Particle	Charge	Mass
<b>I</b>					
$u$	$+\frac{2}{3}$	$2.2^{+0.5}_{-0.4}$ MeV	$e$	-1	0.511 MeV
$d$	$-\frac{1}{3}$	$4.7^{+0.5}_{-0.4}$ MeV	$\nu_e$	0	< 2 eV
<b>II</b>					
$c$	$+\frac{2}{3}$	$1.275^{+0.025}_{-0.035}$ GeV	$\mu$	-1	105.658 MeV
$s$	$-\frac{1}{3}$	$95^{+9}_{-3}$ MeV	$\nu_\mu$	0	< 0.19 MeV
<b>III</b>					
$t$	$+\frac{2}{3}$	$173.0 \pm 0.4$ GeV	$\tau$	-1	$1776.86 \pm 0.12$ MeV
$b$	$-\frac{1}{3}$	$4.18^{+0.04}_{-0.03}$ GeV	$\nu_\tau$	0	< 18.2 MeV

## 2.2 The Standard Model

---

The bosonic content of the SM is shown in table 2.1. Table 2.2 displays the fermionic content: three generations of quarks and leptons, with each generation having increasing mass. Experimental evidence [6, 7] suggests there are no more than three generations of quarks and leptons. In total the SM accounts for 61 distinct fundamental particles: 36 colour states of quarks and antiquarks, 12 leptons and anti-leptons, 8 gluons, 4 electroweak bosons and 1 Higgs boson.

The SM is described by a Lagrangian density  $\mathcal{L}_{\text{SM}}$  which encapsulates the dynamics of the model and is of the form  $\mathcal{L} = T - V$ , where  $T$  and  $V$  are the kinetic and potential terms, respectively. The interactions described by the SM are required to be invariant under local gauge transformations. This *local gauge invariance* leads naturally to the appearance of interaction mediators. The SM can be expressed as the product of the symmetry groups that correspond to fundamental interactions

$$SU(3)_C \times SU(2)_L \times U(1)_Y \tag{2.1}$$

where  $U(n)$  refers to all  $n \times n$  complex unitary matrices and  $SU(n)$  refers to all  $n \times n$  complex unitary matrices with a determinant of one [8]. Each term in equation 2.1 corresponds to a fundamental interaction. The first term  $SU(3)_C$  corresponds to the symmetry group describing quantum chromodynamics (QCD). The term  $SU(2)_L \times U(1)_Y$  represents the symmetry groups generated by left-handed weak isospin  $L$  and hypercharge  $Y$ , together describing the unified electromagnetic and weak interactions, termed the *electroweak* (EW) interaction. The EW interaction undergoes spontaneous symmetry breaking via the Higgs mechanism to generate the observed massive  $W^\pm$  and  $Z$  bosons.

Overall, the SM combines the unified quantum electrodynamics (QED) and weak interaction, QCD, enforced invariance under local gauge transformations and spontaneous symmetry breaking via the Higgs mechanism. The mathematical formalism in this section closely follows the work in [8–10], which provide an overview for the general reader.

### 2.2.1 Quantum Electrodynamics (QED)

QED represents a relativistic quantum mechanical description of classical electrodynamics and is the simplest representation of QFT within the SM as its gauge transformations are of the type  $U(1)_Q$  and commute — they are said to be *Abelian*. In practice, this results in massless exchange quanta of the interactions that are not ‘charged’ and do not self-interact, the experimentally observed photons. A non-interacting spin- $\frac{1}{2}$  particle with mass  $m$  is described by the free Dirac Lagrangian density

$$\mathcal{L} = i\bar{\psi}\gamma^\mu\partial_\mu\psi - m\bar{\psi}\psi \quad (2.2)$$

where  $\psi$  is a 4-component Dirac spinor composed of a left and a right handed chiral component. The adjoint  $\bar{\psi} \equiv \psi^\dagger\gamma^0$  denotes the anti-particle state of  $\psi$ . The gamma matrices  $\gamma^\mu$  are a set of  $4 \times 4$  matrices constructed with the  $2 \times 2$  Pauli matrices and represent transformations of the spinors in 4 dimensions. Transformation of the Dirac Lagrangian density in equation 2.2 under global transformations by a phase  $\theta$

$$\begin{aligned} \psi &\rightarrow e^{i\theta}\psi \\ \bar{\psi} &\rightarrow e^{-i\theta}\bar{\psi} \end{aligned} \quad (2.3)$$

cause the Lagrangian density to remain unchanged. For *local* transformations, where  $\theta$  depends on a coordinate  $x$ , equation 2.2 is no longer invariant as the transformations result in

$$\psi \rightarrow e^{i\theta(x)}\psi \quad (2.4)$$

$$\partial_\mu e^{i\theta(x)}\psi = i(\partial_\mu\theta)e^{i\theta}\psi + e^{i\theta}\partial_\mu\psi \quad (2.5)$$

causing the Lagrangian density to transform as

$$\mathcal{L} \rightarrow \mathcal{L} - \partial_\mu\theta\bar{\psi}\gamma^\mu\psi \quad (2.6)$$

and therefore lose the invariance observed under global transformations.

Invariance of the Lagrangian density under local transformations is restored upon introduction of terms describing the massless photon, the spin-1 field  $A_\mu$ . The full QED Lagrangian describes interactions between massive spin- $\frac{1}{2}$  fermions, anti-fermions

and massless spin-1 photons and is given by

$$\mathcal{L}_{\text{QED}} = \bar{\psi}(i\gamma^\mu\partial_\mu - m)\psi - \frac{1}{4}F^{\mu\nu}F_{\mu\nu} - (q\bar{\psi}\gamma^\mu\psi)A_\mu \quad (2.7)$$

where  $q$  is the charge of the particle and  $F^{\mu\nu} \equiv \partial^\mu A^\nu - \partial^\nu A^\mu$ .

Equivalently, equation 2.2 is invariant under local transformations when the partial derivative  $\partial_\mu$  is replaced with the *covariant derivative*

$$\partial_\mu \rightarrow \mathcal{D}_\mu \equiv \partial_\mu + iqA_\mu \quad (2.8)$$

The Lagrangian in equation 2.7 arises through the ‘simple’ requirement of invariance under local gauge transformations and is achieved by introducing a covariant derivative. This mechanism is the means of generating all fundamental interactions within the SM.

### 2.2.2 Quantum Chromodynamics (QCD)

QCD describes the strong interaction between quarks and gluons, the fundamental constituents of hadrons. It introduces the *colour* quantum number, the ‘charge’ of the strong interaction. Quark flavours appear in mass-degenerate colour states (red, green, blue and their anti-colour equivalents), while only colour-neutral states are observed in nature as a result of *confinement*.

The six colour and anti-colour quark states are

$$\psi = \begin{pmatrix} \psi_r \\ \psi_g \\ \psi_b \end{pmatrix}, \quad \bar{\psi} = (\bar{\psi}_r \ \bar{\psi}_g \ \bar{\psi}_b) \quad (2.9)$$

where each element of  $\psi$  is itself a 4-component Dirac spinor. Following the same procedure as for QED, invariance is required under local gauge transformations of the type  $SU(3)$

$$\psi(x) \rightarrow U(x)\psi(x) \quad (2.10)$$

where  $U(x)$  is any complex unitary  $3 \times 3$  matrix with determinant 1.

## Theoretical Background

---

The covariant derivative is defined in this case to be

$$\mathcal{D}^\mu \equiv \partial^\mu + ig_s T^a A^{a\mu}(x) \quad (2.11)$$

$$T^a = \frac{1}{2} \lambda^a \quad (2.12)$$

where  $\lambda^a$  are the eight  $3 \times 3$  Gell-Mann matrices (equivalent to the Pauli matrices for the  $SU(3)$  case) where  $a$  runs from 1 to 8 and  $g_s$  is the QCD coupling.  $A^\mu(x)$  represents the eight  $SU(3)_c$  vector fields corresponding to colour states of the gluons. The free Lagrangian for the gluons is

$$\mathcal{L}_{\text{gluons}} = -\frac{1}{4} \mathbf{F}^{\mu\nu} \mathbf{F}_{\mu\nu} \quad (2.13)$$

where

$$\mathbf{F}^{\mu\nu} \equiv \partial^\mu \mathbf{A}^\nu - \partial^\nu \mathbf{A}^\mu - 2g(\mathbf{A}^\mu \times \mathbf{A}^\nu) \quad (2.14)$$

and the ‘cross-product’ in equation 2.14 is a substitution for

$$(B \times C)_\alpha = \sum_{\beta, \gamma=1}^8 f_{\alpha\beta\gamma} B_\beta C_\gamma \quad (2.15)$$

where  $f^{ijk}$  are the  $SU(3)$  structure constants, obtained from the commutators of the elements of the Gell-Mann matrices

$$[\lambda^\alpha, \lambda^\beta] = 2if^{\alpha\beta\gamma} \lambda^\gamma \quad (2.16)$$

The non-zero nature of the structure constants shows the non-Abelian nature of transformations in  $SU(3)$  and results in the self-interaction of the gluons. The full QCD Lagrangian for each quark flavour is then

$$\mathcal{L}_{\text{QCD}} = \bar{\psi}(i\gamma^\mu \mathcal{D}_\mu - m)\psi - \frac{1}{4} \mathbf{F}^{\mu\nu} \mathbf{F}_{\mu\nu} \quad (2.17)$$

with six replicas required to account for all quark flavours.

### 2.2.3 Electroweak Interaction

A unified electromagnetic and weak interaction was proposed by Glashow in 1961 and represented a crucial step in the formation of the SM. The formalism was completed

## 2.2 The Standard Model

---

with the addition of the Higgs mechanism by Weinberg in 1967 [11] and Salam in 1968 [12] to generate massive vector bosons while preserving gauge invariance.

The 4-component Dirac spinors describing spin- $\frac{1}{2}$  fermions in the SM are divided into a left- and right-handed chiral component. The weak interaction couples solely with the left-handed components of Dirac spinors, which are arranged into doublets of weak isospin and shown in table 2.3.

Table 2.3 Spin- $\frac{1}{2}$  massless left-handed fermion doublets and right-handed fermion singlets (and vice versa for their anti-particles) in the SM. Doublets are formed from particles of the same generation.

Quarks		Leptons	
Doublet	Singlet	Doublet	Singlet
$\begin{pmatrix} \nu^e \\ e \end{pmatrix}_L$	$\begin{pmatrix} \bar{\nu}^e \\ \bar{e} \end{pmatrix}_R$	$e_R, \bar{e}_L$	$\begin{pmatrix} u \\ d \end{pmatrix}_L, \begin{pmatrix} \bar{u} \\ \bar{d} \end{pmatrix}_R$ $u_R, d_R, \bar{u}_L, \bar{d}_L$
$\begin{pmatrix} \nu^\mu \\ \mu \end{pmatrix}_L$	$\begin{pmatrix} \bar{\nu}^\mu \\ \bar{\mu} \end{pmatrix}_R$	$\mu_R, \bar{\mu}_L$	$\begin{pmatrix} c \\ s \end{pmatrix}_L, \begin{pmatrix} \bar{c} \\ \bar{s} \end{pmatrix}_R$ $c_R, s_R, \bar{c}_L, \bar{s}_L$
$\begin{pmatrix} \nu^\tau \\ \tau \end{pmatrix}_L$	$\begin{pmatrix} \bar{\nu}^\tau \\ \bar{\tau} \end{pmatrix}_R$	$\tau_R, \bar{\tau}_L$	$\begin{pmatrix} t \\ b \end{pmatrix}_L, \begin{pmatrix} \bar{t} \\ \bar{b} \end{pmatrix}_R$ $t_R, b_R, \bar{t}_L, \bar{b}_L$

Right-handed particles exist in singlet states and do not couple to the gauge bosons of the weak interaction. The unified EW interaction is described by the  $SU(2)_L \times U(1)_Y$  symmetry group. The  $SU(2)_L$  term describes the group of left-handed weak isospin.  $U(1)_Y$  describes the group of weak hypercharge  $Y$  and is related to the electromagnetic charge  $Q$  by  $Y = 2(Q - T_3)$ , where  $T_3$  is the third component of weak isospin. Hypercharge  $Y$  is the generator of the group  $U(1)_Y$ , similarly to  $Q$  acting as the generator of  $U(1)_Q$ .

The EW Lagrangian,  $\mathcal{L}_{EW}$ , is formulated from the same principle as QCD and QED, namely by enforcing invariance under local gauge transformations, in this case of the type  $SU(2)_L \times U(1)_Y$ . The full EW Lagrangian is

$$\mathcal{L}_{EW} = i(\bar{\psi}\gamma^\mu\mathcal{D}_\mu - m)\psi - \frac{1}{4}B_{\mu\nu}B^{\mu\nu} - \frac{1}{4}\mathbf{W}_{\mu\nu}\mathbf{W}^{\mu\nu} \quad (2.18)$$

## Theoretical Background

---

with the covariant derivative  $\mathcal{D}_\mu$  defined as

$$\mathcal{D}_\mu \equiv \partial_\mu - ig_W \boldsymbol{\tau} \cdot \mathbf{A}_\mu - ig_Y B_\mu \quad (2.19)$$

where  $\boldsymbol{\tau} = \frac{1}{2}\boldsymbol{\sigma}$  and  $\boldsymbol{\sigma}$  are the Pauli matrices. Four massless gauge fields are introduced to preserve invariance under local gauge transformations and correspond to the three weak vector fields  $\mathbf{W}_\mu \equiv W_\mu^{(1)}, W_\mu^{(2)}, W_\mu^{(3)}$  and a single hypercharge field  $B_\mu$ .

The charged  $W_\mu^\pm$ , neutral  $Z_\mu$  and  $A_\mu$  gauge fields are formed from linear combinations of these gauge fields

$$W_\mu^\pm = \frac{1}{\sqrt{2}}(W_\mu^{(1)} \mp iW_\mu^{(2)}) \quad (2.20)$$

$$Z_\mu = -B_\mu \sin \theta_W + W_\mu^{(3)} \cos \theta_W \quad (2.21)$$

$$A_\mu = +B_\mu \cos \theta_W + W_\mu^{(3)} \sin \theta_W \quad (2.22)$$

where  $\theta_W$  is the Weinberg angle.

Fermion mass terms  $\bar{\psi}\psi$  are not invariant under  $SU(2)_L \times U(1)_Y$  symmetry and as such the chiral fermions are massless in the SM. The short range of the weak interaction can be explained by requiring massive mediating particles, which are observed experimentally. The mechanism for the generation of masses is discussed in section 2.2.4.

### 2.2.4 Symmetry Breaking and the Higgs Mechanism

The Higgs mechanism generates masses for fundamental particles via spontaneous symmetry breaking of  $SU(2)_L \times U(1)_Y \rightarrow U(1)_Q$ . The gauge bosons described in section 2.2.3 have no mass term in the EW Lagrangian, yet the observed quanta of these fields (the  $W^\pm$  and  $Z^0$  bosons) are required to be massive to account for the short range of the weak interaction. Through the Higgs mechanism, mass terms are obtained for these bosons while leaving the photon massless, as required for an interaction with unlimited range.

### 2.2.4.1 Spontaneous Symmetry Breaking

The Lagrangian for the simplest case of  $U(1)$  symmetry with a single scalar field  $\phi$  is

$$\mathcal{L} = \frac{1}{2}(\partial_\mu\phi)(\partial^\mu\phi) - \frac{1}{2}\mu^2\phi^2 - \frac{1}{4}\lambda^2\phi^4 \quad (2.23)$$

with a potential term

$$V(\phi) = \frac{1}{2}\mu^2\phi^2 + \frac{1}{4}\lambda^2\phi^4 \quad (2.24)$$

The term proportional to  $\mu^2$  is the mass term. For  $\mu^2 > 0$ , the potential has a minimum at  $\phi = 0$ . A non-trivial case arises when  $\mu^2 < 0$ , causing the potential to have minima when

$$\phi = \pm v = \pm \left| \sqrt{\frac{\mu^2}{\lambda}} \right| \quad (2.25)$$

creating a non-zero ground (or vacuum) state, with a non-zero vacuum expectation value (VEV),  $v$ . The symmetry of the field is broken when a vacuum state, either  $\phi = +v$  or  $\phi = -v$  is selected.

Introducing a new field  $\eta$  such that

$$\phi = v \pm \eta(x) \quad (2.26)$$

describes a deviation from the minimum of  $\phi$ , and selecting the  $+v$  state allows the Lagrangian to be expressed as

$$\mathcal{L} = \frac{1}{2}(\partial_\mu\eta)(\partial^\mu\eta) - \frac{1}{2}\mu^2(v + \eta)^2 - \frac{1}{4}\lambda(v + \eta)^4 \quad (2.27)$$

where the term with  $\eta^2$  corresponds to the mass term with a value of  $m = -\sqrt{2}\mu$ . Terms with  $\eta^3$  and  $\eta^4$  describe triple and quartic interactions. The Lagrangian in equation 2.27 is, unlike equation 2.23, not invariant under the transformation  $\phi \rightarrow -\phi$ . The symmetry has been broken by the choice of vacuum state from equation 2.25. This symmetry breaking is *spontaneous* as there is no external cause other than the simple choice of a ground state.

For a complex scalar field  $\phi = \phi_1 + i\phi_2$ , the Lagrangian is

$$\mathcal{L} = \frac{1}{2}(\partial_\mu\phi^*)(\partial^\mu\phi) - \frac{1}{2}\mu^2(\phi^*\phi) - \frac{1}{4}\lambda^2(\phi^*\phi)^2 \quad (2.28)$$

## Theoretical Background

---

where  $\mu$ ,  $\lambda$  are real constants. In this case, if  $\mu^2 < 0$ , an infinite set of minima are created on a circle described by

$$\phi_1^2 + \phi_2^2 = \frac{-\mu^2}{\lambda} = v^2 \quad (2.29)$$

and illustrated in figure 2.1.

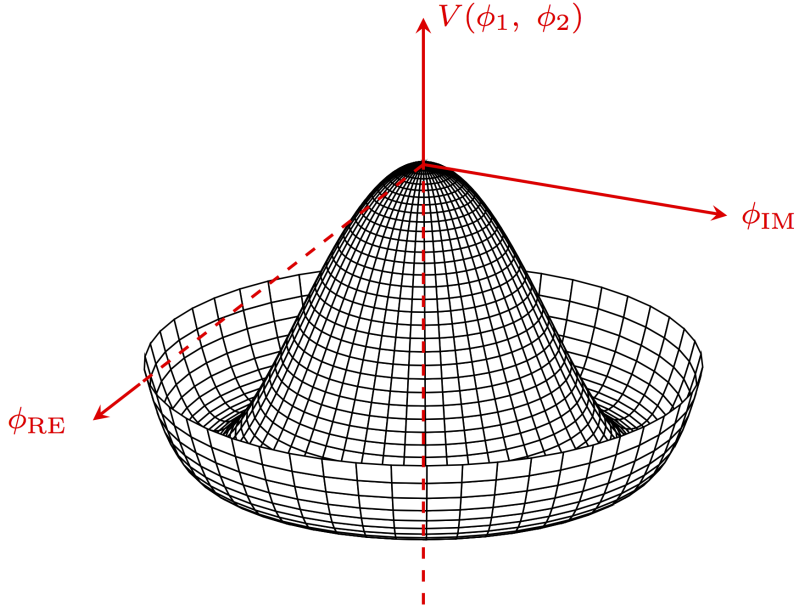


Fig. 2.1 The ‘Mexican Hat’ potential displaying the circle of minima in the case  $\mu^2 < 0$ .

The global  $U(1)$  symmetry is broken when a particular point on the circle is chosen as the minimum. Arbitrarily choosing the vacuum state as

$$\phi_1 = v, \phi_2 = 0 \quad (2.30)$$

and performing fluctuations about the vacuum state such that

$$\phi_1(x) = \eta(x) + v, \phi_2 = \xi(x) \quad (2.31)$$

the Lagrangian can be expressed as

$$\mathcal{L} = \frac{1}{2}(\partial_\mu \eta)(\partial^\mu \eta) - \frac{1}{2}m_\eta^2 \eta^2 + \frac{1}{2}(\partial_\mu \xi)(\partial^\mu \xi) - V_{\text{int}}(\eta, \xi) \quad (2.32)$$

providing a term for a massive scalar field  $\eta$ , where  $m_\eta = \sqrt{2\lambda}v$ , and a massless scalar field  $\xi$ . Excitations where the potential increases (going up the slope in figure 2.1) correspond to excitations of the field  $\eta$ , whereas excitations along the circle of minima correspond to excitations of the massless field  $\xi$ , a ‘Goldstone’ boson.

### 2.2.4.2 The Higgs Mechanism

The Higgs mechanism combines the concept of spontaneous symmetry breaking with the enforcement of local gauge invariance. Extending the formalism discussed in section 2.2.4.1 to the simplest  $SU(2)_L \times U(1)_Y$  case, a pair of complex scalar fields (one neutral and one charged) are introduced as the weak isospin doublet

$$\phi = \begin{pmatrix} \phi^+ \\ \phi^0 \end{pmatrix} = \frac{1}{\sqrt{2}} \begin{pmatrix} \phi_1 + i\phi_2 \\ \phi_3 + i\phi_4 \end{pmatrix} \quad (2.33)$$

with

$$\mathcal{L} = (\partial_\mu \phi)^\dagger (\partial^\mu \phi) - V(\phi) \quad (2.34)$$

$$V(\phi) = \mu^2 \phi^\dagger \phi + \lambda (\phi^\dagger \phi)^2 \quad (2.35)$$

Requiring  $\mu^2 < 0$  as in section 2.2.4.1 yields an infinite set of minima with

$$\phi^\dagger \phi = \frac{1}{2}(\phi_1^2 + \phi_2^2 + \phi_3^2 + \phi_4^2) = -\frac{\mu^2}{2\lambda} = \frac{v^2}{2} \quad (2.36)$$

As before, a non-zero VEV is selected for one of the scalar fields. As the photon remains massless following symmetry breaking, the neutral scalar field  $\phi^0$  is assigned a non-zero VEV at the minimum potential.

Expanding about this minimum

$$\phi = \frac{1}{\sqrt{2}} \begin{pmatrix} \phi_1(x) + i\phi_2(x) \\ v + \eta(x) + i\phi_4(x) \end{pmatrix} \quad (2.37)$$

introduces a single massive scalar field and three massless Goldstone bosons, which provide longitudinal degrees of freedom and therefore masses to the gauge bosons.

## Theoretical Background

---

Similarly to equation 2.19, the covariant derivative is introduced as

$$\mathcal{D}_\mu = \partial_\mu + ig_W \mathbf{T} \cdot \mathbf{W}_\mu + ig_Y \frac{Y}{2} B_\mu \quad (2.38)$$

where  $g_W$  is the weak coupling constant,  $\mathbf{T} = \frac{\sigma}{2}$  and the hypercharge  $Y$  of the Higgs doublet is equal to 1.

The mass generation term in the resulting Lagrangian that is responsible for gauge boson masses contains  $(\mathcal{D}_\mu \phi)^\dagger (\mathcal{D}^\mu \phi)$  and causes masses to appear in the form  $\frac{1}{2} m_W^2 W_\mu W^\mu$ .

The mass of the W boson is proportional to the weak coupling constant  $g_W$  and the Higgs field VEV  $v$ :

$$m_W = \frac{1}{2} g_W v \quad (2.39)$$

As described in equation 2.22, the physically observable  $Z$  boson and photon are formed from linear combinations of the  $B$  and  $W_\mu^{(3)}$  gauge fields, with masses

$$M_A = 0 \quad (2.40)$$

$$M_Z = \frac{1}{2} v \sqrt{g_W^2 + g_Y^2} \quad (2.41)$$

The mass of the Higgs boson is related to the VEV by

$$m_H^2 = 2\lambda v^2 \quad (2.42)$$

where  $v$  is determined from measurements of the weak coupling constant and  $m_W$  to be equal to 246 GeV. The parameter  $\lambda$  is not predicted and therefore requires the mass of the Higgs boson to be determined experimentally.

The Higgs mechanism also generates fermion masses by combining the left and right-handed chiral fermions described by the SM, displayed in table 2.3. Fermion mass terms in the Dirac Lagrangian

$$-m\bar{\psi}\psi = -m(\bar{\psi}_R\psi_L + \bar{\psi}_L\psi_R) \quad (2.43)$$

are not invariant under local transformations as the right and left-handed chiral states ( $L$  and  $R$ ) have differing transformation properties. However, the combination of

local transformations applied to the left-handed fermion doublet  $L$  and the Higgs doublet  $\phi$  are invariant under  $SU(2)_L$  in the combination  $\bar{L}\phi$ , and are invariant under  $SU(2)_L \times U(1)_Y$  in the combination  $\bar{L}\phi R$ . This is also true for the Hermitian conjugate  $(\bar{L}\phi R)^\dagger$ . Terms in the Lagrangian from these combinations arise in the form

$$\mathcal{L} = -g_f[\bar{L}\vec{\phi}R + (\bar{L}\vec{\phi}R)^\dagger] \quad (2.44)$$

$$\mathcal{L} = g_f[\bar{L}\vec{\phi}_C R + (\bar{L}\vec{\phi}_C R)^\dagger] \quad (2.45)$$

with equations 2.44 and 2.45 representing down-type and up-type Dirac fermions, respectively. The two terms describe the complex scalar Higgs field  $\phi$ , its conjugate  $\phi_C$ , their couplings to fermions and interactions between fermions and the quanta of the Higgs field, the Higgs boson. The constant  $v$  is the Higgs field VEV, with  $v = 246$  GeV. The constant  $g_f$  is the Yukawa coupling

$$g_f = \sqrt{2}\frac{m_f}{v} \quad (2.46)$$

and is proportional to the mass of the fermion  $m_f$ . Fermion masses are generated after spontaneous symmetry breaking by coupling the left and right-handed chiral states of the fermion to the non-zero VEV of the Higgs field and to the Higgs boson itself.

### 2.2.5 Jet Physics at Hadron Colliders

Isolated quarks cannot be observed experimentally. Figure 2.2 shows that the strength of the strong coupling  $\alpha_S$  grows with increasing distance (equivalent to lower energies). At large distances corresponding to low energies below 1 GeV, the strength of  $\alpha_S$  increases dramatically and leads to quark *confinement* and their formation into the colour-neutral hadrons observed experimentally. Gluon self-couplings contribute to the *running* of the strong coupling constant  $\alpha_S = \frac{g_s^2}{4\pi}$ . The value of  $\alpha_S$  is dependent upon the energy scale at which it is measured. Figure 2.2 shows a decrease in  $\alpha_S$  with increasing energy (corresponding to shorter distance scales), leading to the phenomenon of *asymptotic freedom*. Measurements of  $\alpha_S$  provide a valuable probe of QCD and verify the predicted behaviour of asymptotic freedom, in which the strong interaction is increasingly weaker at higher energy scales. In the perturbative QCD regime with

## Theoretical Background

processes involving high momentum transfer  $Q$ ,  $\alpha_S$  is measured at the energy scale  $\mu_R$  associated with renormalisation, the removal of divergences introduced by perturbative corrections to QCD. Choosing  $\mu_R = Q$  allows the strong coupling strength to be calculated for a particular process. Quoted values of  $\alpha_S$  are typically calculated for  $Q = M_Z$ , in which case  $\alpha_S \sim 0.1$  [5].

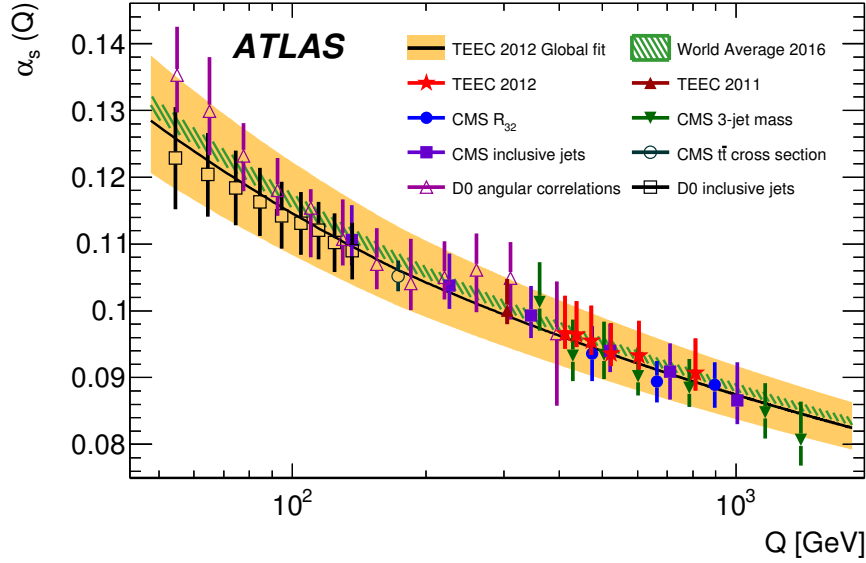


Fig. 2.2 Measurements of  $\alpha_S$  as a function of energy using the transverse energy-energy correlation (TEEC), a jet-based quantity, with ATLAS data. Measurements from the CMS and D0 experiments are provided along with the 2016 world average and associated uncertainty. The dependence of  $\alpha_S$  on the energy scale  $Q$  is clearly observed. Figure from [13].

The dependence of  $\alpha_S$  on the energy scale  $\mu = Q$  is defined by the beta function for QCD shown in equation 2.47

$$\beta(\alpha_S) = Q^2 \frac{\partial \alpha_S}{\partial Q^2} = -(b_0 \alpha_S^2 + b_1 \alpha_S^3 + b_2 \alpha_S^4 + \dots) \quad (2.47)$$

where  $b_0 = (33 - n_f)/(12\pi)$  is the one-loop coefficient and  $n_f$  is the number of quark flavours available at momentum transfer  $Q$ . The negative sign in equation 2.47 causes  $\alpha_S$  to decrease with increasing  $Q$ .

The separation of a quark-antiquark pair eventually results in the production of a pair of quarks and the collimated *hadronisation* of the quarks, detected by experiments as jets.

An overview of the hadronisation process is shown in figure 2.3 for a high momentum quark-antiquark pair moving in opposing directions. As the distance between the two particles increases, the energy stored within the colour field increases until a point where it is energetically favourable to produce additional quark-antiquark pairs. This process concludes when the momentum of the quarks reduces to a point at which colourless hadrons form along the momentum vector of the initial high momentum quark. The process depicted in figure 2.3 results in the production of two observable back-to-back jets of hadrons. Top quarks do not hadronise, but instead decay in approximately  $0.5 \times 10^{-24}$  s, before the hadronisation process can occur [5].

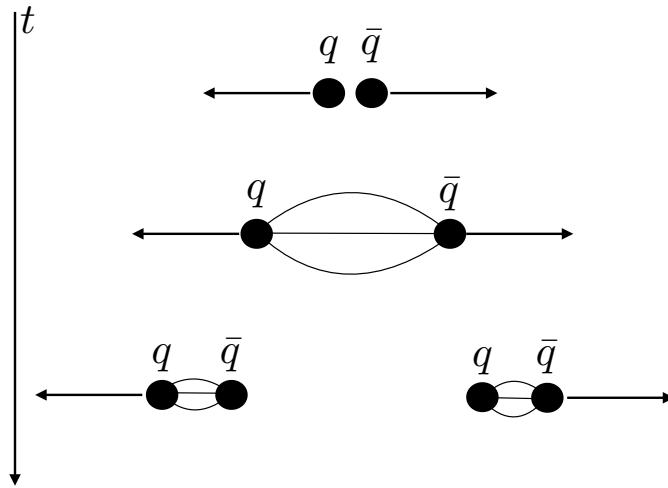


Fig. 2.3 A schematic view of the hadronisation process that follows the production of a high momentum quark-antiquark pair travelling in opposing directions. The increasing energy stored in the colour field as the quark-antiquark pair approach large distances is eventually sufficient to allow the creation of additional  $q\bar{q}$  pairs. The process pictured results in two back-to-back jets of hadrons. Figure adapted from [10].

As quark production only occurs in pairs, three-jet events necessarily include two quark jets and a third jet that arises from the radiation of a gluon from one of the high momentum quarks in a process termed ‘hard gluon bremsstrahlung’ (in analogy with electromagnetic bremsstrahlung). The hard gluon then subsequently hadronises and is detected as a jet. Hard gluons may go on to split into a pair of gluons ( $g \rightarrow gg$ ) or into a quark-antiquark pair ( $g \rightarrow q\bar{q}$ ), potentially increasing the number of observed hadronic jets within a detector.

### 2.2.5.1 Parton Interactions

Proton-proton collisions at the LHC occur at high centre-of-mass collision energies, corresponding to short distance interactions with low  $\alpha_S$ . As a result, an LHC collision involves momentum transfer between the constituent partons of the proton: the valance quarks, sea quarks and gluons. Partons carry a fraction  $x$  of the total proton momentum, dependent on the energy scale  $Q^2$ . The probability density of a parton possessing a momentum fraction  $x$  at energy scale  $Q^2$  is described by a parton distribution function (PDF).

PDFs are non-perturbative — they are calculated at low energy scales. The dependence of the PDF  $f_{i/p}(x, \mu_F^2)$  for a particle  $i$  on the arbitrarily chosen energy scale  $\mu_F$  is described by DGLAP equations [14–17], shown to leading order in the strong coupling ( $\alpha_S^1$ ) by equation 2.48:

$$\mu_F^2 \frac{\partial f_{i/p}(x, \mu_F^2)}{\partial \mu_F^2} = \sum_j \frac{\alpha_S(\mu_F^2)}{2\pi} \int_x^1 \frac{dz}{z} P_{i \leftarrow j}^{(1)}(z) f_{j/p}\left(\frac{x}{z}, \mu_F^2\right) \quad (2.48)$$

where  $z$  is the ratio of the parton momentum before and after gluon emission and  $P_{i \leftarrow j}^{(1)}(z)$  are the splitting functions [16], which characterise the probability densities of the emission of quarks and gluons from a parton.

After calculating the non-perturbative PDFs, they are evolved to higher energy scales using the DGLAP equations. Figure 2.4 shows an example PDF set calculated at next-to-leading order (NLO) in the strong coupling ( $\alpha_S^2$ ). The quarks present inside the proton at two energy scales are also shown, with  $b$  quarks not present until the momentum transfer  $Q$  is greater than the  $b$  quark mass, around 4.2 GeV.

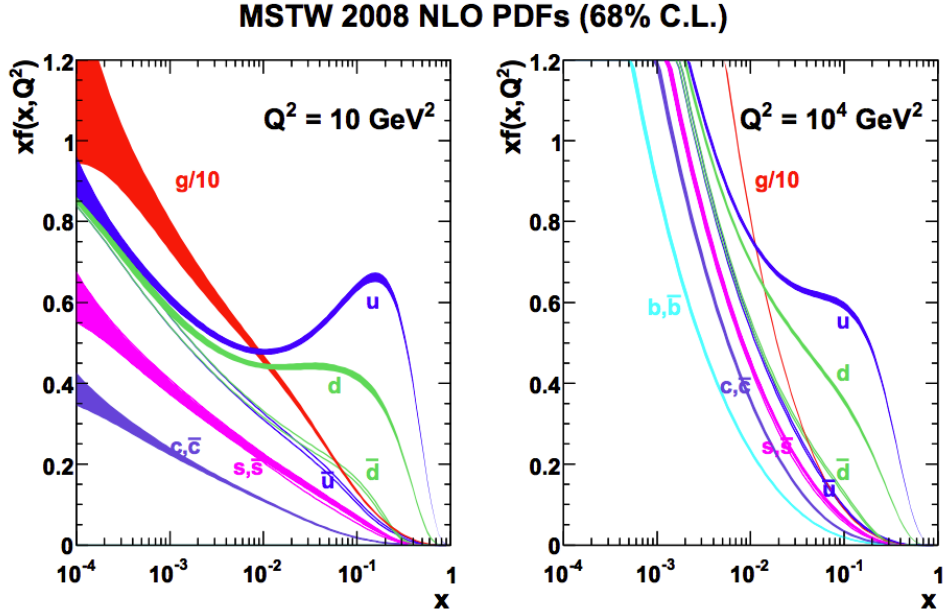


Fig. 2.4 Martin-Stirling-Thorne-Watt (MSTW) 2008 PDFs calculated at next-to-leading order (NLO) in  $\alpha_S$ . The left plot shows the PDF for  $Q^2 = 10 \text{ GeV}^2$  while the right plot shows the PDF for  $Q^2 = 10^4 \text{ GeV}^2$ . Gluons are observed to dominate at low  $x$ , while the light first generation quarks dominate at high values of  $x$ . Unlike the right plot with  $Q^2 = 10^4 \text{ GeV}^2$ , the left plot with  $Q^2 = 10 \text{ GeV}^2$  does not include  $b$  quarks as there is insufficient energy for their production. Similarly,  $t$ -flavour quarks are not accessible at either energy scale. Figure from [18].

The cross-section for the inclusive production of all particles as a result of parton scattering at the LHC is a combination of long and short distance effects and can be calculated as the product of the PDF and the cross-section of the hard parton scattering, derived from perturbative QCD, and is shown by equation 2.49 [19]:

$$\sigma(P_1 P_2 \rightarrow X) = \sum_{1,2} \int dx_1 dx_2 \underbrace{f_i(x_1, \mu_F^2) f_j(x_2, \mu_F^2)}_{\text{PDF}} \underbrace{\hat{\sigma}_{ij}(p_1, p_2, \alpha_S(\mu_R^2), Q^2/\mu_F^2, Q^2/\mu_R^2)}_{\text{hard scattering process}} \quad (2.49)$$

where  $X$  is any produced particle,  $i$  and  $j$  are the scattering partons,  $f(x, \mu_F)$  are the PDFs,  $p_{1,2}$  are the momenta of the scattering partons and  $\hat{\sigma}_{ij}$  is the cross-section for the hard parton interaction. The partonic cross-section can be expanded in powers of  $\alpha_S$ , with the lowest order of  $\alpha_S$  referred to as leading order (LO), the next lowest

## Theoretical Background

referred to as next-to-leading-order (NLO) and so on. The measured cross-section for inclusive jet production at  $\sqrt{s} = 13$  TeV within the ATLAS detector is shown in figure 2.5 as a function of  $p_T$  and jet rapidity. The NLO prediction shown in figure 2.5 describes the data well over a range of transverse momenta.

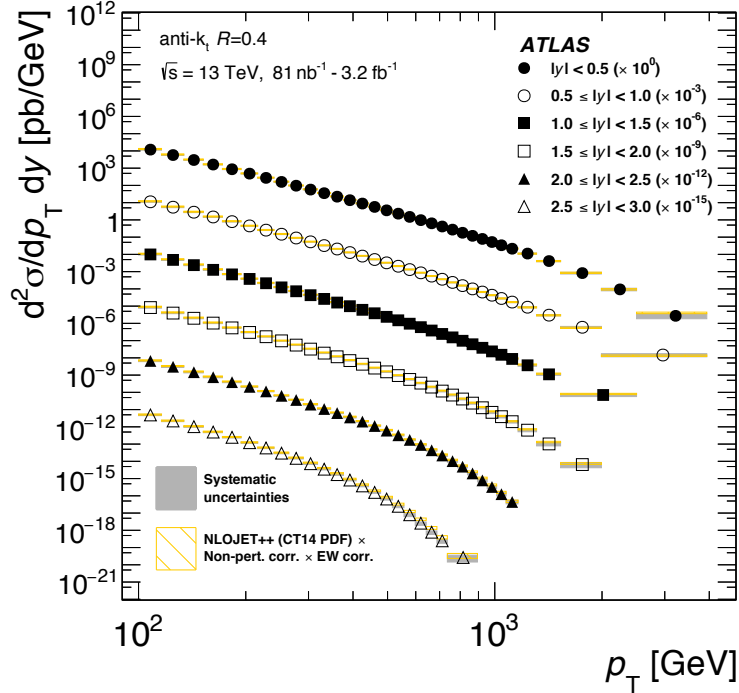


Fig. 2.5 Inclusive jet production cross-section in the ATLAS detector as a function of jet transverse momentum and rapidity  $y$  at  $\sqrt{s} = 13$  TeV. Data is shown with black points, while predictions derived with perturbative QCD to NLO in  $\alpha_S$  are shown by yellow bands. Jets are defined using the anti- $k_t$  algorithm [20] with  $\Delta R = 0.4$ . Figure from [21].

### 2.2.5.2 The Structure of an Event

Events in the ATLAS detector are defined by selecting a collision of interest and identifying the origin of a hard parton scattering from the final collection of observed objects, while discounting additional activity in the detector that does not arise from the hard interaction. Jets observed in the detector are intrinsically linked to the initial hard scattering and their measurement can be viewed as a test of QCD.

Energetic partons may emit *initial state radiation* (ISR) as partons prior to the hard scatter of interest, which may undergo further fragmentation and momentum loss before hadronisation and measurement in the detector. Any parton emission, showering and hadronisation occurring directly as a result of the hard interaction is referred to as *final state radiation* (FSR). Partons present in the proton-proton collision that do not take part in the hard interaction may still scatter with other partons before undergoing parton showering and hadronisation – this process is referred to as the *underlying event* (UE). A simulated event in a hadron collider is shown in figure 2.6 at the parton level.

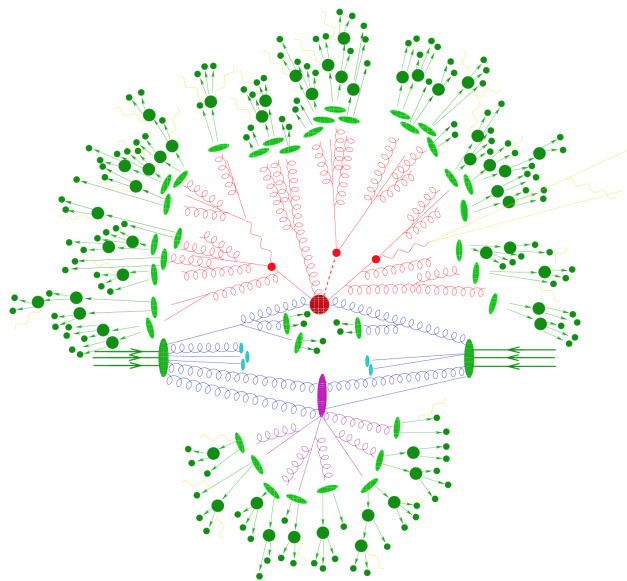


Fig. 2.6 Diagram of a  $t\bar{t}H$  event in a hadron-hadron collision simulated by the SHERPA Monte Carlo event generator [22]. The largest red circle represents the hard interaction, while the smaller red circles represent the production of a pair of  $t$  quarks and a Higgs boson. Top quark and Higgs decays are represented by the lines emanating from the smaller red circles. Hard QCD radiation is shown by red lines. The underlying event is shown in purple. Particles shower and form colourless hadrons (light green ovals) that may decay and be observed in a detector (dark green circles). Radiation of leptons is shown in yellow. Figure from [22].

The hard collision in the figure occurs between two gluons radiated from the hadrons and is shown by the large red circle. The production of a pair of  $t$ -quarks and a Higgs boson is shown by the smaller red circles. The underlying event, collisions occurring between those partons not present in the hard interaction, is shown by the purple circle. Partons are then observed to shower, splitting into additional partons of lower

## Theoretical Background

---

momentum (predominantly collinearly with the original parton [5]) before undergoing the process of hadronisation shown in light green in figure 2.6 at a sufficiently low momentum. Finally, the decay of unstable hadrons is shown in dark green in figure 2.6. Collimated bunches of hadrons are then detected and arranged into jets.

## 2.3 Limitations of the Standard Model

Despite the success of the SM, various observed phenomena are left entirely unexplained by the model.

The presence of Dark Matter (DM) in the universe was inferred by the inability of visible matter to account for the shape of galactic rotation curves. Galactic rotation curves show the relationship between the velocity of objects within a galaxy as a function of their distance from the galactic centre. Predictions of the shape of galactic rotation curves derived from all visible matter in a galaxy do not account for the observed curves, leading to the conclusion that invisible matter is present within a galaxy in addition to luminous matter [23]. DM is believed to compose around 25% of the energy density of the universe, yet no candidate particle exists within the SM.

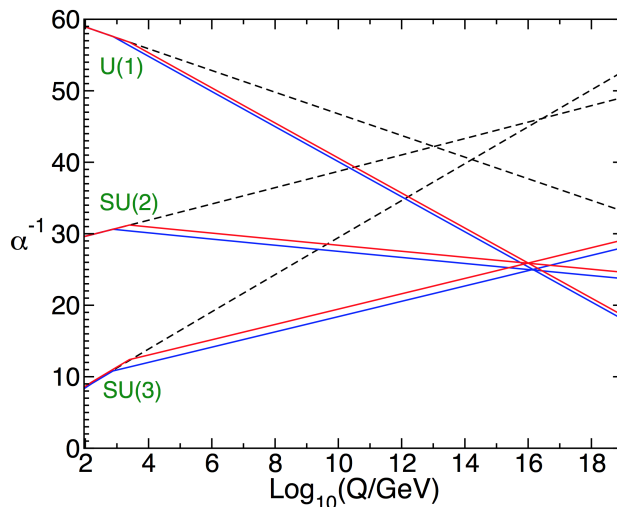


Fig. 2.7 Evolution of the inverse coupling strengths for the three fundamental interactions described by the Standard Model as a function of energy scale  $Q$ . The evolution of the coupling strength is calculated at the two-loop level. The dashed lines show the evolution of the coupling constants as a function of energy scale within the SM, where they do not cross. The solid lines display the same evolution within the MSSM, where the couplings achieve the same value at high energies due to the extra particle content. Figure from [24].

The existence of a ‘Grand Unified Theory’ unifying the strong and electroweak interactions at some high energy scale could have a profound impact on our understanding of the universe. The dashed lines in figure 2.7 show the running couplings for the interactions within the SM. There is no energy scale at which the strength of couplings of the strong and electroweak interactions are equivalent. The additional particles present in the MSSM (shown by the solid line in figure 2.7) cause the coefficients of the beta-functions describing the running couplings to increase. This has the effect of allowing the coupling constants to converge at an energy scale of around  $10^{16}$  GeV.

### 2.3.1 Hierarchy Problem

One of the main motivations for the construction of models of physics beyond the standard model is the search for a solution to the *hierarchy problem* [25–28]. New physics is required at some scale below the Planck scale  $M_P \sim 10^{18}$  GeV to explain physical phenomena unaccounted for by the SM. It appears unlikely that no new physics exists in the vast range between the weak and Planck scales. As described in

## Theoretical Background

---

section 2.2.4.2, the coupling of a particle to the Higgs field is proportional to the mass of the particle. The mathematical formalism that follows in this section and section 2.4 closely follows [24]. The square of the Higgs mass  $m_H^2$  receives corrections from every particle that couples to the Higgs field, proportional to the mass of the particle. The mass of the observed Higgs boson is a combination of the bare Higgs mass and the additional contributions from the particles that couple to the Higgs field

$$m_H^{\text{obs}} = m_H^{\text{bare}} + \Delta m_H \quad (2.50)$$

The neutral component of the SM Higgs field has potential

$$V = m_H^2 |H|^2 + \lambda |H|^4 \quad (2.51)$$

with  $H$  a complex scalar and  $\lambda$  the Yukawa coupling strength. The correction to the squared Higgs mass from fermions with mass  $m_f$  is

$$\Delta m_H^2 = -\frac{|\lambda_f|}{8\pi^2} \Lambda_{\text{UV}}^2 + \dots \quad (2.52)$$

where  $\Lambda_{\text{UV}}$  is the ultraviolet momentum cutoff scale, the minimum energy scale at which effects from new physics become important. As the SM is an effective field theory, it is assumed to work only up to this energy scale. The correction to  $m_H^2$  due to all fermions is shown in figure 2.8, with the  $t$  quark providing the largest correction to  $m_H^2$ .

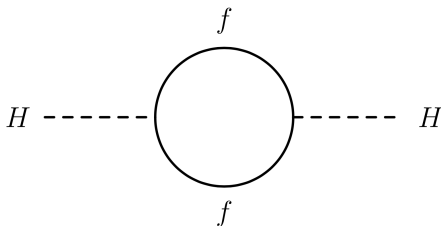


Fig. 2.8 Fermionic one-loop correction to the squared Higgs mass  $m_H^2$ .

If  $\Lambda_{\text{UV}}$  is set to  $M_P$ , the correction is quadratically divergent. These corrections could be cancelled ‘by hand’, however the problem remains that the squared Higgs mass is extremely sensitive to corrections from any heavy particles with masses far greater than the weak scale. It could be expected that such large corrections to  $m_H^2$  would

cause the Higgs boson to have a mass well above the weak energy scale. However, the Higgs boson is observed experimentally to have a mass of approximately 125 GeV. The relatively low mass of the observed Higgs boson (when compared to  $M_P$ ) suggests a high level of fine-tuning to remove correction effects, or some new physical model that can account for the corrections.

## 2.4 Supersymmetry

SUSY [29–34] models suggest a fermion-boson symmetry as an extension to the SM. The symmetry is said to be *broken* as the masses of SUSY particles (sparticles) are expected to be greater than the masses of the SM particles they correspond to, if they are to exist. If physical sparticles and particles were mass-degenerate, sparticle production could occur at similar rate to particle production and their prior discovery would be likely.

If there is such a fermion-boson symmetry the correction to  $m_H^2$  from scalar particles is

$$\Delta m_H^2 = \frac{|\lambda_s|}{16\pi^2} \Lambda_{\text{UV}}^2 + \dots \quad (2.53)$$

and is illustrated in figure 2.9. If there are two complex scalars corresponding to each SM fermion, each with  $\lambda_s = |\lambda_f|^2$ , the relative minus sign between equation 2.52 and equation 2.53 neatly cancels corrections to  $m_H^2$ , providing an elegant solution to the Hierarchy problem.

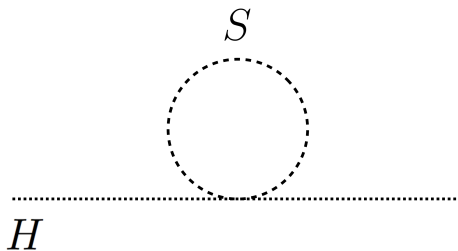


Fig. 2.9 One-loop correction to  $m_H^2$  due to a scalar particle.

The SUSY operator  $Q$  generates transformations of fermions to bosons and vice versa, where  $Q$  and its hermitian conjugate  $Q^\dagger$  are spin-1/2 fermionic operators, which satisfy the (anti-)commutation relations [24]:

$$\{Q, Q^\dagger\} = P^\mu \quad (2.54)$$

$$\{Q, Q\} = \{Q^\dagger, Q^\dagger\} = 0 \quad (2.55)$$

$$[P^\mu, Q] = [P^\mu, Q^\dagger] = 0 \quad (2.56)$$

$$(2.57)$$

and  $P^\mu$  is the four-momentum generator.

SM particles and their superpartners differ by spin- $\frac{1}{2}$ . Particle states in SUSY are arranged in *supermultiplets* containing both particle and superpartner states, where both particles in the supermultiplet have equal mass. Particles located within a supermultiplet share the same electric charge, colour and weak isospin.

SUSY models are categorised by the number of distinct copies of the generators  $Q, Q^\dagger$  they possess — the simplest models contain a single set of SUSY generators and are referred to as  $N = 1$  SUSY models.

### 2.4.1 R-parity

Baryon and lepton-number violating terms can appear in SUSY models. No such process has, to date, been observed experimentally. A symmetry is introduced in some SUSY models (including the MSSM) that enforces the conservation of  $B$  and  $L$  and is termed  $R$ -parity [35], a multiplicative quantum number defined as

$$P_R = (-1)^{3(B-L)+2s} \quad (2.58)$$

with  $B, L, s$  the baryon, lepton and spin quantum numbers, respectively. Values of  $P_R = +1$  are given to SM particles, while  $P_R = -1$  is given to all SUSY particles. The conservation of  $R$ -parity enforces the pair production of sparticles, their decay into odd numbers of lighter sparticles and the existence of a light, stable particle at the end of the decay chain termed the *lightest supersymmetric particle* (LSP). If it is also neutral, it is an ideal candidate for WIMP dark matter as it will interact solely via the gravitational interaction. In particle colliders, direct detection of a neutral LSP is not possible, as there is no mechanism through which the particle can interact with the

detector. Its presence is instead inferred by significant momentum imbalance in the transverse plane of the detector.

### 2.4.2 Soft Supersymmetry Breaking

It is clear that supersymmetry is a broken symmetry, as it otherwise suggests that particle-superpartner pairs are mass degenerate. The lack of observation of these particles in experiments suggests that the superpartners cannot possess the same mass as their SM partner if they are to exist at all. Therefore, some mechanism is required to break supersymmetry. The symmetry must be broken spontaneously but *softly*, in such a way that the terms in the Lagrangian that cancel any corrections to  $m_H^2$ , and that made SUSY an attractive theoretical pursuit in the first place, are retained. The simplest method of introducing soft symmetry breaking is to introduce explicit symmetry breaking terms into the Lagrangian. The MSSM Lagrangian can be written

$$\mathcal{L} = \mathcal{L}_{\text{SUSY}} + \mathcal{L}_{\text{soft}} \quad (2.59)$$

where  $\mathcal{L}_{\text{soft}}$  contains SUSY-violating terms with positive mass dimension. Corrections to the Higgs mass due to the SUSY-breaking term are of the form [24]:

$$\Delta m_H^2 = m_{\text{soft}}^2 \left[ \frac{\lambda}{16\pi^2} \ln \left( \frac{\Lambda_{\text{UV}}}{m_{\text{soft}}} \right) + \dots \right] \quad (2.60)$$

which do not increase as  $\Lambda_{\text{UV}}^2$  and vanish as  $m_{\text{soft}} \rightarrow 0$ .

*Naturalness* arguments suggest that the superpartner particle masses should not be much greater than the TeV scale, or the elegant solution to the hierarchy problem where corrections to  $m_H^2$  cancel with the introduction of SUSY is replaced with a ‘little-hierarchy’ problem where large corrections to  $m_H^2$  remain. Naturalness argues that any residual correction to  $m_H^2$  should be minimal, which results in light masses for SUSY particles [36]. The upper mass limits of the superpartners of the  $t$  and  $b$  quarks are the most constrained by requiring highly natural SUSY, which may be produced as the lightest accessible squarks at the LHC if other squarks are effectively decoupled with much greater mass. Recently it has become increasingly theoretically acceptable to relax previously strict requirements on highly natural SUSY, increasing the upper mass limits of SUSY particles sometimes to masses beyond the capabilities of the LHC [36].

## Theoretical Background

Table 2.4 MSSM supermultiplets of spin- $\frac{1}{2}$  left-handed massless fermions, spin-0 Higgs bosons and their supersymmetric partners (denoted with a tilde). There are three families of (s)quarks and (s)leptons, only the first is displayed in this table. From [24].

Particles	Supermultiplet Name	Spin-0	Spin- $\frac{1}{2}$	$SU(3)_C, SU(2)_L, U(1)_Y$
<b>(s)quarks</b>				
	$Q$	$(\tilde{u}_L, \tilde{d}_L)$	$(u_L, d_L)$	$(\mathbf{3}, \mathbf{2}, \frac{1}{6})$
	$\bar{u}$	$\tilde{u}_R^*$	$u_R^\dagger$	$(\bar{\mathbf{3}}, \mathbf{1}, -\frac{2}{3})$
	$\bar{d}$	$\tilde{d}_R^*$	$d_R^\dagger$	$(\bar{\mathbf{3}}, \mathbf{1}, \frac{1}{3})$
<b>(s)leptons</b>				
	$L$	$(\tilde{\nu}, \tilde{e}_L)$	$(\nu, e_L)$	$(\mathbf{1}, \mathbf{2}, -\frac{1}{2})$
	$\bar{e}$	$\tilde{e}_R^*$	$e_R^\dagger$	$(\mathbf{1}, \mathbf{1}, 1)$
<b>Higgs(inos)</b>				
	$H_u$	$(H_u^+, H_u^0)$	$(\tilde{H}_u^+, \tilde{H}_u^0)$	$(\mathbf{1}, \mathbf{2}, \frac{1}{2})$
	$H_d$	$(H_d^0, H_d^-)$	$(\tilde{H}_d^0, \tilde{H}_d^-)$	$(\mathbf{1}, \mathbf{2}, -\frac{1}{2})$

### 2.4.3 Minimal Supersymmetric Standard Model

The MSSM [35, 37, 38] is an extension of the SM containing the minimal necessary number of additional supersymmetries and conserving  $R$ -parity. The supermultiplets of particles within the MSSM are shown in table 2.4 and table 2.5 and are characterised by their particle content.

The scalar superpartners of quarks and leptons are referred to as *squarks* and *sleptons*. As the superpartners (denoted with a tilde) of the massless left and right handed fermions are complex spin-0 particles, they do not possess the quality of ‘handedness’. Therefore, the subscripts  $L$  and  $R$  in table 2.4 refer to the ‘handedness’ of the corresponding SM particle. Gauge bosons and their spin- $\frac{1}{2}$  superpartners (*gauginos*) are arranged into the supermultiplets shown in table 2.5. The W and B bosons have the superpartners *wino* and *bino*, while the partner to the gluon is referred to as the *gluino*.

The names of the supermultiplets are included in second column of table 2.4. The bar over some supermultiplet names is purely naming convention. The superpartners undergo the same gauge interactions as their SM partners. The left-handed doublet  $(\tilde{u}_L, \tilde{d}_L)$  experiences the weak interaction, whereas the singlet state  $\tilde{u}_R^*$  cannot.

## 2.5 SUSY Production at the LHC

Table 2.5 MSSM supermultiplets of spin-1 gauge bosons and spin- $\frac{1}{2}$  fermionic super-symmetric partners (denoted with a tilde). From [24].

Particles	Spin-1	Spin- $\frac{1}{2}$	$SU(3)_C, SU(2)_L, U(1)_Y$
gluon, gluino	$g$	$\tilde{g}$	$(\mathbf{8}, \mathbf{1}, 0)$
W-bosons, winos	$W^\pm, W^0$	$\tilde{W}^\pm, \tilde{W}^0$	$(\mathbf{1}, \mathbf{3}, 0)$
B-boson, bino	$B^0$	$\tilde{B}^0$	$(\mathbf{1}, \mathbf{1}, 0)$

The Higgs boson is described by a complex scalar doublet in the SM. In the MSSM, two supermultiplets containing scalar spin-0 Higgs bosons and fermionic spin- $\frac{1}{2}$  *higgsinos* are required to retain electroweak gauge invariance. The supermultiplets are termed  $H_u$  and  $H_d$  and give masses to up-type and down-type quarks, respectively. The Higgs supermultiplets form five Higgs bosons: a light neutral Higgs boson  $h$ , a heavy neutral Higgs  $H^0$ , two charged Higgs bosons  $H^\pm$  and a pseudo-scalar  $A$ . The Higgs boson discovered at the LHC in 2012 with a mass of approximately 125 GeV is believed to correspond to the light neutral Higgs  $h$  in the MSSM.

Gauginos and Higgsinos mix in neutral and charged states to produce distinct mass eigenstates. Combinations of the neutral bino  $\tilde{B}^0$ , wino  $\tilde{W}^0$  and higgsinos  $\tilde{H}_u^0, \tilde{H}_d^0$  form four *neutralinos*:  $\tilde{\chi}_{1,2,3,4}^0$  with  $\tilde{\chi}_1^0$  the lightest neutralino, commonly assumed to be the LSP. Similarly, charged winos  $\tilde{W}^\pm$  and the charged higgsinos  $\tilde{H}_u^\pm, \tilde{H}_d^\pm$  form four *charginos*  $\tilde{\chi}_{1,2}^\pm$ . The squarks  $\tilde{q}_L$  and  $\tilde{q}_R$  mix to form two mass eigenstates  $\tilde{q}_1$  and  $\tilde{q}_2$ , where a larger subscript indicates greater mass.

## 2.5 SUSY Production at the LHC

The production of squarks and gluinos via the strong interaction represents the largest potential SUSY production cross-section at the LHC and is therefore targeted by many ATLAS and CMS analyses. Figure 2.10 shows the potential SUSY production cross sections for inclusive strong production and the production of the superpartners of the third generation squarks at LHC centre-of-mass collision energy of  $\sqrt{s} = 13$  TeV.

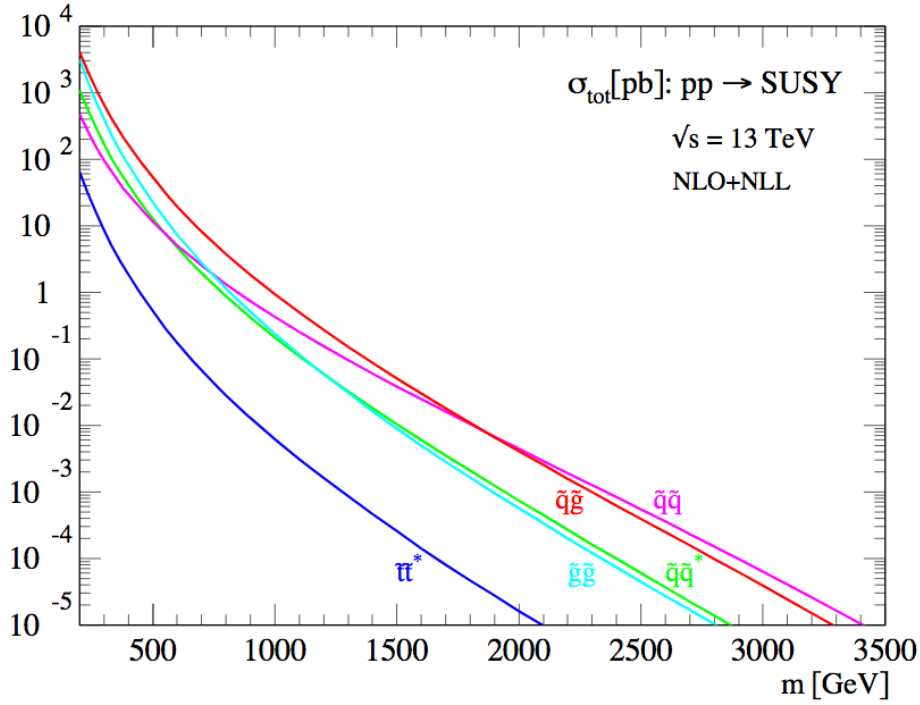


Fig. 2.10 Estimated SUSY production cross-sections at  $s = \sqrt{13}$  TeV are shown for various processes. Figure from [39].

In searches for strongly produced SUSY, the supersymmetric partners of the first two generations of left and right-handed quarks  $q_{L,R}$  mix to form squarks with mass eigenstates  $\tilde{q}_{1,2}$ , denoted by increasing mass. Searches for inclusive squark and gluino production often interpret their results in simplified MSSM-inspired models, which consider the supersymmetric partners of the first and second generation quarks to be mass-degenerate and accessible by the LHC, with any other supersymmetric particle mass too large for production at  $\sqrt{s} = 13$  TeV. Figure 2.11 shows the interactions responsible for squark and gluino production at the LHC.

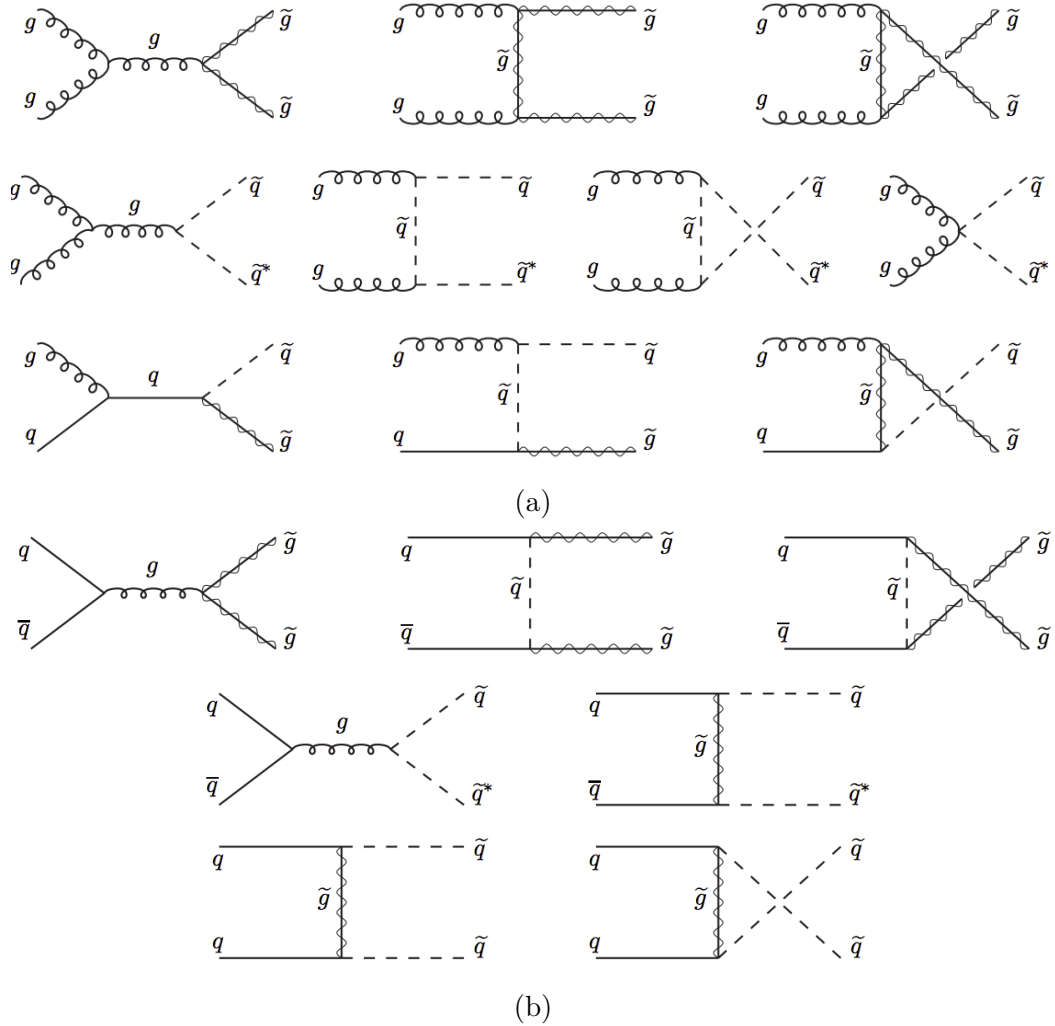


Fig. 2.11 Feynman diagrams showing the various processes through which the strong production of squarks and gluinos may occur in the LHC. Squark and gluino production via gluon-gluon and quark-quark fusion is shown in (a), while (b) shows  $q\bar{q}$  annihilation and  $qq$  scattering. Figure from [24].

The direct production of the superpartners of third generation quarks has a lower potential cross-section than inclusive squark or gluino production. However, if the SUSY mass hierarchy is such that gluinos and the superpartners of the first two quark generations are too massive for production at  $\sqrt{s} = 13$  TeV, direct production of third generation squarks may represent the largest SUSY production cross-section at the LHC.

Searches for the direct production of the supersymmetric partners of third-generation quarks consider simplified models where the mass eigenstates  $\tilde{b}_1$  and  $\tilde{t}_1$  (formed by the

## Theoretical Background

---

mixing of the superpartners of the left and right-handed chiral components of the  $t$  and  $b$  quarks  $\tilde{b}_{(L,R)}$  and  $\tilde{t}_{(L,R)}$  are the lightest squarks and the only ones accessible by the LHC. In this scenario, all other SUSY particles are too massive for LHC production at  $\sqrt{s} = 13$  TeV.

R-parity conserving (RPC) SUSY searches at the LHC, on which this thesis focuses, do not allow the production of SUSY particles with subsequent decay to final states of exclusively SM particles. While SM particles often feature in the decay chain of heavy SUSY particles in simplified SUSY models, a stable LSP remains amongst the other SM decay products. ATLAS SUSY searches that enforce R-parity conservation are often characterised by final states of leptons and jets (arising from the decay of a SUSY particle) in addition to the presence of significant missing transverse momentum in the detector, interpreted as the production of the LSP which escapes without detection.

### 2.5.1 Previous Inclusive SUSY Searches at the LHC

This section provides a brief overview of the status of inclusive searches for SUSY at the LHC prior to the start of the  $\sqrt{s} = 13$  TeV collision energy campaign, a classification of SUSY searches which were considered to have the greatest chance of making an early SUSY discovery at the higher collision energy.

Inclusive SUSY searches [40] place the least stringent requirements on the number of particles observed in the final state of an LHC collision and are therefore potentially sensitive to the early discovery of an excess of events consistent with the production of a SUSY particle. SUSY particles may undergo complex decay chains producing many high- $p_T$  SM particles and will result in the detection of large missing transverse momentum due to the undetected LSP. Inclusive searches consider states of two or more jets accompanied by large missing transverse momentum and zero or more leptons.

Prior to 2015 the LHC provided a centre-of-mass collision energy of  $\sqrt{s} = 8$  TeV. A rich SUSY search programme was undertaken during this first era of LHC operation by both the ATLAS and CMS experiments, exploring large regions of the parameter space of various SUSY signal models. No evidence for SUSY production was found. Lower limits were placed on the masses of SUSY particles in the context of simplified

MSSM-inspired models where only one or two SUSY particles of interest are within the energy reach of the LHC. Limits on the masses of squarks and gluinos for varying  $\tilde{\chi}_1^0$  masses in the context of simplified models are shown in figures 2.12–2.14, obtained from both experiments.

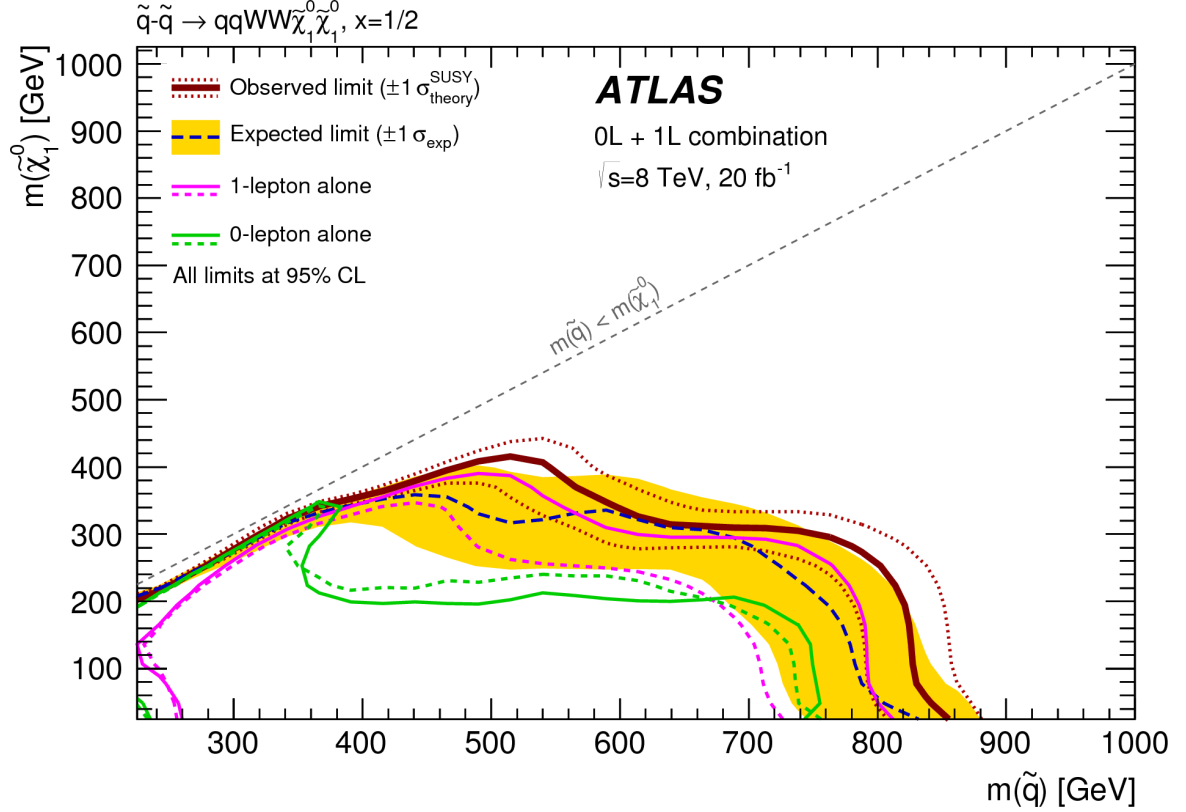


Fig. 2.12 Exclusion limits in simplified MSSM-inspired models featuring squark pair production followed by a decays to  $\tilde{\chi}_1^\pm$  with the subsequent decay of the  $\tilde{\chi}_1^\pm$  to  $\tilde{\chi}_1^0$  and a W boson due to using  $20 \text{ fb}^{-1}$  of ATLAS  $\sqrt{s} = 8 \text{ TeV}$  data. The observed (expected) limits derived from two separate analyses are shown separately by solid (dashed) pink and green lines. The combined expected exclusion limit is shown by the dashed blue line, with yellow bands indicating experimental uncertainties. The observed exclusion limit from the combination of both analyses is shown by the solid dark red line. Dotted red lines show the  $1 \sigma$  uncertainty on the cross-section of the signal process. The boundary of the forbidden region in which  $\tilde{\chi}_1^0$  is more massive than the produced SUSY particle is shown by the diagonal dashed grey line. No evidence for SUSY production was found, areas below the observed limit are excluded at 95% CL. Figures from [41].

## Theoretical Background

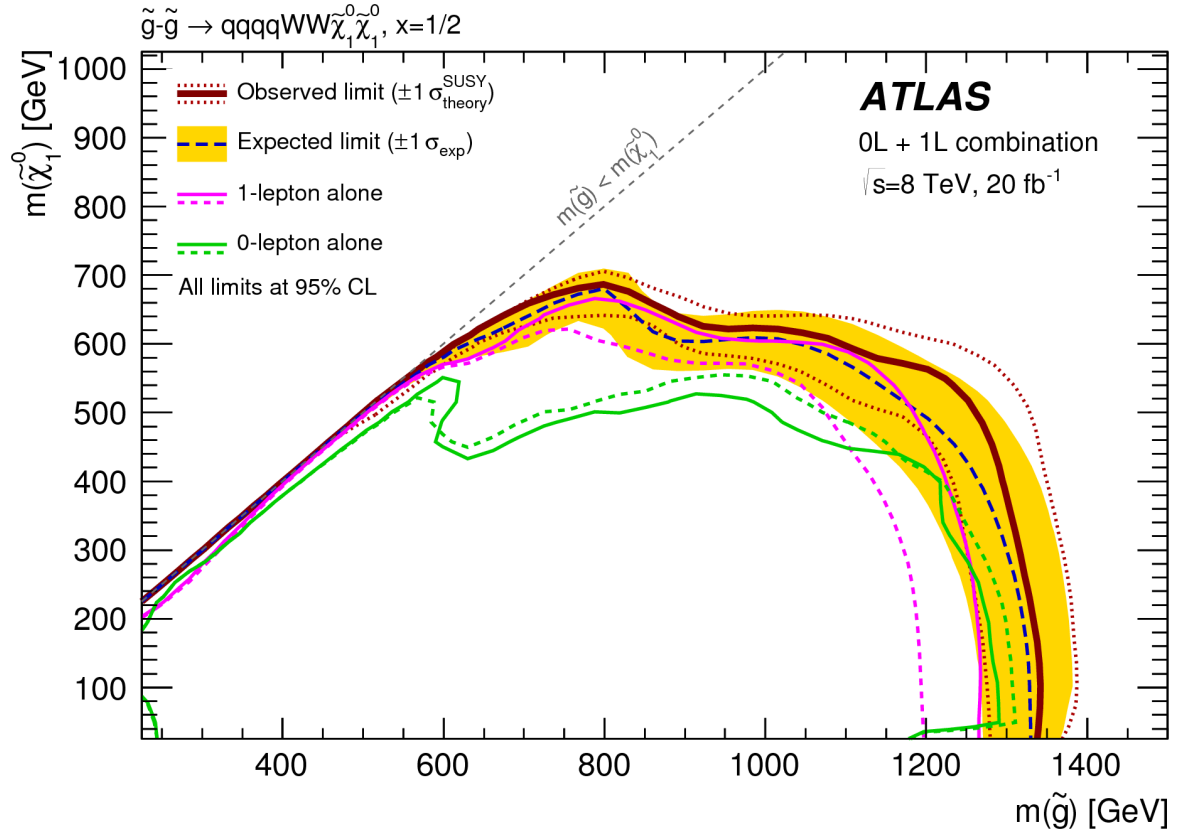


Fig. 2.13 Exclusion limits in simplified MSSM-inspired models featuring gluino pair production followed by a decays to  $\tilde{\chi}_1^\pm$  with the subsequent decay of the  $\tilde{\chi}_1^\pm$  to  $\tilde{\chi}_1^0$  and a W boson due to using  $20 \text{ fb}^{-1}$  of ATLAS  $\sqrt{s} = 8 \text{ TeV}$  data. The observed (expected) limits derived from two separate analyses are shown separately by solid (dashed) pink and green lines. The combined expected exclusion limit is shown by the dashed blue line, with yellow bands indicating experimental uncertainties. The observed exclusion limit from the combination of both analyses is shown by the solid dark red line. Dotted red lines show the  $1 \sigma$  uncertainty on the cross-section of the signal process. The boundary of the forbidden region in which  $\tilde{\chi}_1^0$  is more massive than the produced SUSY particle is shown by the diagonal dashed grey line. No evidence for SUSY production was found, areas below the observed limit are excluded at 95% CL. Figures from [41].

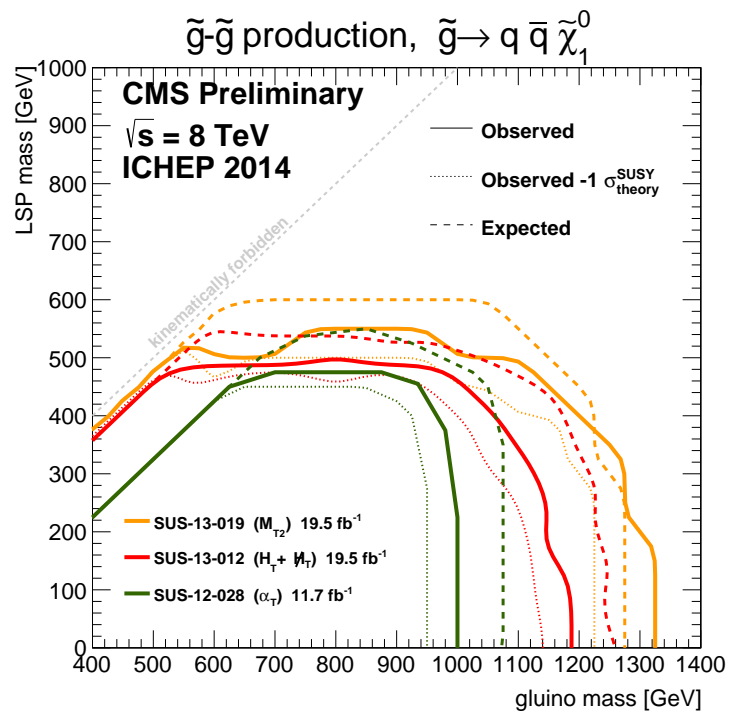
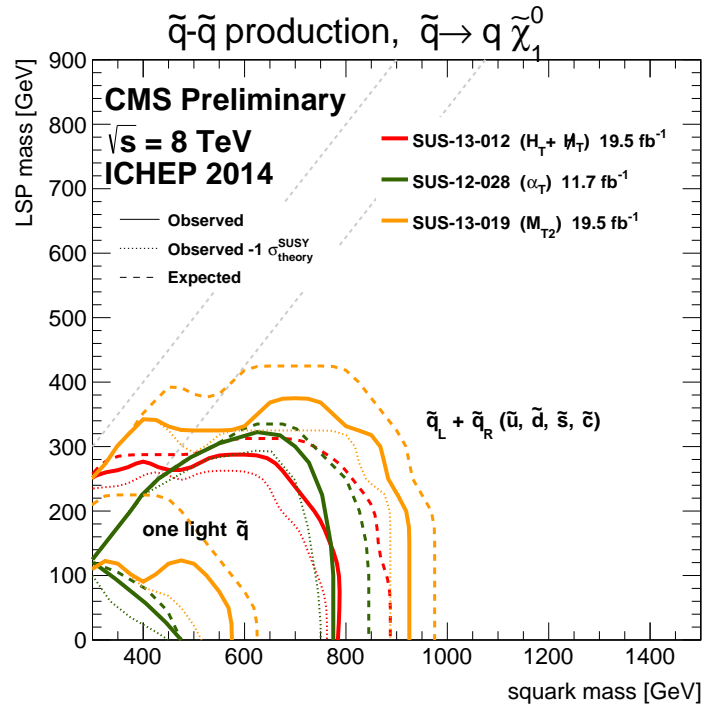


Fig. 2.14 CMS  $\sqrt{s} = 8$  TeV exclusion limits in simplified models for (a) squark pair production directly decaying to quarks and  $\tilde{\chi}_1^0$  and (b) gluino pair production directly decaying to quarks and  $\tilde{\chi}_1^0$ . No evidence for SUSY production was found, exclusion limits are shown. Figures from [42].

## Theoretical Background

---

The initial LHC search campaign excluded gluino masses less than 1.3 TeV and squark masses less than approximately 850 GeV in the case of a massless  $\tilde{\chi}_1^0$ . Lower mass limits are excluded for squarks and gluinos in more compressed regions, where the mass difference between the LSP and  $\tilde{q}$  or  $\tilde{g}$  is small. Much of the MSSM parameter space was left unexplored at  $\sqrt{s} = 8$  TeV and SUSY as a concept was far from excluded.

# Chapter 3

## The ATLAS Detector at the LHC

This chapter provides a brief overview of the components of the ATLAS detector situated at the LHC. The general concepts of hadron colliders and aspects of the analysis of the collision data obtained is discussed.

### 3.1 Physics with Hadron Colliders

In circular colliding beam experiments two beams of particles are accelerated and brought together to collide at interaction points situated within or near a detector. At the centre-of-mass collision energies reached at the LHC, hadron collisions are preferred over electrons in order to mitigate the large energy losses faced by electrons in circular colliders. The energy of the electromagnetic radiation emitted by a charged particle accelerated along a circular path, synchrotron radiation, is inversely proportional to the mass of the accelerating particle and follows the relation [43]:

$$\frac{dE}{dt} \propto \frac{E^4}{m^4} \quad (3.1)$$

where  $E$  and  $m$  are the energy and mass of the charged particle.

Electron colliders feature collisions between two elementary particles, leaving the entire centre-of-mass collision energy from the two electrons available for the production of

new particles. Hadronic  $p$ - $p$  collisions, however, result in a hard scattering between constituent partons of each colliding proton, with a fraction  $x$  of the total proton momentum described by PDFs and discussed in section 2.2.5.1. The quoted  $p$ - $p$  centre-of-mass collision energy of  $\sqrt{s} = 13$  TeV is not equal to the actual collision energy involved in the hard scattering of two partons. The centre-of-mass energy of the hard scattering process is proportional to  $\sqrt{s}$ , but is necessarily lower and equal to

$$\sqrt{s_{\text{hard scatter}}} = \sqrt{x_1 x_2 s} \quad (3.2)$$

where  $x_1$  and  $x_2$  are the momentum fractions carried by the partons taking part in the hard scatter. Hadron colliders therefore face a source of uncertainty in the actual centre-of-mass collision energy in each hard scattering that is not present in electron colliders. The LHC collides bunches of protons, with each bunch containing up to  $1.15 \times 10^{11}$  protons per bunch [44], often resulting in multiple proton collisions within each bunch crossing. This effect is termed pile-up and is discussed in section 3.4.1.1.

### 3.1.1 Luminosity

Particle accelerators are characterised by their instantaneous luminosity  $\mathcal{L}$ . When coupled with the cross-section  $\sigma$  of a process, the number of events generated each second by particle collisions for that particular process can be determined. The instantaneous luminosity is given by [10]:

$$\mathcal{L}(t) = f \frac{n_1 n_2}{4\pi\sigma_x\sigma_y} \quad (3.3)$$

where  $f$  is the collision frequency of proton bunches,  $n_1$  and  $n_2$  are the number of particles in each of the two colliding bunches,  $\sigma_{x,y}$  correspond to the  $x$  and  $y$  dimensions of the beam and it is assumed that the bunches collide head-on with a Gaussian profile. The LHC operates with a 25 ns bunch spacing, corresponding to a collision frequency  $f = 40$  MHz.

For a given process, the total number of events recorded in a particular amount of time is equal to

$$N_{\text{event}} = \sigma_{\text{event}} \int \mathcal{L}(t) dt \quad (3.4)$$

where  $\int \mathcal{L}(t) dt$  is commonly denoted as  $L$ , the *integrated luminosity* with dimensions of inverse area. In the ATLAS [1] and CMS (**C**ompact **M**uon **S**olenoid) [2] experiments, integrated luminosity is a measure of the amount of data recorded and is commonly expressed in inverse femtobarns  $\text{fb}^{-1}$ , where  $1 \text{ fb}^{-1} = 10^{15} \text{ b}^{-1}$ .

An estimate of the production cross sections of a collection of SM processes in the LHC at various centre of mass collision energies is given in figure 3.1, showing that jet production represents the dominant process of interest and potentially the largest background in analyses following proton-proton collisions at the centre-of-mass energies probed by the LHC.

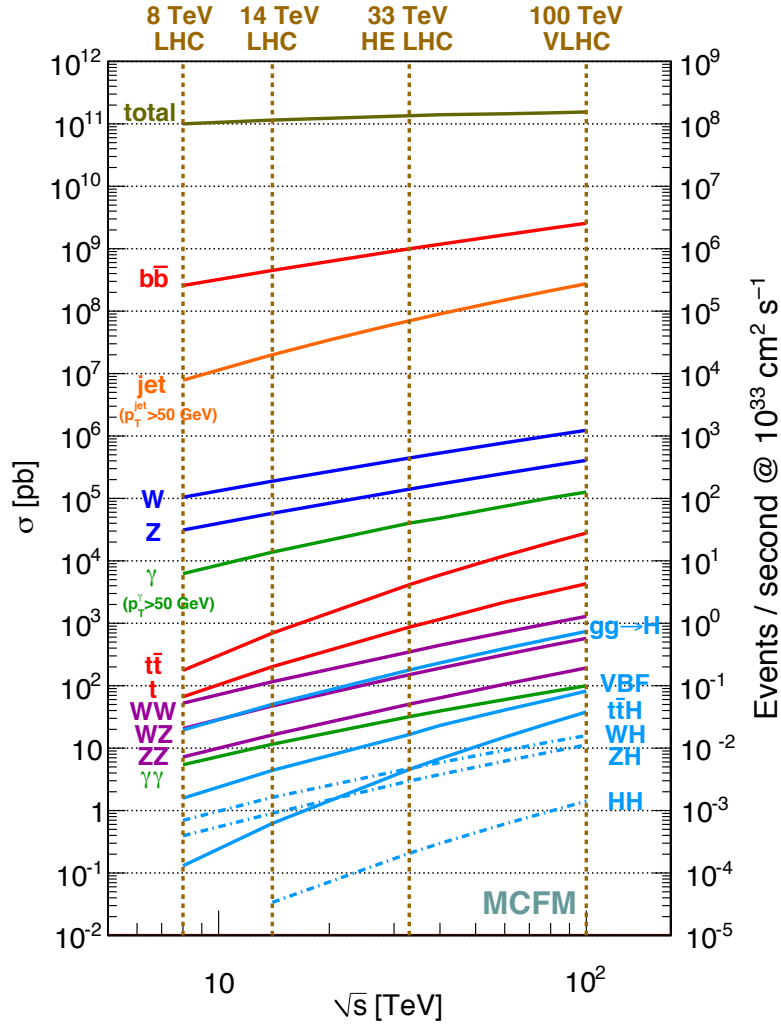


Fig. 3.1 Predictions of proton-proton production cross sections for various SM processes at the LHC using several centre-of-mass collision energies. The matrix elements for the processes considered were calculated at next-to-leading order (NLO) in the strong coupling  $\alpha_S$ . Figure from [45].

### 3.2 The Large Hadron Collider

The LHC is a 26.7 km circumference circular proton-proton ( $p$ - $p$ ) and heavy ion collider located at CERN (European Organisation for Nuclear Research) [46]. Its position within the CERN complex is shown in figure 3.2, where components relevant to the

### 3.2 The Large Hadron Collider

LHC are labelled. The LHC initially performed  $p$ - $p$  collisions at a centre-of-mass collision energy of  $\sqrt{s} = 7$  TeV and subsequently 8 TeV from 2010 to 2012, a data-taking period referred to as ‘Run-1’. The centre-of-mass collision energy was increased to  $\sqrt{s} = 13$  TeV for the ongoing data taking campaign referred to as ‘Run-2’ that began in 2015 and will run until late 2018. The collider is designed to operate at an instantaneous luminosity of  $10^{34}\text{cm}^{-2}\text{s}^{-1}$  for  $\sqrt{s} = 14$  TeV  $p$ - $p$  collisions, while the design instantaneous luminosity for  $\sqrt{s} = 5.5$  TeV lead nucleus collisions is  $10^{27}\text{cm}^{-2}\text{s}^{-1}$  [1].

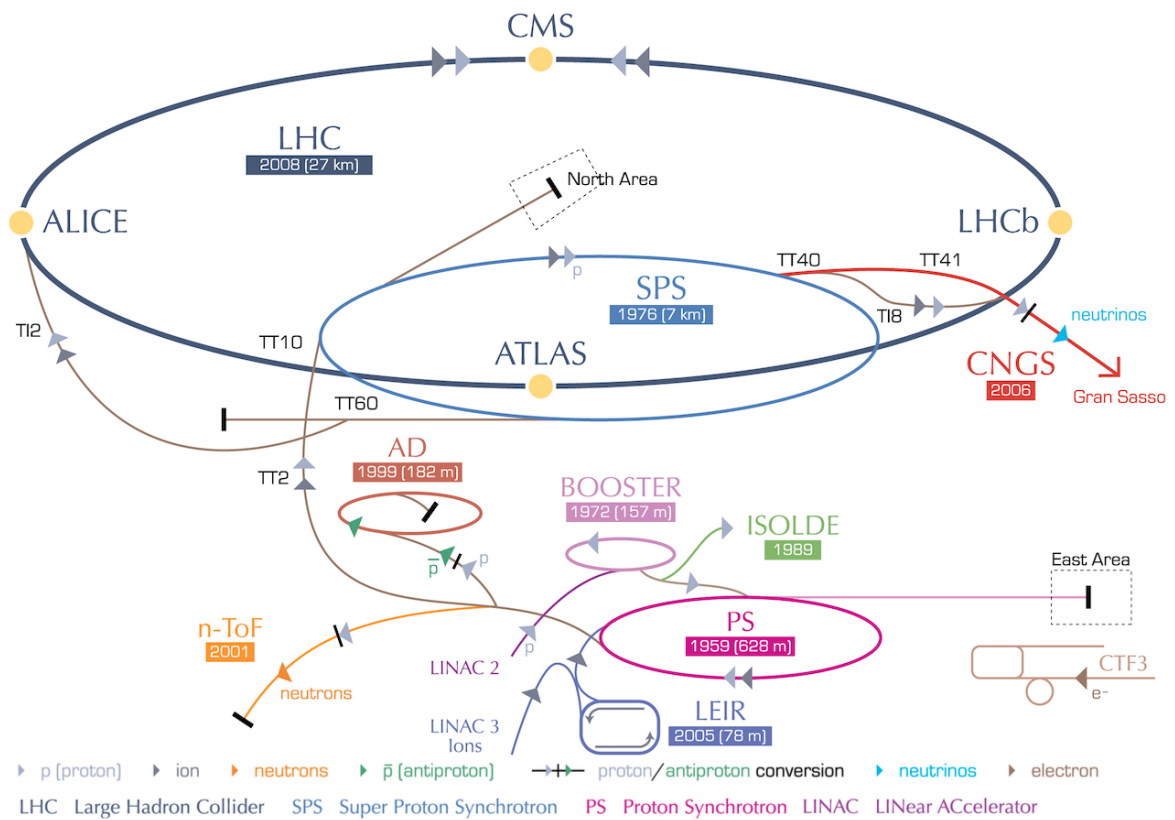


Fig. 3.2 Simplified layout of the CERN accelerator complex. Figure adapted from [47].

Hydrogen gas is ionised to provide a source of protons which are injected into a series of pre-accelerators before injection into the main LHC ring. Protons are first accelerated to 50 MeV using cavities with oscillating electromagnetic fields (RF cavities) in Linac 2 and injected into the Booster where they are accelerated to 1.4 GeV. Protons then enter the Proton Synchrotron (PS) where they are accelerated to 25 GeV and grouped into bunches spaced by 25 ns [48] with a maximum of  $1.15 \times 10^{11}$  protons per bunch [44] before injection into the Super Proton Synchrotron (SPS). The SPS further

accelerates the proton bunches to 425 GeV before they are injected into two rings in the LHC and accelerated up to a maximum energy of 7 TeV per beam. To produce two counter-rotating beams of protons, 1232 NbTi superconducting dipole magnets cooled by superfluid helium at 1.9 K establish opposing magnetic fields of more than 8 T for the two beams. Both beams are located within the same cryostat [44]. This contrasts with particle-antiparticle colliders, where beams of particles and antiparticles can circulate in opposing directions within the same ring due to the opposing charge of the particles. Both beams are brought together at four designated interaction points corresponding to the locations of detectors on the LHC, through the use of quadrupole magnets [44].

The LHC houses four main experiments: ATLAS, CMS, ALICE (**A** **L**arge **I**on **C**ollider **E**xperiment) [49] and LHCb (**L**arge **H**adron **C**ollider **b**eauty) [50]. Their positions on the LHC ring are shown in figure 3.2. ATLAS and CMS serve as the two general purpose detectors and were responsible for the discovery of the Higgs boson in 2012. ALICE is optimised for the study of heavy ion collisions, investigating lead-lead and proton-lead collision data. LHCb is situated forwards of its interaction point to measure the decays of  $B$ -hadrons.

### 3.3 The ATLAS Detector

The ATLAS detector at the Large Hadron Collider (LHC) was designed with the aim of achieving sensitivity to the Higgs boson. While the LEP collider at CERN had previously excluded SM Higgs boson masses below 114.4 GeV [51], ATLAS aimed to discover a SM Higgs boson with a mass in the range  $100 \text{ GeV} < m_H < 130 \text{ GeV}$  via the decay of the Higgs to either a pair of photons or four leptons. This goal was achieved by both the ATLAS and CMS experiments in 2012 [3, 4]. ATLAS is also designed to be capable of searches for new phenomena beyond the SM, such as searches for evidence of SUSY particles. As discussed in Chapter 2, detection of missing transverse momentum ( $E_T^{\text{miss}}$ ) is essential for the discovery of certain SUSY models. To reliably detect  $E_T^{\text{miss}}$ , near hermetic coverage is provided in the calorimeters. The ATLAS detector was designed for a wide range of physics and along with the Compact Muon Solenoid (CMS) is one of the two general purpose detectors at the LHC. A more comprehensive

overview of the individual components of the ATLAS detector may be found within the ATLAS Technical Design Report (TDR) [1].

#### 3.3.1 Overview

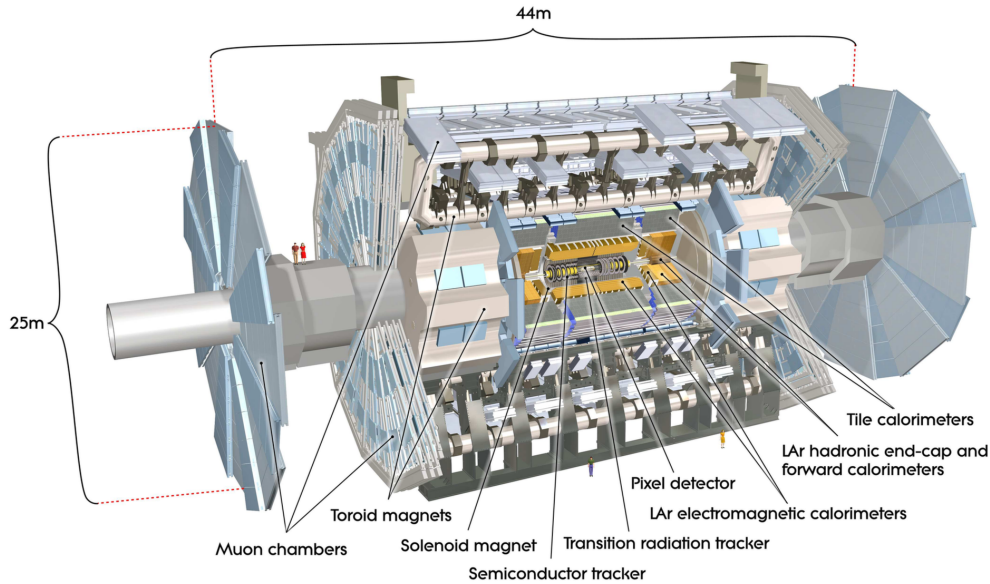


Fig. 3.3 Cross-sectional view of the ATLAS detector showing all subcomponents. Figure from [1].

The ATLAS detector is a general purpose 7000 tonne forward-backward symmetric cylindrical detector with coverage of approximately  $4\pi$  in solid angle around the interaction point, providing excellent potential for the accurate measurement of jets and  $E_T^{\text{miss}}$  (along with other physics objects). The detector is 46 m in length, 25 m in height and 25 m in width. Figure 3.3 shows a cross-sectional view of the entire detector and all sub-components. An Inner Detector (ID) within a 2 T solenoidal field is used for particle tracking, electron identification and momentum measurement. The ID consists of the Insertable B-Layer (IBL) (installed in 2014), Pixel detector, the silicon strip Semiconductor Tracker (SCT) and Transition Radiation Tracker (TRT), in order of increasing distance from the beam axis. Outside of the solenoid lie the electromagnetic and hadronic calorimetry systems used for the energy measurement of electrons, photons, jets and hadrons. The calorimetry systems are immersed in a magnetic field supplied

by three air-core toroidal magnets, which bend the paths of charged particles in the final and outermost layer of the detector, the Muon Spectrometer (MS) system.

### Coordinate System

ATLAS utilises a spherical coordinate system, shown in figure 3.4, with the origin defined as the interaction point and the  $z$ -axis defined as the beam axis. The  $x$ -axis is defined as positive when pointing to the centre of the LHC ring, while the  $y$ -axis is defined as positive when pointing near-vertically upwards from the interaction point. The azimuthal angle  $\phi$  and polar angle  $\theta$  are defined as the angles around and away from the positive  $z$ -axis, respectively.

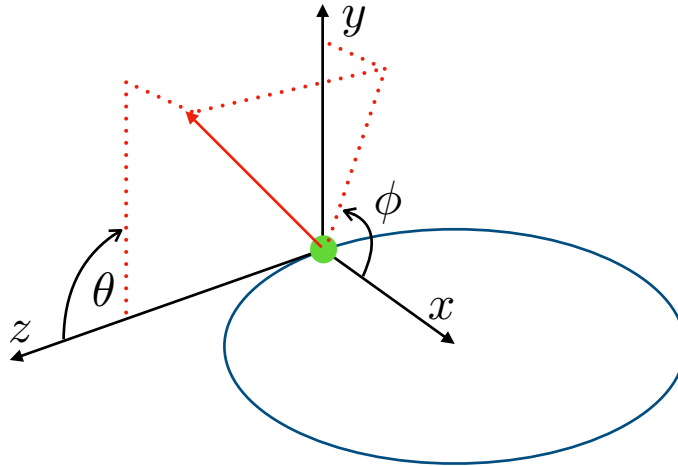


Fig. 3.4 A diagram of the ATLAS coordinate system. The  $z$ -axis points in the direction of the beam pipe, the  $x$ -axis points towards the centre of the LHC ring and the  $y$ -axis points near-vertically upwards. The angles  $\phi$  and  $\theta$  are defined as the angles around and away from the beam axis, respectively.

Due to the uncertainty in the fraction of the proton energy carried by partons in the beam collision (discussed in section 2.2.5.1), the centre-of-mass frame receives an unknown Lorentz boost in the  $z$ -direction and is therefore not at rest in the laboratory frame of reference. Differences in rapidity  $y$ , where

$$y = \frac{1}{2} \left( \frac{E + p_z}{E - p_z} \right) \quad (3.5)$$

and  $c = \hbar = 1$  are invariant under Lorentz boosts. However, there can be some difficulty in measuring the  $z$ -component of momentum due to the presence of the beam pipe itself. In addition, in LHC collisions the centre-of-mass frame is only approximately equivalent to the laboratory frame of reference due to the unknown momentum fraction  $x$  carried by each colliding parton. A useful proxy for rapidity, *pseudorapidity*, is defined as

$$\eta = -\ln \tan \frac{\theta}{2} \quad (3.6)$$

and is approximately equal to the rapidity for highly relativistic particles, such as within LHC collisions. Differences in pseudorapidity between two points are invariant under Lorentz boosts. The region of the detector at high values of  $|\eta|$  is said to be the *forward* region.

Attributes of physics objects (the detected particles) are often referred to in the transverse  $x$ - $y$  plane. In this plane there is negligible overall momentum prior to the hard interaction and therefore also after the interaction if momentum is conserved. Such quantities are denoted with a subscript T, such as  $p_T$ ,  $E_T$  and  $E_T^{\text{miss}}$ . The distance  $\Delta R$  between two points in the  $\eta$ - $\phi$  plane is defined as

$$\Delta R = \sqrt{\Delta\eta^2 + \Delta\phi^2} \quad (3.7)$$

and is also invariant under Lorentz boosts in the  $z$ -direction.

#### 3.3.2 Inner Detector

The ID is a collection of silicon pixel and microstrip detectors in addition to a gaseous straw tube detector immersed in a 2 T solenoidal magnetic field and is responsible for particle tracking, vertex identification and momentum measurement. The components of the ID are situated close to the interaction point and receive the highest radiation dose of any ATLAS component. It covers an acceptance range of  $|\eta| < 2.5$  with full coverage in  $\phi$  [52]. Prior to the installation of the IBL in May 2014, the ID provided a momentum resolution for charged tracks [52] of

$$\sigma_p/p = (4.83 \pm 0.16) \times 10^{-4} \text{GeV}^{-1} \times p_T$$

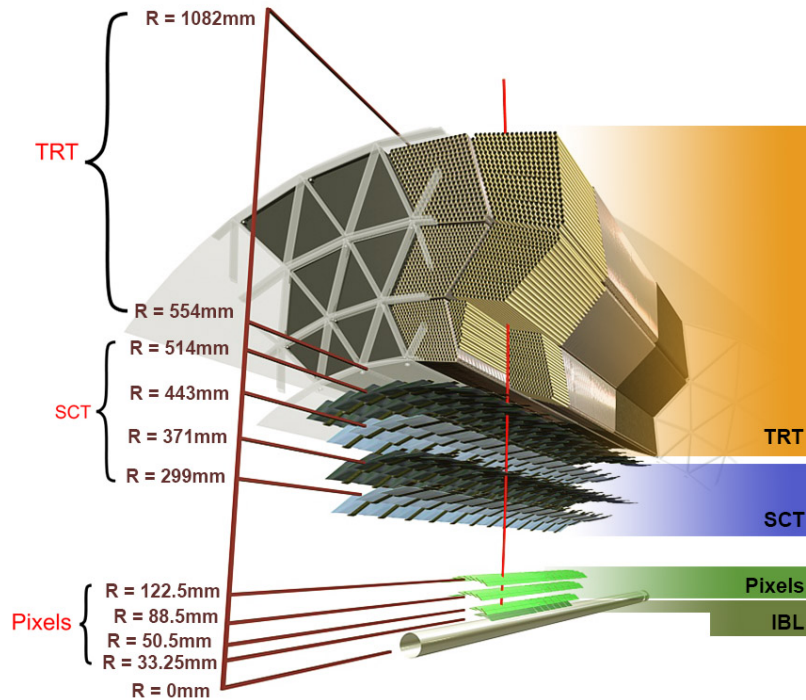


Fig. 3.5 Schematic view of the ATLAS Inner Detector (ID) showing each component of the ID and the radius covered by each sub-detector. Figure from [53].

Figure 3.5 shows a schematic view of the ID and both the relative position and radial distance covered by each of the sub-detectors.

### 3.3.2.1 Insertable B-Layer (IBL)

The IBL [54] is the innermost layer of the ID and is an expansion to the Pixel detector installed in May 2014 and first used to measure  $\sqrt{s} = 13\text{ TeV}$  data. It is situated between the beam pipe and the innermost layer of the Pixel detector at a mean radius of  $33.2\text{ mm}$  [53]. Its installation was motivated by improvements to vertex detection, b-jet identification efficiency and tracking performance. The accumulation of radiation damage (discussed in section 4.2) degrades the performance of silicon detectors by introducing defects within the silicon in addition to damaging the read-out electronics [54] and may result in the loss of measurement points in the existing Pixel detector. The IBL therefore offers some redundancy by providing an additional measurement point.

The IBL consists of 12 million  $50 \mu\text{m} \times 250 \mu\text{m}$  pixels mounted on 14 staves tilted by  $14^\circ$  in  $\phi$  to offer complete coverage around the beam pipe and coverage in  $|\eta| < 3$ . A 1 MeV neutron-equivalent fluence of  $2.5 \times 10^{15} \text{ 1 MeV n}_{\text{eq}} \text{ cm}^{-2}$  will be incident upon the IBL during the collection of an estimated  $300 \text{ fb}^{-1}$  of data before the ATLAS detector is upgraded in 2024 to accommodate peak LHC instantaneous luminosities of up to  $5 \times 10^{34} \text{ cm}^{-2}\text{s}^{-1}$  [55]. The components of the IBL have been designed to remain operational at double this level [56].

#### 3.3.2.2 Pixel Detector

The ATLAS Pixel detector [57] was the innermost layer of the Inner Detector prior to the installation of the IBL.

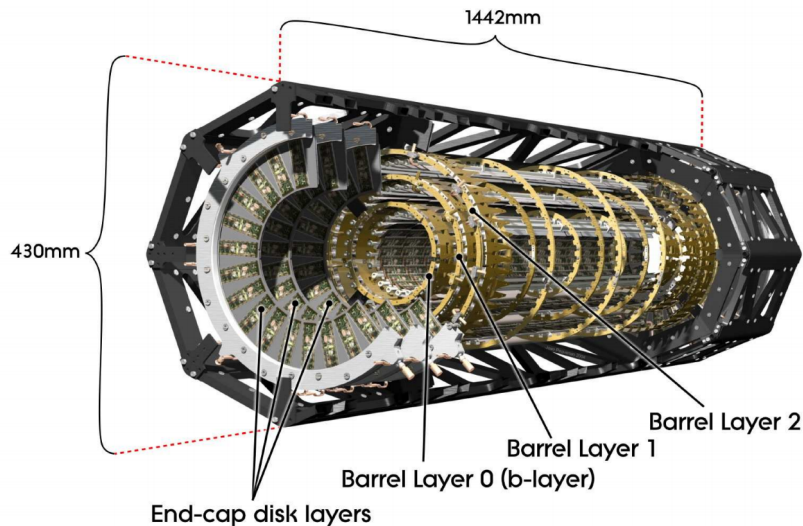


Fig. 3.6 A cut-away view of the Pixel detector and its components. Figure from [57].

The Pixel detector (shown in figure 3.6) is composed of three barrel layers running parallel to the beam pipe and six ‘disks’ positioned transverse to the beam pipe (with three disks at each end of the barrel) providing tracking of charged particles in a pseudorapidity range of  $|\eta| < 2.5$ . The three barrel layers are referred to as the B-Layer, Layer 1 and Layer 2 and are situated at radial distances of 50.5 mm, 88.5 mm and 122.5 mm from the beam axis, respectively [53]. The silicon sensors that comprise both the barrel layers and disks are typically  $50 \mu\text{m} \times 400 \mu\text{m}$  in size with a thickness of  $250 \mu\text{m}$ . Its proximity to the interaction point allows an accurate reconstruction of

secondary vertices from the decay of jets seeded by heavy flavour quarks (discussed in section 5.1.3) and of interaction vertices due to the original  $p$ - $p$  interaction in a high pile-up environment.

### 3.3.2.3 Semiconductor Tracker (SCT)

The SCT, shown in relation to other components of the ID in figure 3.7, covers a radial distance of 299-560 mm. It is comprised of 4088 modules of silicon strip detectors with 2112 modules arranged in four concentric barrels and 1976 modules arranged in two endcaps [58]. Barrel and endcap layers provide measurements of the tracks of charged particles at four points in space to provide a momentum measurement.

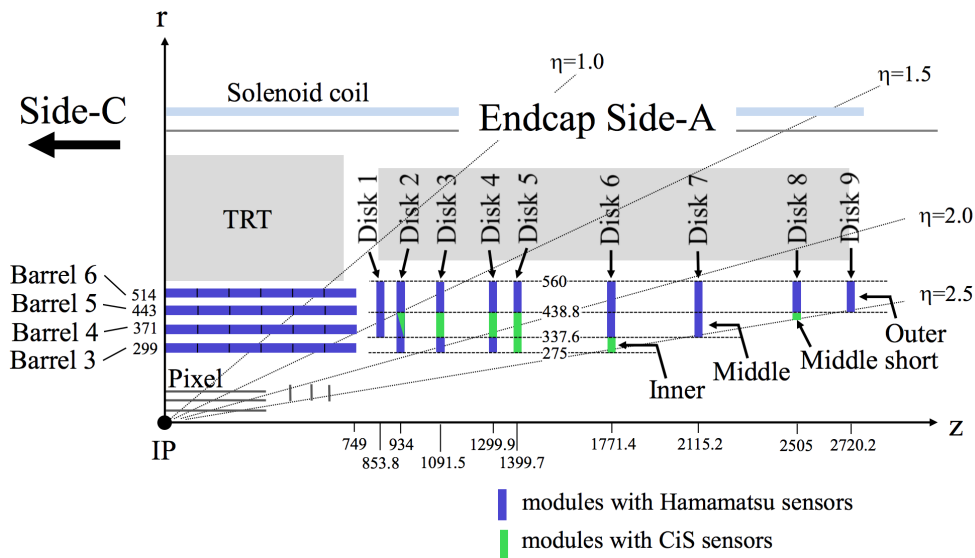


Fig. 3.7 A schematic view of the SCT and its relative position in the Inner Detector. The distances in  $z$  and  $\eta$  covered by the detector are shown. The sensor type used on SCT modules is shown in blue and green. A single set of endcap modules are shown and denoted ‘Side-A’, defined to have positive  $z$  coordinates. The opposite endcap layers, denoted ‘Side-C’ with negative  $z$  coordinates, are not shown in the figure. Figure from [58].

Barrel modules, shown in figure 3.8, are positioned approximately parallel to the beamline. Each barrel module consists of four silicon-strip sensors with two wire-bonded detectors glued back-to-back with a stereo angle of 40 mrad. The strips have a pitch (mid-strip to mid-strip distance) of 80  $\mu\text{m}$  [59] and are mounted on cylindrical

### 3.3 The ATLAS Detector

supports such that the modules of the inner two barrel layers are at an angle of  $11^\circ$  to the tangent of the support with the outer two layers at an angle of  $11.25^\circ$ . This angling coupled with overlap of a few millimetres provides hermetic coverage in azimuth [58].

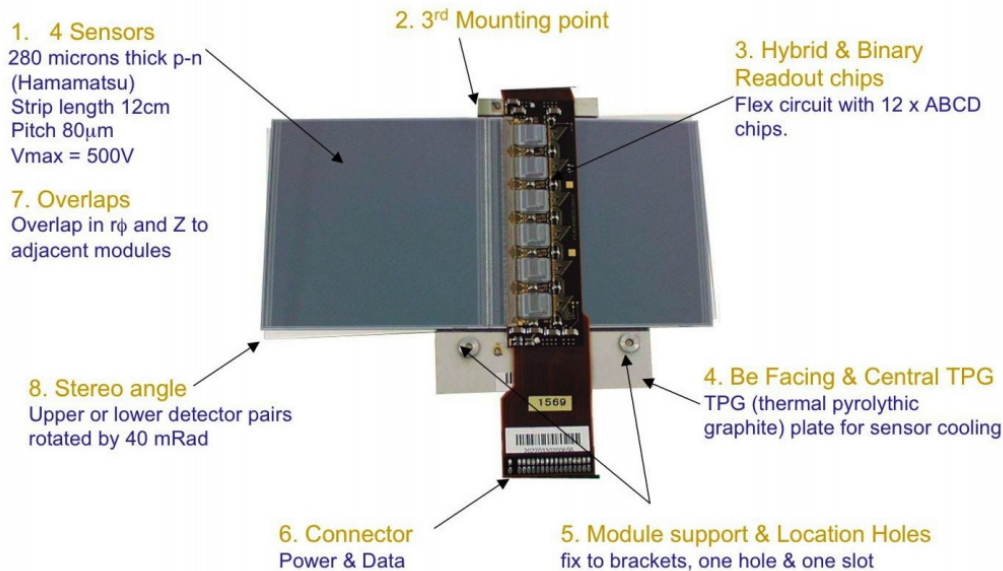


Fig. 3.8 A typical SCT barrel module. Figure from [60].

Endcap modules are glued back-to-back with a 40 mrad stereo angle and are arranged as a series of disks. The SCT utilises  $61\text{ m}^2$  of  $285\mu\text{m}$  thick silicon strip semiconductor sensors with a total of 6.2 million readout channels and has a spatial resolution of  $17\mu\text{m}$  in  $R\text{-}\phi$  and  $580\mu\text{m}$  in  $z$  ( $R$ ) for the barrel (endcap).

All barrel sensors and 75% of endcap sensors were produced by Hamamatsu Photonics<sup>1</sup>. The remaining sensors were produced by CiS<sup>2</sup>. Modules are mainly constructed from silicon wafers with Miller indices  $\langle 111 \rangle$ , however approximately 90 barrel modules are constructed from wafers with  $\langle 100 \rangle$  crystal lattice orientation [58]. Differences in noise performance have been observed between the two, with  $\langle 100 \rangle$  modules showing an decrease in noise [61].

The silicon sensors within SCT modules are composed of doped silicon layers, where impurities are added to the silicon to alter the number of free electrons (donors,  $n$ )

<sup>1</sup>Hamamatsu Photonics Co. Ltd., 1126-1 Ichino-cho, Hamamatsu, Shizuoka 431-3196, Japan.

<sup>2</sup>CiS Institut für Mikrosensorik GmbH, Konrad-Zuse-Strasse 14, 99099 Erfurt, Germany.

or holes (acceptors,  $p$ ) in the material. SCT sensors are composed of an  $n$ -type bulk with higher donor concentration in contact with a  $p$ -type layer with higher acceptor concentration [62]. This configuration is termed  $p$ -in- $n$  and is shown in figure 3.9.

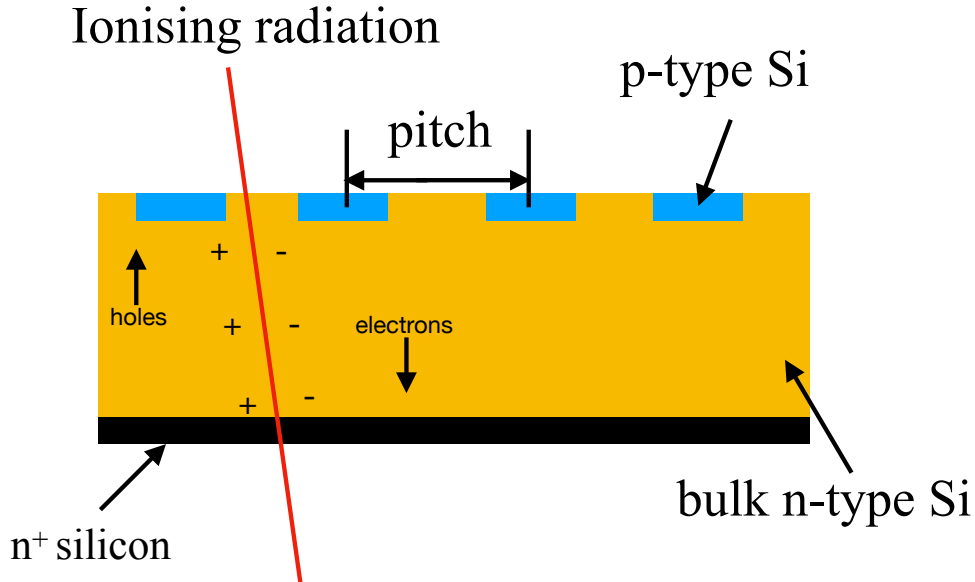


Fig. 3.9 A schematic view of the  $p$ -in- $n$  configuration used in SCT silicon sensors, where a doped  $p$  type silicon layer is brought into contact with the  $n$ -type silicon bulk. The  $p$ -type layer is divided into strips to provide additional spatial detection information. Negatively charged aluminium electrodes (not shown) are attached to the  $p$ -type strips [58] and cause the drift of holes towards the  $p$ -type layer, while applying a positive charge to the  $n$ -type layer causes electrons to drift towards the  $n$ -type layer, creating a central region maximally depleted of free charge carriers in the absence of impinging ionising radiation. The mid-strip to mid-strip distance, or  $pitch$ , is labelled in the figure.

Electrons from the  $n$ -type layer diffuse to the  $p$ -type layer, while the reverse process simultaneously occurs, with holes from the  $p$ -type layer diffusing to the  $n$ -type layer. The result is electron-hole recombination, leaving ionised atoms in each layer which creates charged regions — the  $n$ -type layer develops a positively charged region, while the  $p$ -type layer develops a negatively charged region [63]. This effect is illustrated in figure 3.10.

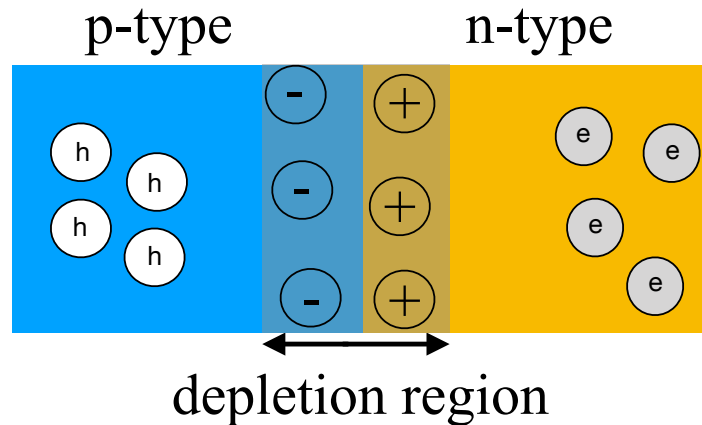


Fig. 3.10 A schematic view of the depletion region formed when a  $p$  type layer is brought into contact with an  $n$ -type layer. Electron-hole recombination occurs across the junction, leaving positively charged ions in the  $n$ -type layer and negatively charged ions in the  $p$ -type layer. The presence of the charged ions induces an additional electric field which prevents further electron-hole recombination and creates a region between the two layers depleted of free charge carriers. Figure adapted from [63].

These charged regions induce an electric field with an associated potential difference, the built-in voltage ( $V_{bi}$ ), which prevents further diffusion across the p-n junction. An equilibrium is established when diffusion across the p-n junction ends. Semiconductor particle detector operation relies heavily on the central depleted region with an absence of free charge carriers. Ionising radiation entering this depleted region within the silicon sensor creates electron-hole pairs which are swept to the edges of the sensor with an applied *bias voltage* which facilitates charge measurement. Applying a positive bias voltage to the n-type bulk, or *reverse-biasing*, increases the width of the depletion region. This occurs due to the attraction of electrons in the n-type bulk away from the p-n junction. A maximally increased width is desirable in particle detectors as it allows for an increase in charge collection from incoming ionising radiation.

An investigation of the effects of radiation damage on the SCT barrel modules is provided in Chapter 4, while a more detailed overview of SCT operation and performance is available within [61].

### 3.3.2.4 Transition Radiation Tracker (TRT)

The TRT [1, 59, 64] is the furthest component of the ID from the interaction point and covers a radial distance of  $617 < R < 1106$  mm. It is a straw tube tracker with 4 mm diameter gas-filled straws arranged within a barrel and two endcaps. TRT barrel straws are 144 cm in length and are positioned parallel to the beam axis. Endcap straws are 37 cm in length and are positioned in wheels transverse to the beam axis. As charged particles are incident upon the TRT straws, they ionise the gas. The straw walls are held at a negative potential difference with respect to a tungsten wire running through the centre of each straw, causing the ionised electrons to drift towards the wire where a signal is detected [65]. The sub-detector covers a pseudorapidity region up to  $|\eta| = 2.0$  and provides approximately 36 measurements in the track of each charged particle passing through the active region. Transition radiation is emitted when highly relativistic charged particles with  $\gamma \geq 1000$  traverse the boundary of two media with differing dielectric constants  $\epsilon_r$  [66].

The Xe and Ar based gas mixtures within the straw tubes absorb transition radiation photons emitted from the polypropylene radiator between straws, which may be of sufficient energy to cause the detection of a signal over the high threshold of around 6 keV [65]. The fraction of electron and pion candidates causing the detection of a signal exceeding the high threshold is shown in figure 3.11 and provides a means of identifying electrons with the TRT.

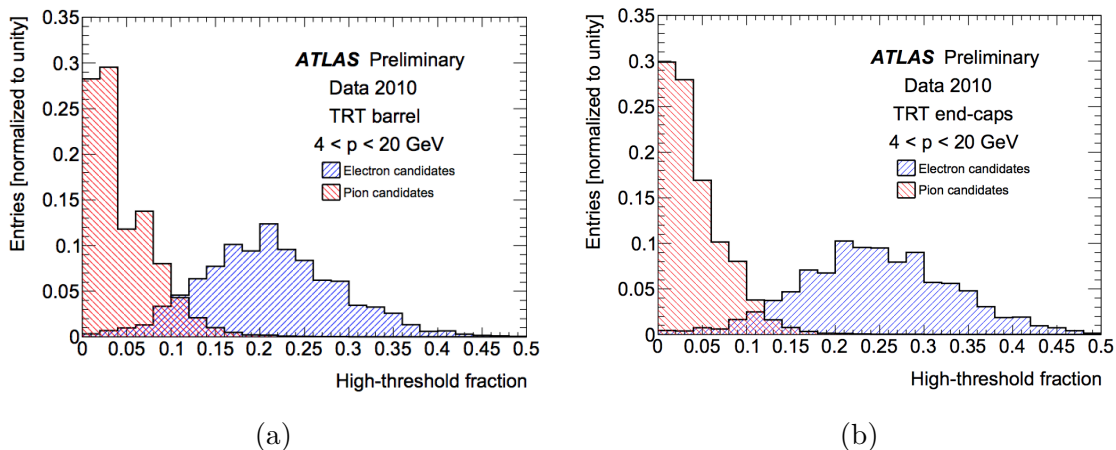


Fig. 3.11 Fractions of pion and electron candidates resulting in the detection of transition radiation exceeding the high threshold of approximately 6 keV in the TRT (a) barrel and (b) endcaps. Figures from [65].

The TRT provides a spatial resolution of  $130 \mu\text{m}$  per straw in the  $R-\phi$  plane [1], with poor performance in the  $z$  direction. However, the combination of all three ID sub-detectors leads to high precision tracking and momentum measurements of charged particles.

### 3.3.3 Calorimetry

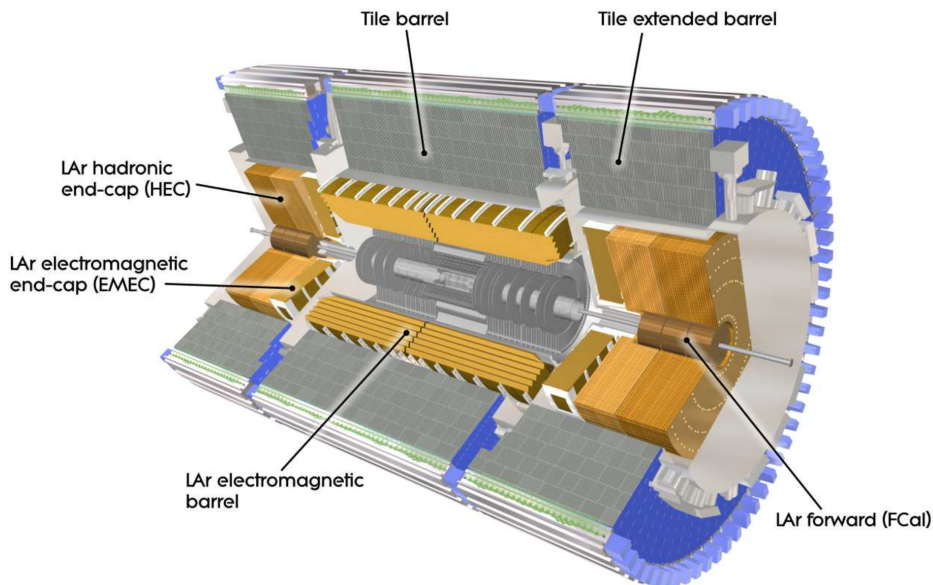


Fig. 3.12 A schematic view of the components of the ATLAS calorimeter system. Figure from [1].

The ATLAS calorimeter system [1] provides energy measurements for electromagnetic and hadronic particles within the detector with liquid Argon (LAr) and plastic scintillating tile sampling calorimeters and is shown in figure 3.12. The calorimeters aim to fully absorb incoming particles, causing the incident particle to produce showers of secondary particles with reduced energies that are absorbed by the detecting medium [67], either through the collection of charge following the ionisation of a gaseous medium or by the detection of photons following scintillation in a solid detector. The calorimeter system is located outside of the ID and solenoid magnet. The fine granularity electromagnetic calorimeter (ECAL) provides energy measurements of electrons and photons with pseudorapidity up to  $|\eta| = 3.2$ . The hadronic calorimeter (HCAL) system, with coarser granularity and situated further radially from the beam pipe than the ECAL, enables

## The ATLAS Detector at the LHC

---

Table 3.1 Energy resolution performance goals of the ATLAS calorimeter components. Design values are quoted and are verified by test beam measurements [1].

	Component	Resolution (GeV)	Coverage in $ \eta $
<b>ECAL</b>	Complete system	$\frac{\sigma_E}{E} = \frac{10\%}{\sqrt{E}} \oplus 0.7\%$	3.2
<b>HCAL</b>			
	Barrel & endcap	$\frac{\sigma_E}{E} = \frac{50\%}{\sqrt{E}} \oplus 3\%$	3.2
	Forward calorimeter	$\frac{\sigma_E}{E} = \frac{100\%}{\sqrt{E}} \oplus 10\%$	$3.1 <  \eta  < 4.9$

measurements of jet energy and  $E_T^{\text{miss}}$  and covers a pseudorapidity region of  $|\eta| < 3.2$ . A dedicated LAr forward calorimeter (FCAL) for the high- $|\eta|$  forward region provides measurements of EM and hadronic showers in the region  $3.1 < |\eta| < 4.9$ .

To provide accurate energy measurements, the calorimeters must be of an adequate depth to contain the entire particle shower to prevent ‘punch-through’ into the MS system. A high pseudorapidity coverage ensures accurate  $E_T^{\text{miss}}$  measurements can be made, which are of particular importance to fully hadronic R-parity conserving SUSY searches.

The energy resolution of the calorimeter system improves with increasing energy and is described by

$$\frac{\sigma}{E} = \frac{a}{\sqrt{E}} \oplus \frac{b}{E} \oplus c \quad (3.8)$$

where  $a$  is the stochastic term accounting for fluctuations of the numbers of particles in the showers on an event-by-event basis,  $b$  represents electronic noise and  $c$  is a constant source of systematic uncertainty due to gaps between calorimeter layers, damaged or non-operational detector material. The  $\oplus$  in this case denotes addition of the uncertainties in quadrature. The energy resolution goals for the components of the calorimeter system are shown in table 3.1. Precision measurements are made in the more central, lower pseudorapidity region of the detector while energy resolution degrades at higher values of pseudorapidity.

Calorimeters are characterised by the *radiation length*  $X_0$  for EM interactions and the *interaction length*  $\lambda_I$  for hadronic interactions. The radiation length  $X_0$  is defined [5] as

$$X_0 \approx \frac{716A}{Z(Z+1) \ln(287/\sqrt{Z})} \text{ [g cm}^{-2}\text{]} \quad (3.9)$$

where  $Z$  is the atomic number of the detector material and  $A$  is the atomic weight. Radiation length represents the amount of material required for the energy of an electron to be reduced via the emission of bremsstrahlung photons to  $E = E_0 \exp(-x/X_0)$ , where  $E_0$  is the original energy.

Hadronic interactions of charged and neutral particles are similarly characterised by  $\lambda_I$ , the average distance travelled within a detecting medium by relativistic hadrons before interacting with the detector material. The distance  $\lambda_I$  is much greater than  $X_0$  [10]. Utilising calorimeters with high  $X_0$  and  $\lambda_I$  aids in the full containment of electromagnetic and hadronic showers.

#### Electromagnetic Calorimeter

The main source of energy loss for electrons with momenta in the GeV range is via bremsstrahlung [5]. Photons with energies above 10 MeV interact mainly through the production of  $e^+e^-$  pairs [10]. The emission of photons from high energy electrons and the subsequent  $\gamma \rightarrow e^+e^-$  process may repeat while sufficient energy is available for both processes to dominate. The sequential production of electrons, positrons and photons with increasingly smaller energies is referred to as an *electromagnetic shower*.

The LAr electromagnetic calorimeter (ECAL) system provides energy measurements for particles interacting via the electromagnetic interaction in the ATLAS detector. It is arranged into a barrel covering  $|\eta| < 1.475$  and two endcap regions covering  $1.375 < |\eta| < 3.2$ . The ECAL uses lead absorbers with LAr active regions arranged in an accordion geometry, shown in figure 3.13, to provide near-hermetic coverage in  $\phi$  around the beam axis. The pseudorapidity regions covered by the barrel and endcap components are detailed in table 3.1.

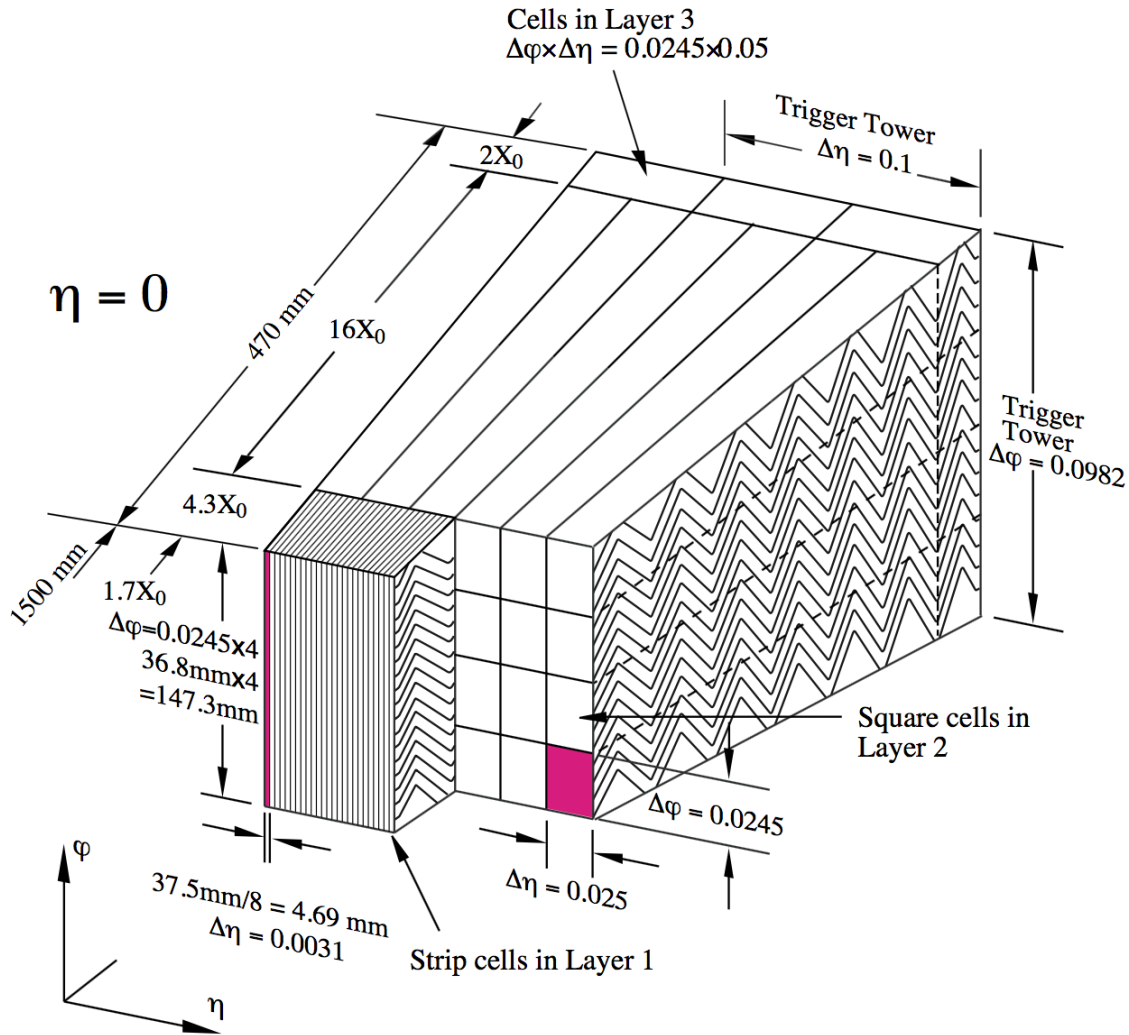


Fig. 3.13 Diagram of an ECAL LAr barrel module displaying ‘accordion geometry’, the granularity in the  $\eta - \phi$  plane and thickness in number of radiation lengths  $X_0$ . Figure from [1].

Barrel and endcap layers are divided into three longitudinal layers for  $|\eta| < 2.5$ , in order of decreasing granularity in  $\eta$ . Layer 1 (EM1) is divided into strips with the highest granularity in  $\eta$ . Most of the energy deposited by EM showers is collected within Layer 2 (EM2), which represents the longest longitudinal portion of the calorimeter. Layer (EM3) compensates for high energy shower leakage out of the EM calorimeter. Figure 3.13 shows the thicknesses and granularities (in  $\eta$  and  $\phi$ ) of the three layers.

A LAr presampler of thickness 1.1 cm (0.5 cm) and granularity  $\Delta\eta \times \Delta\phi = 0.025 \times 0.1$  is used in the  $|\eta| < 1.8$  region in the barrel (endcap) to shower photons and electrons, measuring their energy loss prior to their entry into the ECAL system.

#### Hadronic Calorimeter

The HCAL system measures the energy of strongly interacting particle showers from hadrons and is required for jet energy and  $E_T^{\text{miss}}$  measurements. The calorimeter is divided into a barrel region, two extended barrel regions and two endcap regions. Plastic scintillating tiles are used as the active medium in the barrel and extended barrel regions, with steel absorber plates to initiate particle showering. The barrel region covers  $|\eta| < 1.0$  while the extended barrel covers  $0.8 < |\eta| < 1.7$ .

HCAL endcaps consist of an inner and outer wheel and utilise copper absorber plates with LAr active regions. The HCAL endcaps extend from  $|\eta| = 1.5$  to  $|\eta| = 3.2$  and overlap slightly with the tile region at low  $\eta$  and the forward calorimeter (FCAL) at high  $\eta$  to maintain coverage in the transition regions [1].

#### Forward Calorimeter

The FCAL measures both EM and hadronic particle showers at  $3.1 < |\eta| < 4.9$  and is split into three regions longitudinally. All three use LAr as the active medium. The first region (FCal1) uses copper absorption plates and is optimised for heat transfer and the absorption of electromagnetic particles. The remaining two regions (FCal2 and FCal3) use tungsten absorber plates and are optimised to minimise lateral spread in hadronic showers [1]. Additional copper shielding is placed between FCal3 and the endcaps of the MS to reduce punch-through.

### 3.3.4 Muon Spectrometer (MS)

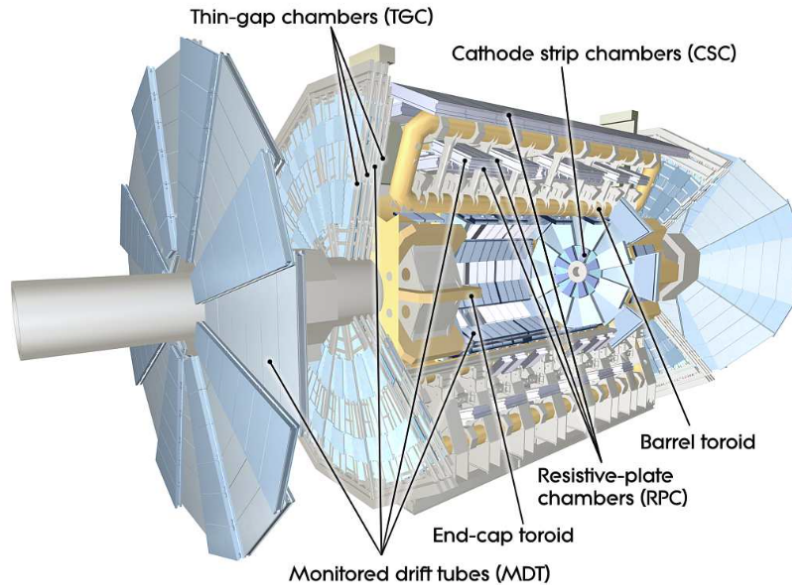


Fig. 3.14 Schematic view of the components of the ATLAS muon system, the toroidal magnets and their relative positions. Figure from [1].

Shown in figure 3.14, the MS [1, 68] provides a measurement of muon momenta via the magnetic deflection of tracks of charged particles not contained by the calorimetry system and contains instrumentation to enable triggering (discussed in section 3.3.6). The muon system is immersed in a toroidal magnetic field supplied by a system of superconducting air core toroid magnets discussed in section 3.3.5. The MS consists of four gaseous detectors divided into two tracking regions and two triggering regions. Monitored drift tubes (MDTs) and Cathode Strip Chamber (CSCs) are arranged into barrel and endcap regions and provide muon tracking information at  $|\eta| < 2.7$  and  $2.0 < |\eta| < 2.7$ , respectively. Resistive Plate Chambers (RPCs) provide triggering information over the barrel region while Thin Gap Chambers (TGCs) cover triggering in endcap regions. The combined triggering system covers  $|\eta| < 2.4$  and has the secondary function of providing a track measurement to complement MDT and CSC measurements. TGCs are capable of measuring tracks up to  $|\eta| = 2.4$ .

Overall, the MS provides a transverse momentum resolution of 10% for 1 TeV charged particle tracks and is capable of measuring muon momenta down to approximately 3 GeV due to the energy lost by muons within the calorimeter system [1].

### 3.3.5 Magnet System

The ATLAS magnet system consists of a solenoid magnet located outside of the ID and a system of three toroid magnets located radially outside of the calorimeter system and working in conjunction with the MS to provide a momentum measurement for muons.

The superconducting solenoid magnet is 5.8 m in length with inner and outer diameters of 2.46 m and 2.56 m. The solenoid is aligned with the beam axis similarly to the barrel regions of detector components described in previous sections. It supplies a 2 T axial magnetic field, in which the inner detector is fully immersed, and is cooled to 4.5 K. The thickness of the solenoid magnet is minimised to reduce particle interactions with material placed in front of the calorimeters [1].

The toroid magnet system works in conjunction with the muon system and is composed of a barrel and two endcap sections. The barrel section is constructed of eight Nb/Ti/Cu coils kept in a vacuum at 4.6 K with a length of 25.3 m, inner and outer diameters of 9.4 m and 20.1 m and generates a toroidal 0.5 T field. Each endcap toroid is composed of eight coils with an axial length of 5.0 m, an inner diameter of 1.65 m and an outer diameter of 10.7 m. The endcap toroids provide a means of bending the trajectory of muons within the endcaps of the MS, where they generate a field of approximately 1 T [1].

### 3.3.6 Trigger and Data Acquisition (TDAQ) System

The LHC Run-2 bunch crossing rate is approximately 40 MHz, while the rate of data recording is limited to around 1 kHz [1]. The ATLAS TDAQ system, shown in figure 3.15, is used to select physics events of interest to be saved for analysis at a suitable rate. The trigger system consists of a hardware and software trigger referred to as the Level 1 (L1) and High Level Trigger (HLT), respectively [69].

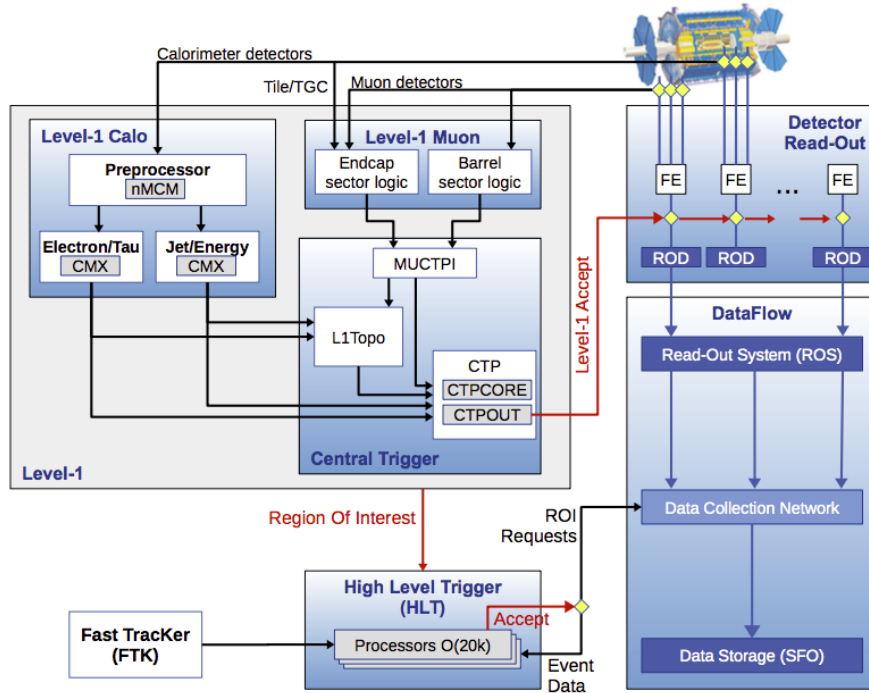


Fig. 3.15 Diagram of the ATLAS Trigger and Data Acquisition (TDAQ) system showing the flow of data from the detector. Figure from [69].

The L1 hardware trigger reduces the event rate from around 40 MHz to 100 kHz [69]. It receives particle identification signals for photons, electrons, muons, jets, the decay products of  $\tau$  particles,  $E_T^{\text{miss}}$  and identifies a *region of interest* (ROI) in areas of the calorimeter where a signal threshold for a particular physics object is passed. ROIs are formed from coarse granularity information from the calorimeters and muon system and are passed to the HLT where a higher level of granularity is used for selection. The 100 kHz rate in the L1 trigger is reduced to the level of 1 kHz by the HLT [69].

Subdetectors have separate electronic components but generally operate on the principle of storing event information in a buffer while a trigger decision is made by the L1 trigger. On passing the L1 trigger, data is sent to readout drivers (RODs) and subsequently stored in readout buffers (ROBs) to seed the ROI-based HLT trigger. Data surviving the HLT decision is then stored centrally for offline reconstruction.

Triggers that select commonly occurring events, such as low  $p_T$  reconstructed jets, are often highly *prescaled*, where the inverse of the prescale value is the fraction of

events that are retained from the trigger of interest, so that they may be recorded at a manageable rate.

### 3.4 Data Processing and Simulation

ATLAS reconstructs events as a collection of observable *physics objects*. These include electrons, photons, muons, jets and  $E_T^{\text{miss}}$ . Their passage through the detector is shown in figure 3.16. The definition of these objects in the context of ATLAS SUSY analyses is discussed in section 5.1.

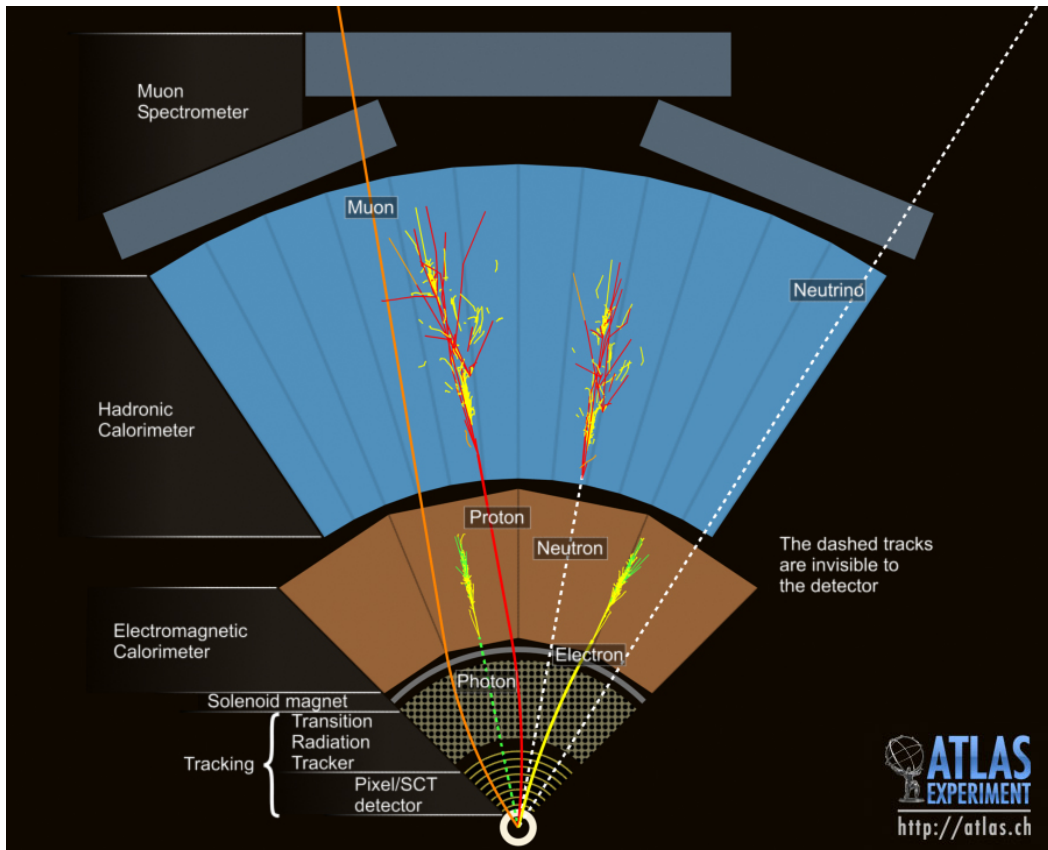


Fig. 3.16 Representation of an event in the ATLAS detector. The appearance of tracks for various particle types is shown, with dotted lines denoting no interaction. Neutrinos are not directly detected at any stage. Figure from [70].

### 3.4.1 ATLAS Events

The  $36.1 \text{ fb}^{-1}$  of data analysed and referred to in subsequent sections of this thesis was recorded at a centre-of-mass energy of 13 TeV between June 2015 and October 2016. In the data set considered, proton bunches are separated by 25 ns. Data taking is divided into *runs*, discrete time periods of data collection identified with a unique *run number*. *Good Run Lists* (GRLs) are used to denote runs where the data is deemed to be of sufficient quality for use in data taking. Data may be excluded from these lists if any issues arose in the recording of that particular run, such as subdetector problems or high levels of noise. The data delivered between 2015 and 2017 by the LHC to the ATLAS detector and the fraction of that data successfully recorded is shown in figure 3.17.

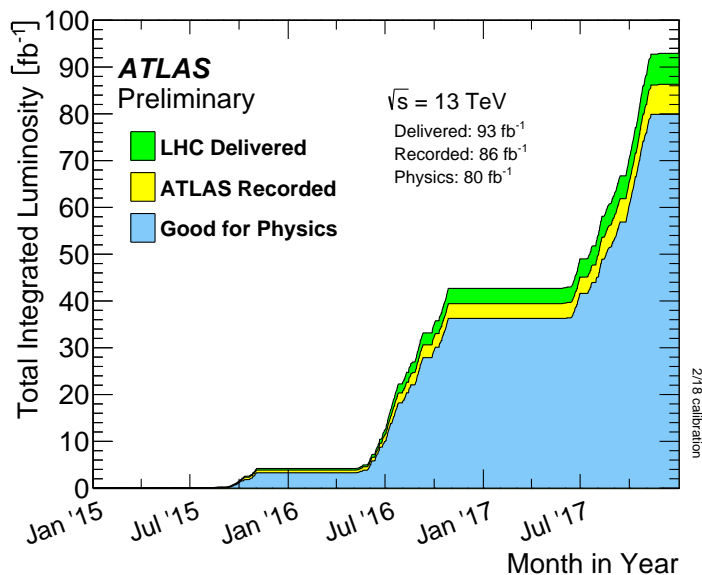


Fig. 3.17 Luminosity delivered by the LHC (green), recorded by the ATLAS detector (yellow) and qualified as ‘Good for Physics’ (blue) at  $\sqrt{s} = 13 \text{ TeV}$  between 2015 and 2017. The  $36.1 \text{ fb}^{-1}$  of data considered in this thesis was recorded between June 2015 and October 2016 and considered ‘Good for Physics’. Figure from [71].

#### 3.4.1.1 Pile-up

Pile-up refers to additional activity within the detector following proton-proton collisions occurring in addition to the specific collision of interest. The average number of proton-

proton collisions per bunch crossing, calculated per bunch, is  $\mu$ :

$$\mu = \frac{L_{\text{bunch}}\sigma_{\text{inelastic}}}{f_r} \quad (3.10)$$

where  $L_{\text{bunch}}$  is the instantaneous per-bunch luminosity,  $\sigma_{\text{inelastic}} = 80 \text{ mb}$  is the  $\sqrt{s} = 13 \text{ TeV}$  cross-section for inelastic  $p$ - $p$  collisions and  $f_r = 11.245 \text{ kHz}$  is the revolution frequency at the LHC [71]. Pile-up is commonly referred to as the bunch-averaged number of proton-proton collisions  $\langle\mu\rangle$ , shown for 2015 and 2016 data taking conditions in figure 3.18 with an average of  $\langle\mu\rangle = 23.7$ .

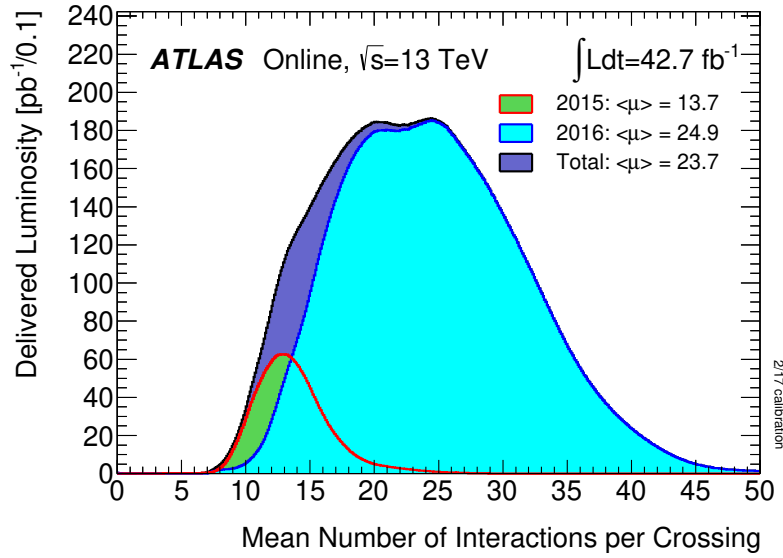


Fig. 3.18 The average number of proton-proton interactions per bunch crossing ( $\mu$ ) during 2015 and 2016 data taking at  $\sqrt{s} = 13 \text{ TeV}$ . Distributions are shown individually for 2015 (green) and 2016 (light blue) in addition to the combined period (purple). The average is shown for each period and a combination of the two, with  $\langle\mu\rangle = 23.7$  for the combined 2015 and 2016 dataset. Figure from [71].

Pile-up is further categorised as either *in-time* or *out-of-time*. Out-of-time pile-up refers to proton-proton collisions that occur in bunch crossings before and after the bunch crossing containing the collision of interest [72]. The severity of the impact of out-of-time pile-up is determined by the time resolution and amount of dead-time of subdetectors. In-time pile-up refers to multiple proton-proton collisions within the same bunch crossing.

### 3.4.2 Event Simulation for ATLAS Analyses

Event simulation in the ATLAS detector [73] is necessary to model both SM processes and BSM signals in searches for deviations from the SM. MC samples are generated and passed through a simulated detector before subsequent event reconstruction. General purpose event generators such as PYTHIA [74] and SHERPA [22] are required to simulate physical processes ranging from hard parton scattering to the lower energy formation of hadrons and their subsequent decay [5]. Event generators calculate the matrix element (ME) of the hard interaction to a certain order in  $\alpha_S$ . These event generators also perform the parton showering (PS) process and are termed ME+PS generators. The stage of the simulation prior to the detector simulation is referred to as the *truth* level simulation. Simulated events are then passed to the detector simulation stage and are reconstructed as detector-level measurements, referred to as the *detector* level. Particles and physical observables such as  $E_T^{\text{miss}}$  may be reconstructed from the detector level simulation in a similar manner to that applied to measured data events.

Simulated dijet MC samples are referred to extensively within this thesis in chapters 6 and 7 and represent the default method of estimating the multijet background available to ATLAS analyses. A well motivated data-driven alternative to the use of dijet MC samples is introduced in chapter 6 and initially uses the same MC samples to derive the energy response in simulated jets. The dijet MC samples use the PYTHIA 8 event generator with the A14 event tune [75] (parameter set) and NNPDF2.3LO [76] PDF set to perform ME calculation to leading order (LO) in  $\alpha_S$ . Additionally, the PS process is also performed using PYTHIA 8. However, simulation of final states involving many hard isolated jets relies more upon accurate ME calculation than the PS calculation. High jet multiplicity events are often modelled by LO ME+PS generators, as the calculation of the matrix element to next-to-leading order (NLO) in  $\alpha_S$  is often computationally impractical for final states containing more than three jets [77].

The ATLAS detector is modelled with GEANT4 [78]. Passing MC events through the GEANT4 simulated detector is referred to as *full simulation*. Full simulation is a time and CPU-intensive process dominated by the simulation of the calorimeters. Improvements are possible with the use of *fast simulation* techniques [79] that simulate particle energy response and spatial distribution within calorimeter cells. Fast simulation combined with fully a simulated inner detector and muon system is used to create MC samples in addition to those completely fully simulated with GEANT4.

# Chapter 4

## Estimating Radiation Damage in the ATLAS SCT

Radiation damage resulting from proton-proton and heavy ion collisions in the ATLAS SCT causes an increase in module leakage current and full depletion voltage. Where referred to in this chapter, *Run 2* refers to the data taking period between 2015 and 2018, while *Run 3* refers to the data taking period from 2021-2023. This chapter details a study undertaken by the author during 2015 and 2016 to determine the level of radiation damage present prior to Run 2 and provides predictions of the level of expected radiation damage over the course of ATLAS data taking up to 2024. Due to the temperature and luminosity dependence of the variables used to quantify radiation damage, several SCT cooling regimes were tested to offer predictions of best and worst case scenarios over the planned lifetime of the SCT.

This study reported for the first time the impact of radiation damage due to increased collision energy in Run 2 and informed the SCT cooling strategy during periods of operation and shutdown.

### 4.1 Introduction

The SCT is subject to radiation damage during operation which affects the properties of the silicon semiconductor modules. To ensure safe and efficient operation, radiation damage in the SCT must be fully understood and mitigated where possible before a

planned upgrade to the inner tracker which is scheduled for 2024. Two properties are used to quantify the level of radiation damage in the SCT: the leakage current and full depletion voltage (hereafter referred to as “depletion voltage”,  $V_{\text{dep}}$ ). Modelling the evolution of these variables under increasing luminosity and varying temperature regimes enables long term prediction of the impact of radiation damage to the SCT.

The Hamburg-Dortmund model [80–82] of leakage current evolution represents the standard predictive model used by the SCT working group and was developed empirically from studies with irradiated silicon pad diodes. The ‘Sheffield-Harper model’ [83] represents an alternative model for the estimation of leakage current and was developed for an ATLAS-specific case by using silicon microstrip sensors irradiated while being cooled to ATLAS operating temperatures to mitigate annealing effects during irradiation, with leakage current measurements additionally taken during irradiations. For the case of depletion voltage evolution, the Hamburg model [80, 81], again an empirically derived model based on silicon pad diode irradiations, was the only such model available.

Leakage current measurements from 2010 to the end of May 2016 are compared with the prediction of both models in the SCT barrel layer closest to the interaction point. In this chapter, Run 1 refers to the period of data taking from 2010 to 2013 where integrated luminosities of  $5.7 \text{ fb}^{-1}$  and  $23.2 \text{ fb}^{-1}$  of proton-proton collision data were delivered at a centre of mass collision energies of 7 and 8 TeV respectively. In the context of this study, ‘early Run 2’ refers to the period of  $\sqrt{s} = 13 \text{ TeV}$  collisions prior to May 2016 within the ATLAS detector, where  $4.99 \text{ fb}^{-1}$  was delivered to ATLAS.

After verifying satisfactory modelling of the observed leakage current, leakage current forecasts were generated until the end of 2023, corresponding to the end of the period of operation of the SCT. Several temperature scenarios were assumed for SCT operation and planned long shutdown following Run 2 (LS2). Predictions of the sensor depletion voltage were generated using the Hamburg model. The lack of available methods for direct measurement of the depletion voltage in ATLAS necessitates a reliance upon predictive models, which successfully predicted the period in which silicon modules were likely to undergo ‘type-inversion’, where the effective donor concentration becomes negative.

Finally, in a related study, SCT current-voltage scans are presented. The scans were performed over a range of 20 to 150 V increasing in 10 V intervals. Measurements taken in 2013 are shown with the 2015 measurements for comparison. These scans represent important tests of the visible impacts of radiation damage within the SCT.

## 4.2 Radiation Damage in SCT Silicon Sensors

An overview of the componentry and mode of operation of the SCT detector is provided in section 3.3.2.3. This section will provide an overview of the primary mechanism through which incident radiation degrades the SCT.

Radiation backgrounds in the SCT are dominated by particles arising from proton-proton collisions, either directly (mainly charged pions), or from neutron albedo originating from hadronic showers in the calorimeters. The radiation fluence received by SCT sensors is dominated by neutrons [80]. The SCT was designed to operate up to an integrated luminosity of  $700 \text{ fb}^{-1}$  [61]. As of May 2016, the total integrated luminosity delivered represented less than 5% of this figure.

The silicon sensors of the SCT are operated with a reverse biased  $p$ - $n$  junction to maximise the depletion width and suppress the flow of current across the  $p$ - $n$  junction in the absence of ionising radiation. A small residual current, termed the *leakage current*, is induced by the creation of electron-hole pairs due to thermal excitations of electrons in the depleted region of the silicon sensor. The radiation damage considered in this analysis is purely due to defect formation in the bulk of the silicon sensors. This process is independent of the charge of particles incident upon the detector and represents the dominant mechanism of radiation damage to the SCT [80]. Particles incident on the silicon bulk may dislodge atoms within the silicon, creating vacancies and interstitial atoms, termed ‘Primary Knock-On Atoms’ (PKAs). The PKA and remaining vacancy are collectively referred to as a Frenkel pair. PKAs with sufficient energy may cause further displacements in the same manner and can cause defects to form with impurity atoms in the depleted region of the detector.

To generalise the incident radiation dose to originate from any possible particle, the non-ionising energy loss (NIEL) hypothesis [84] is employed. The NIEL hypothesis assumes that changes in a material from PKA-type damage scale linearly with the

## Estimating Radiation Damage in the ATLAS SCT

---

energy transferred by the incident particle and allows the radiation dose from all incident particles to be normalised to that of a neutron (the dominant source of received fluence in SCT sensors [80, 83]) with a kinetic energy of 1 MeV over 1 cm<sup>2</sup>. Radiation dose in SCT sensors is measured by the 1 MeV neutron-equivalent fluence  $\Phi$  received in time  $t$  and is quoted in units of 1 MeV  $n_{\text{eq}} \text{ cm}^{-2}$ .

The formation of physical defects alters the relative concentration of donors and acceptors in the material, which in turn affects the full depletion voltage of the sensor. The effective doping concentration is defined as

$$N_{\text{eff}} = N_{\text{D}} - N_{\text{A}} \quad (4.1)$$

where  $N_{\text{D}}$  and  $N_{\text{A}}$  are the donor and acceptor concentrations respectively. Type inversion occurs when the concentration of defect induced acceptors becomes greater than the concentration of donors. To fully deplete the central region of the sensor of free charge carriers, the applied voltage must be equal to or greater than [80]

$$V_{\text{dep}} = \frac{ed^2|N_{\text{eff}}|}{2\epsilon_r\epsilon_0} \quad (4.2)$$

where  $V_{\text{dep}}$  is the full depletion voltage and  $d$  is the width of the depletion region, which is approximately equal to the sensor thickness when fully depleted. The sensor volume must be fully depleted to maximise charge collection. This quantity decreases while the donor concentration is greater than the acceptor concentration, while the reverse process occurs following type inversion and causes an increase in  $V_{\text{dep}}$  over time. The maximum voltage that can be safely applied to SCT modules is approximately 450 V [85].

Leakage currents are also increased due to radiation damage in the sensor. After the creation of stable defects in the sensor the energy required to generate electron-hole pairs is lowered and is more easily accessible by thermal excitations, causing an increase in the detected leakage current in the absence of ionising radiation. This increased leakage current then leads to increased temperatures, which in turn further increases the leakage current in a cyclic process termed *thermal runaway* [83].

### 4.2.1 Annealing

Holding irradiated silicon sensors at temperatures at and above room temperature allows *annealing* processes to occur, potentially removing defects introduced through irradiation following proton-proton collisions as thermal excitations may cause some of the defects introduced through NIEL to become mobile. The mobility of defects can result in their removal as they migrate throughout the silicon lattice, the recombination of an interstitial defect with a vacancy in the silicon lattice or the combination of multiple defects. Compound defects formed by radiation damage may dissociate into their constituents if the available thermal energy is greater than the defect binding energy. The relation between microscopic defect annealing and the effect on macroscopic detector properties is complex and models incorporating annealing are largely empirically driven, as discussed at length in [80].

The effective doping concentration, and therefore the depletion voltage, is observed to be affected by three separate components of annealing [80]. Short term annealing is viewed as a beneficial process in type-inverted detectors as the effective doping concentration is initially negative and becomes less negative, thereby decreasing the depletion voltage. This process is driven by both the removal of stable acceptors and the generation of donors within the silicon bulk where defects are removed after a short period of migration. Short-term annealing is observed to be strongly suppressed at the typical operating temperatures of the ATLAS detector [80], and is therefore a process that can be voluntarily induced during periods of experimental maintenance in the absence of irradiation from particle collisions to decrease the depletion voltage of type-inverted SCT sensors and decrease the leakage current.

Over timescales of the order of months or years, maintaining elevated sensor temperatures in type-inverted sensors is observed to further decrease the already negative effective doping concentration, causing increasingly large depletion voltages [86]. This effect, in contrast to short term beneficial annealing described previously, is undesirable in type-inverted sensors and is termed *reverse annealing*. Reverse annealing is caused by interaction between radiation-induced defects in which defects with no overall space charge become charged defects [86] and increases the concentration of acceptors within the silicon. Additionally, the removal of donor sites within the silicon bulk produces the same change in effective doping concentration. Reverse annealing is not observed to affect leakage currents [80], which undergoes solely beneficial annealing. The effects

of radiation damage in the SCT over the course of its planned lifetime are investigated further in section 4.4 and section 4.5.

### 4.3 Assumptions Used in Model Predictions

The SCT is integral to ATLAS data collection and will remain so until the end of its planned lifetime, after which an upgrade to the entire inner detector will be made [87]. Predictions of the impact of radiation damage and annealing are required to ensure a maximally efficient detector and that the applied bias voltage and leakage current of the modules do not exceed established safe limits. Motivated by an unavoidable temperature increase due to Inner Detector humidity levels in May 2015, leakage current and depletion voltage predictions exploring different temperature ‘scenarios’ were performed. The Sheffield-Harper [83] and Hamburg-Dortmund [80–82] models were utilised for predictions of leakage current evolution. The Hamburg model [80, 81] was used for predictions of depletion voltage evolution and was the only suitable model available.

Table 4.1 Assumed LHC integrated luminosity delivered per year [88, 89]

Year	Collision Energy	Luminosity Delivered
2015	13 TeV	4.2 fb <sup>-1</sup>
2016	13 TeV	40 fb <sup>-1</sup>
2017	13 TeV	40 fb <sup>-1</sup>
2018	14 TeV	40 fb <sup>-1</sup>
2019	No Beam	0 fb <sup>-1</sup>
2020	No Beam	0 fb <sup>-1</sup>
2021	14 TeV	60 fb <sup>-1</sup>
2022	14 TeV	60 fb <sup>-1</sup>
2023	14 TeV	60 fb <sup>-1</sup>

### 4.3 Assumptions Used in Model Predictions

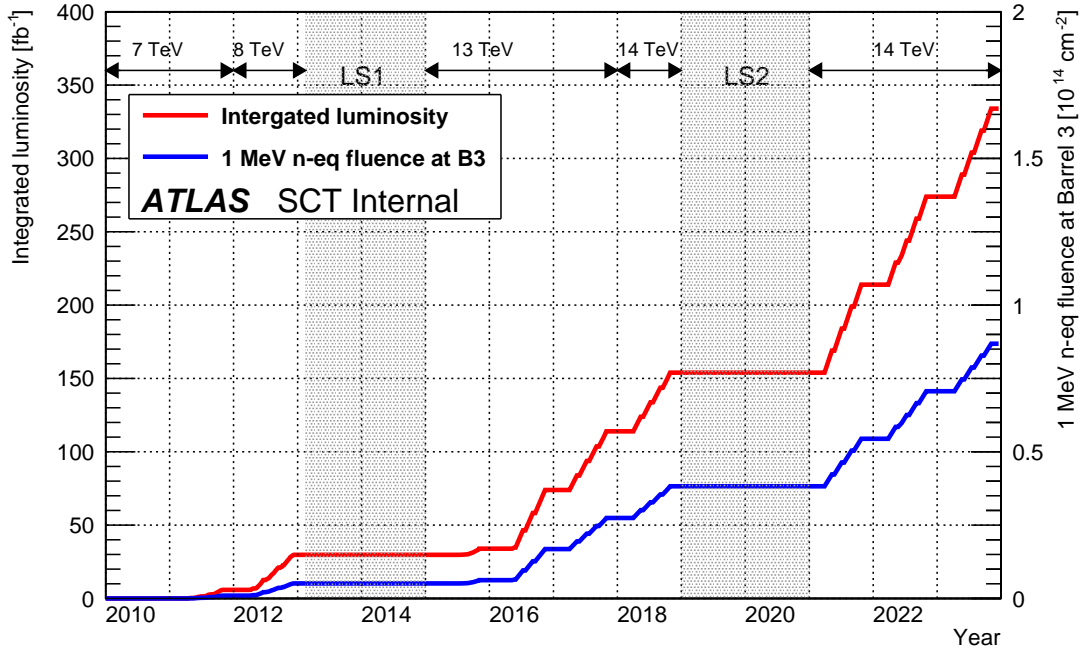


Fig. 4.1 The luminosity plan to December 2023 used in simulations of both leakage current and depletion voltage shown alongside the 1 MeV neutron equivalent fluence in Barrel 3, obtained from [89]. The luminosity until May 2016 is the recorded luminosity. After this, the luminosity is assumed and the received fluence is based on FLUKA simulations at  $\sqrt{s} = 13$  TeV and  $\sqrt{s} = 14$  TeV [90].

Table 4.2 Received fluence per  $1 \text{ fb}^{-1}$  of pp collisions at  $\sqrt{s} = 7, 8, 13$  and  $14$  TeV in each SCT barrel layer derived from FLUKA simulations [90]. Fluences are expressed as the equivalent fluence due to a 1 MeV neutron with units of  $\text{cm}^2 \text{ fb}^{-1}$ .

Barrel layer	Fluence [ $\times 10^{11} \text{ cm}^2 \text{ fb}^{-1}$ ]			
	7 TeV	8 TeV	13 TeV	14 TeV
3	1.65	1.74	2.65	2.70
4	1.30	1.37	2.11	2.15
5	1.07	1.13	1.76	1.79
6	0.92	0.97	1.51	1.55

Figure 4.1 shows the assumed luminosity profile used in all future-predictive scenarios within this chapter. Table 4.1 shows the assumed values of delivered luminosity per

year with the measured figure used for 2015. Measured luminosity data was used until May 2016, after this point the luminosity was taken from early Run 2 LHC profile estimates [88, 89]. The estimate for the total delivered luminosity represents a  $1.5 \text{ fb}^{-1}$  underestimate for 2016 and an underestimate of  $10.2 \text{ fb}^{-1}$  for 2017 when compared to the delivered luminosities as LHC performance exceeded initial estimates [71]. In addition, at the time these assumptions were generated operation at  $\sqrt{s} = 14 \text{ TeV}$  was envisaged from 2018 onwards but was not realised. However, the effective increase in fluence between  $\sqrt{s} = 13 \text{ TeV}$  and  $\sqrt{s} = 14 \text{ TeV}$  is small with respect to the increase from  $\sqrt{s} = 8 \text{ TeV}$ .

The 1 MeV neutron equivalent fluence is based on FLUKA fluence simulations [90]. Table 4.2 shows the simulation results used in this document on barrel layers for 7, 8, 13 and 14 TeV  $p$ - $p$  collision energies. Model predictions were generated for the innermost layer of the SCT barrel, closest in radial position to the interaction point, which receives the highest radiation fluence and consequently the largest changes in leakage current and depletion voltage.

### 4.4 Leakage Current Predictions

Leakage current evolution predictions were generated using two models that take into account the time of irradiation, luminosity delivered and temperature of the SCT modules. Annealing terms feature in both of the models. This study proposed an alternative model to the established model of leakage current evolution in the SCT, the Sheffield-Harper model, developed using data from irradiations of silicon SCT sensors at  $-10^\circ\text{C}$  [83] in which the leakage current evolves as a function of the delivered fluence and the temperature of the module.

$$I_n(T_{\text{ref}}) = \alpha \sum_{i=1}^n g_{n,i} \delta\Phi_i^{eq} \quad (4.3)$$

Equation 4.3 describes the evolution of the temperature-dependent leakage current  $I_n(T_{\text{ref}})$  under the Sheffield-Harper model, where  $\alpha$  is a current-related damage constant and  $\delta\Phi_i^{eq}$  is the NIEL fluence received during time period  $i$ . Beneficial annealing is described within the function  $g_{n,i}$ , while reverse annealing does not feature within the model. A full list of parameters in the model is detailed in appendix A.

## 4.4 Leakage Current Predictions

---

The Hamburg-Dortmund is the established model utilised for predictions of leakage current evolution and was used to make comparisons with leakage current measurements and to provide long-term predictions. The Hamburg-Dortmund model defines the fluence-dependent leakage current of the silicon sensor [80, 82] as

$$I_{\text{leak}} = \alpha(t) \cdot \Phi_{\text{eq}} \cdot V \quad (4.4)$$

where annealing effects are considered within  $\alpha$ , and  $V$  represents the sensor volume. The model and all dependent parameters are fully detailed in appendix A. This model was developed from irradiations of silicon diodes [80, 81], as opposed to the more SCT-specific case of SCT silicon strips in the Sheffield-Harper model. As the Sheffield-Harper model was derived using SCT-specific components, it was thought that a more reliable prediction of leakage current evolution may be obtained from the use of this model.

Initially both models were utilised to track the leakage current evolution over the existing period of data taking within ATLAS. The successful modelling of leakage current using the measured luminosity delivered in the period from 2010 to May 2016 relied upon accurate treatment of annealing by the model, especially in periods of long shutdown of the detector. Additionally, it also relied upon successful implementation of the models in the software framework which would later be used to provide long-term predictions of leakage current evolution.

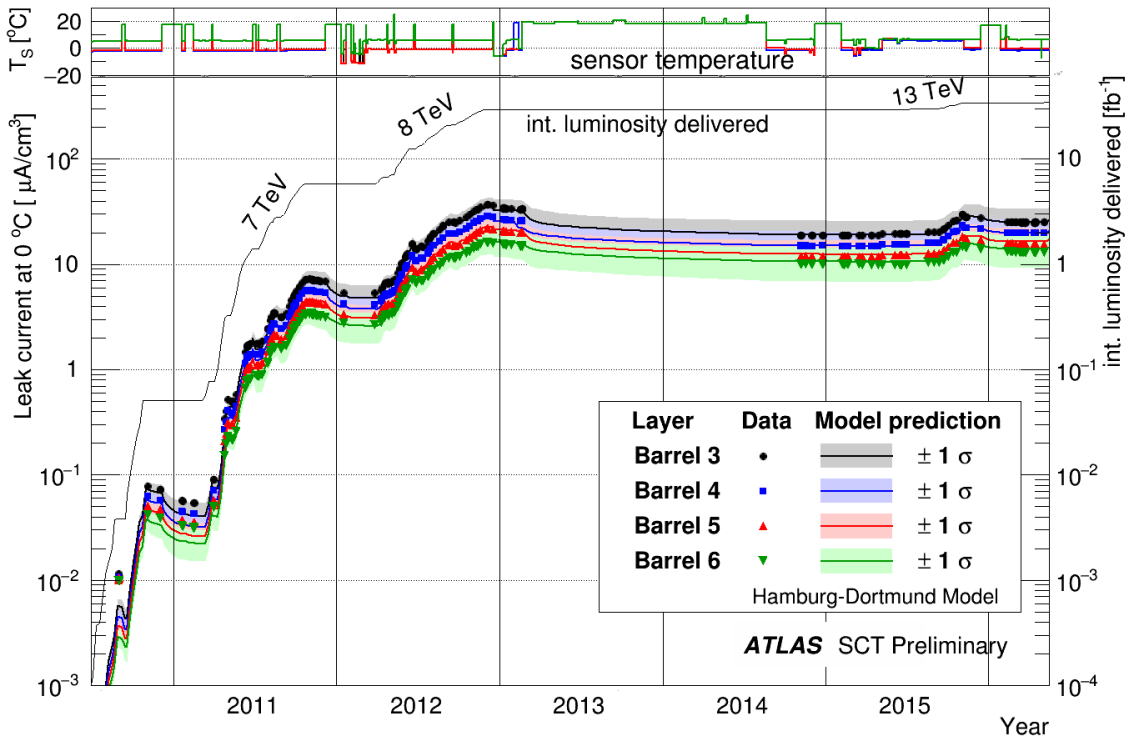


Fig. 4.2 The prediction of the Hamburg-Dortmund model of leakage current per cubic centimetre, normalised to 0°C, until the end of May 2016 with  $1\sigma$  uncertainty and leakage current data overlaid [91]. Values for all four layers of the SCT barrel are provided for both prediction and data. The top panel shows the averaged sensor temperature for each layer.

Figure 4.2 shows good agreement between the Hamburg-Dortmund model and measured leakage current throughout the 2010 to May 2016 data taking period. The decrease in leakage currents due to annealing during the 2013-2015 long shutdown of the detector following Run 1 (LS1) and in the end-of-year shutdown of each year is clearly observed. Model predictions and measured values for all barrel layers are shown, with a  $1\sigma$  uncertainty band for the model prediction overlaid for each barrel layer.

Figure 4.3 shows the equivalent leakage current evolution normalised to 0°C using the Sheffield-Harper model prediction over the same period exclusively for the innermost SCT barrel layer, which also displays good data-model agreement. Both models predict a final value of around  $25 \mu\text{A cm}^{-3}$  at 0°C, with the final measured value well within the  $1\sigma$  uncertainty band, shown in figure 4.4.

## 4.4 Leakage Current Predictions

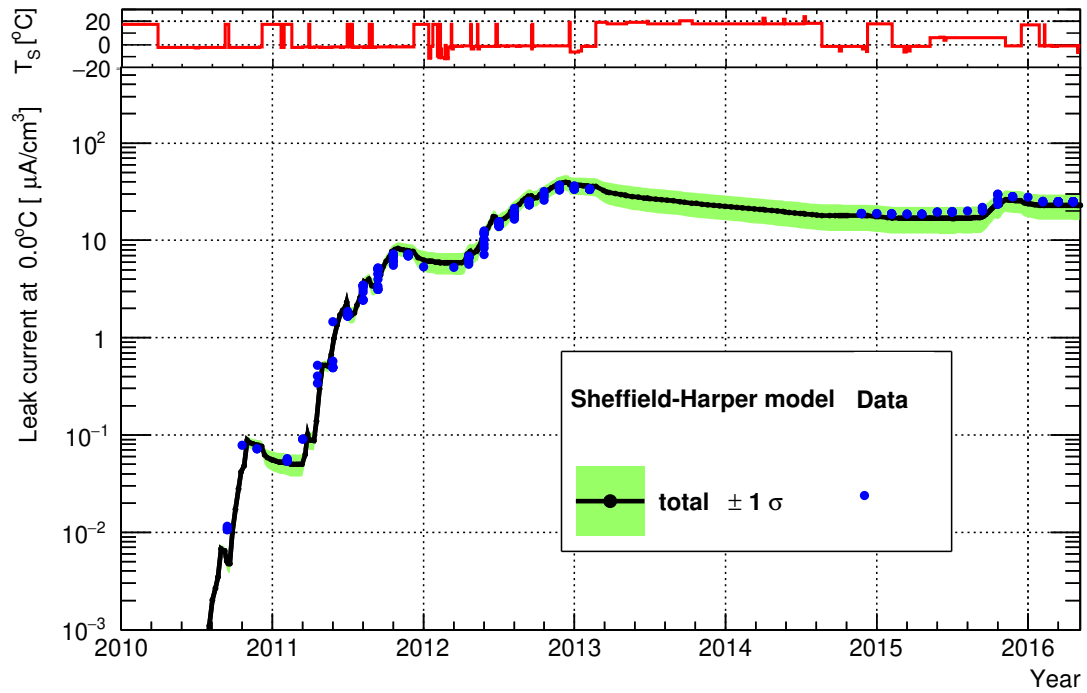


Fig. 4.3 Leakage current prediction using the Sheffield-Harper leakage current model until the end of May 2016 for Barrel 3, with  $1\sigma$  uncertainty and leakage current measurements overlaid. The top panel shows the average module sensor temperature.

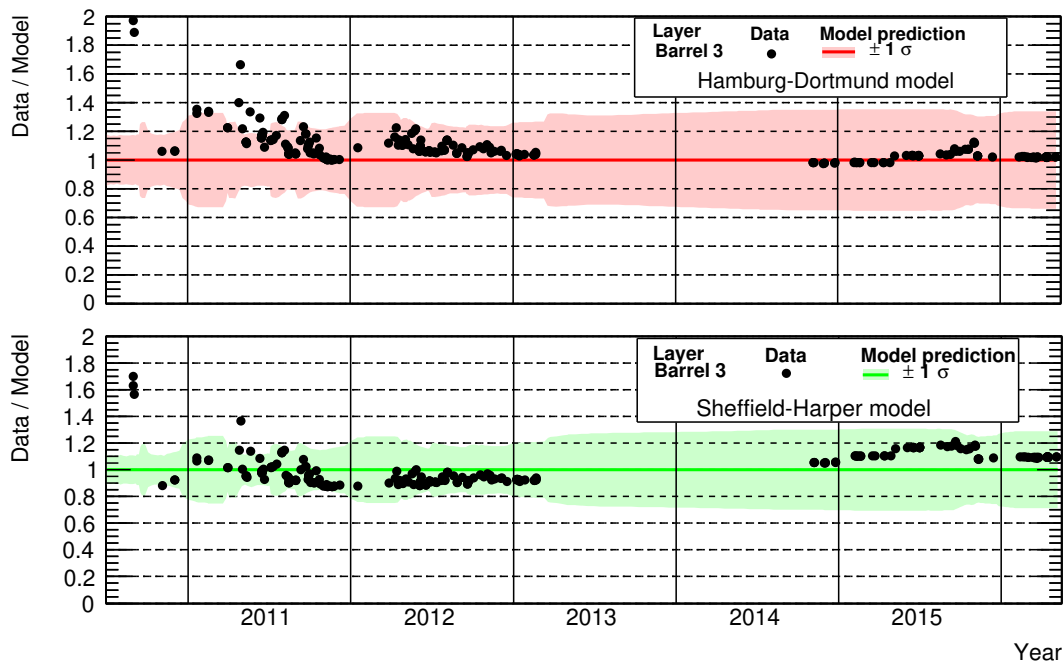


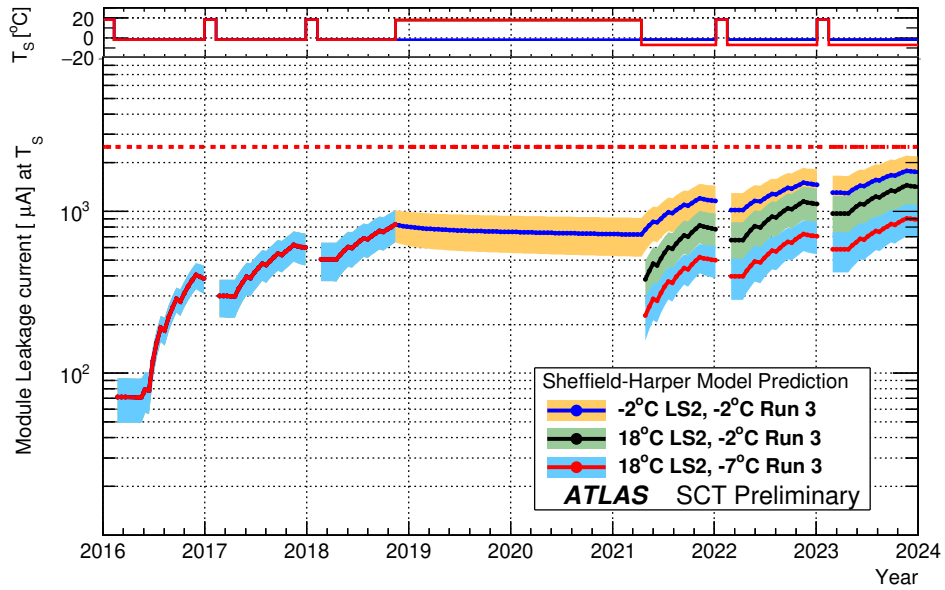
Fig. 4.4 The ratio of data to model prediction with the Hamburg-Dortmund and Sheffield-Harper leakage current models shown in figures 4.2 and 4.3, respectively.

Verification of good quality modelling of the existing data increased confidence in the reliability of the long-term predictive ability of both models. Three scenarios were introduced to vary the temperature at which SCT modules were held during LS2, with predictions derived using each scenario until the end of SCT operation in 2023

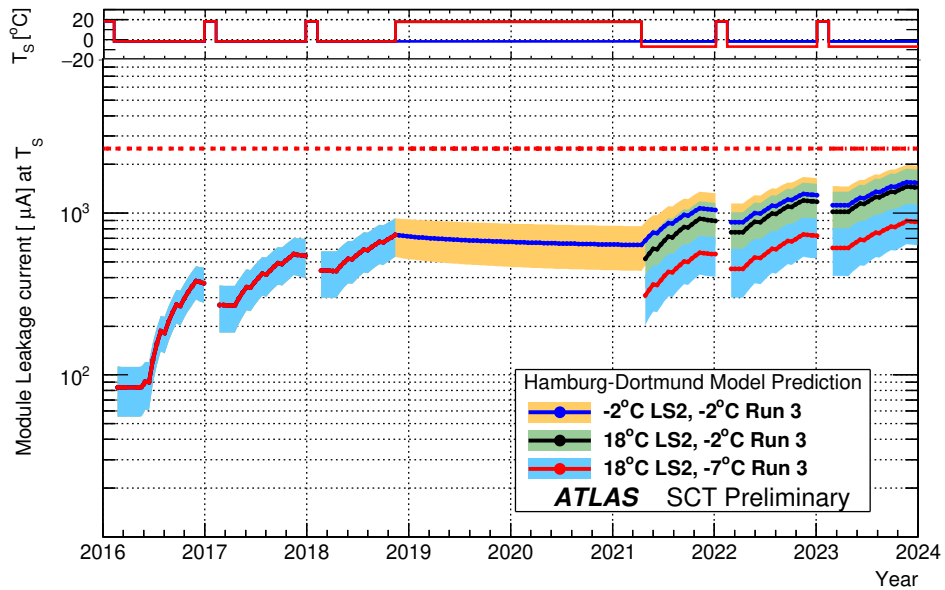
- ‘cold’ operation at  $-2^{\circ}\text{C}$  and annealing at  $-2^{\circ}\text{C}$
- operation at  $-2^{\circ}\text{C}$  with annealing at  $18^{\circ}\text{C}$
- operation at  $-7^{\circ}\text{C}$  during Run 3

All three scenarios are shown in figure 4.5.

## 4.4 Leakage Current Predictions



(a)



(b)

Fig. 4.5 Predicted evolution of leakage current per barrel layer 3 module under (a) the Sheffield-Harper and (b) Hamburg-Dortmund model from 2016-2024 with  $1\sigma$  uncertainty band. The leakage current is measured at the sensor temperature  $T_s$ , shown in the upper panel of each plot. Operation at  $-2^\circ\text{C}$  from 2016 with annealing at  $-2^\circ\text{C}$  during LS2 is shown against an annealing temperature of  $18^\circ\text{C}$ . A third scenario with LS2 annealing at  $18^\circ\text{C}$  and operation at  $-7^\circ\text{C}$  during Run 3 is also shown. The dashed line represents the upper limit for leakage current per module [62]. Values of currents during the  $18^\circ\text{C}$  periods of yearly winter shutdowns or for LS2 are omitted.

The dashed line indicates the upper limit of leakage current per module of around 2.5 mA assuming an applied 450 V bias at  $-7^{\circ}\text{C}$ . This maximum current allows the cooling systems within the SCT to have a factor of two safety margin against thermal runaway [62]. It is clear from figure 4.5 that this limit is not in danger of being crossed prior to the end of Run 3 under normal running conditions and when allowing for annealing during LS2. The Sheffield-Harper model predicts slightly higher final values of leakage current with respect to the Hamburg-Dortmund model. If no time is allowed for annealing of the silicon modules at elevated temperatures during a period of shutdown, the level of leakage current stays approximately constant for the entire period, providing a final value of leakage current that is close to the acceptable upper limit. This is not the case for a ‘warm’ shutdown, where the level of leakage current is seen to decrease over the period with no irradiation. Decreasing the operation temperature of Barrel 3 modules to  $-7^{\circ}\text{C}$  during Run 3 further reduces the final value of leakage current in both models. Such decreases in operation temperature are a potential option to counteract any significant increase in leakage currents due to unforeseen circumstances during SCT running and shutdown.

The close data-model agreement using the Sheffield-Harper model prediction demonstrated that the model may be relied upon for prediction of the leakage current in the future. Offering a similar performance and ultimately predicting higher values of the leakage current in long-term predictions, the model may be used as a more conservative alternative to the Hamburg-Dortmund model. There is a slight difference in the predicted values of the leakage current during LS1 (the period from 2013 to 2015 in figures 4.2 and 4.3) between the two models. Both models accurately reflect the increase in leakage current observed after LS1 and closely predict the measured values.

## 4.5 Depletion Voltage

Direct in-situ measurement of the full depletion voltage in the SCT silicon sensors requires capacitance-voltage profiling to be undertaken and is not possible in installed modules due to access issues. Predictions of the evolution of sensor depletion voltage due to radiation damage are therefore of high importance, and in particular estimates of the point of type-inversion of the sensors is crucial to maintaining a fully efficient

detector. The Hamburg model [80, 81] is the only viable model for depletion voltage predictions and is utilised in this section for all long-term predictions. The model determines the effective donor concentration after a received 1 MeV neutron-equivalent fluence  $\Phi_{\text{eq}}$  in time  $t$  at temperature  $T_a$  as

$$N_{\text{eff}}\left(\Phi_{\text{eq}}, t(T_a)\right) = N_{\text{eff},0} - \Delta N_{\text{eff}}\left(\Phi_{\text{eq}}, t(T_a)\right) \quad (4.5)$$

$$\Delta N_{\text{eff}}(\Phi, t) = N_C(\Phi) + N_a(\Phi, t(T_a)) + N_Y(\Phi, t(T_a)) \quad (4.6)$$

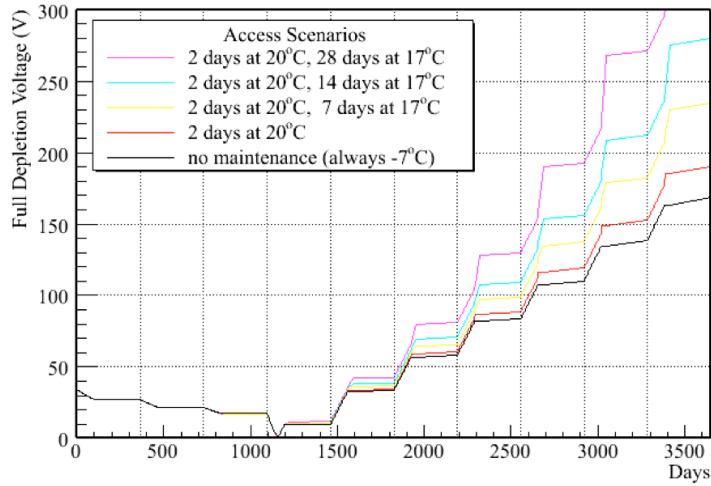
where  $\Delta N_{\text{eff}}(\Phi, t)$  represents the change in effective doping concentration due to radiation damage and is divided into three components:  $N_C$ ,  $N_a$  and  $N_Y$ . The  $N_C$  term refers to the *stable damage* component of radiation damage and is independent of annealing. Stable damage is comprised of the incomplete removal of donors from the silicon and the introduction of stable acceptors within the silicon, with both processes dependent on the received fluence.  $N_a$  describes the short term beneficial annealing which serves to increase  $N_{\text{eff}}$  in type-inverted sensors. Reverse annealing features in the model and is described by the  $N_Y$  term, causing the depletion voltage to rise over long time periods. Beneficial and reverse annealing are dependent on the annealing time  $t$  and the temperature at which annealing occurs,  $T_a$  [80, 81].

Over the lifetime of the SCT the long-term reverse annealing will become the dominant form of annealing. There are also contributions from the creation of stable and unstable acceptors. The contribution from each process and a full list of parameters used in the Hamburg model of depletion voltage is provided in Appendix A. The depletion voltage is derived from the effective doping concentration using equation 4.2.

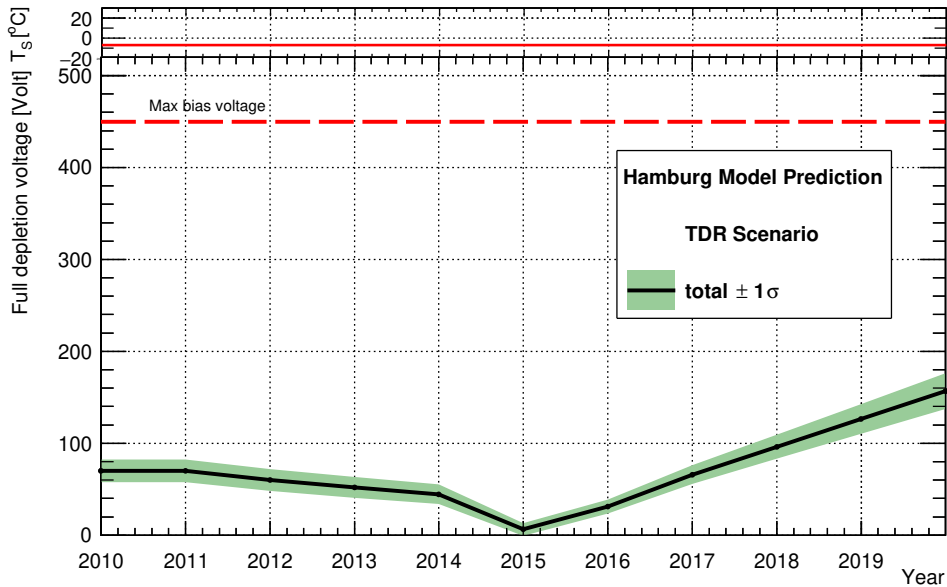
A previous study of depletion voltage [92] used the assumed SCT temperature plan of the ATLAS Inner Detector TDR [93] and modelled the evolution of depletion voltage under the Hamburg model. The TDR used an independent model that could not be replicated, and so this study was used as a test of the implementation of the Hamburg model for depletion voltage predictions. The ATLAS TDR assumed a delivered luminosity of  $10 \text{ fb}^{-1}$  per year for three years of ATLAS operation, followed by 7 years of  $100 \text{ fb}^{-1}$  per year. The total delivered luminosity by 2020 is assumed to be approximately  $700 \text{ fb}^{-1}$ . For the purpose of comparison in this study, shutdown and warming-up periods were ignored. The TDR temperature scenarios have the SCT

## Estimating Radiation Damage in the ATLAS SCT

modules at  $-7^{\circ}\text{C}$  for 349 days of the year, with optional schemes for access during each year. The “no maintenance” scenario of continuous  $-7^{\circ}\text{C}$  SCT operation (denoted by a black line) in figure 4.6a was compared to the equivalent scenario in the implementation of the Hamburg model for this study, shown in figure 4.6b.



(a)



(b)

Fig. 4.6 (a) Evolution of full depletion voltage under the access scenarios set out in the ATLAS ID TDR [93] for continuous running at  $-7^{\circ}\text{C}$  (shown by the black line) in the Hamburg model implementation of the previous study [92]. (b) The evolution of depletion voltage under the Hamburg model running at  $-7^{\circ}\text{C}$  from 2010 until 2020. The dotted line represents the assumed upper limit for depletion voltage of 450 V.

Good agreement between the Hamburg model and the TDR model was observed for this scenario, the final value for the depletion voltage is found to be 160 V in the TDR (figure 4.6a) and 164 V in the previous Hamburg model implementation of the TDR ‘no maintenance’ scenario [92]. The result from the Hamburg model implementation in this study is shown in figure 4.6b. The values from both previous studies lie within the  $1\sigma$  uncertainty band of the value obtained in this study, confirming a successful implementation of the Hamburg model.

Upon confirming the correct implementation of the Hamburg model, two boundary cooling scenarios were considered using the assumed LHC luminosity profile shown in figure 4.1. An *optimal* scenario sets the operating temperature at  $-7^\circ\text{C}$  and the annealing temperature at  $18^\circ\text{C}$  during LS2 and winter warm-up periods and represents optimal running conditions for the SCT. The *hot* scenario simulates a total failure of the cooling system during 2015 that is not rectified before 2024 (assuming some access issues, for instance). This scenario features operating and annealing temperatures of  $18^\circ\text{C}$ . Optimal and hot scenarios are shown in figures 4.7 and 4.8 respectively.

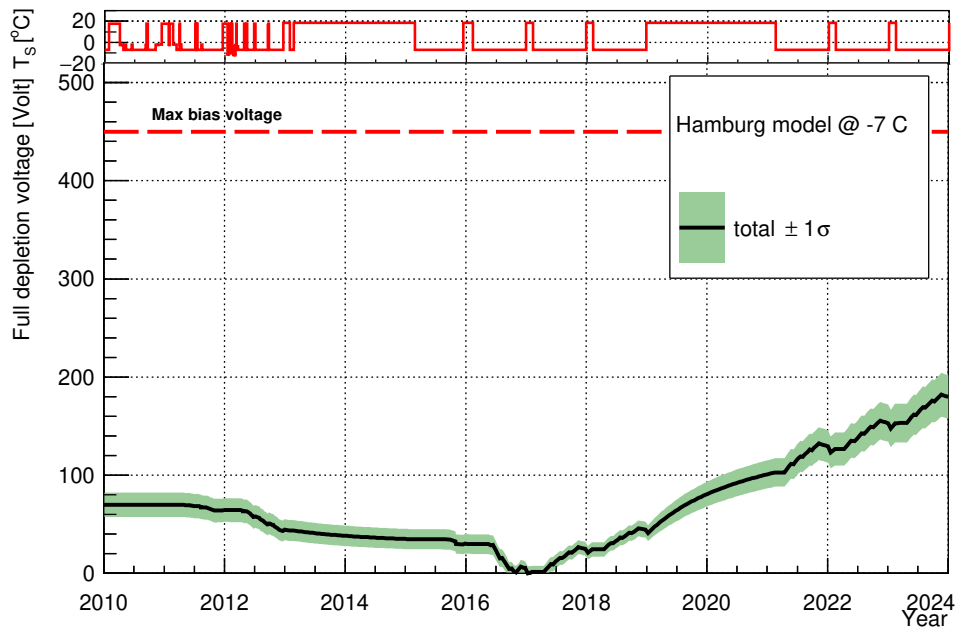


Fig. 4.7 The evolution of the depletion voltage under the Hamburg model assuming an *optimal* operating temperature of  $-7^\circ\text{C}$  with an annealing temperature of  $18^\circ\text{C}$ . The upper limit for depletion voltage of 450 V is shown by the red dashed line.

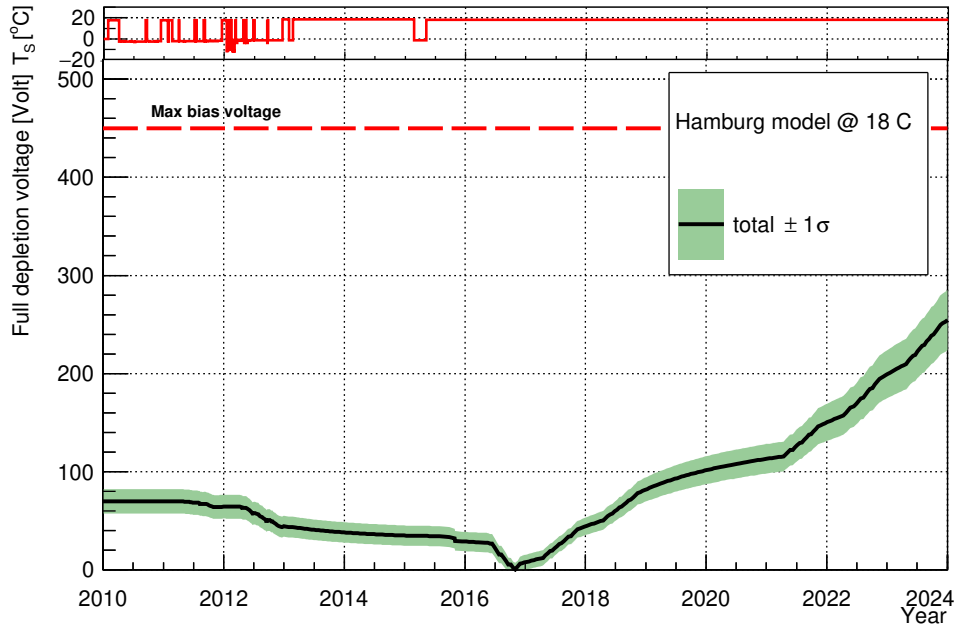


Fig. 4.8 The evolution of the depletion voltage under the Hamburg model assuming a *hot* operating and annealing temperature of 18°C. The upper limit for depletion voltage of 450 V is shown by the red dashed line.

Figures 4.7 and 4.8 show the point of type inversion occurring in late 2016 or early 2017, with increased operation temperatures bringing forward the point of type inversion. The *hot* scenario in figure 4.8 predicts a final value for depletion voltage of approximately 230 V and does not cross the 450 V upper limit for depletion voltage. Figure 4.7 shows the final value of depletion voltage for the *optimal* scenario is approximately 175 V. The length of time the SCT is held at room temperature during LS2 is the dominant effect on depletion voltage compared to operating time at -7°C in the ‘optimal’ scenario, which may explain the relatively small variance in depletion voltage between the two maximal scenarios.

Table 4.3 Realistic cases

Case	Barrel 3 Operating Temperature (°C)	Barrel 3 LS2 Temperature (°C)
1	-2°C	18°C
2	-2°C	-2°C

## 4.5 Depletion Voltage

Increasingly ‘realistic’ scenarios (shown in Table 4.3) with warm-up at every winter shutdown which more closely mirror the SCT operation schedule were investigated after testing model predictions for boundary scenarios. The period of the operating temperature of  $-2^{\circ}\text{C}$  is defined as starting after May 2015, prior to the start of Run 2.

Figures 4.9 and 4.10 show that allowing the detector to anneal at room temperature during LS2 will increase the level of depletion voltage in the SCT by around 55 V. Such a rise is due to the long term reverse annealing process. At no point in the prediction does the depletion voltage go above the upper limit of 450 V (shown by the dotted line), suggesting that allowing periods for annealing during LS2 to lower the leakage current will not cause the depletion voltage to reach unsafe levels.

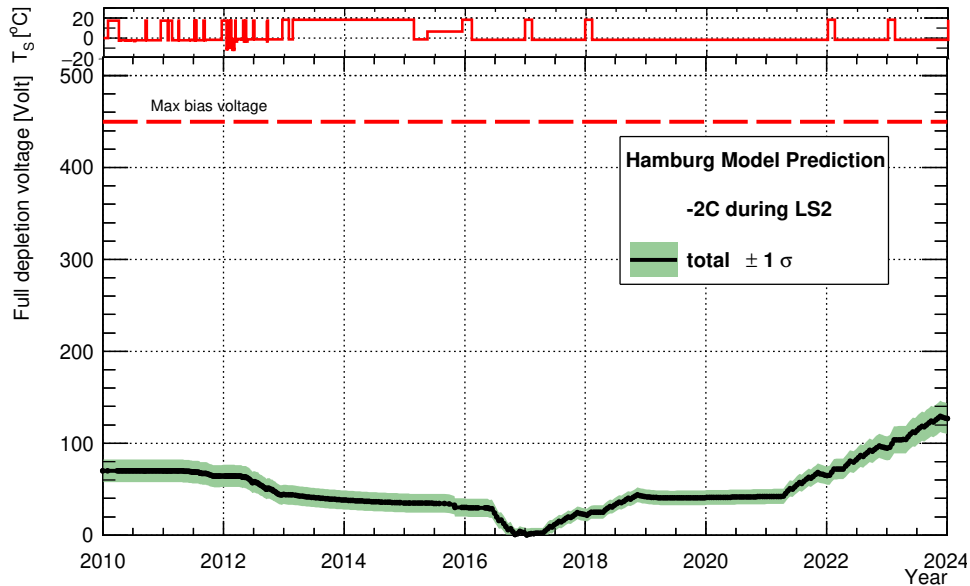


Fig. 4.9 The evolution of depletion voltage of SCT Barrel 3 under the Hamburg model assuming an operating temperature of  $-2^{\circ}\text{C}$  with a temperature of  $-2^{\circ}\text{C}$  during LS2. The upper limit for depletion voltage of 450 V is shown by the red dashed line.

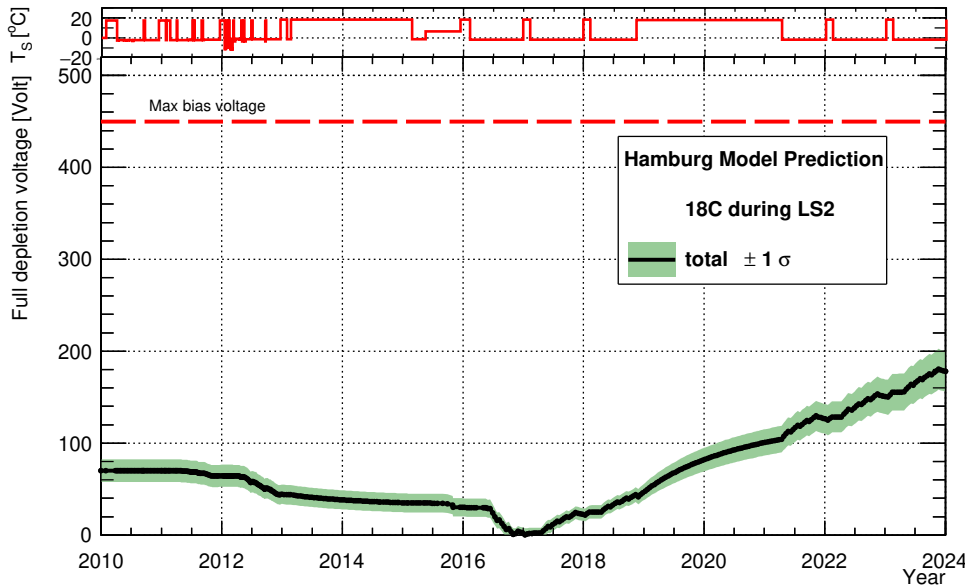


Fig. 4.10 The evolution of depletion voltage of SCT Barrel 3 under the Hamburg model assuming an operating temperature of  $-2^{\circ}\text{C}$  with a temperature of  $18^{\circ}\text{C}$  during LS2. The upper limit for depletion voltage of 450 V is shown by the red dashed line.

This study was performed prior to the point at which sensors within SCT modules underwent type inversion. This process has since occurred, and future consideration of the depletion voltage evolution will be crucial for the planning of SCT cooling as reverse annealing becomes the dominant annealing process following type inversion. With no method of directly measuring the depletion voltage in the SCT available, predictions from the Hamburg model are essential. This study recommended to the SCT working group the development of alternative models with conservative uncertainties with which to perform cross-checks with the Hamburg model.

## 4.6 Current-Voltage Profiling

Measurements of the current of SCT modules with increasing voltage are used to monitor effects of radiation on the SCT. In February 2015, barrel and endcap module leakage currents were measured by the author over a period of 10 hours, with the bias voltage increased from 20 to 150 V in 10 V intervals. Previous I-V scans of SCT barrel modules were also taken in 2013 (shortly after the beginning of LS1), with a larger scan

## 4.6 Current-Voltage Profiling

range, from 10 to 200 V. Measurements of the SCT barrel were of particular interest in light of the model predictions obtained within section 4.4. The results obtained from both scans are shown in figures 4.11 and 4.12 and represent the average measurement obtained from all SCT modules within each barrel layer.

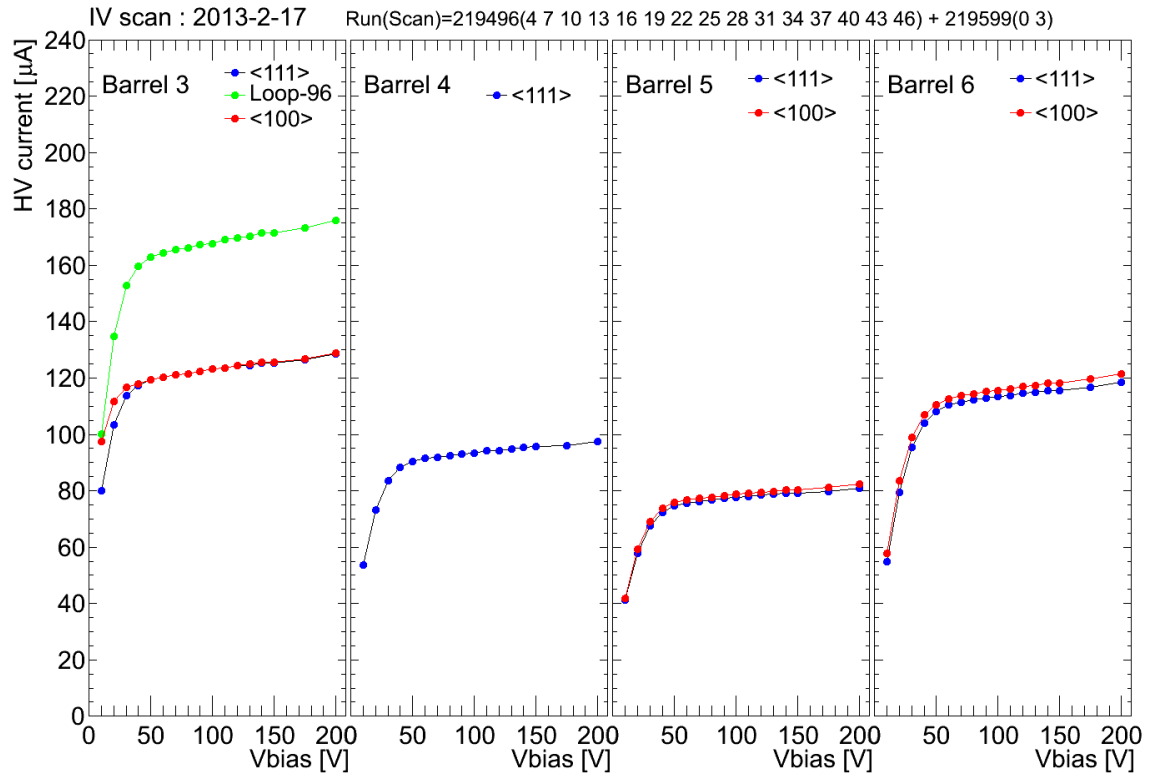


Fig. 4.11 Layer averaged I-V responses measured in 2013, prior to LS1. All four layers of the SCT barrel are shown. Figure from [94].

## Estimating Radiation Damage in the ATLAS SCT

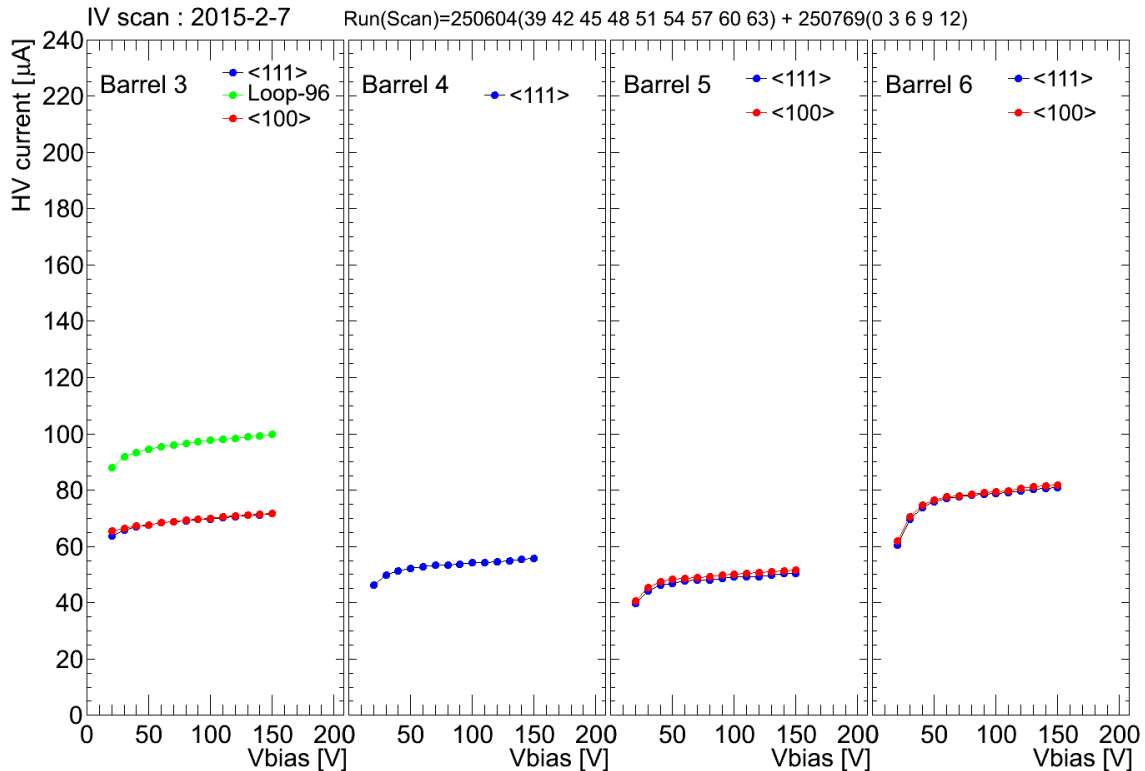


Fig. 4.12 Layer averaged I-V responses measured in February 2015, corresponding to the end of LS1. All four layers of the SCT barrel are shown.

Figures 4.11 and 4.12 show the evolution of the I-V response over the course of LS1 between 2013 and 2015 for four barrel layers. A general decrease in leakage current over LS1 is observed in all barrel layers and in general  $\langle 100 \rangle$  and  $\langle 111 \rangle$  type modules show a similar level of current at all voltages. Barrel 3 modules composed of  $\langle 100 \rangle$  and  $\langle 111 \rangle$  type sensors see a decrease of approximately  $55 \mu\text{A}$  between 2013 and 2015. Barrel 3 modules on the warmer cooling loop-96 (left-most plot in figures 4.11 and 4.12) show a higher current at all voltages than  $\langle 100 \rangle$  and  $\langle 111 \rangle$  sensors in both 2013 and 2015, and also show a decrease of approximately  $70 \mu\text{A}$  over LS1. The general decrease in current is caused by annealing, introduced in section 4.2. In both sets of measurements the current is seen to rise rapidly with voltage until a turning point is reached. At this point the applied voltage is approximately the depletion voltage and the rate of current increase drops noticeably. The turning point is observed to be around 10 V lower in 2015 than 2013. This is also the case in the Hamburg model prediction of depletion voltage, where figure 4.10 shows a value of depletion voltage of  $43.4 \pm 10.6$  in early 2013 and  $34.8 \pm 10.3$  in early 2015. The current levels are progressively lower

in Barrel 4 and Barrel 5 as expected due to lower levels of received radiation fluence. An exception to this trend is observed in the barrel 6 current, which is found to be at a similar level to Barrel 3 as it operates at a temperature approximately 5°C higher than other layers.

No major radiation damage was visible in the 2015 measurements. Continued measurement of the I-V response has proven an important resource for the SCT working group and will continue to do so as an increasing integrated luminosity is delivered over the course of Run 2 and Run 3.

## 4.7 Conclusions

The SCT will receive an increasing amount of radiation damage throughout the remaining Run 2 and the upcoming Run 3. Two macroscopic indicators of radiation damage present themselves in the leakage current and depletion voltage variables, which must both be monitored and kept under their respective safe operating limits to ensure efficient running of the detector until the planned Inner Detector upgrade in 2024 while avoiding *thermal runaway*. Providing adequate cooling and annealing periods will allow the SCT to record data efficiently throughout its running. An increase in humidity behind the inner detector endplates forced higher running temperatures to be used for most of 2015. For this reason, it is vital that predictions of depletion voltage and leakage current evolution are accurate and can be cross-checked, and that unexpected boundary scenarios are tested.

The Sheffield-Harper and Hamburg-Dortmund models have been used to explore leakage current evolution and were compared with leakage current data in figures 4.3 and 4.2, respectively. Both models are observed to accurately predict the evolution of leakage current during ATLAS Run 1 operation, LS1 and early Run 2 with observed data from leakage current measurements agreeing with the predicted values from both models within  $1\sigma$  uncertainties. The well-established Hamburg-Dortmund model was used as a benchmark model against which the Sheffield-Harper was tested. The Sheffield-Harper model was presented as an alternative predictive model and originates from SCT silicon strip irradiations at -10°C, whereas the Hamburg-Dortmund model has its origins in room temperature diode measurements [80]. The Sheffield-Harper model parameters may therefore represent a more realistic scenario for the SCT, especially over the longer

## Estimating Radiation Damage in the ATLAS SCT

---

term when annealing effects will play an increasingly important role. Both models were used to provide estimates of the leakage current under various operating scenarios until the end of 2023 in figure 4.5. The evolution of leakage current is seen to be influenced heavily by the amount of time the detector is allowed to anneal at room temperature. An upper threshold of leakage current of 2.5 mA was defined assuming a maximum acceptable depletion voltage of 450 V in the predictive scenarios, which was not exceeded by any scenario under either model. Though it is not exceeded, the final predicted values of leakage current were close enough to the upper limit to cause concern at the time of the study and lead to a recommendation to decrease operating temperatures for Run 3 where possible to ensure that leakage currents are maintained at a reasonable level. Without careful consideration of SCT module operating temperatures and long shutdown temperatures, it is likely that the leakage currents will reach values close to the upper limit towards the end of Run 3.

The Hamburg model provided the sole means of estimating the depletion voltage over the course of LS1 and in early Run 2 and this remains the case presently. As direct measurements of the depletion voltage are not possible due to access issues, this study strongly recommended to the SCT working group that an alternative depletion voltage model be investigated as a high priority to avoid solely relying upon the predictions of a single model. This chapter has demonstrated that SCT depletion voltages should remain comfortably under the upper limit of 450 V until the end of 2023 through the use of boundary scenarios in figures 4.7 and 4.8 and scenarios more closely following realistic ATLAS temperature scenarios in figures 4.9 and 4.10, where only the temperature during LS2 was varied. This conclusion was dependent on the assumed delivered luminosity meeting the expectations used within this chapter, which were revised downwards to approximately  $300 \text{ fb}^{-1}$  by the end of 2023 based on the performance of the LHC in 2016, less than half of the initial LHC goal of  $700 \text{ fb}^{-1}$ .

The current-voltage profiling measurements taken in February 2015 show clearly the effects of annealing due to the first long shutdown at the LHC. The level of leakage current is seen to drop as expected due to annealing effects. The approximation of the full depletion voltage derived from the observed turning point of the I-V curve for barrel 3 in figures 4.11 and 4.12 was found to be adequately predicted by the Hamburg model prediction of depletion voltage in figure 4.10. Regular use of current-voltage profiling has continued to be necessary to monitor the effects of radiation damage within the SCT. Currently little degradation has been observed through these measurements,

although as the delivered luminosity increases over the course of Run 2 and Run 3, the effects should be more pronounced.



# Chapter 5

## Analysis Tools

This chapter summarises the techniques necessary for the reconstruction of physical observables with the ATLAS detector that are used in the analyses described in chapter 7.

### 5.1 Physics Object Reconstruction

The physical observables following a proton-proton collision are reconstructed from information provided by the various sub-components of the ATLAS detector, described in chapter 3, in both data and MC simulated events. *Physics objects* such as jets, electrons, muons, photons and  $E_T^{\text{miss}}$  are defined in a consistent manner across an analysis.

Objects passing a selection with loose requirements in  $p_T$ ,  $\eta$  and isolation are referred to as *baseline* objects. A process of *overlap removal* is applied to baseline objects to avoid double counting by removing physics objects appearing within a distance  $\Delta R$  of other objects, for instance an electron detected within a jet. Objects passing a set of more stringent analysis-specific  $p_T$ ,  $\eta$  and isolation requirements after overlap removal are classified as *signal* objects.

### 5.1.1 Tracks and Vertices

The trajectories of charged particles in the ATLAS ID are referred to as *tracks* and are heavily relied upon in the reconstruction of physics objects. Track reconstruction algorithms were optimised for the start of Run 2 [95], motivated in part by the increase in centre-of-mass collision energy to  $\sqrt{s} = 13$  TeV which led to an increase in the production of energetic jets. Such jets may contain highly collimated charged particles with average separation in  $(\eta, \phi)$  of the order of the sensitivity of the individual elements of the ID. Tracks are seeded by Pixel and SCT clusters and hits in the TRT [96]. Silicon detector clusters are reconstructed by grouping sensors containing *hits*: raw measurements where charged particles deposit energy above a threshold in a sensor. Three-dimensional *space-points* are then derived from clusters. One cluster is equivalent to one space-point in the Pixel detector, whereas in the SCT a combination of clusters from both sides of a single strip layer is used to obtain the space-point. Track candidates are required to have  $p_T > 400$  MeV,  $|\eta| < 2.5$ ,  $\geq 7$  Pixel and SCT clusters,  $\leq 1$  shared Pixel cluster or  $\leq 2$  SCT clusters on any layer,  $\leq 1$  *hole* in the Pixel detector (or  $\leq 2$  *holes* when also considering the SCT), a transverse impact parameter  $d_0 < 2.0$  mm and a longitudinal impact parameter<sup>1</sup>  $z_0 \sin \theta < 3.0$  mm. Holes are defined as regions of active detector where a hit is expected from track trajectory but not detected. The missing hit must occur between successive hits assigned to the same track to be classified as a hole. After a track candidate from the Pixel and SCT is found, tracks are extended to the TRT in a dedicated track finding algorithm [97]. Tracks with a TRT portion but no detection in the silicon detectors are termed TRT-standalone tracks.

Tracks originate from vertices in the detector, points of particle interaction or decay. The vertex with the highest summed track  $p_T$  is referred to as the primary vertex, defined as the point in space at which the hard interaction occurs in the detector. In Run 2 analyses the reconstructed primary vertex is required to have two or more associated tracks with  $p_T > 400$  MeV. Tracks from the products of decaying particles are said to originate from *secondary* vertices. One such case is discussed in section 5.1.3.

---

<sup>1</sup>The longitudinal impact parameter  $z_0$  represents the  $z$  coordinate at the distance of closest approach between the track and primary vertex.

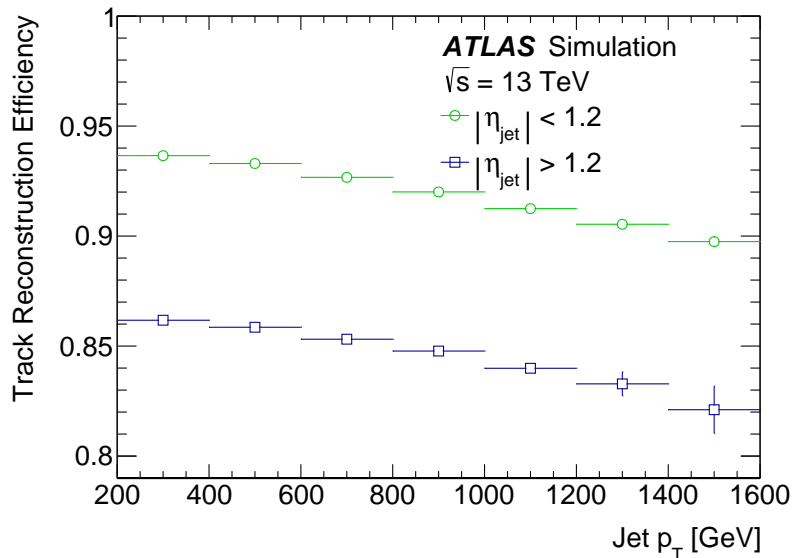


Fig. 5.1 Simulated reconstruction efficiency of tracks from charged particles within jets as a function of  $p_T$  for  $|\eta| < 1.2$  and  $|\eta| > 1.2$  at  $\sqrt{s} = 13$  TeV. Figure from [95].

The reconstruction efficiency for charged particle tracks in jets as a function of jet  $p_T$  is shown in figure 5.1 for low and high  $|\eta|$  cases.

## 5.1.2 Jets

Jets are the observable quantity associated with partons, which hadronise within the detector. Collimated sprays of hadrons resulting from parton showering within the detector are reconstructed as colour-neutral jets. Jet reconstruction algorithms define jets at the reconstruction stage, grouping the particles that constitute a jet and defining its momentum and topological footprint within the detector in both data and MC simulated events.

### 5.1.2.1 Infrared and Collinear Safety

Jet algorithms are required to produce jets which are both infrared and collinear (IRC) safe. The showering process following hard parton scattering contains many instances of parton emission collinear with the original parton. Collinear emission of partons is also a potential outcome of the decay of hadrons within a jet, occurring at lower

energy scales. Jets may also randomly emit low energy particles, termed infrared. IRC safety dictates that the occurrence of either process should not affect the final number of hard jets reconstructed by the jet algorithm [98]. Cone-type jet algorithms have traditionally been used in jet reconstruction, where (most commonly) the jet is defined by a seed particle, with the jet axis taken as the direction of the seed particle and the jet momentum is equal to that of all particles contained within a circle in  $(\eta, \phi)$ . Having a well-defined jet area is beneficial experimentally when determining the area of a calorimeter in which a jet can be said to be fully contained [98]. However, cone-type jet algorithms generally have issues with IRC unsafety [98]. As a result, ATLAS uses a sequential recombination jet algorithm described in section 5.1.2.2 which by design produces roughly conical jets with a well-defined area.

An example of a collinear and infrared unsafe jet finding algorithm is shown in figure 5.2, where either the emission of a low energy particle or the splitting of a single high momentum particle into two lower momentum particles changes the number of reconstructed jets.

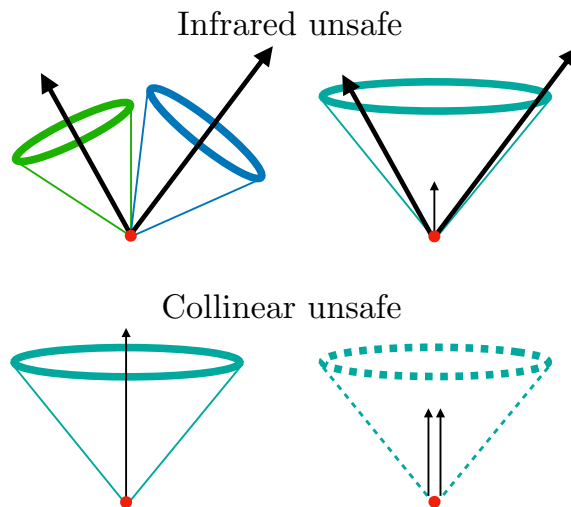


Fig. 5.2 Representation of an infrared unsafe jet algorithm (top) and a collinear unsafe jet algorithm (bottom). Reconstructed jets are shown by solid coloured lines, the transverse momentum of a particle within the jet is shown by a black arrow whose magnitude is proportional to the length of the arrow. The infrared safe algorithm reconstructs two jets in the absence of the emission of a soft particle and one jet otherwise. The collinear unsafe algorithm fails to reconstruct a jet when a high momentum particle splits into two lower momentum particles. Figure adapted from [99].

### 5.1.2.2 ATLAS Anti- $k_t$ Jets

ATLAS uses the IRC-safe anti- $k_t$  jet clustering algorithm [20] in the reconstruction of jets. The jet reclustering algorithm is seeded by three-dimensional positive-energy *topo-clusters*, topologically linked calorimeter cell signals due to particle energy loss via electromagnetic and hadronic showers with a signal significance relative to background noise [100]

$$\zeta_{\text{cell}}^{\text{EM}} = \frac{E_{\text{cell}}^{\text{EM}}}{\sigma_{\text{noise}}} \quad (5.1)$$

where background noise includes effects from electronic noise and pile-up and is defined [100]:

$$\sigma_{\text{noise}} = \sqrt{(\sigma^{\text{electronic}})^2 + (\sigma^{\text{pile-up}})^2} \quad (5.2)$$

and the cell signal energy  $E^{\text{EM}}$  is measured at the scale at which energy lost by electrons and photons in EM showers is correctly measured and that does not include any hadronic corrections. Topo-clusters are formed from calorimeter cells with high signal significances, termed ‘seed cells’. Seed cells with  $\zeta_{\text{cell}}^{\text{EM}} > 4$  are identified and ordered in decreasing  $\zeta_{\text{cell}}^{\text{EM}}$  and form ‘proto-clusters’ [100]. Any adjacent calorimeter cells within a single calorimeter layer (or within another layer while overlapping in  $(\eta, \phi)$ ) containing signals with a significance  $\zeta_{\text{cell}}^{\text{EM}} > 2$  [101] are incorporated into the proto-cluster. In the case that the calorimeter cell adjacent to the seed cell also possesses  $\zeta_{\text{cell}}^{\text{EM}} > 4$  both proto-clusters are combined. This is also the case when a calorimeter cell with  $\zeta_{\text{cell}}^{\text{EM}} > 2$  is adjacent to multiple seed cells [100]. Negative signals within calorimeter cells, resulting mainly from pile-up and electronic noise, are not used to reconstruct physics objects [101]. Resulting proto-clusters may be spatially large and are split if they possess multiple cells with signals  $E_{\text{cell}}^{\text{EM}} > 500$  MeV surrounded by  $> 4$  adjacent cells with smaller signals. Topo-clusters are the resultant objects formed following proto-cluster splitting [100].

The algorithm reconstructs jets with a well defined circular area in  $(\eta, \phi)$ , as illustrated by figure 5.3 where it is compared to other candidate jet algorithms. Hadrons are formed into conical jets with a user-defined radius. The nomenclature “AntiKt $X$ ” is used to refer to denote jets reconstructed within ATLAS as a cone via the anti- $k_t$  algorithm with a radius parameter  $\Delta R = X \times 10^{-1}$  in the  $(\eta, \phi)$  plane as defined in equation 3.7 and where  $X$  is an integer. Jets discussed in this thesis generally use  $X = 4$ , resulting in jets with a radius of  $\Delta R = 0.4$ , unless otherwise specified.

## Analysis Tools

The momentum-weighted distance between particles  $i$  and  $j$  with transverse momentum  $k_{ti}, k_{tj}$  and the distance between  $i$  and the beam  $B$  are defined as

$$d_{ij} = \min(k_{ti}^{2p}, k_{tj}^{2p}) \frac{\Delta_{ij}^2}{\Delta R^2} \quad (5.3)$$

$$d_{iB} = k_{ti}^{2p} \quad (5.4)$$

where  $\Delta_{ij}^2 = (y_i - y_j)^2 + (\phi_i - \phi_j)^2$  between the rapidity and  $\phi$  components of the two particles, the parameter  $p = -1$  is included to define the relationship of energy versus the geometrical scale  $\Delta_{ij}$  in jet reconstruction and  $\Delta R$  is the radius parameter [20]. The use of  $k_t$  to denote particle transverse momentum is purely convention within the algorithm.

A list of the entities  $i$  and  $j$  are provided as an input to the algorithm with distances  $d_{ij}$  defined between the two entities and  $d_{iB}$  defined between  $i$  and the beam  $B$ . The lesser of  $d_{ij}$  and  $d_{iB}$  is identified; the algorithm combines  $i$  and  $j$  in the case of  $d_{ij} < d_{iB}$ , otherwise if  $d_{iB} < d_{ij}$  the entity  $i$  is classed as a jet and removed from the initial list of entities. This process repeats until a jet with a cone of radius  $\Delta R$  is constructed.

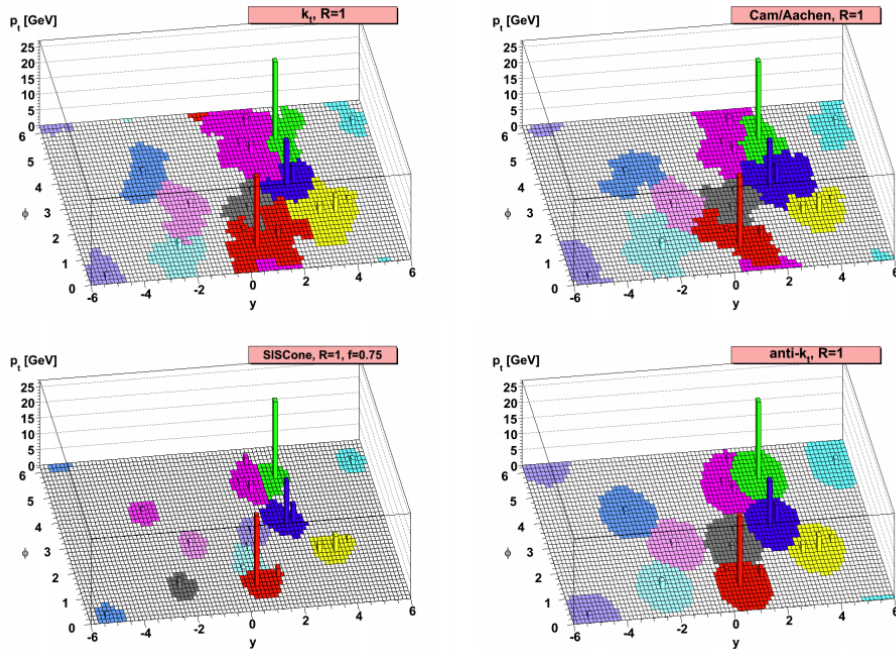


Fig. 5.3 A simulated parton-level event illustrating the differences between various jet algorithms. The anti- $k_t$  algorithm, used to reconstruct jets in ATLAS, is shown in the bottom right of the figure. This algorithm is IRC safe and creates jets with a well-defined area. Figure from [20].

The anti- $k_t$  algorithm is applied to topo-clusters measured at the EM scale passing an energy threshold of 7 GeV [102]. Jets reconstructed from topo-clusters at the EM scale are referred to as **EMTopo** jets.

### Jet Energy Scale

The energy of reconstructed **EMTopo** jets is calibrated to the truth jet energy scale via *jet energy scale* (JES) calibrations, shown in figure 5.4.

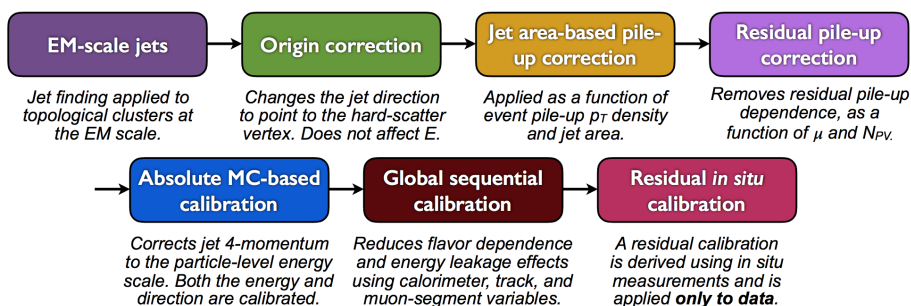


Fig. 5.4 Calibration and correction stages for EMTopo jets in 2015. All calibrations except origin correction are applied to the jet four-momenta. The variables  $\mu$  and  $N_{PV}$  refer to the number of proton-proton interactions per bunch crossing and the number of primary vertices, respectively. Figure from [102].

Physics objects referred to as *truth jets* are reconstructed using the anti- $k_t$  jet algorithm with distance parameter  $\Delta R = 0.4$  from stable particles<sup>2</sup> produced from MC generators (excluding muons, neutrinos and particles from pile-up) and are measured at the particle-level energy scale [102]. A brief summary of the Run 2 JES calibrations [103] is provided in this section, based upon the calibrations used in Run 1 [104, 105]. Systematic uncertainties related to JES calibrations are discussed in section 5.2.1. JES calibrations are broadly divided into MC-based and *in-situ* calibrations. MC-based calibrations correct reconstructed jet four-momenta in MC to the truth level, while in-situ calibrations correct the jet response in data.

Origin corrections initially recalculate the four momenta of reconstructed jets to point to the primary vertex where the jet originated, producing an  $\eta$  resolution of jets of  $\Delta\eta = 0.045$  for  $p_T = 20$  GeV and  $\Delta\eta = 0.006$  for  $p_T = 200$  GeV. Corrections are

<sup>2</sup>Particles with  $c\tau > 10$  mm, where  $\tau$  is the proper lifetime of the particle.

applied to jets to remove additional energy arising from pile-up using simulated pile-up conditions based upon those measured in the detector and are described in [103].

Absolute jet energy scale and  $\eta$  calibration uses MC to correct reconstructed jet four momenta to the truth level and corrects any biases in  $\eta$ . The average energy response distribution is plotted using matched truth jets (truth jets within  $\Delta R = 0.3$  of reconstructed jets) and well-isolated reconstructed jets. Well isolated jets are defined as having no other jets with  $p_T > 7$  GeV within  $\Delta R = 0.6$  and no more than one truth jet with  $p_T^{\text{truth}} > 7$  GeV within  $\Delta R = 1.0$ . The jet energy response is defined as the mean of a Gaussian fit to the central portion of the distribution of  $E^{\text{reco}}/E^{\text{truth}}$  binned in jet  $\eta$  pointing from the centre of the detector ( $\eta_{\text{det}}$ ) and is shown for 2015 conditions in figure 5.5. Plotted as a function of  $\eta$ , the degradation of the response due to gaps and transition regions within the detector in simulated jets is visible.

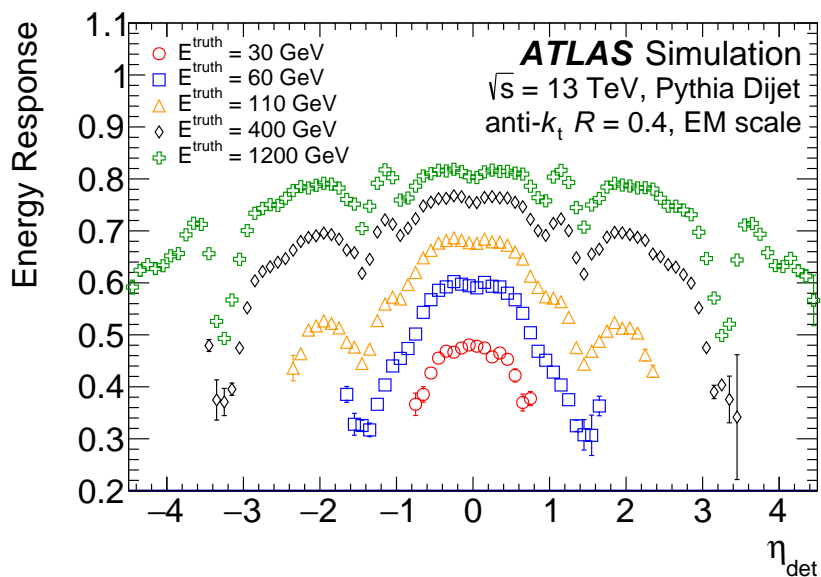


Fig. 5.5 Average energy response as a function of  $\eta_{\text{det}}$  for a range of truth jet energies from 30 to 1200 GeV using PYTHIA MC simulated dijet events. Figure from [103].

Global sequential calibration (GSC) [106] then attempts to remove dependencies of the JES on the jet shape and flavour composition of the jet. In-situ calibrations represent the final stage of jet calibration and rectify the differences between jets in data and MC. Jets with  $0.8 < |\eta_{\text{det}}| < 4.5$  undergo energy scale correction to match jets with  $|\eta_{\text{det}}| < 0.8$  in a dijet balance analysis ( $\eta$ -intercalibration). Jets with  $|\eta| < 0.8$  and  $p_T \leq 950$  GeV are calibrated by balancing jet  $p_T$  back-to-back with a  $\gamma$  or  $Z$  ( $Z/\gamma$ +jet

## 5.1 Physics Object Reconstruction

balance). Calibration of jets with  $p_T$  up to 2 TeV is performed by balancing a high- $p_T$  jet against a collection of  $\geq 3$  calibrated lower  $p_T$  jets in the *multijet balance* (MJB) calibration [103]. These calibrations define an in-situ jet response for both data and MC simulated events

$$\mathcal{R}_{\text{in situ}} = \frac{p_T^{\text{jet}}}{p_T^{\text{reference}}} \quad (5.5)$$

where  $p_T^{\text{reference}}$  refers to the reference object recoiling against the jet in question [103]. The combined calibration from all in-situ procedures is shown in figure 5.6. Differences between data and MC can arise due to inaccurate modelling of the detector and its response in MC, leading to poor jet reconstruction.

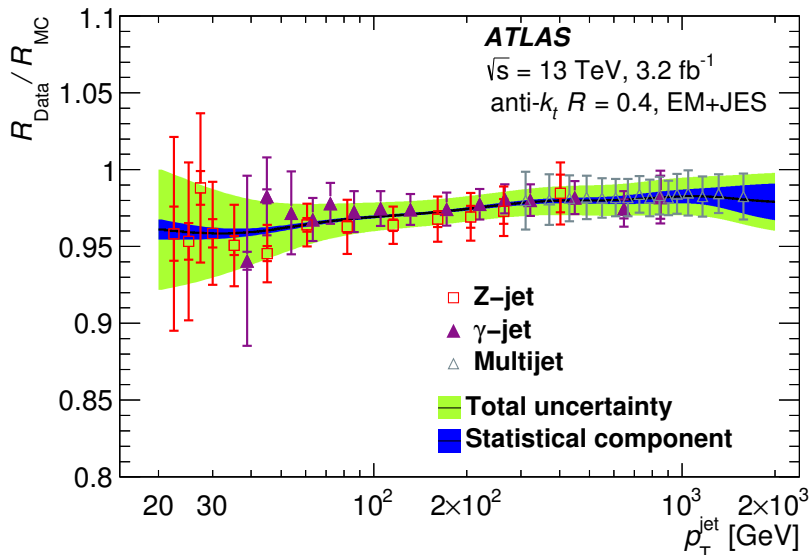


Fig. 5.6 Ratio of the in-situ jet response defined in equation 5.5 in  $\sqrt{s} = 13$  TeV data events to that derived using MC simulated events for the  $Z/\gamma$ +jet and multijet calibration procedures described in section 5.1.2.2 as a function of jet  $p_T$ . The correction and associated uncertainty is shown by the black line and coloured bands. Figure from [103].

### Jet Quality Requirements

Jet quality requirements are imposed to reduce the appearance of *fake* jets that are not associated with the initial hard parton scattering. Fake jets may arise from non-collision sources or due to detector noise [107]. Non-collision background sources include the beam induced background (BIB) and cosmic ray showers. BIB is divided into beam-gas events due to proton collisions with gas within the beam pipe and beam-halo events

## Analysis Tools

---

which occur due to collisions between protons and beam collimation apparatus [104]. Inelastic beam-gas interactions can cause secondary cascades leading to high energy muons being mis-reconstructed as jets in the detector [108]. Cosmic ray showers overlapping with the collision of interest provide an additional source of non-collision background, mostly in the form of muons. Calorimeter cells with high levels of noise (permanently or sporadically) are masked prior to jet and  $E_T^{\text{miss}}$  reconstruction. Jet quality criteria listed below, with variables defined in table 5.1, are designed to identify ‘fake’ jets, physics objects incorrectly reconstructed as jets in the detector. The quality factor  $Q_{\text{cell}}^{\text{LAr}}$  is a simplified  $\chi^2$  test used to measure the level of agreement between the measured and simulated signal amplitudes in calorimeter cells due to ionising particles, proportional to the energy lost by the ionising particle [1, 107]. Large values of the quality factor indicate that measured signal is due to noise.

Table 5.1 Variables used in jet quality requirements, taken from [107], where a full definition of the jet quality variables used in Run 2 analyses can be found.

Variable	Description
$Q_{\text{cell}}^{\text{LAr}}$	Quality factor (c.f. $\chi^2$ ) from quadratic difference between measured and expected ionisation signal shape in a LAr calorimeter cell expressed in arbitrary ADC counts [107]
$\langle Q \rangle$	Unitless energy-squared weighted average of the quality factor normalised to $0 < \langle Q \rangle < 1$
$f_{\text{Q}}^{\text{LAr}}$	Fraction of energy in LAr calorimeter cells of a jet with $Q_{\text{cell}}^{\text{LAr}} > 4000$
$f_{\text{Q}}^{\text{HEC}}$	Fraction of energy in HCal-endcap cells of a jet with $Q_{\text{cell}}^{\text{LAr}} > 4000$
$E_{\text{neg}}$	Sum of all (fake) negative energy deposits in calorimeter cells due to noise
$f_{\text{EM}}$	Ratio of energy deposited in ECAL to total jet energy
$f_{\text{HEC}}$	Ratio of energy deposited in HCal-endcap to total jet energy
$f_{\text{max}}$	Maximum energy fraction in any single calorimeter layer
$f_{\text{ch}}$	Ratio of the summed $p_T$ of jet-associated tracks to jet $p_T$

Fake jets are identified by their classification as either `LooseBad` or `TightBad`. The `LooseBad` selection is designed to ensure a high efficiency in identifying ‘good’ jets. A jet is identified as a `LooseBad` jet in ATLAS physics analyses at  $\sqrt{s} = 13$  TeV if it meets one or more of the following criteria defined within [107]:

## 5.1 Physics Object Reconstruction

---

- $f_{\text{HEC}} > 0.5$  and  $|f_{\text{Q}}^{\text{HEC}}| > 0.5$  and  $\langle Q \rangle > 0.8$
- $|E_{\text{neg}}| > 60$  GeV
- $f_{\text{EM}} > 0.95$  and  $f_{\text{Q}}^{\text{LAr}} > 0.8$  and  $\langle Q \rangle > 0.8$  and  $|\eta| < 2.8$
- $f_{\text{max}} > 0.99$  and  $|\eta| < 2$
- $f_{\text{EM}} < 0.05$  and  $f_{\text{ch}} < 0.05$  and  $|\eta| < 2$
- $f_{\text{EM}} < 0.05$  and  $|\eta| \geq 2$

The **TightBad** selection provides a higher rate of fake jet rejection at the cost of lower efficiency identification of ‘good’ jets. Jets are identified as **TightBad** if they are classified as **LooseBad** or alternatively have  $f_{\text{ch}}/f_{\text{max}} < 0.1$  and  $|\eta| < 2.4$  [107]. Any jets failing to pass the above criteria are considered ‘good’ jets. Jets are classified as **Loose** jets with  $> 99.5\%$  efficiency over all  $p_{\text{T}}$  if they do not pass the **LooseBad** criteria, and **Tight** with  $> 95\%$  efficiency over all  $p_{\text{T}}$  if they do not pass the **TightBad** criteria [107].

Further removal of jets originating from pile-up is achieved by placing requirements on the value of the jet vertex tagger (JVT) variable, constructed with the variables  $\text{corrJVF}$  and  $R_{p_{\text{T}}}$  [109]:

$$\text{corrJVF} = \frac{\sum_k p_{\text{T}}^{\text{trk},k}(\text{PV}_0)}{\sum_l p_{\text{T}}^{\text{trk},l}(\text{PV}_0) + \zeta} \quad (5.6)$$

$$\zeta = \frac{\sum_{n \geq 1} \sum_l p_{\text{T}}^{\text{trk},l}(\text{PV}_n)}{(k \cdot n_{\text{trk}}^{\text{PU}})} \quad (5.7)$$

$$R_{p_{\text{T}}} = \frac{\sum_k p_{\text{T}}^{\text{trk},k}(\text{PV}_0)}{p_{\text{T}}^{\text{jet}}} \quad (5.8)$$

where  $\sum_k p_{\text{T}}^{\text{trk},k}(\text{PV}_0)$  is the summed  $p_{\text{T}}$  of jet tracks associated with the hard interaction vertex,  $\sum_{n \geq 1} \sum_l p_{\text{T}}^{\text{trk},l}(\text{PV}_n)$  is the summed  $p_{\text{T}}$  of jet tracks associated with pile-up interactions,  $n_{\text{trk}}^{\text{PU}}$  is the number of pile-up tracks and  $k = 0.01$ .  $\text{CorrJVF}$  is defined as the ratio of the summed  $p_{\text{T}}$  of jet tracks associated with the PV to the summed  $p_{\text{T}}$  of all jet tracks, corrected for the average momentum contribution from pile-up tracks.  $R_{p_{\text{T}}}$  is defined as the ratio of the summed  $p_{\text{T}}$  of jet tracks associated with the PV to the total jet  $p_{\text{T}}$ . Both variables are used as inputs to determine the likelihood-based JVT variable [109].

### 5.1.3 $b$ -tagged Jets

Jets originating from  $b$ -quarks contain one or more  $B$ -hadrons that may decay, producing a secondary vertex in addition to the primary vertex.

The identification of a  $b$ -jet is referred to as *tagging* and is crucial for third generation SUSY searches. Tagging is informed by tracking information provided by the inner detector.

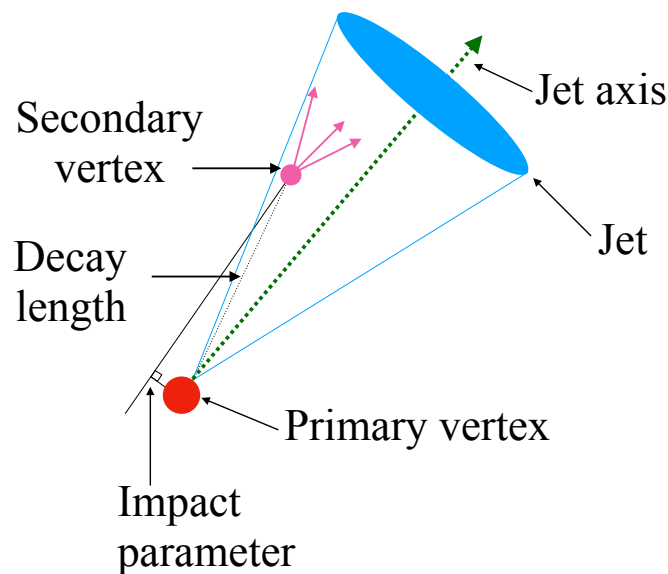


Fig. 5.7 Schematic view of a jet originating from a  $b$ -quark at the primary vertex. The trajectory of the  $B$ -hadron is highlighted and subsequently decays at the secondary vertex, shown in pink. The impact parameter  $d_0$  is shown as the transverse distance between the primary and secondary vertices. Figure adapted from [110].

Figure 5.7 shows the delayed decay of a  $B$ -hadron in a jet seeded by a  $b$ -quark, creating a distinct secondary vertex. The distance of closest approach between the secondary and primary vertex is referred to as the *impact parameter*.  $B$ -hadrons often display large impact parameters due to their characteristic long lifetime of  $\sim 1.5 \times 10^{-12}$  s [5].

Identification of  $b$ -jets in Run 2 [111] uses Inner Detector tracks as inputs to three groups of algorithms: impact parameter-based algorithms (IP2D and IP3D), a secondary vertex finding algorithm (SV) [112] and a decay chain multi-vertex algorithm [113]

that attempts to recreate each step of B-hadron decays within the jet. IP2D and IP3D takes tracks that have [111]:

- $p_T > 1$  GeV
- $|d_0| < 1$  mm,  $|z_0 \sin \theta| < 1.5$  mm
- $\geq 7$  hits in the silicon detectors with  $\leq 2$  holes ( $\leq 1$  in the Pixel detector)

and calculate impact parameter significances  $d_0/\sigma(d_0)$  and  $z_0 \sin \theta/\sigma(z_0 \sin \theta)$ . PDFs are built from the impact parameter significances in MC for  $b$ ,  $c$  and light flavour jets. A log-likelihood ratio discriminant is calculated from the impact parameter significance PDFs to separate jets based on flavour.

The SV algorithm reconstructs displaced vertices within jets by adding all tracks arising from two-track vertices consistent with  $b$ -jets. Tracks are required to have  $\geq 7$  hits in the Pixel and SCT with  $\leq 1$  hit shared between the two detectors. Tracks are also required to pass a  $\chi^2$  fit quality requirement. For Run 2, the algorithm was modified in the following ways:

- an upper limit of 25 tracks (ordered in decreasing  $p_T$ ) per secondary vertex for jets with  $p_T > 300$  GeV to reduce the fake vertex reconstruction rate
- hit requirements for jets with  $|\eta| > 1.5$  were increased by one due to degrading track parameter resolution with decreasing amounts of detector material at high- $|\eta|$
- removal of tracks with  $d_0/\sigma(d_0) < 2$  and  $z_0/\sigma(z_0) > 6$  for further fake vertex reduction

The results of these basic algorithms are combined in a multivariate algorithm [114], MV2. The MV2 algorithm is trained using jets from MC simulated  $t\bar{t}$  events with  $b$ -jets considered to be the signal alongside a background of jets originating from  $c$ -quarks and light flavour jets from  $u$ ,  $d$  and  $s$  quarks. Variants of the algorithm are available; the default used by analyses in 2016 data was the MV2c10 variant, where the background composition is 7%  $c$ -quark jets and 93% light flavour jets, updated from MV2c20 used for 2015 data [111]. The MV2c10 algorithm is by default set to the operating point providing an average 77%  $b$ -jet identification efficiency as a function of  $p_T$  in a  $t\bar{t}$  sample using jets with  $p_T > 20$  GeV. The performance of the two algorithms for  $b$ -jet identification and light flavour jet rejection is shown in figures 5.8 and 5.9, while the

## Analysis Tools

---

rejection factor for  $c$ -jets and light flavour jets are shown for each working point in table 5.2.

Table 5.2 MV2c10  $b$ -tagging algorithm operating points with average  $b$ -tagging efficiencies and  $c$ -jet and light jet rejection rates calculated in  $t\bar{t}$  MC simulated events from [107]. Rejection factors are defined as the inverse of the rate at which a jet of the type listed is identified as a  $b$ -jet [115].

$b$ -jet ID	Efficiency [%]	$c$ -jet Rejection Factor	Light-jet Rejection Factor
60		34	1538
70		12	381
77		6	134
85		3.1	33

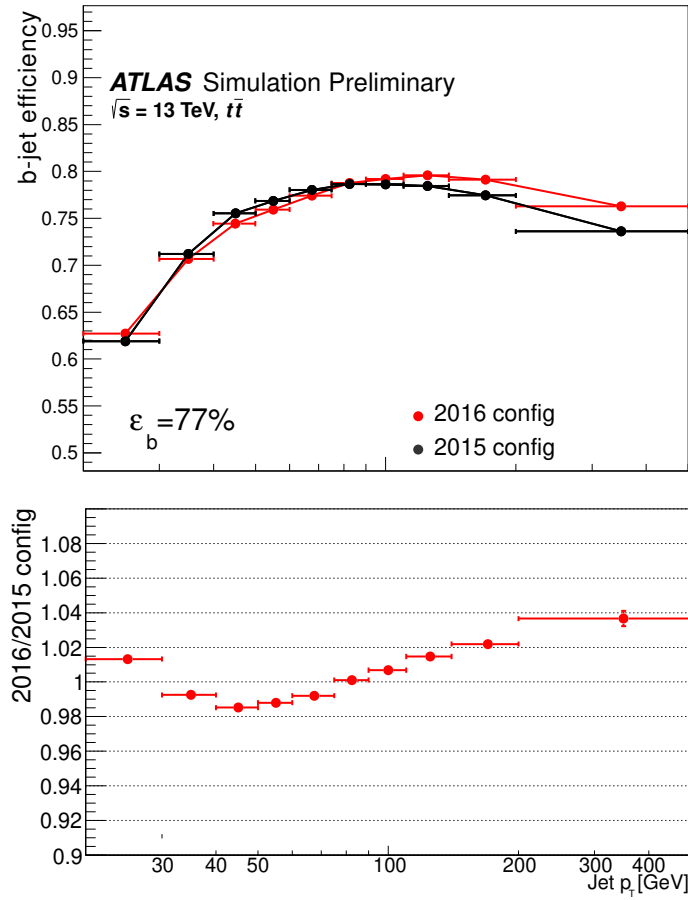


Fig. 5.8  $b$ -jet identification efficiency as a function of  $p_T$  using a fixed 77%  $b$ -jet efficiency requirement in  $t\bar{t}$  MC events. Efficiencies are plotted separately for the MV2c10 and MV2c20 algorithms, representing the default  $b$ -tagging algorithms for 2016 and 2015 respectively. Figures from [111].

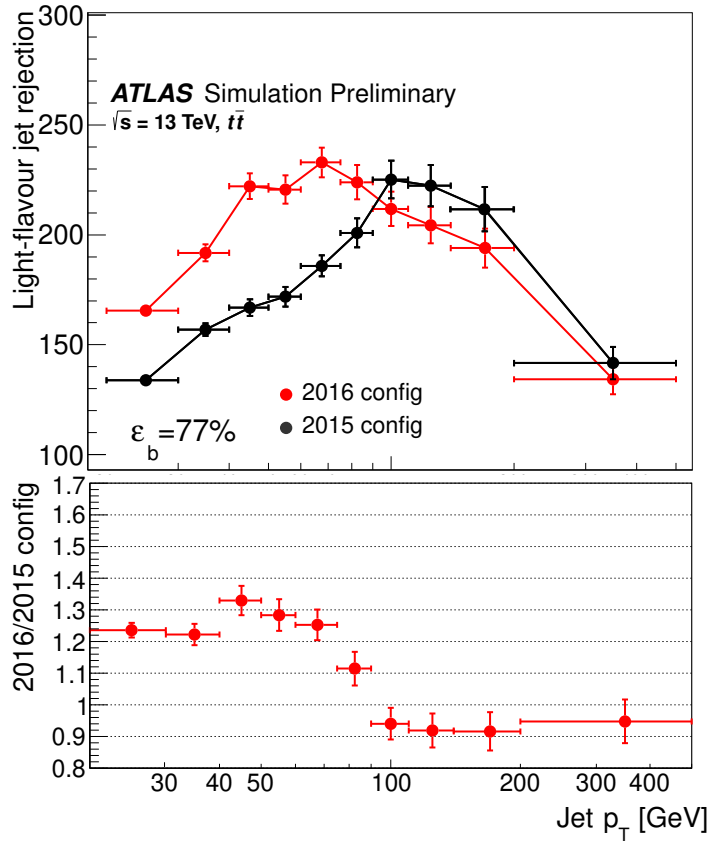


Fig. 5.9 Light flavour jet rejection efficiency as a function of  $p_T$  using a fixed 77%  $b$ -jet efficiency requirement in  $t\bar{t}$  MC events. Efficiencies are plotted separately for the MV2c10 and MV2c20 algorithms, representing the default  $b$ -tagging algorithms for 2016 and 2015 respectively. Figures from [111].

Scale factors (SFs) are calculated for the  $b$ -tagging process and are used to weight MC events in analyses, scaling them to data. SFs in the context of  $b$ -tagging are the  $p_T$ -dependent ratios in  $b$ -tagging efficiency between data and MC for  $t\bar{t}$  events [116].

$$\text{SF}_{b\text{-tag}} \equiv \frac{\epsilon_b^{\text{data}}}{\epsilon_b^{\text{sim}}} \quad (5.9)$$

where  $\epsilon_b^{\text{data}}$  and  $\epsilon_b^{\text{sim}}$  are the  $b$ -tagging efficiencies in data and MC, respectively. SFs are applied to simulated events to ensure proper modelling of the  $b$ -tagging efficiency in data.

### 5.1.4 Electrons and Photons

Electrons (defined to include positrons) and photons are reconstructed in the detector region of  $|\eta| < 2.47$  using clusters of ECAL energy deposits and tracks reconstructed within the Inner Detector.

ECAL energy clusters are constructed with a *sliding window algorithm* [117]. The ECAL is divided into a grid of  $N_\eta \times N_\phi = 200 \times 256$  ‘towers’ in  $(\eta, \phi)$  with fixed size  $\Delta\eta \times \Delta\phi = 0.025 \times 0.025$ , optimised for seed cluster finding efficiency and fake seed cluster rejection. The energy of calorimeter cells from all longitudinal ECAL layers (including the presampler for  $|\eta| < 1.8$ ) within a tower is summed to provide the *tower energy*. Large cells with energies distributed across multiple towers distribute energy among towers according to the fractional area of the cell within each tower. A window with size  $N_\eta^{\text{window}} \times N_\phi^{\text{window}}$  with units of  $\Delta\eta \times \Delta\phi$  moves across each element of the  $N_\eta \times N_\phi$  grid and measures the transverse energy encapsulated by the window. If a local maximum is found above an energy threshold  $E_T^{\text{threshold}} = 2.5$  GeV a seed cluster is formed, with duplicate seed clusters removed [118]. Clusters are then built by taking all cells within a rectangle of size  $N_\eta^{\text{cluster}} \times N_\phi^{\text{cluster}}$  centred around the (layer dependent) position of the seed cluster. In contrast to Run 1, Run 2 cluster size is not determined by predicted particle type, but purely the location within the calorimeter [118]. The size is optimised to contain a maximal amount of the energy deposited by a particle within the calorimeter while minimising additional electronic and pile-up noise considered by the inclusion of extra cells. In the ECAL barrel, electron showers are wider than photon showers due to increased interaction with detector material and the emission of bremsstrahlung photons.

The barrel cluster size corresponds to  $3 \times 7$  cells of size  $0.025 \times 0.025$  in  $(\eta, \phi)$  in the middle ECAL layer EM2. Endcap cluster sizes correspond to  $5 \times 5$  cells in the middle layer and are larger in  $\eta$  than the barrel due to the smaller size of the cells in the endcap. The efficiency of the cluster search process is 95% at  $E_T = 7$  GeV, increasing to  $> 99\%$  for  $E_T > 15$  GeV.

Inner Detector tracks are associated with clusters if there are sufficient hits in the pixel and silicon layers. Clusters with no associated tracks are identified as unconverted photons. Clusters with matching tracks and an absence of a secondary vertex corresponding to a photon conversion into an electron-positron pair are identified

as electrons. Clusters matched to one or two tracks with no hits in the innermost pixel layers and a secondary vertex corresponding to an electron within the TRT are considered to be converted photons.

### 5.1.4.1 Electrons

Electron candidates require one or more ID tracks to be matched to an ECAL cluster [118, 119]. On passing shower shape requirements, a ROI is formed within a cone of  $\Delta R < 0.3$  around the cluster barycentre [118]. Electron track candidates are then fitted with the ATLAS Global  $\chi^2$  Track Fitter [120] using a specific electron-based track reconstruction algorithm. Candidate tracks passing this fit are loosely matched to EM cluster barycentres in  $\eta$  and  $\phi$  after extrapolation to EM2, the layer in which most of the energy from EM showers is deposited.

Electron identification is performed with a likelihood (LH) based method to determine the probability of an electron candidate being *signal*-like or *background*-like. The LH method uses shower shape related variables, TRT information, track information and bremsstrahlung as inputs to discriminate between signal and background-like effects such as hadronic jets or particles arising from the conversion of photons. The IBL, discussed in section 3.3.2.1, provides improved discrimination between converted photons and electrons. A description of the electron identification process in Run 2, along with the variables utilised by identification algorithms, is given in [118]. The ID algorithms were re-optimised for Run 2 using electron candidates in  $Z \rightarrow ee$ ,  $J/\Psi \rightarrow ee$ , dijet and minimum bias MC samples. The LH algorithm provides three operating points, in order of increasing background rejection: *loose*, *medium* and *tight*. The electron identification efficiencies in  $Z \rightarrow ee$  decays and background rejection efficiencies in dijet MC of the three working points are shown in figure 5.10.

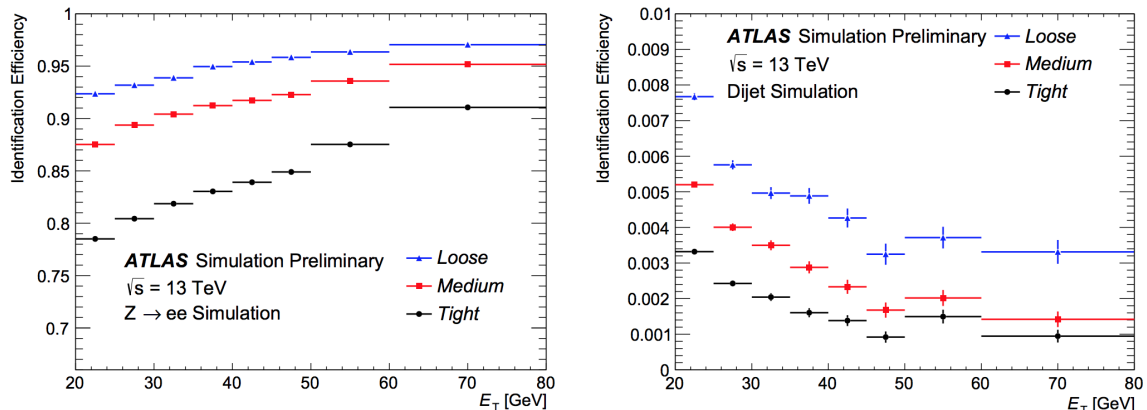


Fig. 5.10 Left: electron identification efficiency in MC  $Z \rightarrow ee$  decays at the *loose*, *medium* and *tight* working points. Right: rate of electron mis-identification in MC dijet events at the same working points. The 45 GeV bin is the highest  $p_T$  bin used for optimisation of the electron identification. Figure from [118].

#### 5.1.4.2 Photons

Photon reconstruction relies on many of the same principles as electron reconstruction, in particular ECAL energy cluster construction and reconstructed tracks loosely matched to these clusters. An overview of the process of energy cluster formation and track matching is provided in section 5.1.4. ECAL clusters with no matched tracks are considered to be unconverted photons, while those with a pair of charged-particle tracks with differing charge and an identifiable secondary vertex are considered to be converted photons. Due to poor efficiency of track detection at large radii, clusters with a single associated track are considered to be converted photons if there are no hits in the innermost layer of the pixel detector.

Photons are also reconstructed in the case where they are misidentified as electron candidates with tracks that have no hits in silicon detectors and  $p_T < 2$  GeV or a ratio of energy over momentum greater than 10. The process of recovering unconverted photons from misidentified electron candidates has an efficiency of approximately 85% [121].

A full description of the photon reconstruction and identification process is given in [121], with isolation requirements for Run 2 provided in [122].

### 5.1.5 Muons

Muon tracks are reconstructed using independent measurements from the ID up to  $|\eta| = 2.5$  and MS up to  $|\eta| = 2.7$ . A combination of the two measurements is used to increase the topological area over which muons can be reconstructed within the detector. Muon track reconstruction in the ID occurs in the same manner as for other charged particles. Track candidates in the MS are reconstructed from hits in the various MS subdetectors with trajectories both in the plane of and orthogonal to the magnetic bending plane of the detector [123]. Muon identification aims to reject background (mostly arising from kaon and pion decays [123]) while maintaining a high efficiency in identifying prompt muons.

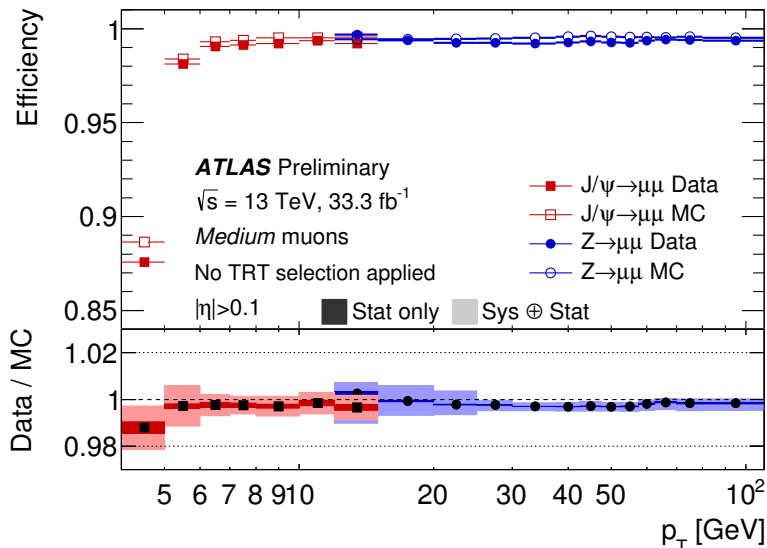


Fig. 5.11 Muon reconstruction efficiencies for the *Medium* muon identification selection (with no TRT selection required) measured in  $J/\Psi \rightarrow \mu\mu$  and  $Z \rightarrow \mu\mu$  events as a function of transverse momentum.  $J/\Psi \rightarrow \mu\mu$  events are shown by filled circles in data and by empty circles in MC. Similarly,  $Z \rightarrow \mu\mu$  events are shown as filled squares for data and as empty squares for MC events. Only statistical uncertainties are shown in the top panel. The darker bands in the bottom panel denote the statistical uncertainty, while the lighter band shows the quadratically summed statistical and systematic uncertainties. Figure from [124].

Muons are divided into four classifications: *Medium*, *Loose*, *Tight* and *High- $p_T$* , with *Medium* muons representing the default muon selection within ATLAS. Figure 5.11

shows the reconstruction efficiency as a function of muon  $p_T$  for the *Medium* muon selection using the full 2016 dataset.

### 5.1.6 Missing Transverse Momentum

In collider experiments, there is negligible net momentum transverse to the beam axis prior to the collision. The application of the principle of momentum conservation implies that this should also be the case following the collision. The production of particles that escape the detector environment without detection<sup>3</sup> can cause significant amounts of missing transverse momentum ( $\vec{E}_T^{\text{miss}}$ ) in an event, where

$$\vec{E}_T^{\text{miss}} = - \sum_{\text{visible}} \vec{p}_T = \sum_{\text{invisible}} \vec{p}_T \quad (5.10)$$

Missing transverse energy ( $E_T^{\text{miss}}$ ) [125, 126] is reconstructed as the magnitude of the negative vector sum of the  $\vec{p}_T$  of the event, the quantity obtained by equation 5.10. The presence of a significant amount of  $E_T^{\text{miss}}$  is essential for the discovery of evidence of R-parity conserving SUSY. Searches for supersymmetric particles produced within the detector decaying to a stable, weakly interacting LSP ( $\tilde{\chi}_1^0$ ) that escapes without detection necessarily have final states with large  $E_T^{\text{miss}}$ . In fully hadronic R-parity conserving SUSY searches, jets and  $E_T^{\text{miss}}$  are often the only physics objects present in the final state.  $E_T^{\text{miss}}$  can also arise in these analyses due to poor reconstruction or mismeasurement of particles, incorrect removal of hard objects or the presence of neutrinos from heavy-flavour jet decays.  $E_T^{\text{miss}}$  arising from such sources is referred to as ‘fake’  $E_T^{\text{miss}}$ , which analyses aim to mitigate.

$E_T^{\text{miss}}$  contains a *hard term* composed of all detected and calibrated particles along with a *soft term*. During Run 1 the soft term was reconstructed using calorimeter energy deposits unassociated with any high- $p_T$  physics object. In Run 2, the Track-based Soft Term (TST) is used and is more resistant to conditions with increasing pile-up. The TST contains reconstructed ID tracks associated with the hard-scatter vertex that cannot be associated to any calibrated object considered within the hard term. The  $E_T^{\text{miss}}$  resolution measured by the RMS width of the distributions of the components of  $E_T^{\text{miss}}$  in  $x$  and  $y$  is shown in figure 5.12 as a function of  $\sum E_T$  for three  $E_T^{\text{miss}}$  definitions.

---

<sup>3</sup>These particles are referred to as *invisible particles*, in contrast to the *visible* particles that it is possible to detect following a collision.

$E_T^{\text{miss}}$  constructed with the TST is compared with versions constructed using the calorimeter cell soft term and using solely track information in figure 5.12, where  $E_T^{\text{miss}}$  constructed with the TST is found to have an improved resolution at lower  $\sum E_T$  due to higher pile-up event rejection [127].

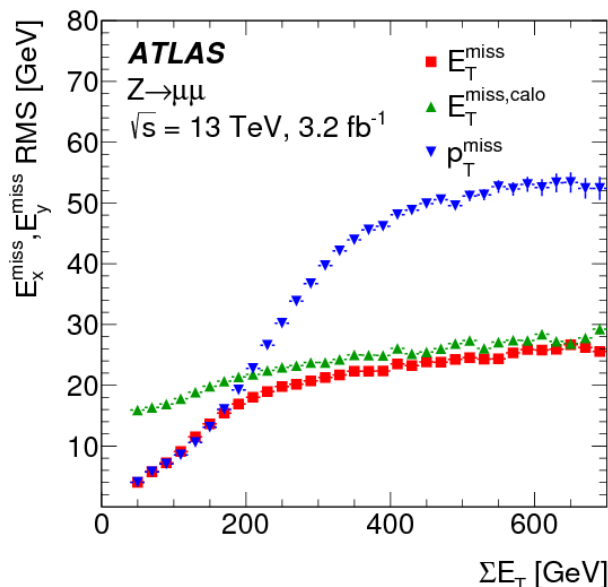


Fig. 5.12 RMS width of distributions of the  $x$  and  $y$  component of  $E_T^{\text{miss}}$  binned in  $\sum E_T$  in  $Z \rightarrow \mu\mu$  events in  $3.2 \text{ fb}^{-1}$  of  $\sqrt{s} = 13 \text{ TeV}$  data when using  $E_T^{\text{miss}}$ -constructed using the TST (shown by red squares),  $E_T^{\text{miss}}$  constructed using a calorimeter-based soft term (shown by green triangles), and a definition using track information only (shown by blue triangles).  $E_T^{\text{miss}}$  using the calorimeter based soft term has worse resolution at low values of  $\sum E_T$  when compared to  $E_T^{\text{miss}}$  constructed with the TST. At higher values of  $\sum E_T$  the resolution is comparable. Figure from [127].

The  $x$  and  $y$  components of  $E_T^{\text{miss}}$  are defined in the analyses considered in this thesis as

$$E_{x(y)}^{\text{miss}} = E_{x(y)}^{\text{miss},e} + E_{x(y)}^{\text{miss},\gamma} + E_{x(y)}^{\text{miss},\text{jets}} + E_{x(y)}^{\text{miss},\mu} + E_{x(y)}^{\text{miss},\text{soft}} \quad (5.11)$$

where each term in equation 5.11 represents the magnitude of the negative vectorial sum of the momenta of the respective calibrated object. The order of the terms (excepting the soft term, which is track-based) represents the sequence in which calorimeter signals are associated with physics objects. The angle  $\phi^{\text{miss}}$  and magnitude  $E_T^{\text{miss}}$  are calculated

from equation 5.11 as

$$\phi^{\text{miss}} = \arctan \frac{E_y^{\text{miss}}}{E_x^{\text{miss}}} \quad (5.12)$$

$$E_T^{\text{miss}} = \sqrt{(E_x^{\text{miss}})^2 + (E_y^{\text{miss}})^2} \quad (5.13)$$

Physics objects considered by the  $E_T^{\text{miss}}$  calculation are required to pass basic selection criteria. The requirements for physics objects in Run 2 is provided within [127] and is as follows.

- Reconstructed ID tracks are required to have  $p_T > 0.4$  GeV and  $|\eta| < 2.5$ , in addition to basic reconstruction requirements.
- Vertices, reconstructed with tracks that pass a requirement on a threshold number of ID hits, are required to have a transverse impact parameter  $d_0 < 1.5$  cm and longitudinal impact parameter  $z_0 < 1.5$  cm. The primary vertex with the highest  $\sum p_T^2$  is regarded as the hard-scatter vertex.
- Muons considered by the  $E_T^{\text{miss}}$  calculation are required to have  $p_T > 10$  GeV and  $|\eta| < 2.7$ .
- Calibrated electrons are required to have  $p_T > 10$  GeV and  $|\eta| < 1.37$  or  $1.52 < |\eta| < 2.47$  to avoid mis-reconstruction of electrons falling in the transition region between the ECAL barrel and endcap. Photons have the same pseudorapidity requirements as electrons, but an increased requirement of  $p_T > 25$  GeV.
- Calibrated jets are required to have  $p_T > 20$  GeV. An additional requirement on the JVT variable [109] is required for jets with  $|\eta| < 2.4$  and  $p_T < 60$  GeV to reduce the presence of jets originating from pile-up. Tracks associated with the jets that fail these selection requirements are included in the calculation of the TST.
- The TST is built using tracks that have  $p_T < 0.4$  GeV with momentum uncertainty  $< 40\%$ ,  $|\eta| < 2.5$  and that are associated with the primary vertex through impact parameter requirements.  $E_T^{\text{miss}}$  built with TST is more pile-up resistant than when using a calorimeter-based soft term, but does not consider soft neutral particles.

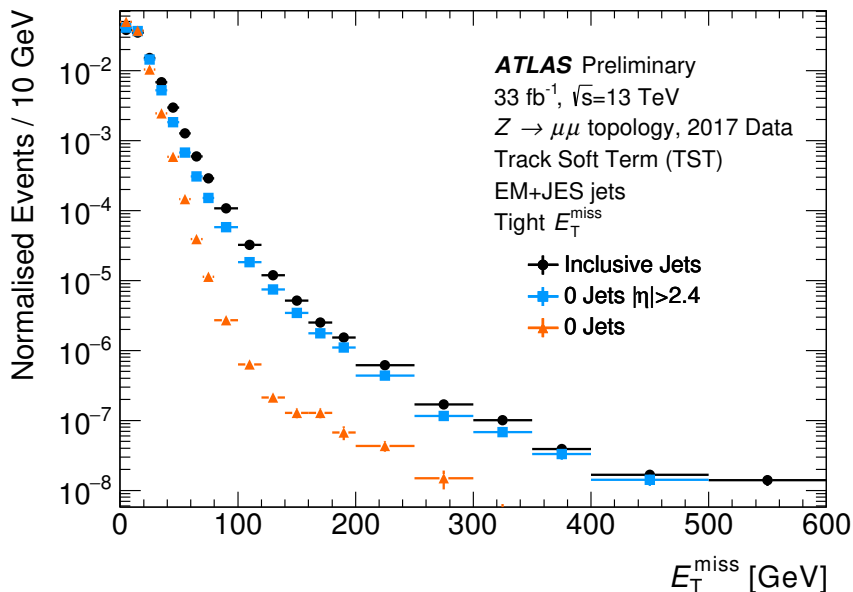


Fig. 5.13  $E_T^{\text{miss}}$  distribution computed from reconstructed electrons, muons, jets and the Track-based Soft Term (TST) from a  $Z \rightarrow \mu\mu$  selection in 2017 ATLAS data. The distribution uses the *Tight* working point, which requires calibrated jets with  $|\eta| > 2.4$  to have  $p_T > 30$  GeV. Black points have no requirement on the number of jets, blue points require no jets with  $|\eta| > 2.4$  and orange points require no jets with  $p_T > 20$  GeV at  $|\eta| < 2.4$ . Figure from [128].

The  $E_T^{\text{miss}}$  distribution in 2017  $Z \rightarrow \mu\mu$  data events (where no genuine  $E_T^{\text{miss}}$  is expected) is shown in figure 5.13 with a tighter requirement on jet  $p_T$  above  $|\eta| > 2.4$ . The significant  $E_T^{\text{miss}}$  contribution made by jets, particularly at large  $E_T^{\text{miss}}$ , is clearly visible as the number of jets in the event is increased.

### 5.1.7 Resolving Overlapping Objects

Multiple candidate physics objects may be reconstructed in the same area in the  $(\eta, \phi)$  plane of the detector. Physics objects are said to *overlap* if they fall within a distance  $\Delta R$  of one another, with the treatment of physics objects referred to as *overlap removal*.

An example of the order of resolution of ambiguities between overlapping jets, electrons and muons in the 0-lepton + 2-6 jets +  $E_T^{\text{miss}}$  analysis [129] is given below:

- Jet candidates not identified as  $b$ -jets lying within a distance  $\Delta R = 0.2$  of an electron are discarded.
- Any  $b$ -tagged jet candidates lying within  $\Delta R = 0.2$  of an electron are classified as jets with the overlapping electron discarded.
- Electrons found within  $0.2 \leq \Delta R < 0.4$  of a jet that passes the JVT selection are discarded. Muons found within  $0.2 \leq \Delta R < (0.4, 0.04 + 10\text{GeV}/p_{\text{T}}^{\mu})_{\text{min}}$  of a jet passing JVT selection are discarded.
- Jets and muons within  $\Delta R < 0.2$  are treated as muons and the jet is discarded if it is associated with more than 3 tracks of  $p_{\text{T}} > 500$  MeV. If the jet is associated with fewer than 3 tracks of  $p_{\text{T}} > 500$  MeV, the muon is ignored.
- Electron candidates sharing the same ID track with a muon candidate are discarded.

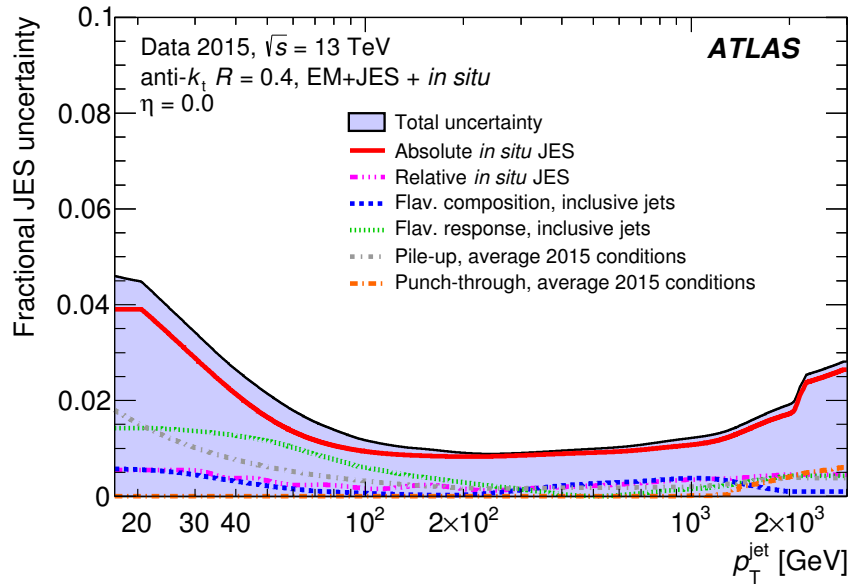
Physics objects surviving the overlap removal procedure are then used in analyses.

## 5.2 Object Uncertainties

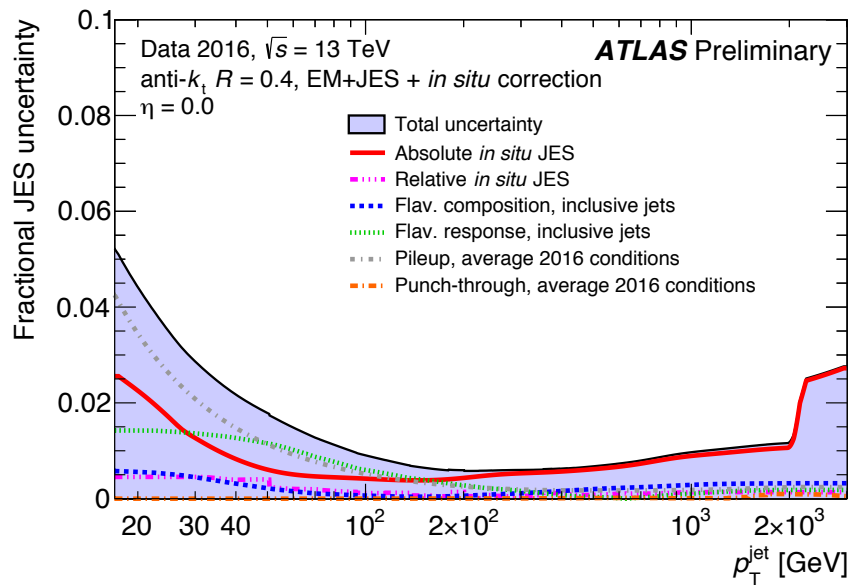
The reconstructed physics objects described in section 5.1 rely upon calibration to truth-level objects which carries with it associated systematic uncertainties.

### 5.2.1 Jet Energy Scale (JES)

JES corrections calibrate the energy of jets reconstructed at the EM scale to the energy of jets reconstructed from stable simulated particles through a process detailed in figure 5.4. These calibrations use simulated MC events to correct the energy scale of reconstructed jets in both data and MC, in addition to in-situ measurements using jets reconstructed from data events.



(a)



(b)

Fig. 5.14 (a) Fractional JES systematic uncertainty in  $3.2 \text{ fb}^{-1}$  of 2015 data at a centre-of-mass energy of  $\sqrt{s} = 13 \text{ TeV}$  as a function of  $p_T$  in fully calibrated anti- $k_t$  jets with a distance parameter  $\Delta R = 0.4$  and  $\eta = 0.0$ . The flavour composition is taken from PYTHIA MC simulated dijet events. Punch-through refers to the uncertainty on the muon-based stage of global sequential correction. Absolute in-situ JES refers to uncertainties from  $Z/\gamma$ +jet and multijet balance measurements while relative in-situ JES refers to uncertainties from  $\eta$ -intercalibration. The total uncertainty from each component summed in quadrature is shown by the solid black line covering the solid blue region [103]. (b) Plot updated with 2016 data [130].

The JES calibration procedure and calculation of uncertainties was derived using 2011 data with  $\sqrt{s} = 7$  TeV [104] and was adapted for a centre-of-mass collision energy of  $\sqrt{s} = 13$  TeV in 2015 [103]. In-situ calibrations represent the largest source of JES systematic uncertainties. In Run 2, sources of systematic uncertainty were combined and reduced to four scenarios [131], where each scenario varies the correction given to the two leading jets to determine the sensitivity of analyses to JES corrections. Figure 5.14 shows the fractional systematic uncertainty from JES corrections as a function of  $p_T$  in 2015 and 2016 data. Low  $p_T$  jets carry the largest uncertainty, although a sharp rise is seen at around 2 TeV where multijet balance measurements are no longer used and the single-particle response with larger uncertainties is relied upon.

### 5.2.2 Jet Energy Resolution (JER)

The energy of a jet reconstructed in a detector has an intrinsic uncertainty which limits the precision of the energy measurement. Accurate knowledge of the *jet energy resolution* (JER) is essential in searches for SUSY due to its potential impact on the  $E_T^{\text{miss}}$  in an event. MC events are reconstructed by simulating the response of the detector and convoluting the true jet energies with the detector response. Measurements of the JER in data inform corrections to the Gaussian core of the simulated detector response, ensuring that the resolution of jets in simulated events appropriately mirrors that of data events. In Run 1, the JER measurement was performed using techniques that balance the  $p_T$  of high  $p_T$  jets [132]. JER uncertainties arise from the associated uncertainties of the techniques used to measure the energy resolution of jets.

### 5.2.3 Jet Vertex Tagger (JVT)

Requirements are placed on the JVT variable, introduced in section 5.1.2.2, to reduce jets originating from pile-up. Comparison of the JVT jet selection efficiency at three working points was performed in data and MC simulated events [109] with  $Z(\rightarrow \mu\mu) + \text{jets}$  events where the  $Z$  recoils against the jets. A source of uncertainty is also derived from discrepancies between the efficiencies of two MC event generators used to create the  $Z(\rightarrow \mu\mu) + \text{jets}$  samples. JVT requirements in analyses are only placed on jets with  $p_T < 60$  GeV; the total uncertainty on JVT efficiency for jets ranges from 2% to 1% for jets with  $p_T$  in the range 20 to 60 GeV [109].

## 5.2.4 $b$ -jet Identification Efficiencies

Measurement and calibration of the  $b$ -tagging scale factors is discussed in section 5.1.3, with the method used during Run 2 detailed within [115]. Tagging efficiencies are calibrated using data and MC simulated  $t\bar{t}$  events where  $t \rightarrow W + b$  and each  $W$  boson decays leptonically, such that events considered contain exactly two  $b$ -jets and exactly two oppositely charged leptons [115]. A tag-and-probe method is employed to calculate the  $b$ -tagging efficiency in events containing two differing flavour leptons where a *tag* jet is identified as a  $b$ -jet at the 85% efficiency working point and the other jet is identified as a *probe* jet [115], with the  $b$ -tagging efficiencies compared in data and simulated events. A likelihood-based method is also used for  $e\mu$  and combined  $ee/\mu\mu$  final states to calculate the  $b$ -tagging efficiency in  $t\bar{t}$  and  $Z/\gamma^* + \text{jets}$  events. Measured uncertainties in  $b$ -tag SFs range from 2-12% over a  $p_T$  range of 20-300 GeV [115]. SFs are additionally varied to estimate the uncertainty from extrapolating the  $b$ -tagging efficiencies to high  $p_T$  jets in analyses [116].

## 5.2.5 Lepton Efficiencies

Scale factors are applied to MC to calibrate simulated events to match lepton reconstruction, identification and isolation efficiencies in data. The derivation of both electron and muon identification efficiencies is discussed in sections 5.1.4.1 and 5.1.5, respectively. Systematic uncertainties are taken into account by considering the difference between variations of scale factors. In addition, the energy scale and resolution of electrons and muons is measured and calibrated in a similar manner to jets, with associated uncertainties.

## 5.2.6 $E_T^{\text{miss}}$

Uncertainties on the objects provided as inputs for the  $E_T^{\text{miss}}$  calculation propagate to uncertainties on the  $E_T^{\text{miss}}$  term itself. The uncertainties on the TST in Run 1 [125] were split into the parallel ( $E_{\parallel}^{\text{miss,soft}}$ ) and perpendicular ( $E_{\perp}^{\text{miss,soft}}$ ) projections of the soft term onto the transverse momentum vector of the hard component of the  $E_T^{\text{miss}}$ . Distributions of these variables in data events are fitted with a *smear*ed version of the distributions in MC, where *smearing* refers to the convolution of the distribution with

a Gaussian function. The mean and width of the Gaussian are used to parametrise the differences between data and MC, with the largest values from the fit taken as the systematic uncertainties. Systematic uncertainties for the soft term are constructed with variations of increasing and decreasing resolution and energy scale, aiming to account for the discrepancy between data and MC. A similar procedure is utilised for Run 2 [126].

### 5.2.7 Luminosity

The ATLAS luminosity measurement of the 2015 and 2016 dataset used the Run 1 method, detailed in [133], where dedicated luminosity detectors measure interaction rates during  $x - y$  beam-separation scans in special beam conditions with a low interaction rate  $\mu$ . The integrated luminosity recorded and found suitable for physics between 2015 and 2016 at  $\sqrt{s} = 13$  TeV was  $36.1 \text{ fb}^{-1}$  with an average uncertainty of 3.2% [129].



# Chapter 6

## The *Jet Smearing* Method

*Jet Smearing* is a data-driven methodology for QCD multijet background estimation used to produce large collections of *pseudo-data* and is presented as an alternative to MC estimates. Jet smearing uses the energy response of jets in simulated MC events, which is calibrated to data in dedicated analyses described in this chapter, to convolute the four-momenta of well-measured jets in ATLAS analyses. *Smearing* refers to the process in which a number is drawn randomly from the  $p_T$ -dependent calibrated jet energy response and is convoluted with the four-momentum of jets within well-measured events. The process of *smearing* jet four-momenta is repeated many times per event to create large collections of pseudo-data which can be used by analyses in the estimation of the QCD multijet background. A discussion of the development of the technique for ATLAS Run 2 is provided, with results from calibration analyses shown. Finally, a discussion of the origin of  $E_T^{\text{miss}}$  in analyses searching for SUSY pair production and decay to fully hadronic final states with jets and  $E_T^{\text{miss}}$  is presented.

### 6.1 Jet Smearing Overview

The production of multiple jets due to QCD in LHC collisions is a potentially dominant background in searches for new physics and is referred to as the *multijet background*. By designing kinematic regions enriched in SUSY signal-like events while minimising the contamination from background-like events the multijet background can be reduced to a residual (if poorly understood) background. The low acceptance of multijet events in

## The *Jet Smearing* Method

---

these regions coupled with the very large production cross section causes the production of MC simulated events to be extremely CPU and time intensive, while still providing a large associated statistical uncertainty. MC simulated multijet events additionally may fail to accurately model the various non-Gaussian detector effects that degrade the accuracy of jet reconstruction. For this reason, the use of MC simulation in the estimation of the multijet background in SUSY analyses is avoided, with data-driven alternatives sought. One such technique is the *jet smearing* methodology [134–137], which creates large sets of pseudo-data to use in place of MC simulated events. This technique provides a computationally fast technique that models the various detector effects that modify the energy response of jets within the detector.

Equation 3.8 shows the resolution for an imperfect calorimeter. The accuracy of the reconstruction of the energies and momenta of physics objects is limited, at best, to the intrinsic resolution of the detector. The energy response of a jet within the detector is defined as

$$R = \frac{E^{\text{reco}}}{E^{\text{truth}}} \quad (6.1)$$

where ‘reco’ and ‘truth’ refer to reconstructed and event generator-level objects, respectively. Truth information is available in MC simulation, while in data the use of proxy-variables is necessary to approximate the ‘true’ physics of an event. Equation 6.1 can equivalently refer to the jet  $p_T$  response in jets with sufficiently high momenta, as it is assumed that jet momentum is far greater than the jet mass. Idealised detectors would provide a jet energy response in the form of a delta function, while in a realistic case the response is broadened by jet  $p_T$  measurement fluctuations due to both Gaussian effects, such as the non-zero calorimeter resolution, or non-Gaussian effects. Non-Gaussian effects further degrade the jet response in a non-uniform manner, manifesting themselves as position-dependent effects or effects applied to certain jets that can broaden the jet response at high or low values. Broadening of the jet response at low values can cause jet  $p_T$  to be underestimated and therefore introduces a source of fake  $E_T^{\text{miss}}$ , which is undesirable in SUSY analyses where signal-like events are expected to have significant  $E_T^{\text{miss}}$ .

Non-Gaussian effects that cause the downward fluctuation of the measured jet  $p_T$  include:

- Regions in which there is degraded calorimeter coverage, such as the transition region between the barrel and endcap may have a degraded (broader) jet energy response.
- Jets depositing energy within non-operational regions of the calorimeter or within material situated prior to the calorimeter can give rise to downward fluctuations of measured jet  $p_T$ .
- Cases where the hadronic shower is not fully contained in the hadronic calorimeter and leaks into the muon system.
- Poor jet reconstruction may result in some of the jet constituents being outside of the jet cone. This effect can be somewhat mitigated by the use of larger jet cone sizes where wide lateral hadronic showers are expected.
- Heavy flavour jet decay chains can include neutrinos which escape the detector and are observed as  $E_T^{\text{miss}}$ .

Jet smearing uses the jet energy response as initially measured in MC simulated events, termed  $R_{\text{MC}}$ , and applies calibrations to data using two dedicated analyses. After applying the calibrations and taking into account the uncertainties introduced by their application, the data-corrected jet energy response is used to convolute, or *smear*, the four momentum of jets in well-measured *seed* data events by multiplying all components of the jet four-momentum with a randomly selected value from the jet response at the corresponding truth jet  $p_T$ . All components of the four-momentum are multiplied by the same randomly drawn value. An assumption is made that the truth jet  $p_T$  is equivalent to the reconstructed jet  $p_T$  as a consequence of selecting well-measured events which minimises the prevalence of fake  $E_T^{\text{miss}}$  in the event and therefore considers only well-measured jets. The method focuses on the smearing of well-measured events within data, rather than MC simulated events, as this ensures that the introduction of systematic uncertainties associated with reconstructing physics objects within MC simulated events and their calibration to data events discussed in section 5.2 is avoided.

For  $m$  jets in a seed event, the jet four-momentum is convoluted with values drawn randomly from the jet energy response  $n_{\text{smear}} \times m$  times, where  $n_{\text{smear}}$  is generally selected to be  $\mathcal{O}(1000)$ , to create a collection of pseudo-data. The number of smears selected represents a compromise between low computation time and a sufficient

## The *Jet Smearing* Method

---

amount of pseudo-data events entering analysis regions. The smearing of jets within well-measured events fluctuates the  $p_T$  of the jets upwards and downwards, potentially decreasing or increasing the  $E_T^{\text{miss}}$  present in the event. A single smearing is depicted in figure 6.1, where the downward fluctuation in the  $p_T$  of jets within a well-measured event introduces additional fake  $E_T^{\text{miss}}$  in the smeared event. As all components of the jet four-momentum are convoluted with the same value drawn randomly from the jet response, smeared jets often retain a similar  $\phi$  distribution to the original seed events. An additional smearing of jet- $\phi$  is applied such that the  $\phi$  distribution of jets in pseudo-data matches that of data. The calibration of the additional  $\phi$ -smearing is described in section 6.4.2.

Jet smearing is applied on a jet-by-jet basis rather than on an event-wide scale and therefore assumes a negligible impact of properties of the event as a whole, such as the total number of jets in the event, on the individual response of a jet. The impact of multiple applications of the jet smearing procedure on a single seed event is shown in figure 6.2, in which  $n_{\text{smear}} = 3000$ .

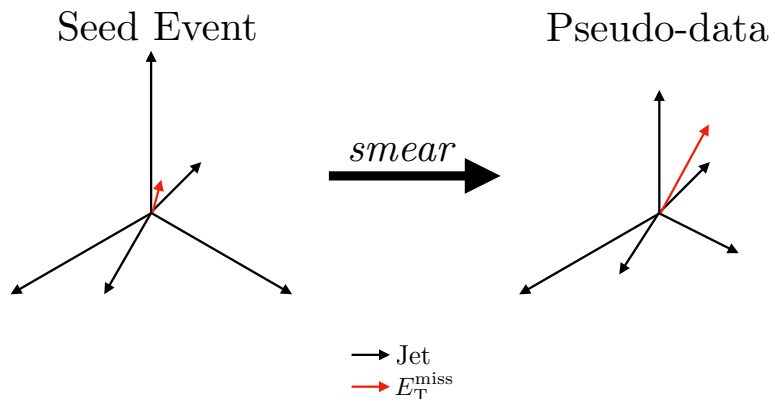


Fig. 6.1 Schematic view of a single iteration of the jet smearing procedure in the plane transverse to the beam. A well-measured ‘seed event’ is selected and the jets in the seed event are *smeared* by convolution of their four vectors with a value drawn randomly from the response maps used as inputs to the jet smearing software tool. The jet vectors shown in the ‘pseudo-data’ case do not necessarily retain the direction in  $\phi$  of the jet prior to smearing.

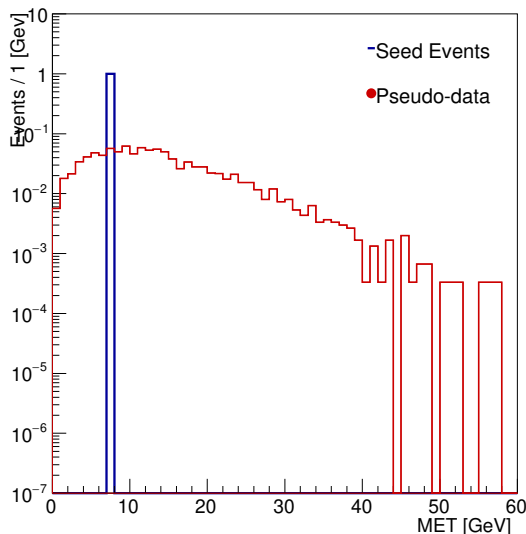


Fig. 6.2 Distribution of  $E_T^{\text{miss}}$  following 3000 applications of the jet smearing procedure to a single seed event, shown in blue. The normalised distribution of pseudo-data generated from the single seed event is shown in red.

A well measured data event containing  $i$  jets with  $p_T(j_i)$  is smeared  $\mathcal{O}(1000)$  times to produce a large collection of pseudo-data with jets whose energy and  $p_T$  response mirrors those of the entire collection of jets in data. This set of pseudo-data models the upward and downward fluctuations of measured jet  $p_T$  due to jet  $p_T$  mismeasurement and the decay of heavy flavour jets, altering the  $\vec{E}_T^{\text{miss}}$  in the event so that  $\vec{E}_T^{\text{miss}} \rightarrow \vec{E}_T^{\text{miss}'}$  where

$$\vec{E}_T^{\text{miss}'} = \vec{E}_T^{\text{miss}} - \sum_i \vec{p}_T'(j_i) + \sum_i \vec{p}_T(j_i) \quad (6.2)$$

and primed quantities represent smeared quantities within pseudo-data. The smeared- $E_T^{\text{miss}}$  in an pseudo-data event (equation 6.2) is therefore the magnitude of the vectorial sum of the  $E_T^{\text{miss}}$  and jet  $p_T$  vectors in the seed event with the  $p_T$  vectors of smeared jets subtracted. The fluctuation of jet  $p_T$  may change both the magnitude and orientation in  $\phi$  of  $\vec{E}_T^{\text{miss}}$  in pseudo-data events.

Other sources introducing fake  $E_T^{\text{miss}}$  are not taken into account by the *jet smearing* method by design and so its application is necessarily limited to topologies where jet mismeasurement and heavy flavour decay are the dominant contributions to fake  $E_T^{\text{miss}}$ .

## The *Jet Smearing* Method

---

The software implementation of the jet smearing methodology was developed for Run 1 analyses at  $\sqrt{s} = 7$  and  $\sqrt{s} = 8$  TeV and is extensively documented [134–138]. The methodology described in this chapter represents an update for Run 2 ATLAS analyses at  $\sqrt{s} = 13$  TeV, where it has been used by several analyses [129, 139–144] searching for evidence of SUSY and BSM particle production.

An overview of the procedure for the preparation and use of the jet smearing software is given below:

- Generate  $p_T$ -dependent jet energy *response maps* using the jet response defined in equation 6.1 with MC simulated dijet events. The response maps are binned in truth jet  $p_T$  and are generated separately for  $b$ -tagged and non  $b$ -tagged ( $b$ -veto) jets to account for the presence of extra  $E_T^{\text{miss}}$  from heavy flavour decays in  $b$ -jets. Response maps are an essential input to the jet smearing software tool and dictate the nature of pseudo-data distributions.
- Generate any necessary corrections to the central ‘Gaussian core’ region of the jet response such that the Gaussian core of the initial MC simulation-derived response mirrors that measured in data.
- Determine calibrations to the applied *phi smearing* (described in section 6.4.2), which corrects the  $\phi$  distribution of smeared pseudo-data jets to match the  $\phi$  distribution of jets measured in data. This step is observed to be necessary as smeared jets largely retain the back-to-back topologies of well-measured seed events.
- Calibrate the non-Gaussian low-side ‘tail’ of the jet response. Unlike corrections generated for the Gaussian core and  $\phi$  distribution of pseudo-data jets, *tail corrections* are generated in the form of modified response maps rather than a set of input parameters applied in the jet smearing software to the original MC simulation-derived response. Tail corrected response maps are produced separately for  $b$ -tagged and  $b$ -veto jets, from which a weight is derived to account for the systematic uncertainties arising from the tail correction technique.
- Response maps and input parameters for the jet smearing software tool are provided to analyses to smear well-measured seed events to generate sets of pseudo-data with which an estimate of the multijet background contribution can be made in place of dijet MC simulated events. Jet four-momentum smearing

and  $\phi$  smearing are applied separately within the software implementation of the method.

*Well-measured* events are defined by the choice of a seed event selection variable, discussed in section 6.3. In the analysis of data recorded in 2015 and 2016, analyses were offered a choice of variations on the requirement of the seed event selection variable to be optimised per analysis. This step (along with the choice of the number of smears per seed event) represents the only point at which analyses can calibrate the jet smearing tool. All other calibrations to  $\sqrt{s} = 13$  TeV data were derived by the author.

## 6.2 Determination of the Jet Response

The initial jet response is calculated using PYTHIA 8 [74] MC simulated dijet events using the NNPDF2.3LO leading order PDF set [76] with the A14 parameter set [75]. The jet energy response is calculated according to equation 6.1 as a function of the truth-level  $p_T$ . The reconstructed and truth categorisations considered in the construction of the MC energy response are designed to accurately model the  $E_T^{\text{miss}}$  observed in data events and as such are not solely composed of jets.

### 6.2.1 Response Map Construction Method

The procedure for the construction of the energy response for use with Run 2 data is as follows:

- Reconstructed jets are defined as anti- $k_t$  EMTopo jets with a distance parameter  $\Delta R = 0.4$  (defined in equation 3.7) and include energy deposits from electrons in the calorimeter. Reconstructed jets must not be classified as LooseBad, must survive the overlap removal procedure, satisfy  $|\eta| < 2.8$  and have  $p_T > 20$  GeV.
- Truth jets are defined using the anti- $k_t$  algorithm with distance parameter  $\Delta R = 0.4$  and include truth electrons by construction. Truth jets must satisfy  $20 \text{ GeV} < p_T < 6500 \text{ GeV}$  with  $|\eta| < 2.8$  to mirror the reconstructed jet collection as closely as possible.

## The *Jet Smearing* Method

---

- A matching procedure is applied to pair reconstructed jets to truth jets. Events must contain one or more reconstructed jets to be considered by the matching procedure. A truth jet is considered, with reconstructed jets sorted by decreasing proximity in  $\Delta R$  (defined in equation 3.7) to the truth jet. The closest reconstructed jet in  $\Delta R$  is considered matched to the truth jet if it is within  $\Delta R < 0.3$ . If the second-closest reconstructed jet is also within  $\Delta R < 0.6$  of the truth jet, the match is not considered a unique match and the next truth jet in the event is considered. Isolation requirements are placed on the reconstructed (truth) jet, such that no other reconstructed (truth) jet may be within  $\Delta R < 0.6$ . A truth and reconstructed jet are considered matched if they are uniquely matched and are both isolated objects. The matching criteria were loosely based upon those detailed in section 5.1.2.2. Objects that do not satisfy the unique matching requirements are not used in the construction of the jet response.
- The four-momenta of reconstructed muons with  $p_T > 7$  GeV and  $|\eta| < 2.7$  surviving the overlap removal procedure situated within  $\Delta R < 0.4$  of reconstructed jets are added to reconstructed jet four-momenta.
- The four-momenta of muons present at the truth-level within  $\Delta R < 0.4$  of a truth-level jet are added to the truth jet four-momentum.
- The four-momenta of neutrinos present at the truth-level within  $\Delta R < 0.4$  of a truth-level jet are added to the truth jet four-momentum.
- The energy response is constructed by taking the ratio of the energy component of the reconstructed and truth-level four-momentum.

*Response maps* are then constructed by plotting the energy response as a function of the  $p_T$  of the truth-level four-momentum in bins of 20 GeV. Separate response maps are produced for  $b$ -tagged and  $b$ -veto jets to correctly account for the additional  $E_T^{\text{miss}}$  present due to  $b$ -jet decays.

Twelve PYTHIA 8 [74] samples are used for response map generation, with each sample covering a truth jet  $p_T$  range shown in table 6.1.

## 6.2 Determination of the Jet Response

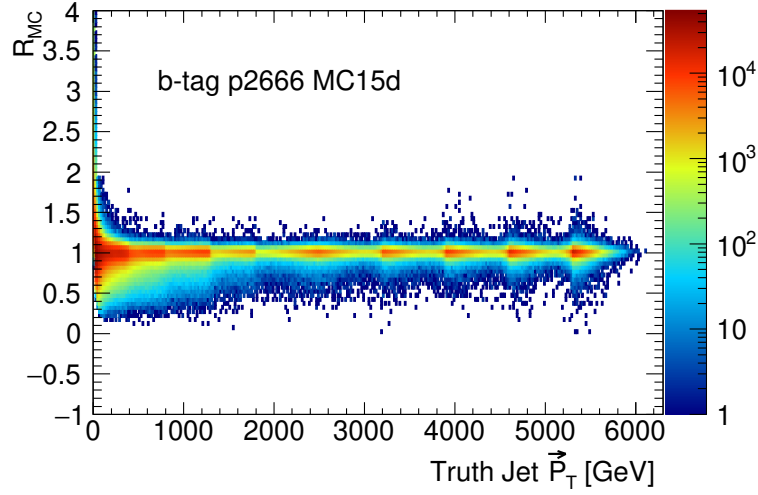
---

Table 6.1 Samples of MC simulated dijet events used in response map generation and the truth jet  $p_T$  range covered by each sample. Values taken from [145].

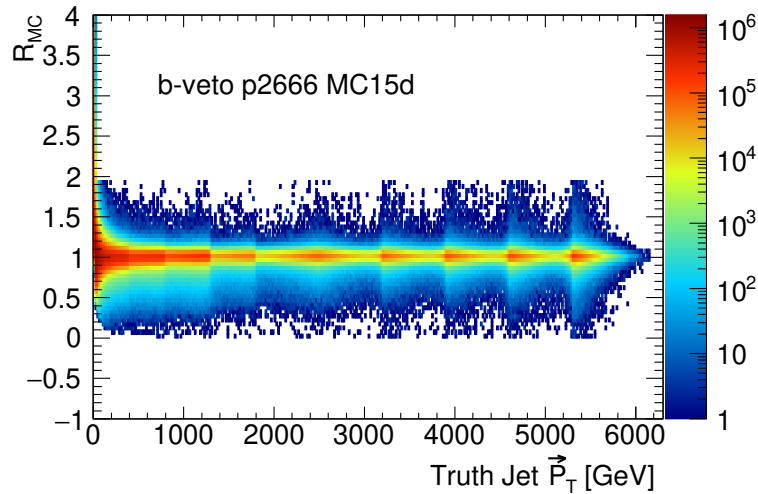
Sample	Lowest truth jet $p_T$	Highest truth jet $p_T$
JZ1	20	60
JZ2	60	160
JZ3	160	400
JZ4	400	800
JZ5	800	1300
JZ6	1300	1800
JZ7	1800	2500
JZ8	2500	3200
JZ9	3200	3900
JZ10	3900	4600
JZ11	4600	5300
JZ12	$\geq 5300$	—

### 6.2.2 Response Maps for 2015 and 2016 Data

The set of response maps constructed for  $b$ -tagged and  $b$ -veto jets using MC simulated events with pile-up conditions mirroring those of the data-taking conditions in 2015 and 2016 is shown in figure 6.3. This set of response maps represents the main set considered in this thesis for calibration and use in analyses. As Jet Smearing is applied on a jet-by-jet basis and does not rely upon event-wide quantities, the response is created with unweighted dijet MC samples. As such, the transition between MC samples covering different  $p_T$  ranges (table 6.1) is visible at several points in figure 6.3.

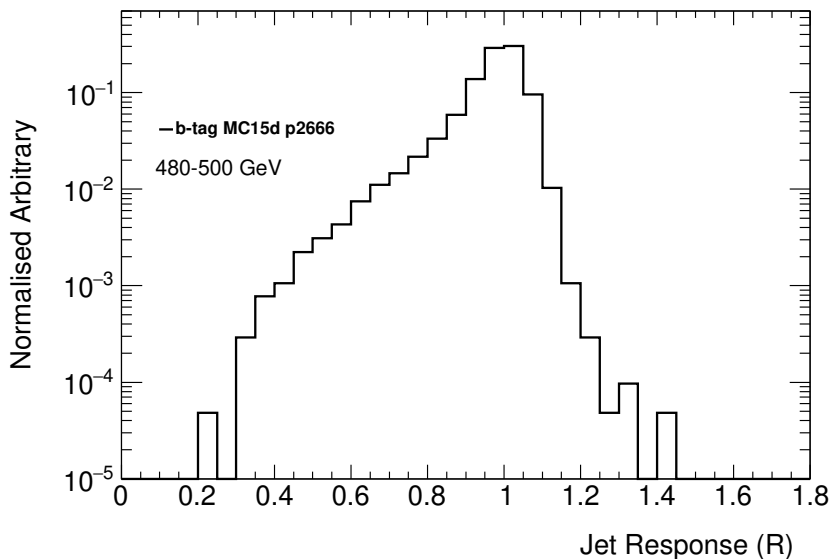


(a)

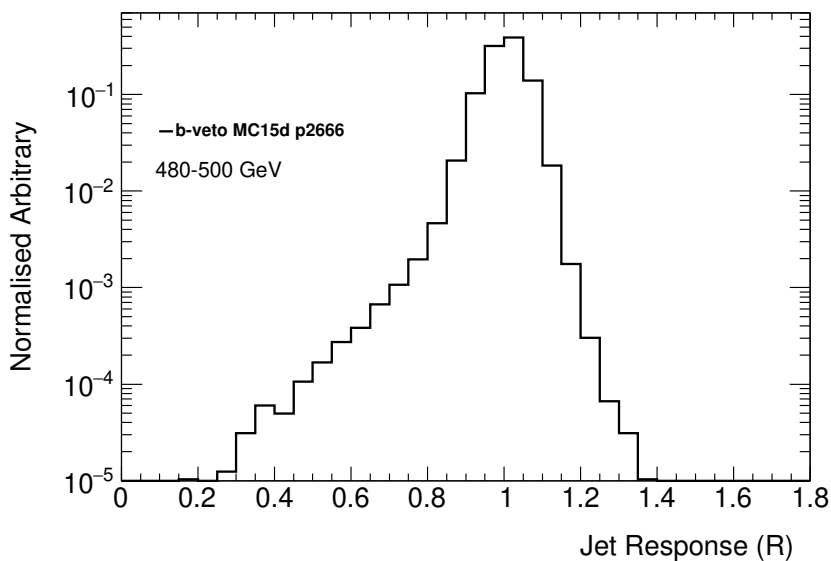


(b)

Fig. 6.3 Energy response maps constructed as described in section 6.2.1 using MC simulated events with a pile-up profile simulated to match that of data recorded in 2015 and 2016. The response maps are plotted as a function of truth jet  $p_T$  in bins of 20 GeV for (a)  $b$ -tagged jets and (b) light flavour jets (requiring the absence of a  $b$ -tag). Response maps are generated using simulated dijet events at the truth and reconstruction level in twelve  $p_T$ -sliced PYTHIA 8 [74] samples produced with the NNPDF2.3LO PDF set [76] and A14 parameter set [75]. A matching procedure (detailed in section 6.2.1) is used to combine the four momenta of nearby truth-level and reconstructed objects with jets to generate the jet energy response defined in equation 6.1.



(a)



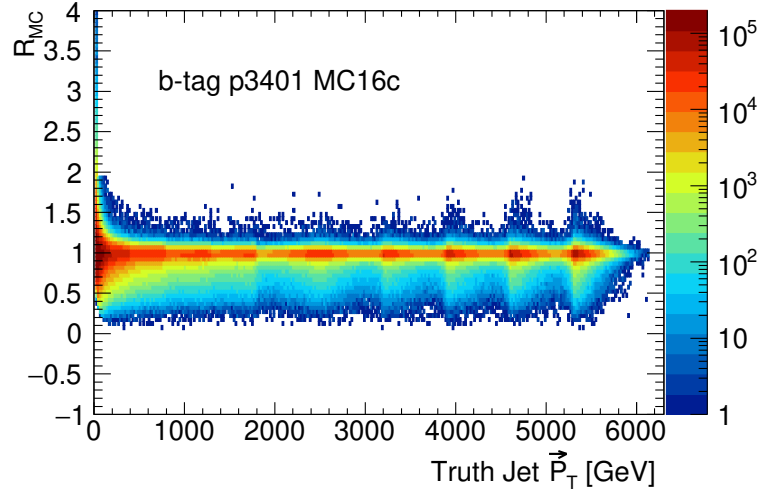
(b)

Fig. 6.4 One dimensional projection of the 2D response maps (figure 6.3) constructed using MC simulated events with a pile-up profile simulated to match that of data recorded in 2015 and 2016 for  $480 < p_T < 500$  GeV using (a)  $b$ -tagged jets and (b) light flavour jets (requiring the absence of a  $b$ -tag). The *Gaussian core* of the response is defined as the Gaussian-like region of the jet response between  $0.8 \leq R \leq 1.2$ . The increased low-side non-Gaussian tail of the response in the  $b$ -tagged case with respect to the  $b$ -veto case is clearly visible.

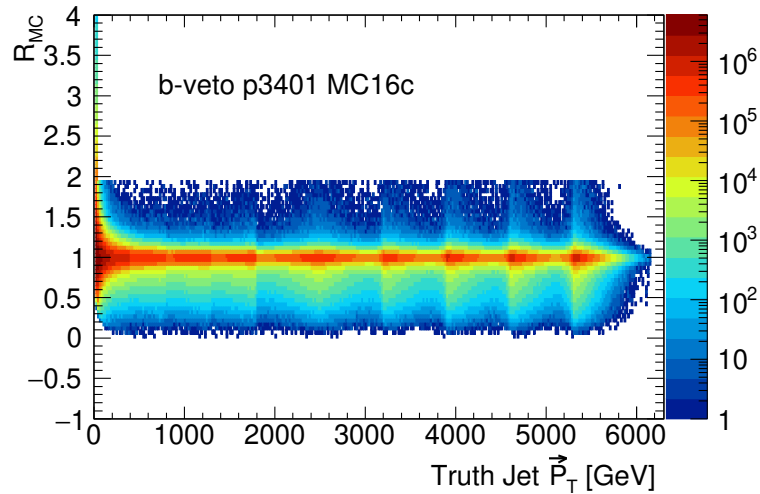
One dimensional projections of the response maps in figure 6.3 are shown in figure 6.4 for truth jets with  $480 \leq p_T \leq 500$  GeV and are useful in identifying features of the responses. The increase in the low-side tail of the jet response for  $b$ -tagged jets with respect to  $b$ -veto jets due to the undetected products of  $b$ -jet decay is visible in figure 6.4.

### 6.2.3 Response Maps Constructed for 2017 Data

Response maps were additionally generated using MC simulated dijet events with an updated pile-up profile that estimated the data-taking conditions in 2017, in addition to taking into account updated object definitions and calibrations generated during 2017. Response maps for both  $b$ -tagged and  $b$ -veto jets plotted as a function of truth jet  $p_T$  are shown in figure 6.5. One dimensional projections of the response maps within figure 6.5 are displayed in red in figure 6.6 for the  $b$ -tagged and  $b$ -veto cases with  $480 \leq p_T \leq 500$  GeV for truth jets, with the equivalent response from figure 6.4 overlaid in black.

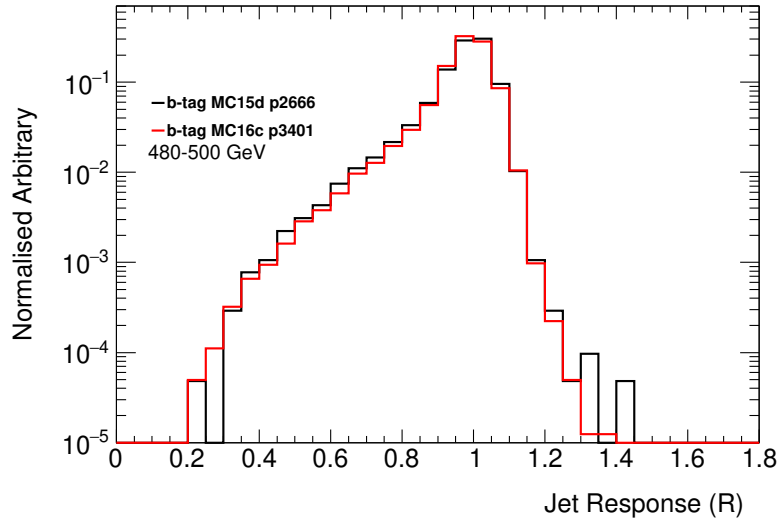


(a)

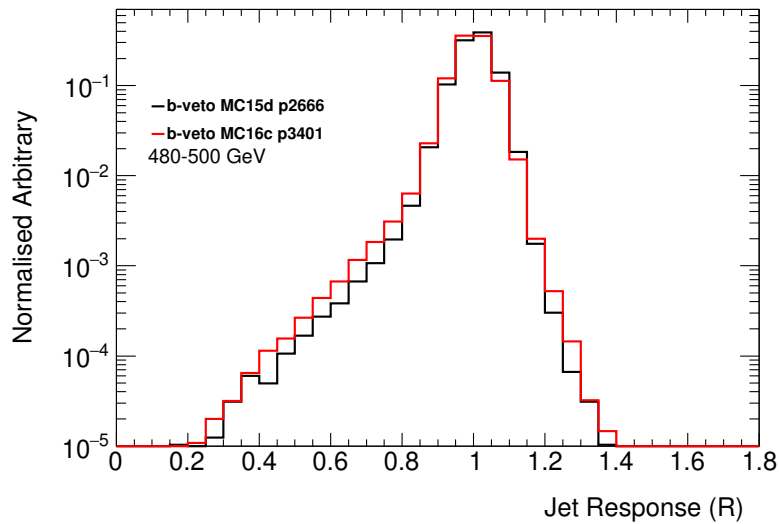


(b)

Fig. 6.5 Response maps constructed as described in section 6.2.1 using MC simulated events with a pile-up profile simulated to match that of data recorded in 2017. The response maps are plotted as a function of truth jet  $p_T$  in bins of 20 GeV for (a)  $b$ -tagged jets and (b) light flavour jets (requiring the absence of a  $b$ -tag). Response maps are generated using simulated dijet events at the truth and reconstruction level in twelve  $p_T$ -sliced PYTHIA 8 [74] samples produced with the NNPDF2.3LO PDF set [76] and A14 parameter set [75]. A matching procedure (detailed in section 6.2.1) is used to combine the four momenta of nearby truth-level and reconstructed objects with jets to generate the jet energy response defined in equation 6.1.



(a)



(b)

Fig. 6.6 One dimensional projection of the 2D response maps (figure 6.5) constructed using MC simulated events with a pile-up profile simulated to match that of data recorded in 2017 (shown in black) and that of data recorded in 2015 and 2016 (shown in red) for  $480 < p_T < 500$  GeV using (a) *b*-tagged jets and (b) light flavour jets (requiring the absence of a *b*-tag). The *Gaussian core* of the response is defined as the Gaussian-like region of the jet response between  $0.8 \leq R \leq 1.2$ . The increased low-side non-Gaussian tail of the response in the *b*-tagged case with respect to the *b*-veto case is clearly visible.

The one dimensional projections of the response derived for 2017 pile-up conditions are observed to be sufficiently consistent with the existing response maps, although with a slightly broader response for  $b$ -veto events. The replication of the previous jet response confirmed the suitability of the new response maps for use in analyses using data recorded in 2017, although no new corrections to the jet response were generated for this dataset by the author.

## 6.3 Determination of Seed Selection

Candidate events for the jet smearing procedure are required to be identified as *well-measured*, requiring that an event has low  $E_T^{\text{miss}}$ -significance  $S$ , where

$$S \equiv \frac{E_T^{\text{miss}}}{\sqrt{\sum E_T}} \text{ [GeV}^{1/2}\text{]} \quad (6.3)$$

Selecting events with low  $E_T^{\text{miss}}$ -significance to define a collection of well-measured events incorporates the improvement of calorimeter resolution with increasing  $\sum E_T$ .

During Run 1, the  $E_T^{\text{miss}}$ -significance was defined as in equation 6.3. Changes to the ATLAS  $E_T^{\text{miss}}$  reconstruction for Run 2 (discussed in section 5.1.6) caused the definition of  $E_T^{\text{miss}}$ -significance to be re-evaluated. In particular, the  $E_T^{\text{miss}}$  definition was modified to use a track-based soft term rather than the calorimeter cell-based soft term used in Run 1. The track based soft term only considers charged particles, but is more resilient to conditions of increasing pile-up. Due to the change in the fundamental quantity used to define seed events within jet smearing, a re-evaluation of the seed event selection variable was made. A generalised definition of the distribution of  $E_T^{\text{miss}}$ -significance is given by [146]:

$$S = \frac{E_T^{\text{miss}} - M \text{ [GeV]}}{\sqrt{\sum E_T}} \text{ [GeV}^{1/2}\text{]} \quad (6.4)$$

where it is assumed that  $S$  is a Gaussian function centred about a mean, which is shifted by a value  $M$ . Setting  $M = 0$  recovers the Run 1 definition of  $E_T^{\text{miss}}$ -significance provided by equation 6.3. However, early research and development during Run 2 found that setting  $M = 0$  resulted in the selection of a higher proportion of high- $p_T$  jets within seed (and therefore pseudo-data) data events with respect to all data events. To account for this introduced bias, several values of  $M$  were studied to attempt to

## The Jet Smearing Method

correct for the bias in seed jet  $p_T$  distributions. Figure 6.7 shows a comparison of seed events selected using  $S < 0.5 + 0.1 \times N_{\text{b-jet}} [\text{GeV}^{1/2}]$  where  $S$  is defined as in equation 6.4. Several values of  $M$  are compared in the figure. In addition,  $E_T^{\text{miss}} < 50 \text{ GeV}$  is used as a seed event selection requirement in place of equation 6.4 for comparison purposes.

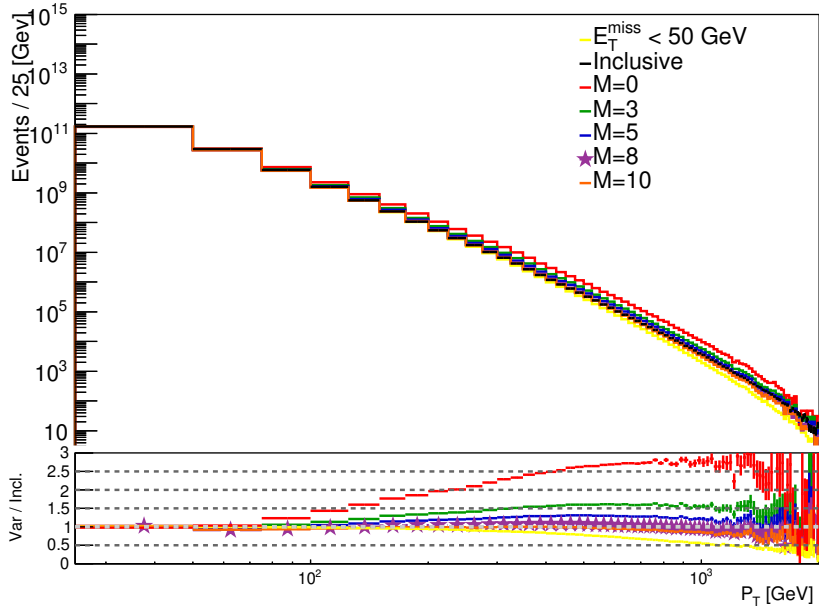


Fig. 6.7 Distributions of the leading jet  $p_T$  in seed events selected using  $S$  as defined in equation 6.4 for several values of  $M$  and also  $E_T^{\text{miss}} < 50 \text{ GeV}$  for  $2.2 \text{ fb}^{-1}$  of  $\sqrt{s} = 13 \text{ TeV}$  data recorded in 2016. A ratio of the seed selection variable to an inclusive jet selection is shown in the lower panel, where  $M = 8 \text{ GeV}$  is shown by the purple starred line. The inclusive selection using all events containing jets.

A value of  $M = 8 \text{ GeV}$  was found to produce the optimal agreement with an inclusive leading jet  $p_T$  distribution.

Lowering the requirement on  $S$  increases the confidence that events are well-measured but causes fewer events to be classified as seed events. Selecting and smearing too few seed events results in few events appearing in the kinematic regions of analyses with large statistical uncertainties. For the dataset recorded in 2015 and 2016, the ‘default’ seed selection was chosen to be

$$S < 0.3 + (0.1 \times N_{\text{b-jet}}) [\text{GeV}^{1/2}] \quad (6.5)$$

### 6.3 Determination of Seed Selection

where the requirement on  $S$  is relaxed as the number of  $b$ -jets in the event increases to take into account the real  $E_T^{\text{miss}}$  in these events arising from  $b$ -jet decay. Seed events selected in data are also required to pass one of a range of single-jet  $p_T$  triggers, where the leading jet  $p_T$  must exceed some threshold requirement. From 2016, jet triggers using HLT jets were used and are shown in table 6.2.

Table 6.2 Single HLT-jet triggers used to define the seed events considered by the *Jet Smearing* tool. Values shown represent the jet  $p_T$  in GeV.

HLT Jet Trigger	HLT Jet Trigger
HLT_j400	HLT_j150
HLT_j380	HLT_j110
HLT_j360	HLT_j100
HLT_j320	HLT_j85
HLT_j300	HLT_j60
HLT_j260	HLT_j55
HLT_j200	HLT_j25
HLT_j175	HLT_j15

An event weight is generated and applied to account for the prescale (see section 3.3.6) associated with each jet trigger. The trigger HLT\_j380 represented the lowest  $p_T$  single-jet trigger with no associated prescale. In the event that a jet satisfies the requirements of multiple single-jet triggers, the highest- $p_T$  trigger is selected with the corresponding prescale used to weight the event. The efficiency of the lowest non-prescaled single-jet trigger seeded by HLT jets with  $|\eta| < 2.8$ , along with a selection of prescaled HLT-seeded single-jet triggers is shown in figure 6.8.

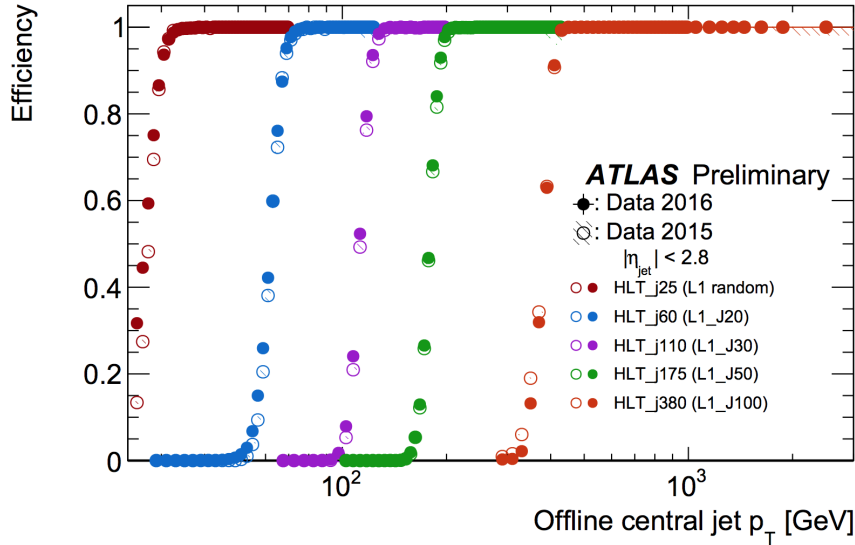


Fig. 6.8 Single-jet trigger efficiencies for HLT central jets with  $|\eta| < 2.8$  measured in 2016 data. A selection of the prescaled HLT jet triggers and the lowest un-prescaled HLT jet trigger (HLT\_j380) used to define seed events is shown. Figure from [147]

## 6.4 Correcting the Initial Response

The response maps created using MC simulated dijet events and described in section 6.2 contain no corrections informed by data and cannot *a priori* be assumed to replicate the jet response observed in data. Two dedicated analyses are described in this section that derive corrections to the initial response maps through calibration to data. The Gaussian core of the response (the central region of approximately  $0.8 \leq R \leq 1.2$  in figure 6.4) is calibrated to data in the dijet balance analysis, which balances the  $p_T$  of back-to-back dijet events to measure the  $p_T$ -asymmetry distribution of the event as a function of the average  $p_T$  of the dijet pair. The non-Gaussian low-side tail of the response derived from MC simulation (the region where  $R_{MC} < 0.8$  in figure 6.4) is calibrated to data in an analysis that considers the fluctuation in  $p_T$  of jets within three jet events and is described in section 6.4.3.

### 6.4.1 Dijet Balance Analysis



Fig. 6.9 Schematic view of a dijet event observed in the transverse plane. The  $p_T$  of the two jets is balanced by placing requirements on  $\Delta\phi(j_1, j_2)$  between the two leading jets, such that they are back-to-back.

Back-to-back dijet events are selected as shown in figure 6.9, with the resulting  $p_T$  asymmetry  $A$  between the two jets given by

$$A = \frac{p_T(j_1) - p_T(j_2)}{p_T(j_1) + p_T(j_2)} \quad (6.6)$$

The width of the asymmetry distribution in pseudo-data events produced using the MC-derived jet response is determined by fitting a Gaussian function to the distribution. The width of the Gaussian is then calibrated to the width of the asymmetry distribution of data events as a function of the average  $p_T$  of the dijet pair

$$\langle p_T^{jj} \rangle = \frac{p_T(j_1) + p_T(j_2)}{2} \quad (6.7)$$

The Gaussian function fitted to the asymmetry distribution has a width determined by [132]

$$\sigma_A = \frac{\sqrt{\sigma(p_T(j_1))^2 + \sigma(p_T(j_2))^2}}{p_T(j_1) + p_T(j_2)} \quad (6.8)$$

Assuming that both jets are located in the same rapidity region such that

$$\begin{aligned} \sigma(p_T, j_1) &= \sigma(p_T, j_2) = \sigma(p_T) \\ p_T(j_1) + p_T(j_2) &= 2 \times p_T \end{aligned}$$

allows  $\sigma_A$  to be expressed in terms of the fractional jet  $p_T$  resolution  $\frac{\sigma(p_T)}{p_T}$  (and equivalently the fractional energy resolution)

$$\sigma_A \simeq \frac{1}{\sqrt{2}} \frac{\sigma(p_T)}{p_T} \quad (6.9)$$

## The Jet Smearing Method

---

The distribution of the value of  $\sigma_A$  is plotted as a function of average jet  $p_T$  in the range  $100 \text{ GeV} \leq \langle p_T \rangle \leq 1000 \text{ GeV}$  in both data and pseudo-data. A function is then fitted to the  $\sigma_A$  distribution with the form

$$\sigma_A = \frac{A^{\text{DJB}}}{\langle p_T \rangle} + \frac{B^{\text{DJB}}}{\sqrt{\langle p_T \rangle}} + C^{\text{DJB}} \quad (6.10)$$

Corrections to the pseudo-data  $\sigma_A$  distribution produced using the initial, uncorrected MC-derived response (denoted  $\sigma_{A,\text{MC}}$ ) are applied if it is observed that the width of the Gaussian function fitted to the pseudo-data asymmetry distribution is narrower than the equivalent distribution in data ( $\sigma_{A,\text{data}}$ ). Corrections are applied such that the pseudo-data distribution then matches that of the data. This case was observed during Run 1 [136], with the method used for generating corrections applied to Run 2.

A correction is applied by convolution of Gaussian functions

$$\left( \frac{\sigma_{\text{total}}(p_T)}{p_T} \right)^2 = \left( \frac{\sigma_{\text{MC}}(p_T)}{p_T} \right)^2 + \sigma_{\text{correction}}^2(p_T) \quad (6.11)$$

where the approximation in equation 6.9 is used to equate the  $\sigma_A$  distribution with the fractional  $p_T$  resolution,  $\sigma_{\text{correction}}(p_T)$  is the  $p_T$ -dependent width of a Gaussian convoluted with the Gaussian with width  $\sigma_{A,\text{MC}}$  and  $\sigma_{\text{total}}(p_T)$  is the corrected  $p_T$  resolution in pseudo-data. The correction procedure equates  $\sigma_{\text{total}}(p_T)$  with  $\sigma_{\text{data}}(p_T)$  and  $\sigma_{\text{correction}}$  is obtained from equation 6.11 by again using the assumption in equation 6.9

$$\begin{aligned} \left( \frac{\sigma_{\text{data}}(p_T)}{p_T} \right)^2 &= \left( \frac{\sigma_{\text{MC}}(p_T)}{p_T} \right)^2 + \sigma_{\text{correction}}^2(p_T) \\ 2 \times (\sigma_{A,\text{data}})^2 &= 2 \times (\sigma_{A,\text{MC}})^2 + (\sigma_{\text{correction}}(p_T))^2 \end{aligned} \quad (6.12)$$

$$\sigma_{\text{correction}}(p_T) = \sqrt{2} \sqrt{(\sigma_{A,\text{data}})^2 - (\sigma_{A,\text{MC}})^2} \quad (6.13)$$

The correction to the asymmetry width distribution of pseudo-data is fully described by the set of parameters  $A^{\text{DJB}}, B^{\text{DJB}}$  and  $C^{\text{DJB}}$  from equation 6.10, with separate parameters for data and pseudo-data. These parameters are used as settings within the jet smearing software to perform a ‘secondary smearing’ which corrects the Gaussian

core of the jet response at the time that Jet Smearing is applied to produce a calibrated collection of pseudo-data.

### 6.4.1.1 Event Selection

The event selection for the dijet balance analysis is shown in table 6.3.

Table 6.3 Criteria for event selection in the dijet balance analysis for events that pass one of the single-jet triggers shown in table 6.2.

Variable	Requirement
$N_{\text{jet}}$	2
$p_{\text{T}}(j_1)$	$> 100$ GeV
$p_{\text{T}}(j_2)$	$> 50$ GeV
$\pi -  \Delta\phi(j_1, j_2) $	$< 0.25$
$E_T^{\text{miss}}$	$< 0.1 \langle p_{\text{T}}^{jj} \rangle$

Only events satisfying the requirements specified in table 6.3 were considered in the subsequent dijet balance analysis, where  $N_{\text{jet}}$  refers to signal jets.

### 6.4.1.2 Results

A set of corrections to the Gaussian central region of the jet response was originally derived with the  $3.2 \text{ fb}^{-1}$  of data recorded in 2015, before being updated to include the full  $36.1 \text{ fb}^{-1}$  of data recorded in 2015 and 2016.

#### 2015 Dataset

The dijet balance asymmetry distribution for  $3.2 \text{ fb}^{-1}$  of data recorded in 2015 and the associated collection of pseudo-data produced with the uncorrected MC jet response is plotted as a function of average jet  $p_{\text{T}}$  for exclusively non  $b$ -tagged jets in figure 6.10.

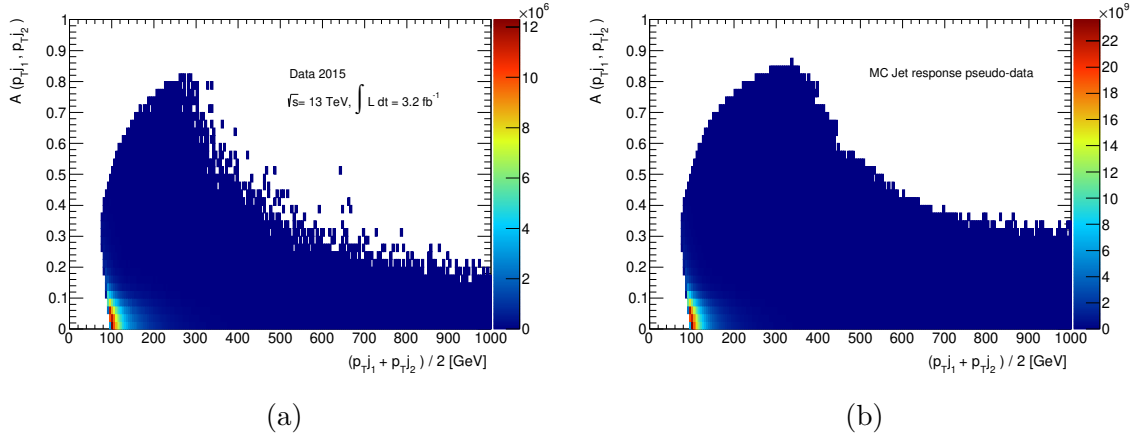


Fig. 6.10 The 2D asymmetry distribution for data events (excluding  $b$ -jets) as a function of average jet  $p_T$ . The data in this figure represents  $3.2 \text{ fb}^{-1}$  of  $\sqrt{s} = 13 \text{ TeV}$  data recorded in 2015. Events considered in this figure are required to satisfy the requirements shown in table 6.3.

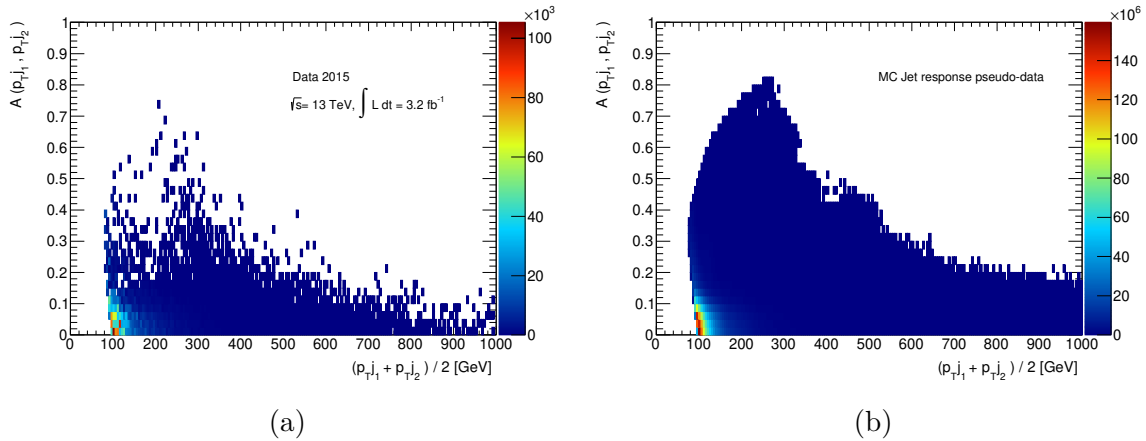


Fig. 6.11 The 2D asymmetry distribution for data events (exclusively  $b$ -jets) as a function of average jet  $p_T$ . The data in this figure represents  $3.2 \text{ fb}^{-1}$  of  $\sqrt{s} = 13 \text{ TeV}$  data recorded in 2015. Events considered in this figure are required to satisfy the requirements shown in table 6.3.

Figure 6.11 shows the equivalent distributions from 6.10 for exclusively  $b$ -tagged jets. The low number of data events with  $b$ -tagged jets entering the analysis is visible in figure 6.11a.

Events considered by this analysis were required to satisfy the requirements given in table 6.3. Seed events were selected using  $S < 0.5 + (0.1 \times N_{b\text{-jet}}) [\text{GeV}^{1/2}]$ . Slices of 50 GeV in average jet  $p_T$  were taken from figure 6.10 for data and pseudo-data with

## 6.4 Correcting the Initial Response

both distributions fitted with a Gaussian function of width  $\sigma_A$ . The fit to data and pseudo-data points for  $A < 0.10$  for  $400 \text{ GeV} \leq \langle p_T^{jj} \rangle < 450 \text{ GeV}$  is shown in figure 6.12.

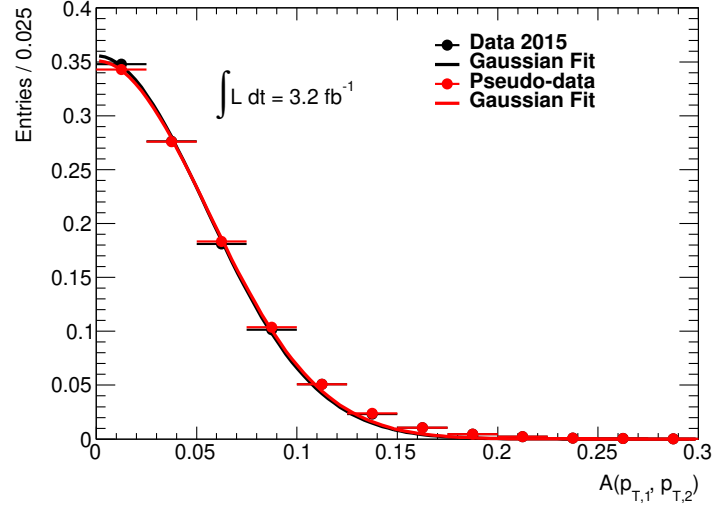


Fig. 6.12 Asymmetry distribution for  $b$ -veto dijet 2015 data and pseudo-data events in the range  $400 \text{ GeV} \leq \langle p_T^{jj} \rangle < 450 \text{ GeV}$ . A Gaussian function is fitted in the region  $0 < A \leq 0.1$  for both data and pseudo-data for each bin (width 50 GeV) in the range  $100 \leq \langle p_T^{jj} \rangle \leq 1000 \text{ GeV}$ , with the distribution of the width of each Gaussian function used to calibrate pseudo-data to data.

A value of  $\sigma_A$  is then extracted from the fit in figure 6.12 for data and pseudo-data. Values of  $\sigma_A$  extracted for each 50 GeV bin in the range  $100 \text{ GeV} \leq \langle p_T^{jj} \rangle \leq 1000 \text{ GeV}$  are plotted as a function of  $\langle p_T^{jj} \rangle$  in figure 6.13 for data and pseudo-data and fitted with a function of the form of equation 6.10.

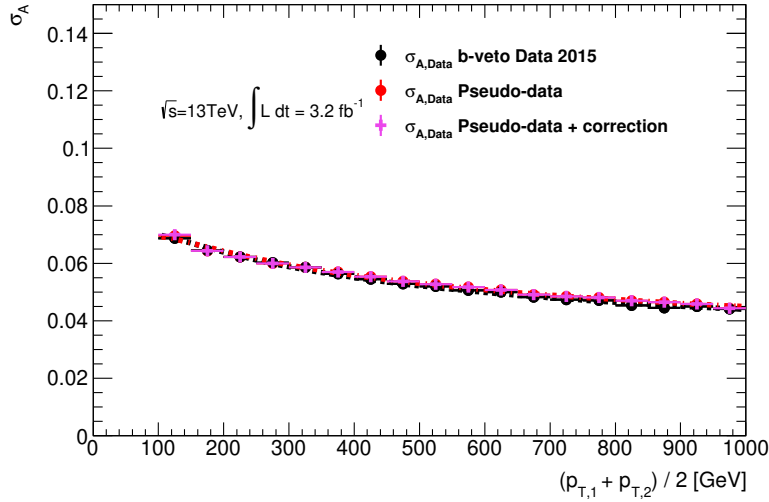


Fig. 6.13 The  $p_T$ -dependent  $\sigma_A$  distribution for data (in black) and pseudo-data (in red) dijet events (excluding  $b$ -jets) as a function of average jet  $p_T$ . The data in this figure represents  $3.2 \text{ fb}^{-1}$  of  $\sqrt{s} = 13 \text{ TeV}$  data recorded in 2015. The dijet MC used to construct the jet response and smear well-measured data events to produce *pseudo-data* replicates the pile-up conditions within the detector during 2015. The seed events used to generate the pseudo-data were required to pass one of a range of single-jet triggers and satisfy  $S < 0.5 + (0.1 \times N_{b\text{-jet}}) [\text{GeV}^{1/2}]$ . All events considered in this figure are further required to satisfy the requirements shown in table 6.3. The corrected pseudo-data distribution is shown by the magenta data points.

From figure 6.13, plotted with the first significant amount of data collected during Run 2, it was concluded that corrections to the Gaussian core of the jet response were of negligible importance when compared with those generated for Run 1 [136]. An insufficient number of events entered the analysis when  $b$ -tagged jets were considered exclusively and so no dedicated calibration was provided for the 2015 dataset.

### Combined 2015 and 2016 Dataset

Using the combined 2015 and 2016 dataset provided an integrated luminosity of  $36.1 \text{ fb}^{-1}$ , increasing the number of events passing the seed selection requirements to be considered by Jet Smearing. As a result, the seed selection criteria were made more stringent, identifying events with

$$S < 0.3 + (0.1 \times N_{b\text{-jet}}) [\text{GeV}^{1/2}] \quad (6.14)$$

## 6.4 Correcting the Initial Response

as seed events while retaining adequate statistics in a  $b$ -jet specific Gaussian core calibration. Figures 6.14 and 6.15 show the asymmetry distribution as a function of the average  $p_T$  of the dijet pair for  $b$ -veto and  $b$ -tagged events, respectively.

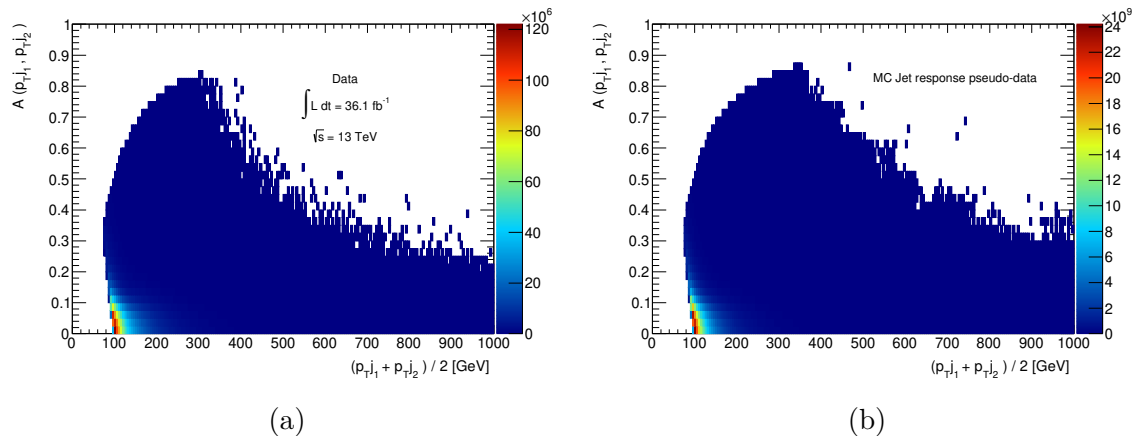


Fig. 6.14 The 2D asymmetry distribution for data events (excluding  $b$ -jets) as a function of average jet  $p_T$ . The data in this figure represents  $36.1 \text{ fb}^{-1}$  of  $\sqrt{s} = 13 \text{ TeV}$  data recorded in 2015 and 2016. Events considered in this figure are required to satisfy the requirements shown in table 6.3.

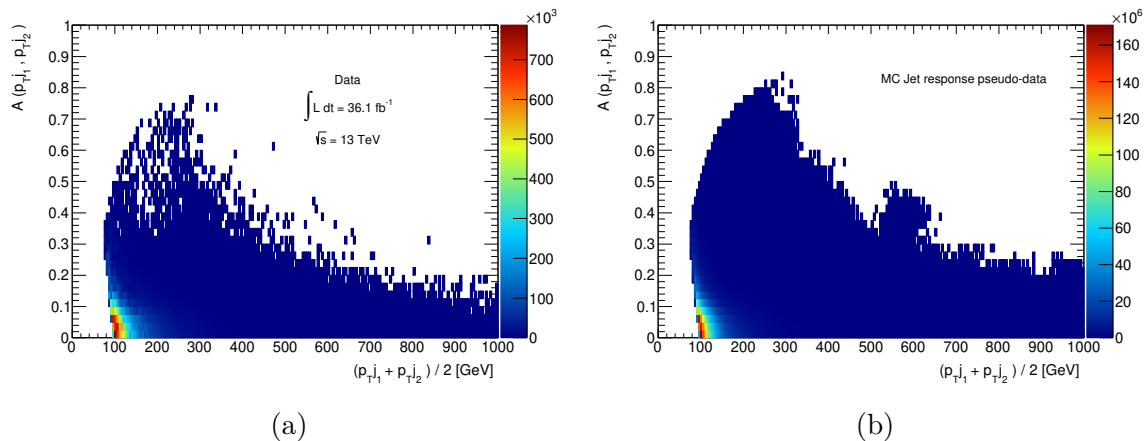
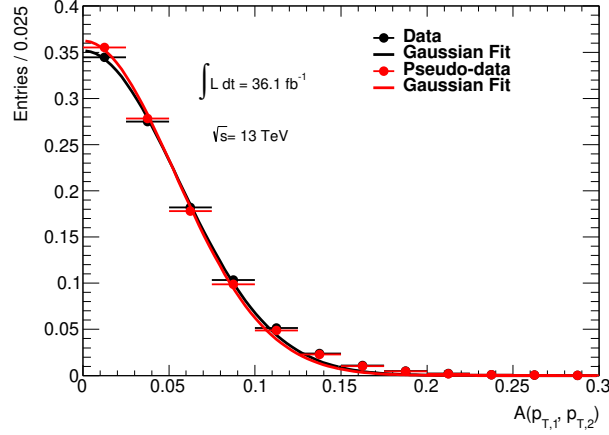


Fig. 6.15 The 2D asymmetry distribution for data events (exclusively  $b$ -jets) as a function of average jet  $p_T$ . The data in this figure represents  $36.1 \text{ fb}^{-1}$  of  $\sqrt{s} = 13 \text{ TeV}$  data recorded in 2015 and 2016. Events considered in this figure are required to satisfy the requirements shown in table 6.3.

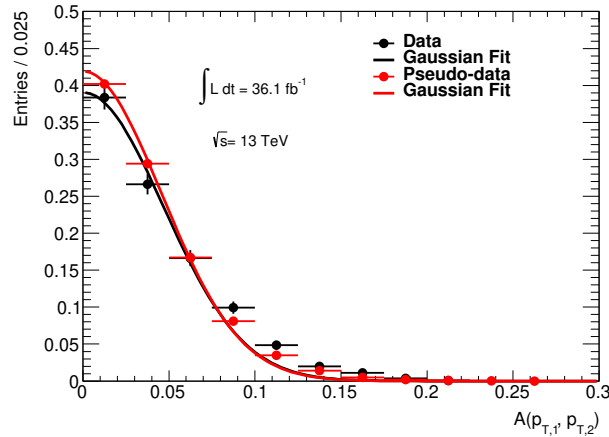
A value of  $\sigma_A$  is then extracted from the fit of the asymmetry distribution for data and pseudo-data in each 50(100) GeV bin of the two-dimensional distributions for the

## The Jet Smearing Method

$b$ -veto ( $b$ -tagged) case shown in figure 6.14 (figure 6.15). The result of the fit for both cases is shown in figure 6.16.



(a)

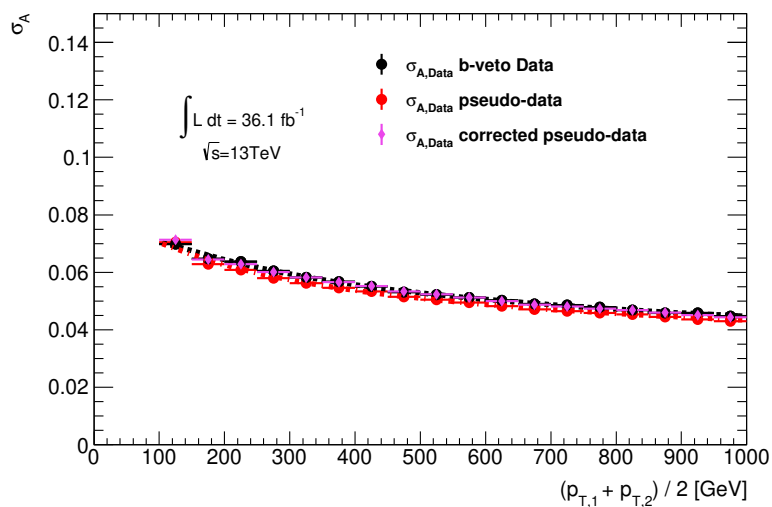


(b)

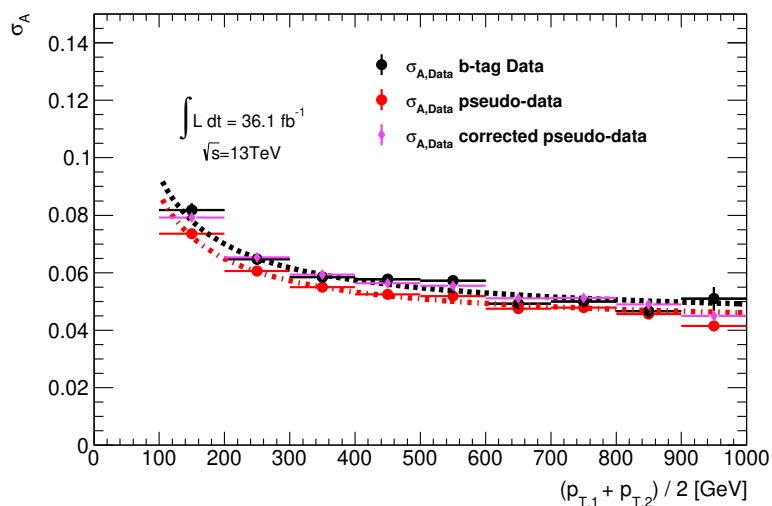
Fig. 6.16 Asymmetry distribution for (a)  $b$ -vetoed and (b)  $b$ -tagged dijet events in data recorded in 2015 and 2016 and pseudo-data events in the range  $400 \leq \langle p_T^{jj} \rangle < 450$  GeV. A Gaussian function is fitted in the region  $0 < A \leq 0.1$  ( $0 < A \leq 0.07$ ) for both data and pseudo-data  $b$ -veto ( $b$ -tagged) events for each 50(100) GeV bin in the range  $100 \leq \langle p_T^{jj} \rangle \leq 1000$  GeV.

Values of  $\sigma_A$  extracted for each 50 (100) GeV bin for  $b$ -veto ( $b$ -tagged) events in the range  $100 \text{ GeV} \leq \langle p_T^{jj} \rangle \leq 1000 \text{ GeV}$  are plotted as a function of  $\langle p_T^{jj} \rangle$  in figure 6.17 for data and pseudo-data and fitted with a function of the form of equation 6.10. An increased bin size is used for the Gaussian fit to the asymmetry distribution in  $b$ -tagged events to increase the number of events entering each bin of the fit.

## 6.4 Correcting the Initial Response



(a)



(b)

Fig. 6.17 The  $p_T$ -dependent  $\sigma_A$  distribution for data (in black) and pseudo-data (in red) dijet events (excluding  $b$ -jets) as a function of average jet  $p_T$ . The data in this figure represents  $36.1 \text{ fb}^{-1}$  of  $\sqrt{s} = 13 \text{ TeV}$  data recorded in 2015 and 2016. All events considered in this figure are required to satisfy the requirements shown in table 6.3. The corrected pseudo-data distribution is shown by the magenta data points.

The parameters in equation 6.10 obtained from the fitting procedure performed on the distributions shown in figure 6.17 are shown in table 6.4.

## The *Jet Smearing* Method

---

Table 6.4 Parameters obtained from the dijet balance analysis by fitting a function with the form of equation 6.10 to the average  $p_T$ -dependent asymmetry width distribution of dijet events using  $36.1 \text{ fb}^{-1}$  of  $\sqrt{s} = 13 \text{ TeV}$  data and associated pseudo-data. The parameters are used as inputs to the Jet Smearing tool to calibrate the Gaussian core of the pseudo-data jet response distribution to data.

Fit parameter	Value	Uncertainty
<b><i>b-veto</i></b>		
$A_{\text{data}}^{\text{DJB}}$	-4.43	0.101
$B_{\text{data}}^{\text{DJB}}$	0.957	0.011
$C_{\text{data}}^{\text{DJB}}$	0.0189	0.0003
$A_{\text{pseudo-data}}^{\text{DJB}}$	-3.382	0.009
$B_{\text{pseudo-data}}^{\text{DJB}}$	0.839	0.001
$C_{\text{pseudo-data}}^{\text{DJB}}$	0.020	0.000
<b><i>b-tag</i></b>		
$A_{\text{data}}^{\text{DJB}}$	4.016	2.253
$B_{\text{data}}^{\text{DJB}}$	0.124	0.251
$C_{\text{data}}^{\text{DJB}}$	0.041	0.007
$A_{\text{pseudo-data}}^{\text{DJB}}$	4.168	0.052
$B_{\text{pseudo-data}}^{\text{DJB}}$	0.056	0.007
$C_{\text{pseudo-data}}^{\text{DJB}}$	0.040	0.000

These parameters were used as inputs to the jet smearing software in order to calibrate the Gaussian core of the MC-derived jet response to data prior to the generation of corrections to the low-side tail of the jet response.

### 6.4.2 Dijet $\phi$ Smearing

The  $\phi$  distribution of jets in pseudo-data may differ from that of jets in data, due to the seed event selection favouring back-to-back well-measured jet topologies. Prior to smearing of the jet four-momentum, the axis of a jet in a well-measured seed event is assumed to be approximately equal to the axis of the truth jet in the event.

After smearing the four-momentum of the seed jet, the jet  $p_T$  fluctuates upwards or downwards (potentially significantly so) while the topology of the dijet event remains back-to-back. Mismeasured dijet events in data in which jets undergo large  $p_T$  fluctuations are unlikely to retain a back-to-back topology and the jet axis cannot be assumed to be equivalent to the truth jet axis. As SUSY analyses rely heavily upon the  $\Delta\phi(\text{jet}, E_T^{\text{miss}})_{\text{min}}$  variable to suppress multijet background events in signal regions, it is vital that the  $\phi$ -distribution of jets within pseudo-data mirrors that of jets within data. This discrepancy is addressed by applying smearing to pseudo-data jet  $\phi$  in dijet events in order to produce pseudo-data with  $\Delta\phi(j_1, j_2)$  distributions mirroring those observed in data.

A dedicated analysis is utilised to calibrate the  $\Delta\phi(j_1, j_2)$  distribution in pseudo-data events to that of data events, similar to the procedure described in section 6.4.1. Dijet  $\phi$  smearing has been utilised as part of the Jet Smearing tool since Run 1 [136], with calibrations to data updated for early Run 2 analyses.

### 6.4.2.1 Correction Calculation Procedure

In a similar fashion to the  $p_T$  corrections calculated for the dijet balance analysis (discussed in section 6.4.1) the  $\Delta\phi$  correction calculation initially considers the same dijet events used in the dijet balance analysis as specified by table 6.3 but places no requirement on the back-to-back nature of the events, omitting the

$$|\pi - \Delta\phi(j_1, j_2)| < 0.25$$

criterion. The full list of requirements for consideration by the  $\phi$  smearing analysis is shown in table 6.5.

## The *Jet Smearing* Method

---

Table 6.5 Criteria for event selection in the dijet  $\phi$ -smearing analysis. Events must also pass one of the single-jet triggers listed in table 6.2.

Variable	Requirement
$N_{\text{jet}}$	2
$p_{\text{T}}(j_1)$	> 100 GeV
$p_{\text{T}}(j_2)$	> 50 GeV
$E_{\text{T}}^{\text{miss}}$	< $0.1\langle p_{\text{T}}^{jj} \rangle$

The  $\Delta\phi(j_1, j_2)$  distribution is plotted as a function of the average  $p_{\text{T}}$  of the dijet pair,  $\langle p_{\text{T}}^{jj} \rangle$ , with a Gaussian function fitted to the distribution with a corresponding width  $\sigma(\Delta\phi(j_1, j_2))$ . The distribution of  $\sigma(\Delta\phi(j_1, j_2))$  in data and pseudo-data is plotted as a function of  $\langle p_{\text{T}}^{jj} \rangle$  and fitted with a function of the form

$$\sigma(\Delta\phi(j_1, j_2)) = \frac{A^\phi}{\langle p_{\text{T}} \rangle} + \frac{B^\phi}{\sqrt{\langle p_{\text{T}} \rangle}} + C^\phi \quad (6.15)$$

similar to the form of equation 6.10. The function defined in equation 6.15 was found empirically to produce the best agreement with distributions of  $\sigma(\Delta\phi(j_1, j_2))$  in data and pseudo-data.

The correction to data is achieved through the convolution of two Gaussians, such that

$$\sigma_{\text{final}}(\Delta\phi(j_1, j_2))^2 = (\sigma_{\text{pseudo-data}}(\Delta\phi(j_1, j_2)))^2 + (\sigma_{\text{correction}}(\Delta\phi(j_1, j_2)))^2 \quad (6.16)$$

where  $\sigma_{\text{final}}(\Delta\phi(j_1, j_2))$  should be equivalent to  $\sigma_{\text{data}}(\Delta\phi(j_1, j_2))$ , leading to

$$\sigma_{\text{correction}}(\Delta\phi(j_1, j_2))^2 = [\sigma_{\text{data}}(\Delta\phi(j_1, j_2))]^2 - [\sigma_{\text{pseudo-data}}(\Delta\phi(j_1, j_2))]^2 \quad (6.17)$$

The correction to the distribution of  $\Delta\phi(j_1, j_2)$  was found empirically to be related to the per-jet correction by

$$\sigma_{\text{correction}}(\Delta\phi(j_1, j_2)) = 2 \times \sigma_{\text{correction}}(\phi) \quad (6.18)$$

By replacing the correction term for the  $\Delta\phi(j_1, j_2)$  distribution in equation 6.17 with the per-jet correction shown in equation 6.18, the correction given to the  $\phi$ -distribution of pseudo-data jets is given by

$$\sigma_{\text{correction}}(\phi) = \frac{1}{\sqrt{2}} \sqrt{[\sigma_{\text{data}}(\Delta\phi(j_1, j_2))]^2 - [\sigma_{\text{pseudo-data}}(\Delta\phi(j_1, j_2))]^2} \quad (6.19)$$

The factor of 2 present in equation 6.18 subsequently present as a factor of  $1/\sqrt{2}$  in equation 6.19 was observed to be necessary to avoid over-correction of pseudo-data.

### 6.4.2.2 Results

The  $\phi$ -smearing calibration was initially performed with  $3.2 \text{ fb}^{-1}$  of  $\sqrt{s} = 13 \text{ TeV}$  data to allow analyses relying upon the tool to perform searches early in Run 2. A later calibration was provided with the full  $36.1 \text{ fb}^{-1}$  of  $\sqrt{s} = 13 \text{ TeV}$ . The results of both calibration procedures are provided in this section.

#### 2015 Dataset

Seed events used to generate the pseudo-data in the following figures were required to pass one of a range of single-jet triggers and satisfy  $S < 0.5 + (0.1 \times N_{\text{b-jet}}) [\text{GeV}^{1/2}]$ . The two dimensional distribution of  $|\pi - \Delta\phi(j_1, j_2)|$  as a function of average dijet  $p_T$  for data events from the  $3.2 \text{ fb}^{-1}$  of data recorded in 2015 is shown in figure 6.18.

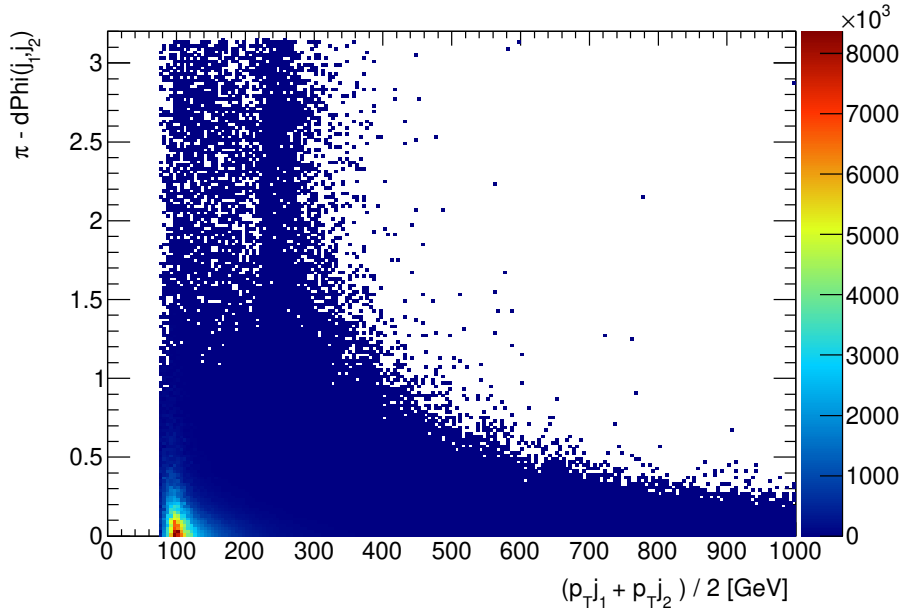


Fig. 6.18 The 2D distribution of  $|\pi - \Delta\phi(j_1, j_2)|$  for data events (excluding  $b$ -jets) as a function of average jet  $p_T$ , with 5 GeV  $p_T$  bins. The data in this figure represents  $3.2 \text{ fb}^{-1}$  of  $\sqrt{s} = 13 \text{ TeV}$  data recorded in 2015. Events considered in this figure are required to satisfy the requirements shown in table 6.5.

Slices of 40 GeV in average jet  $p_T$  were taken from figure 6.18 for data and pseudo-data. Both distributions were fitted with a Gaussian function of width  $\sigma_{\Delta\phi}$ . The fit to data and pseudo-data points for  $|\pi - \Delta\phi(j_1, j_2)| < 0.1$  for  $280 \leq \langle p_T^{jj} \rangle < 320 \text{ GeV}$  is shown in figure 6.19.

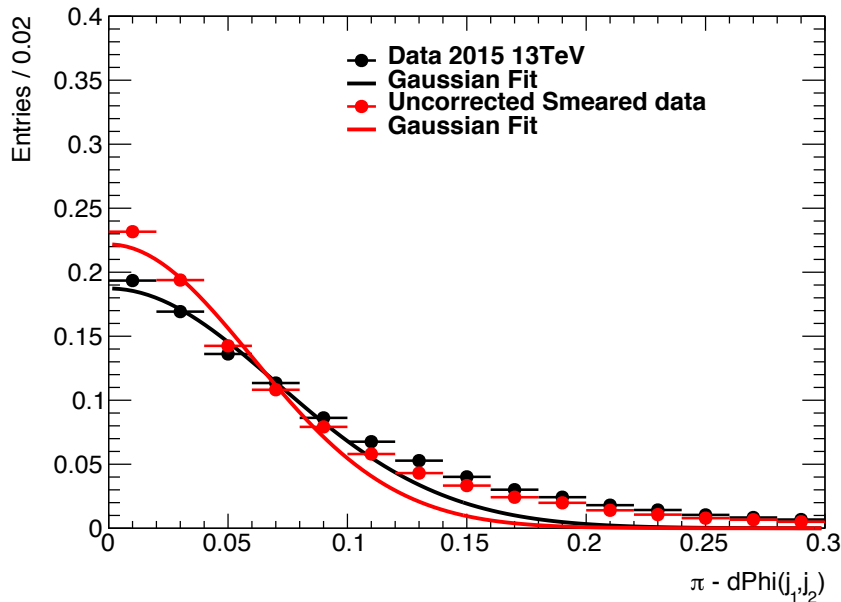
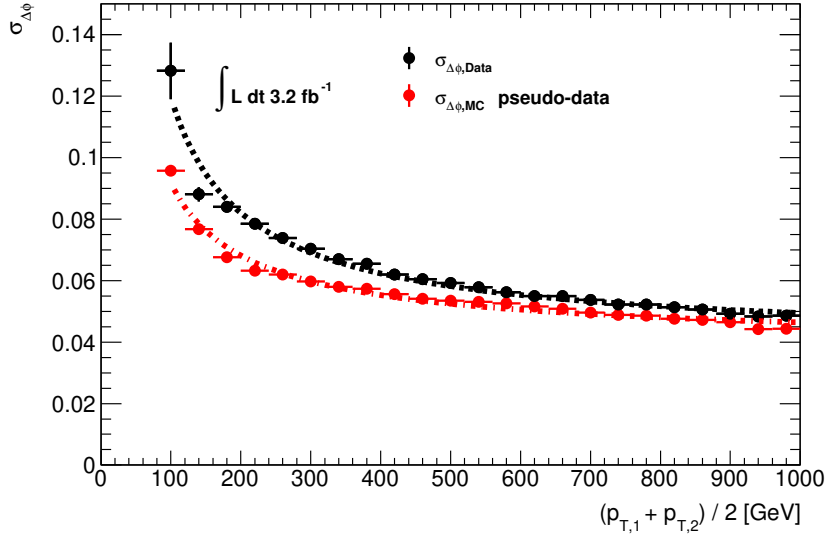
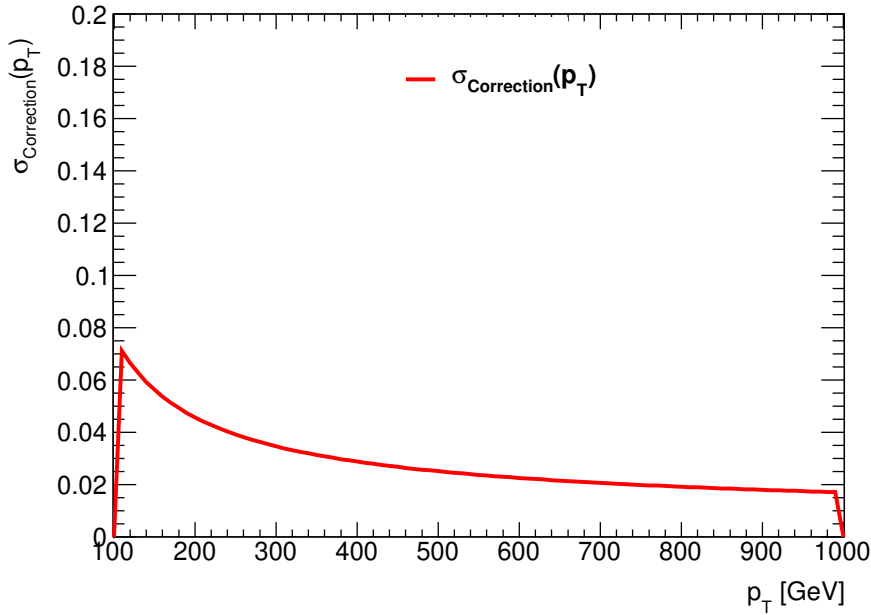


Fig. 6.19  $|\pi - \Delta\phi(j_1, j_2)|$  distribution for data and pseudo-data events (excluding  $b$ -jets) with  $280 \leq \langle p_T^{jj} \rangle < 320$  GeV. The data in this figure represents  $3.2 \text{ fb}^{-1}$  of  $\sqrt{s} = 13$  TeV data recorded in 2015. Events considered in this figure are required to satisfy the requirements shown in table 6.5.

A value of  $\sigma_{\Delta\phi}$  is then extracted from the fit shown in figure 6.19 for data and pseudo-data. Values of  $\sigma_{\Delta\phi}$  extracted for each 40 GeV bin in the range  $100 \text{ GeV} \leq \langle p_T^{jj} \rangle \leq 1000$  GeV are plotted as a function of  $\langle p_T^{jj} \rangle$  in figure 6.20a for data and pseudo-data and fitted with a function of the form of equation 6.15. The  $p_T$ -dependent correction to the  $\phi$  distribution of pseudo-data jets is shown in figure 6.20b.



(a)



(b)

Fig. 6.20 (a) The  $p_T$ -dependent distribution of the width of the  $|\pi - \Delta\phi(j_1, j_2)|$  distribution (excluding  $b$ -jets) as a function of average jet  $p_T$ . The data in this figure represents  $3.2 \text{ fb}^{-1}$  of  $\sqrt{s} = 13 \text{ TeV}$  data recorded in 2015. The dijet MC used to construct the jet response and smear well-measured data events to produce pseudo-data replicates the pile-up conditions within the detector during 2015. All events considered in this figure are further required to satisfy the requirements shown in table 6.5. (b) The  $p_T$ -dependent correction calculated in equation 6.19 applied to the pseudo-data distribution shown in (a).

## 6.4 Correcting the Initial Response

---

The parameters in equation 6.15 were obtained from the fitting in figure 6.20a and are shown in table 6.6. Parameters were derived from  $b$ -veto events and applied to all pseudo-data events. A lack of events entering the  $b$ -jet regions meant that no correction was derived specifically for  $b$ -jet events.

Table 6.6 Parameters obtained from the  $\phi$  smearing analysis by fitting a function with the form of equation 6.15 to the distribution of  $\sigma(\Delta\phi(j_1, j_2))$  using 2015 data and associated pseudo-data. The parameters were used as inputs to the Jet Smearing tool to calibrate the pseudo-data jet  $\phi$  distribution to data.

Fit parameter	Value
$A_{\text{data}}^\phi$	6.42
$B_{\text{data}}^\phi$	0.178
$C_{\text{data}}^\phi$	0.0374
$A_{\text{pseudo-data}}^\phi$	3.54
$B_{\text{pseudo-data}}^\phi$	0.194
$C_{\text{pseudo-data}}^\phi$	0.0367

No additional systematic uncertainty was associated with the  $\phi$ -smearing calibration procedure derived using the 2015 dataset.

### Combined 2015 and 2016 Dataset

Once again the increased integrated luminosity of  $36.1 \text{ fb}^{-1}$  allowed the requirement on  $E_T^{\text{miss}}$ -significance defined in equation 6.14 to be used to define seed events. The increased integrated luminosity additionally allowed  $\phi$ -smearing calibrations to be generated for  $b$ -tagged events for the first time. Two dimensional distributions of the angle  $\phi$  between the pair of jets in dijet events as a function of the average dijet  $p_T$  are shown in figures 6.21 and 6.22 for  $b$ -veto and  $b$ -tagged events, respectively.

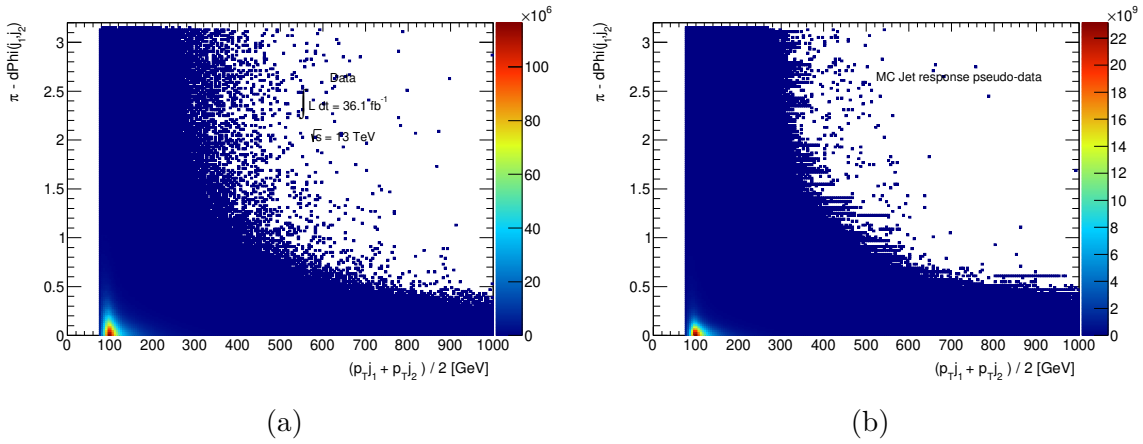


Fig. 6.21 The 2D distribution of  $|\pi - \Delta\phi(j_1, j_2)|$  for (a) data and (b) pseudo-data events excluding  $b$ -jets as a function of average jet  $p_T$ , with 5 GeV  $p_T$  bins. The data in this figure represents  $36.1 \text{ fb}^{-1}$  of  $\sqrt{s} = 13 \text{ TeV}$  data recorded in 2015 and 2016. Events considered in this figure are required to satisfy the requirements shown in table 6.5.

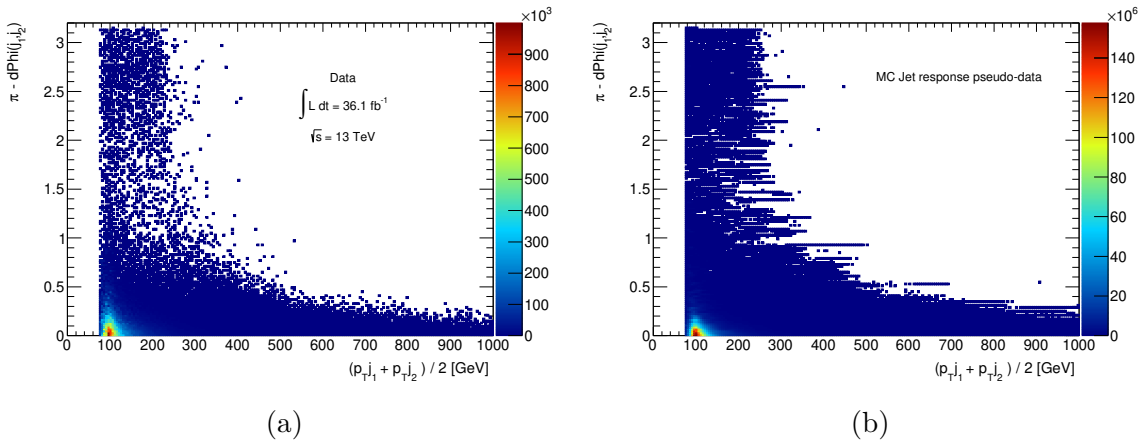
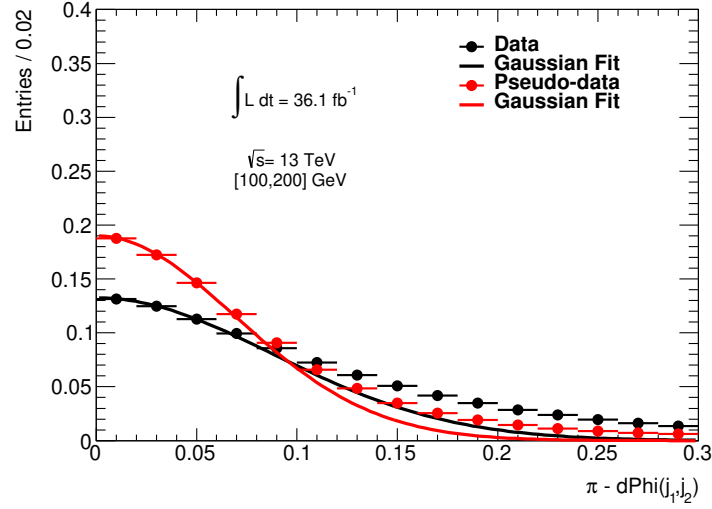


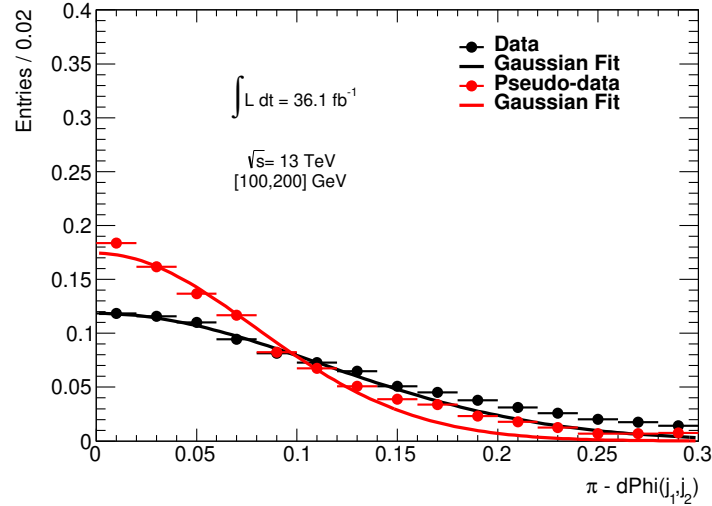
Fig. 6.22 The 2D distribution of  $|\pi - \Delta\phi(j_1, j_2)|$  for (a) data and (b) pseudo-data events with  $b$ -jets as a function of average jet  $p_T$ , with 5 GeV  $p_T$  bins. The data in this figure represents  $36.1 \text{ fb}^{-1}$  of  $\sqrt{s} = 13 \text{ TeV}$  data recorded in 2015 and 2016. Events considered in this figure are required to satisfy the requirements shown in table 6.5.

One dimensional projections of 100 GeV in average jet  $p_T$  were taken from figures 6.21 and 6.22 for data and pseudo-data. Both distributions were fitted with a Gaussian function of width  $\sigma_{\Delta\phi}$ . The fit to data and pseudo-data points for  $|\pi - \Delta\phi(j_1, j_2)| < 0.05$  ( $|\pi - \Delta\phi(j_1, j_2)| < 0.15$ ) for  $b$ -veto ( $b$ -tagged) events with  $100 \leq \langle p_T^{jj} \rangle < 200 \text{ GeV}$  is shown in figure 6.23 for the  $b$ -veto and  $b$ -tagged cases.

## 6.4 Correcting the Initial Response



(a)



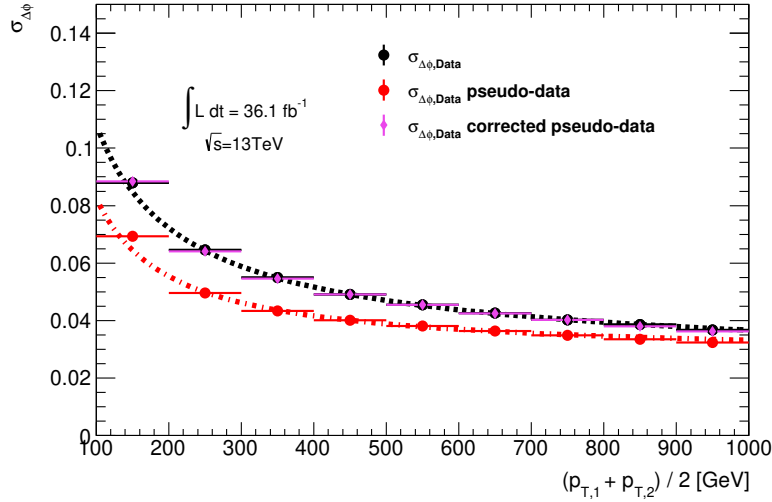
(b)

Fig. 6.23  $|\pi - \Delta\phi(j_1, j_2)|$  distribution for data and pseudo-data events for (a)  $b$ -veto events and (b)  $b$ -tag events with  $100 \leq \langle p_T^{jj} \rangle < 200$  GeV. The data in this figure represents  $36.1 \text{ fb}^{-1}$  of  $\sqrt{s} = 13 \text{ TeV}$  data recorded in 2015 and 2016. Events considered in this figure are required to satisfy the requirements shown in table 6.5.

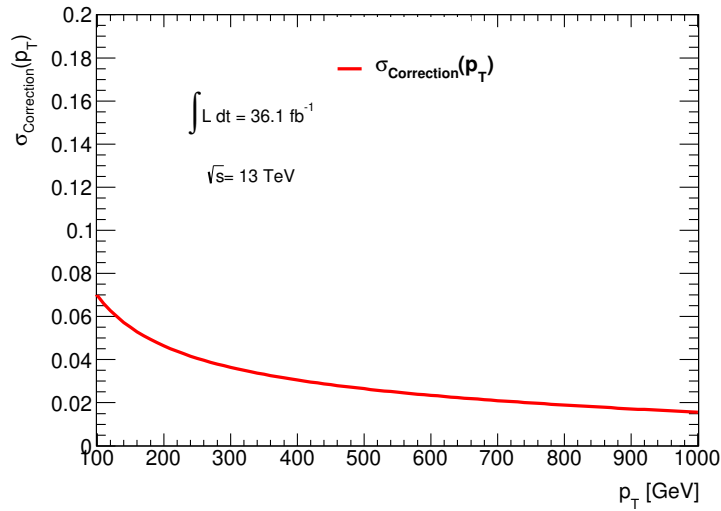
A value of  $\sigma_{\Delta\phi}$  is then extracted from the fits shown in figure 6.23 for data and pseudo-data. Values of  $\sigma_{\Delta\phi}$  extracted for each 100 GeV bin in the range  $100 \text{ GeV} \leq \langle p_T^{jj} \rangle \leq 1000 \text{ GeV}$  and are plotted as a function of  $\langle p_T^{jj} \rangle$  in figures 6.24a and 6.25a for  $b$ -veto and  $b$ -tagged events in data and pseudo-data. Data and pseudo-data distributions are

## The Jet Smearing Method

fitted with a function of the form of equation 6.15. The  $p_T$ -dependent correction to jet  $\phi$  is shown in figures 6.24b and 6.25b.

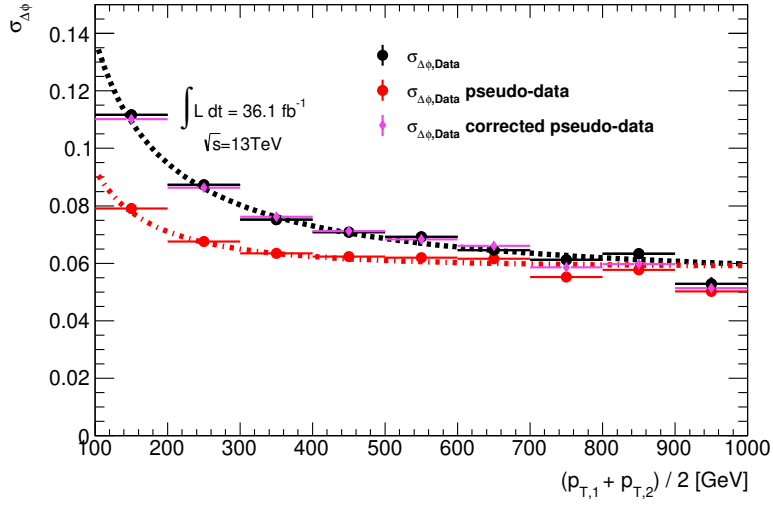


(a)

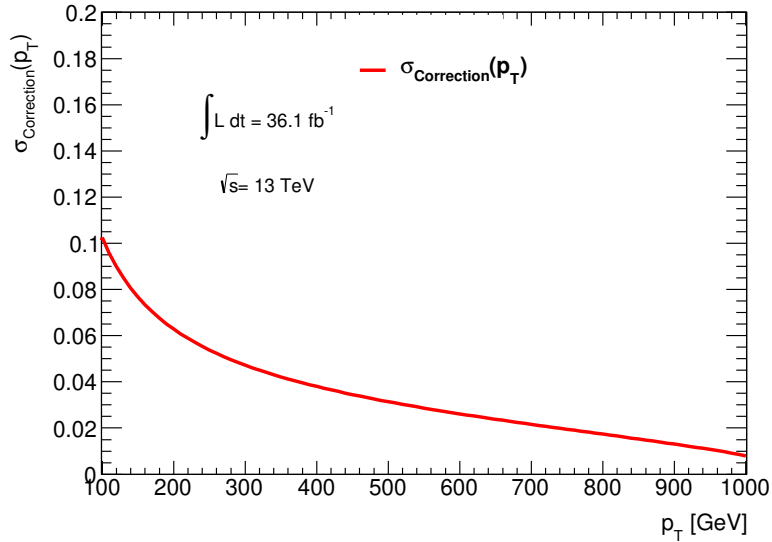


(b)

Fig. 6.24 (a) The  $p_T$ -dependent distribution of the width of the  $|\pi - \Delta\phi(j_1, j_2)|$  distribution for events excluding  $b$ -jets as a function of average jet  $p_T$ . The data in this figure represents  $36.1 \text{ fb}^{-1}$  of  $\sqrt{s} = 13 \text{ TeV}$  data recorded in 2015 and 2016. All events considered in this figure are further required to satisfy the requirements shown in table 6.5. Data is shown in black, while pseudo-data is shown in red. Corrected pseudo-data events are shown with magenta points and largely overlap with data. (b) The  $p_T$ -dependent correction calculated in equation 6.19 applied to the pseudo-data distribution shown in (a).



(a)



(b)

Fig. 6.25 (a) The  $p_T$ -dependent distribution of the width of the  $|\pi - \Delta\phi(j_1, j_2)|$  distribution for events with  $b$ -jets as a function of average jet  $p_T$ . The data in this figure represents  $36.1 \text{ fb}^{-1}$  of  $\sqrt{s} = 13 \text{ TeV}$  data recorded in 2015 and 2016. All events considered in this figure are further required to satisfy the requirements shown in table 6.5. Data is shown in black, while pseudo-data is shown in red. Corrected pseudo-data events are shown with magenta points and largely overlap with data. (b) The  $p_T$ -dependent correction calculated in equation 6.19 applied to the pseudo-data distribution shown in (a).

## The *Jet Smearing* Method

---

The parameters in equation 6.15 were obtained from the fitting in figures 6.24 and 6.25 and are shown in table 6.7.

Table 6.7 Parameters obtained from the  $\phi$  smearing analysis by fitting a function with the form of equation 6.15 to the distribution of  $\sigma(\Delta\phi(j_1, j_2))$  using  $36.1 \text{ fb}^{-1}$  of  $\sqrt{s} = 13$  TeV data and associated pseudo-data. The parameters are used as inputs to the Jet Smearing tool to calibrate the pseudo-data jet  $\phi$  distribution to data

Fit parameter	Value	Uncertainty
<b><i>b</i>-veto</b>		
$A_{\text{data}}^\phi$	4.596	0.400
$B_{\text{data}}^\phi$	0.441	0.037
$C_{\text{data}}^\phi$	0.018	0.001
$A_{\text{pseudo-data}}^\phi$	5.221	0.022
$B_{\text{pseudo-data}}^\phi$	0.035	0.002
$C_{\text{pseudo-data}}^\phi$	0.027	0.000
<b><i>b</i>-tag</b>		
$A_{\text{data}}^\phi$	8.442	1.743
$B_{\text{data}}^\phi$	0.035	0.192
$C_{\text{data}}^\phi$	0.050	0.005
$A_{\text{pseudo-data}}^\phi$	6.308	0.033
$B_{\text{pseudo-data}}^\phi$	-0.342	0.005
$C_{\text{pseudo-data}}^\phi$	0.064	0.000

The parameters listed were used as inputs to the jet smearing tool to calibrate the  $\phi$ -distribution of pseudo-data events to data prior to the generation of corrections to the low-side tail of the jet response in a process described in section 6.4.3.

### 6.4.3 Tail correction via the Mercedes analysis

The Mercedes analysis aims to calibrate the low-side non-Gaussian core (generally the region  $R_{\text{MC}} < 0.8$ ) of the MC-derived jet response to match that observed in data. The

## 6.4 Correcting the Initial Response

low-side tail of the response is targeted in particular as downward fluctuations in jet  $p_T$  measurement represent the dominant contribution to fake  $E_T^{\text{miss}}$  observed in signal regions considered by analyses using the jet smearing tool. The  $\phi$  direction of  $\vec{E}_T^{\text{miss}}$  provides a means of discriminating between upward and downward fluctuations of the jet  $p_T$ , which is unavailable in the dijet balance analysis discussed in section 6.4.1. The analysis selects three-jet events, generalised into two event categories dependent on the relative orientation in  $\phi$  of  $\vec{E}_T^{\text{miss}}$  to the jets in the event: the parallel and anti-parallel orientation. A schematic view of both configurations is given in figure 6.26. The parallel configuration corresponds to a downward fluctuation in jet  $p_T$ , while the anti-parallel configuration corresponds to scenarios in which the jet  $p_T$  fluctuates upwards. In both orientations, the  $\vec{E}_T^{\text{miss}}$  is clearly associated with one of the jets in the event. The jet- $E_T^{\text{miss}}$  association is performed by requiring

$$\Delta\phi(\text{jet}, E_T^{\text{miss}}) < 0.1 \quad (6.20)$$

OR

$$\pi - \Delta\phi(\text{jet}, E_T^{\text{miss}}) < 0.1 \quad (6.21)$$

where equation 6.20 and 6.21 are used for the parallel and anti-parallel selections, respectively.

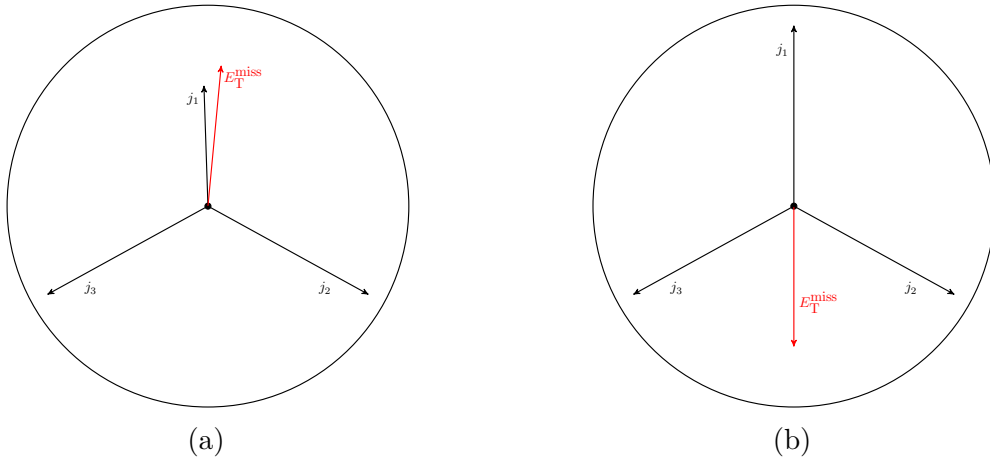


Fig. 6.26 Schematic view of a three jet Mercedes event observed in the transverse plane in the (a) parallel and (b) anti-parallel configuration, with respect to  $\vec{E}_T^{\text{miss}}$  in the event, which is observed to be clearly associated with one of the jets in the event.

## The *Jet Smearing* Method

---

For the jet clearly associated with the  $\vec{E}_T^{\text{miss}}$  (and assuming that the dominant source of  $E_T^{\text{miss}}$  in the event is due to a fluctuation in jet  $p_T$ ), the truth-level jet  $p_T$  is approximated by reconstructed objects with

$$\vec{p}_T^J(\text{truth}) \simeq \vec{p}_T^J(\text{reco}) + \vec{E}_T^{\text{miss}} \quad (6.22)$$

and the jet associated with  $\vec{E}_T^{\text{miss}}$  has a response defined by

$$R = \frac{\vec{p}_T^J(\text{reco}) \times \vec{p}_T^J(\text{truth})}{|\vec{p}_T^J(\text{truth})|^2} \quad (6.23)$$

By using the identity given in equation 6.22 in equation 6.23, the Mercedes analysis-specific response  $R_2$  is obtained, where

$$R_2 \simeq \frac{\vec{p}_T^J(\text{reco}) \times (\vec{p}_T^J(\text{reco}) + \vec{E}_T^{\text{miss}})}{|\vec{p}_T^J(\text{reco}) + \vec{E}_T^{\text{miss}}|^2} \quad (6.24)$$

$R_2$  acts as a probe for the general jet response  $R$ , where  $R$  is defined in equation 6.1. Selecting low values of  $R_2$  targets the low-side non-Gaussian tail of the jet response  $R$  and is the means of generating specific low-side response tail corrections.

### 6.4.3.1 Event Pre-selection

Events considered by the Mercedes analysis require one of the single-jet triggers listed in table 6.2 to be passed, in addition to the selection requirements shown in table 6.8.

## 6.4 Correcting the Initial Response

---

Table 6.8 Criteria for event selection in the Mercedes analysis for events passing one of the single-jet triggers shown in table 6.2.

Variable	Requirement
$N_{\text{jet}}$	$\geq 3$
$p_{\text{T}}(j_1)$	$> 210 \text{ GeV}$
$p_{\text{T}}(j_2)$	$> 50 \text{ GeV}$
$p_{\text{T}}(j_3)$	$> 40 \text{ GeV}$
$E_{\text{T}}^{\text{miss}}$	$> 30 \text{ GeV}$

The selections used in the analysis using Run 2 data are influenced by the selections chosen in Run 1 [136], which were designed to veto events containing soft  $E_{\text{T}}^{\text{miss}}$  and the effects of the  $Z(\rightarrow \nu\nu) + \text{jets}$  background by selecting high  $p_{\text{T}}$  leading jets while retaining adequate statistics in the  $b$ -tagged analysis.

### 6.4.3.2 Angular Event Selection

Jets in the events passing the pre-selection are sorted by their angular proximity to  $\vec{E}_{\text{T}}^{\text{miss}}$  in the event  $\Delta\phi(\text{jet}, E_{\text{T}}^{\text{miss}})$ . Jets  $(j_1, j_2, \dots, j_N)$ , where  $N = N_{\text{jet}}$ , are labelled such that  $j_1$  has minimal  $\Delta\phi(\text{jet}, E_{\text{T}}^{\text{miss}})$  and  $j_N$  has the maximum possible  $\Delta\phi(\text{jet}, E_{\text{T}}^{\text{miss}})$  in the event. The jet  $j_N$  is identified as the jet that most closely approaches a back-to-back arrangement with  $\vec{E}_{\text{T}}^{\text{miss}}$  in the event. In the description that follows, the *candidate jet* is the jet considered to be clearly associated with the  $\vec{E}_{\text{T}}^{\text{miss}}$ .

Events satisfying the parallel selection (figure 6.26a) undergoing downward  $p_{\text{T}}$  fluctuations are required to satisfy the requirements shown in table 6.9. Events satisfying the anti-parallel selection (figure 6.26b) and undergoing upward  $p_{\text{T}}$  fluctuations satisfied the requirements shown in table 6.10. In both tables,  $\Delta\phi^{\text{match}}$  is defined as the angular requirement ensuring that the candidate jet is associated with the  $E_{\text{T}}^{\text{miss}}$  and the requirement on  $\Delta\phi_1^{\text{iso}}$  ensures that the candidate jet is *uniquely* associated with the  $\vec{E}_{\text{T}}^{\text{miss}}$ .

## The Jet Smearing Method

---

Table 6.9 Criteria for event selection in the parallel selection (figure 6.26a) of the Mercedes analysis.

Variable	Requirement
$ \Delta\phi(j_1, \vec{E}_T^{\text{miss}}) $	$< \pi -  \Delta\phi(j_N, \vec{E}_T^{\text{miss}}) $
$ \Delta\phi(j_1, \vec{E}_T^{\text{miss}}) $	$< \Delta\phi^{\text{match}}$
$ \Delta\phi(j_2, \vec{E}_T^{\text{miss}}) $	$> \Delta\phi_1^{\text{iso}}$

Table 6.10 Criteria for event selection in the anti-parallel selection (figure 6.26b) of the Mercedes analysis.

Variable	Requirement
$\pi -  \Delta\phi(j_1, \vec{E}_T^{\text{miss}}) $	$<  \Delta\phi(j_N, \vec{E}_T^{\text{miss}}) $
$\pi -  \Delta\phi(j_N, \vec{E}_T^{\text{miss}}) $	$< \Delta\phi^{\text{match}}$
$\pi -  \Delta\phi(j_{N-1}, \vec{E}_T^{\text{miss}}) $	$> \Delta\phi_1^{\text{iso}}$

The values of  $\Delta\phi^{\text{match}}$  and  $\Delta\phi_1^{\text{iso}}$  used in the analysis of data collected in 2015 and 2016 are given in table 6.11.

Table 6.11 Angular selections used to ensure unique jet- $E_T^{\text{miss}}$  association in the parallel and anti-parallel Mercedes analysis selections.

Variable	Requirement [rad]
$\Delta\phi^{\text{match}}$	0.10
$\Delta\phi_1^{\text{iso}}$	1.00
$\Delta\phi_2^{\text{iso}}$	0.25

At this stage the candidate jet is labelled  $j_{\text{can}}$ . In the parallel selection,  $j_{\text{can}}$  has minimal  $\Delta\phi(j, \vec{E}_T^{\text{miss}})$ . Conversely in the anti-parallel selection,  $j_{\text{can}}$  has maximal  $\Delta\phi(j, \vec{E}_T^{\text{miss}})$  and is approximately back-to-back with the  $\vec{E}_T^{\text{miss}}$ . The jet with maximal  $\Delta\phi(j_{\text{can}}, j)$  is the jet most back-to-back with the candidate jet  $j_{\text{can}}$  and is labelled  $j_{\text{btb}}$ . In the parallel selection,  $j_{\text{btb}}$  is  $j_N$ , while  $j_{\text{btb}}$  is  $j_1$  in the anti-parallel selection. The relabelled parallel and anti-parallel topologies are shown in figure 6.27.

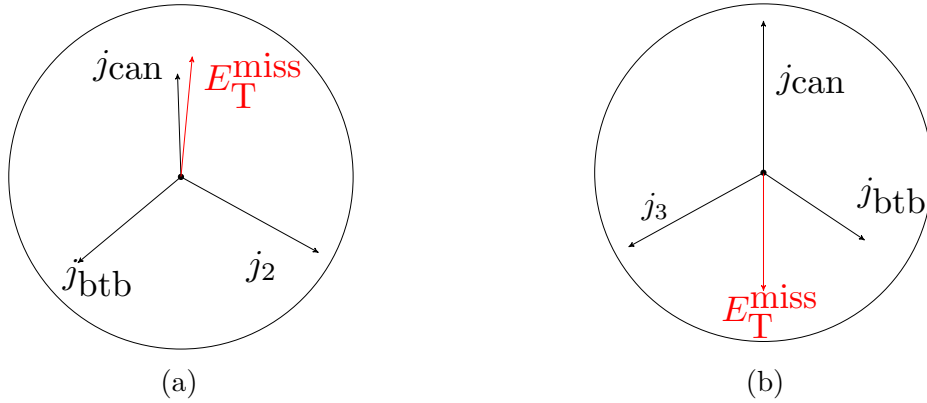


Fig. 6.27 Schematic view of the Mercedes analysis topological configurations for the (a) parallel and (b) anti-parallel cases, relabelled to identify the candidate jet ( $j_{\text{can}}$ ) and  $j_{\text{btb}}$ , which is the jet most back-to-back with  $j_{\text{can}}$ .

Additional isolation requirements are placed on  $j_{\text{btb}}$  to ensure that only  $j_{\text{can}}$  is associated with the  $\vec{E}_T^{\text{miss}}$

$$\pi - |\Delta\phi(j_{\text{btb}}, \vec{E}_T^{\text{miss}})| > \Delta\phi_2^{\text{iso}} \quad (6.25)$$

$$|\Delta\phi(j_{\text{btb}}, \vec{E}_T^{\text{miss}})| > \Delta\phi_2^{\text{iso}} \quad (6.26)$$

where equation 6.25 is utilised in the parallel selection and equation 6.26 is applied to the anti-parallel selection.

Following the angular selection, in which the initially  $p_T$ -sorted jet collection is reordered according to  $\Delta\phi(\text{jet}, \vec{E}_T^{\text{miss}})$ , the candidate jet is then required to pass the minimum jet  $p_T$  requirement defined in table 6.8.

### 6.4.3.3 Modification of the response low-side tail

Pseudo-data produced using jets smeared with a value of  $R_2$  from the low-side tail experiences a downward  $p_T$  fluctuation from the seed jet  $p_T$  and introduces  $\vec{E}_T^{\text{miss}}$  aligned with the jet corresponding to the parallel configuration depicted in figure 6.27a. The procedure for correction of the low-side tail is well documented within Run 1 analyses [135, 136]. The Run 2 procedure presented in this section is based upon the same methodology. Corrections to the low-side tail are generated independently for  $b$ -tagged and  $b$ -veto jets to correctly account for the real  $E_T^{\text{miss}}$  present in  $b$ -jet decay chains. A summary of the methodology for the correction of the low-side tail is given below.

## The *Jet Smearing* Method

---

- The  $R_2$  distribution is plotted for various truth jet  $p_T$  ranges, where the truth  $p_T$  is defined in equation 6.22. The low-side tail region is identified in each truth jet  $p_T$  bin through the use of a *Crystal Ball* function [148].
- A Gaussian function with width  $\sigma_{\text{Gauss}}$  is fitted to the low-side tail distribution.
- The Gaussian function with width  $\sigma_{\text{Gauss}}$  is convoluted with an additional Gaussian function of width  $\sigma_{\text{tail}}$ , modifying the tail of the response. A range of  $\sigma_{\text{tail}}$  values are used to modify the shape of the low-side tail and produce a range of *low-side tail response maps*.
- Collections of pseudo-data are produced using each of the low-side tail response maps.
- The value of  $\sigma_{\text{tail}}$  is extracted from the pseudo-data distribution that when combined with non-QCD MC most closely models the distribution in data in each truth jet  $p_T$  bin of the  $R_2$  distribution. This value is denoted  $\sigma_{\text{tail}}^{\text{optimal}}$ .
- The associated systematic uncertainty of the method (discussed in section 6.5) is taken into account by finding  $\sigma_{\text{tail}}^{\text{high}}$  and  $\sigma_{\text{tail}}^{\text{low}}$  variations of  $\sigma_{\text{tail}}^{\text{optimal}}$ .

The low-side tail region of the jet response is defined using a Crystal Ball function [148] fitted to the MC-derived jet response in the region  $0.0 < R_{\text{MC}} < 1.2$ , where  $R_{\text{MC}}$  is defined by equation 6.1 and constructed as described in section 6.2. The Crystal Ball function is composed of a Gaussian core region with a non-Gaussian low-side tail and is defined as

$$f(x; \alpha, n, \bar{x}, \sigma, N_{\text{CB}}) = N_{\text{CB}} \cdot \begin{cases} \exp\left(-\frac{(x-\bar{x})^2}{2\sigma^2}\right) & \text{for } \frac{x-\bar{x}}{\sigma} > -\alpha \\ A_{\text{CB}} \cdot \left(B_{\text{CB}} - \frac{x-\bar{x}}{\sigma}\right)^{-n} & \text{for } \frac{x-\bar{x}}{\sigma} \leq -\alpha \end{cases} \quad (6.27)$$

where

$$A_{\text{CB}} = \left(\frac{n}{|\alpha|}\right)^n \cdot \exp\left(-\frac{|\alpha|^2}{2}\right) \quad (6.28)$$

$$B_{\text{CB}} = \frac{n}{|\alpha|} - |\alpha| \quad (6.29)$$

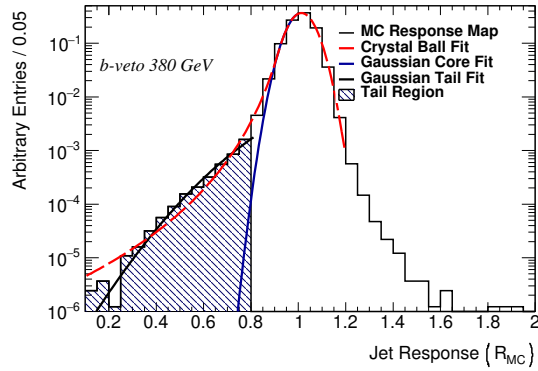
$$C_{\text{CB}} = \frac{n}{|\alpha|} \cdot \frac{1}{n-1} \cdot \exp\left(-\frac{|\alpha|^2}{2}\right) \quad (6.30)$$

## 6.4 Correcting the Initial Response

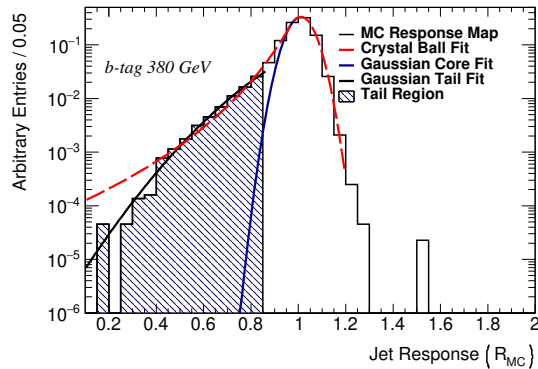
$$D_{\text{CB}} = \sqrt{\frac{\pi}{2}} \left( 1 + \operatorname{erf} \left( \frac{|\alpha|}{\sqrt{2}} \right) \right) \quad (6.31)$$

$$N_{\text{CB}} = \frac{1}{C_{\text{CB}} + D_{\text{CB}}} \quad (6.32)$$

and  $\alpha$ ,  $n$ ,  $\bar{x}$  and  $\sigma$  are fitting parameters and  $N_{\text{CB}}$  represents a normalisation factor [148]. A Crystal ball function is utilised through a fit to the jet response to determine the transition region between the low-side tail region of the jet response and the Gaussian core region. Figure 6.28 shows the Crystal Ball fit to the jet response in the region  $380 \leq p_{\text{T}} < 400$  GeV.



(a)



(b)

Fig. 6.28 One dimensional projections of jet responses constructed using PYTHIA dijet MC simulated events for use with data recorded in 2015 and 2016 for the (a)  $b$ -veto and (b)  $b$ -tag cases in the range  $380 \leq p_{\text{T}} < 400$  GeV.  $R_{\text{MC}}$  is defined by equation 6.1 and constructed as described in section 6.2. Gaussian and Crystal Ball function fits are overlaid. The Crystal Ball function fit over the region  $0.0 < R_{\text{MC}} < 1.2$  (shown in red) includes a transition point between the Gaussian core and non-Gaussian low-side tail of the jet response. The Gaussian fit of the core of the jet response is shown in blue, a Gaussian fit to the low-side tail region of the jet response is shown by the black line.

## The *Jet Smearing* Method

---

The Crystal Ball function in both plots of figure 6.28 is intended to provide a good fit to the Gaussian core region of the jet response and used solely to define the low-side tail of the response as the region of jet response following the Crystal Ball transition point, defined by equation 6.27 as  $x = \bar{x} - \alpha\sigma$ . The upper limit of the tail region (the point nearest the Gaussian core) is defined as  $x = \bar{x} - \alpha\sigma - 0.1$  to ensure the Gaussian tail fit is not applied to the Gaussian core. The study of the jet response transition point confirmed the initial assumption that regions of the response with  $R < 0.8$  are likely to correspond to the low-side tail of the response, with any contamination from the Gaussian-like core of the response being the sub-dominant contribution.

The low-side tail modifications are applied by multiplying the width of the Gaussian fitted to the low-side tail (shown in figure 6.28) by a unitless factor, termed  $\Delta\sigma_{\text{tail}}$ , in each bin of truth jet  $p_T$  of the jet response. A series of low-side tail response maps are produced using  $0.2 \leq \Delta\sigma_{\text{tail}} \leq 1.8$  in increments of  $\Delta\sigma_{\text{tail}} = 0.05$ . Collections of pseudo-data are produced using each of the low-side tail response maps. Figures 6.29 and 6.30 show the effect on the low-side tail of the jet response after varying  $\Delta\sigma_{\text{tail}}$  for a selection of values.

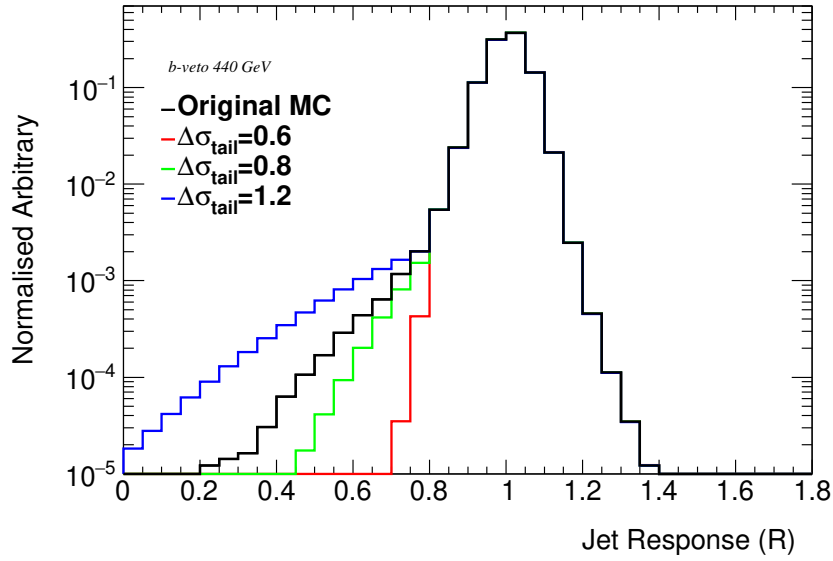


Fig. 6.29 One dimensional projections of low-side tail jet response variations for three values of  $\Delta\sigma_{\text{tail}}$  plotted alongside the original jet response with unmodified low-side tail in the range  $420 \leq p_T < 440$  GeV for events with a  $b$ -jet veto.

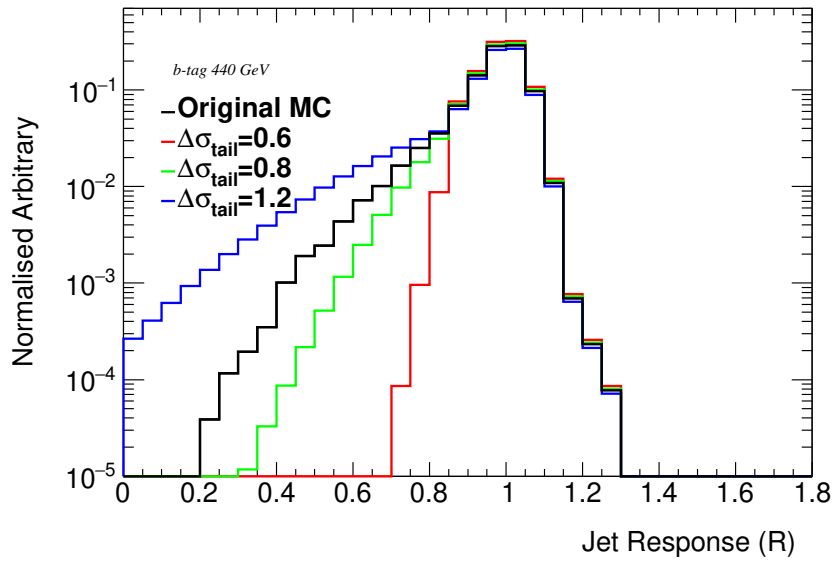


Fig. 6.30 One dimensional projections of low-side tail jet response variations for three values of  $\Delta\sigma_{\text{tail}}$  plotted alongside the original jet response with unmodified low-side tail in the range  $420 \leq p_T < 440$  GeV for events with  $b$ -jets.

Distributions of  $R_2$  (defined in equation 6.24) are plotted separately for the  $b$ -veto and  $b$ -tagged cases using the entire collection of response maps with a varied low-side

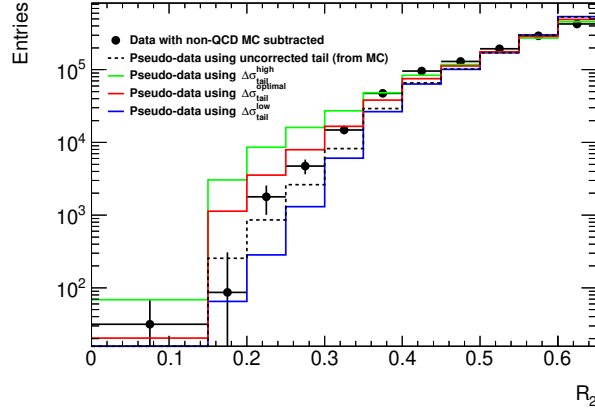
## The *Jet Smearing* Method

---

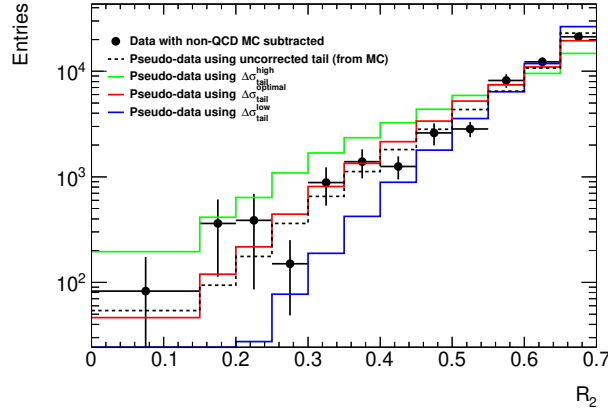
tail over the truth jet  $p_T$  ranges specified in table 6.12 and table 6.13, respectively. Optimal values (with high and low variations) for the tail modification are chosen from a combination of the quality of a  $\chi^2$  fit in the tail region (shown in figures 6.31 and 6.32) and overall agreement between data and the combined estimate of pseudo-data and non-QCD MC simulated events in distributions of  $R_2$ , shown in figures 6.33 and 6.34. The ‘data’ considered in figures 6.31 and 6.32 has  $W + \text{jets}$ ,  $Z + \text{jets}$ ,  $t\bar{t}$  and single top MC simulated events (the dominant contributions from non-multijet sources) subtracted such that purely multijet events in data are compared with the multijet estimate provided by the pseudo-data, mirroring the method utilised in Run 1 [136]. In the event of this subtraction causing a negative number of events in a truth  $p_T$  bin, the bin contents were combined with the next bin until a positive number of events was present in the bin. The pseudo-data distribution is then normalised to the modified ‘multijet data’ distribution, denoted ‘data with non-QCD MC subtracted’ in figures 6.31 and 6.32. The contribution from multijet MC events is shown in orange in figures 6.33 and 6.34 for comparison purposes only and is not included in any estimate that follows. Additionally, the hatched red band in figures 6.33 and 6.34 shows the combined statistical uncertainty and the systematic uncertainty arising from the high and low tail variation.

The non-continuous nature of the data distribution in some regions within figures 6.31 and 6.32 is due to the presence of highly prescaled events in certain bins of the distribution. This feature caused the results of the  $\chi^2$  fit to become unreliable, and so a combination of the fit result and a by-eye comparison was employed to determine the optimal and systematic tail variations.

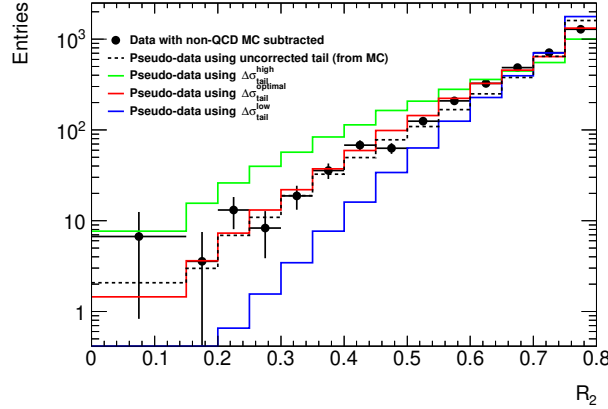
## 6.4 Correcting the Initial Response



(a)  $b$ -veto, truth jet  $100 \leq p_T < 300$  GeV

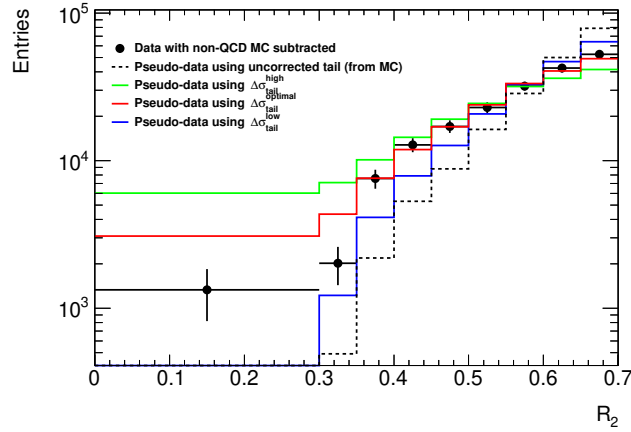


(b)  $b$ -veto, truth jet  $300 \leq p_T < 600$  GeV

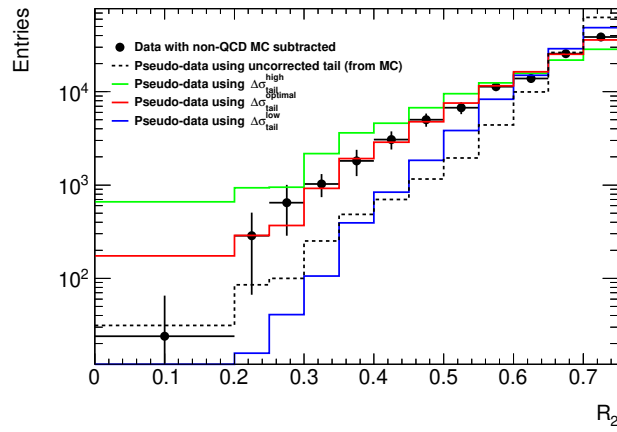


(c)  $b$ -veto, truth jet  $600 \leq p_T < 2000$  GeV

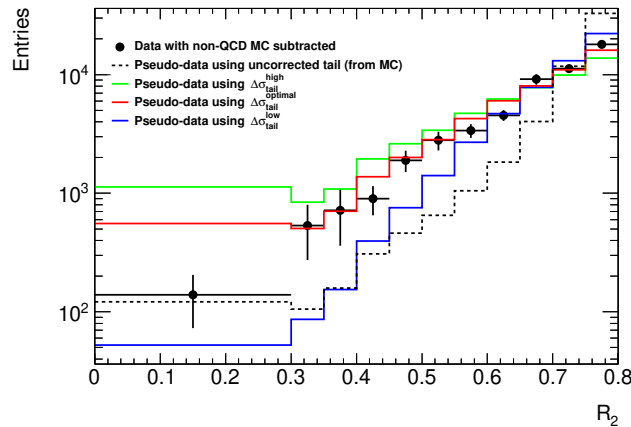
Fig. 6.31 Normalised low-side tail regions extracted from  $R_2$  distributions for events with a  $b$ -jet veto for truth jet  $p_T$  (a)  $100 \leq p_T < 300$  GeV, (b)  $300 \leq p_T < 600$  GeV and (c)  $600 \leq p_T < 2000$  GeV. The tail shape providing the best quality agreement with data was identified as the optimal response (in red), with a high and low systematic variations shown in green and blue, respectively.



(a)  $b$ -tag, truth jet  $100 \leq p_T < 200$  GeV



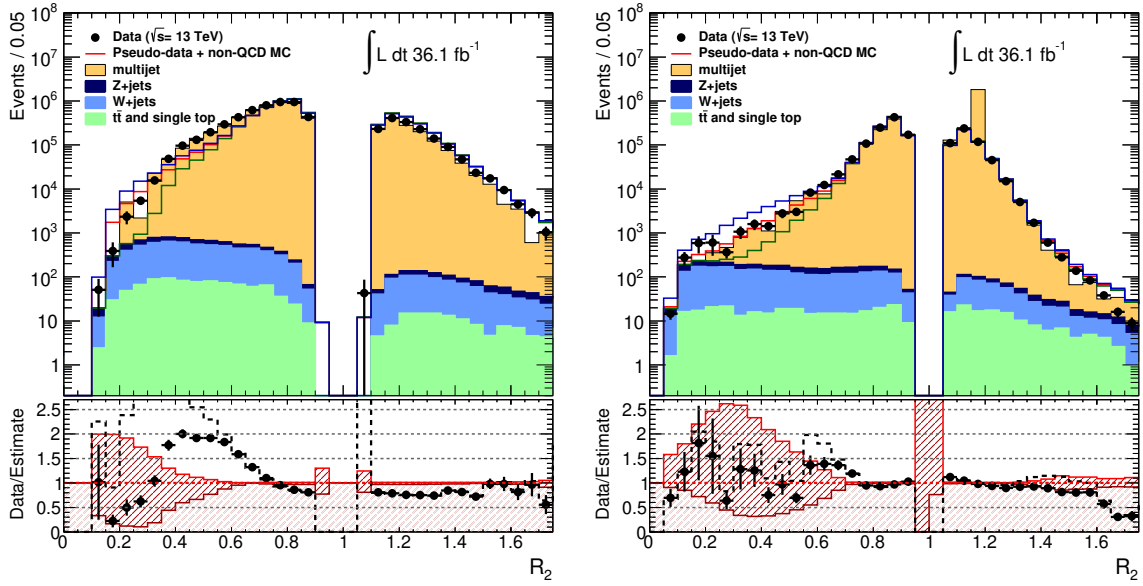
(b)  $b$ -tag, truth jet  $200 \leq p_T < 300$  GeV



(c)  $b$ -tag, truth jet  $300 \leq p_T < 2000$  GeV

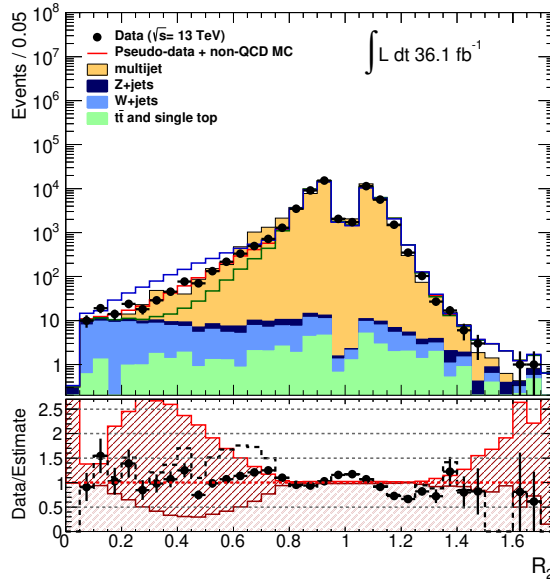
Fig. 6.32 Normalised low-side tail regions extracted from  $R_2$  distributions for events with  $b$ -jets for truth jet  $p_T$  (a)  $100 \leq p_T < 200$  GeV, (b)  $200 \leq p_T < 300$  GeV and (c)  $300 \leq p_T < 2000$  GeV. The tail shape providing the best quality agreement with data was identified as the optimal response (in red), with a high and low systematic variations shown in green and blue, respectively.

## 6.4 Correcting the Initial Response



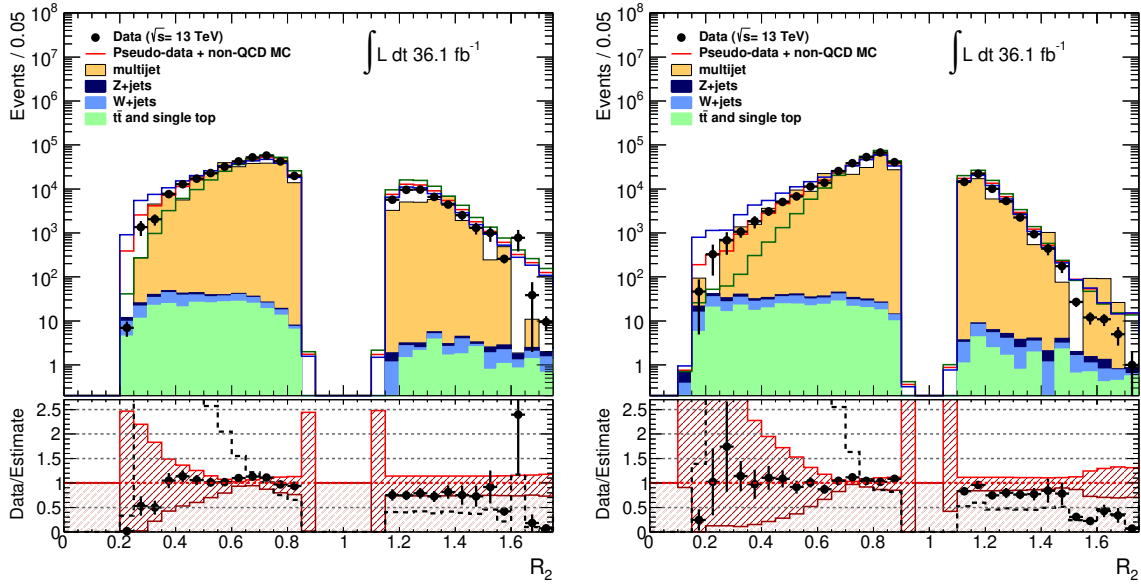
(a)  $b$ -veto, truth jet  $100 \leq p_T < 300$  GeV

(b)  $b$ -veto, truth jet  $300 \leq p_T < 600$  GeV



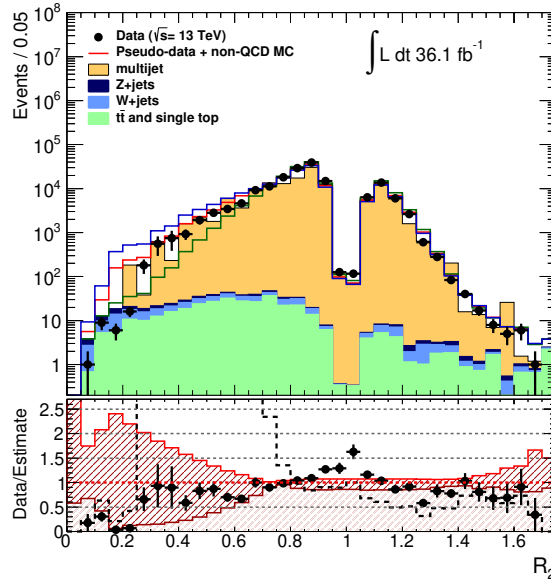
(c)  $b$ -veto, truth jet  $600 \leq p_T < 2000$  GeV

Fig. 6.33 Distribution of  $R_2$  for the candidate jet in events with a  $b$ -jet veto using data recorded in 2015 and 2016 for truth jet  $p_T$  (a)  $100 \text{ GeV} \leq p_T < 300$  GeV, (b)  $300 \text{ GeV} \leq p_T < 600$  GeV and (c)  $600 \text{ GeV} \leq p_T < 2000$  GeV. The combined pseudo-data and non-QCD MC estimate, shown in red, was derived using the ‘optimal’ low-side tail response established for the truth jet  $p_T$  region of interest. High and low variations used in place of the optimal low-side tail response are shown with blue and green lines, respectively. Multijet MC simulated events are shown in orange purely for comparison with the estimate derived from the use of pseudo-data and does not feature in the ratio plot in the lower portion of the figure. The black dotted line within the ratio plot shows the equivalent data/estimate distribution when using an unmodified low-side tail.



(a)  $b$ -tag, truth jet  $100 \leq p_T < 200$  GeV

(b)  $b$ -tag, truth jet  $200 \leq p_T < 300$  GeV



(c)  $b$ -tag, truth jet  $300 \leq p_T < 2000$  GeV

Fig. 6.34 Distribution of  $R_2$  for the candidate jet in events with  $b$ -jets using data recorded in 2015 and 2016 for truth jet  $p_T$  (a)  $100 \leq p_T < 200$  GeV, (b)  $200 \leq p_T < 300$  GeV and (c)  $300 \leq p_T < 2000$  GeV. The combined pseudo-data and non-QCD MC estimate, shown in red, was derived using the ‘optimal’ low-side tail response established for the truth jet  $p_T$  region of interest. High and low variations used in place of the optimal low-side tail response are shown with blue and green lines, respectively. Multijet MC simulated events are shown in orange purely for comparison with the estimate derived from the use of pseudo-data and does not feature in the ratio plot in the lower portion of the figure. The black dotted line within the ratio plot shows the equivalent data/estimate distribution when using an unmodified low-side tail.

## 6.4 Correcting the Initial Response

The values of  $\Delta\sigma_{\text{tail}}$  extracted for the optimal, high and low cases for events with  $b$ -jets and events with a  $b$ -jet veto in the relevant truth jet  $p_T$  ranges are shown in tables 6.12 and 6.13, respectively.

Table 6.12 Values of the unitless factor  $\Delta\sigma_{\text{tail}}$  producing optimal agreement between data and MC simulated events with a  $b$ -jet veto, with high and low variations taking into account uncertainties arising from correcting the low-side tail of the jet response.

Truth jet $p_T$ [GeV]	$\Delta\sigma_{\text{tail}}^{\text{optimal}}$	$\Delta\sigma_{\text{tail}}^{\text{high}}$	$\Delta\sigma_{\text{tail}}^{\text{low}}$
[100, 300]	1.25	1.45	0.95
[300, 600]	1.10	1.30	0.90
[600, 2000]	1.10	1.30	0.90

Table 6.13 Values of  $\Delta\sigma_{\text{tail}}$  producing optimal agreement between data and MC simulated events with  $b$ -jets, with high and low variations taking into account uncertainties arising from correcting the low-side tail of the jet response.

Truth jet $p_T$ [GeV]	$\Delta\sigma_{\text{tail}}^{\text{optimal}}$	$\Delta\sigma_{\text{tail}}^{\text{high}}$	$\Delta\sigma_{\text{tail}}^{\text{low}}$
[100, 200]	1.20	1.40	0.90
[200, 300]	1.00	1.15	0.80
[300, 2000]	1.05	1.15	0.85

Optimally tail-corrected jet response maps were then constructed using the parameters shown in tables 6.12 and 6.13 for  $b$ -veto and  $b$ -tag events and included the high and low systematic variations which were interpreted as weights within the software implementation of the method. The combination of the set of tail-corrected response maps and any applicable corrections to the Gaussian central region of the jet response or to the pseudo-data  $\phi$  distribution represents the complete calibration of the jet smearing methodology.

## 6.5 Jet Smearing Uncertainties

Several sources of uncertainty arising from a combination of statistical and systematic sources due to the use of the jet smearing method and from its calibration to data are discussed in this section.

### 6.5.1 Seed Statistics

Jet Smearing selects  $n$  seed events, smearing them  $N_{\text{smear}}$  times to produce  $N_{\text{tot}} = n_{\text{seed}} \times N_{\text{smear}}$  pseudo-data events which are used in place of MC simulated dijet events to produce an estimate of the multijet background. A treatment of the statistical uncertainty arising from using a finite number of seed events is provided within [134, 136] and is summarised here.

After smearing  $i$  seed events, a distribution of an event observable ( $E_T^{\text{miss}}$  or similar) will have  $N_j$  events in histogram bin  $j$ . The weighted contribution to the  $j^{\text{th}}$  histogram bin due to the  $i^{\text{th}}$  seed event,  $w_{ij}$ , is defined as

$$w_{ij} = \frac{N_{ij}}{N_{\text{smear}}} \quad (6.33)$$

where  $N_{ij}$  is the number of events in the  $j^{\text{th}}$  histogram bin due to the  $i^{\text{th}}$  seed event.

As the number of smearing applications  $N_{\text{smear}}$  approaches infinity, the probability density for a weighted contribution  $w$  in the  $j^{\text{th}}$  bin of the histogram, normalised to  $N_{\text{tot}}$ , is given by

$$\rho_j(w) = \frac{1}{n_{\text{seed}}} \sum_i \delta(w - w_{ij}) \quad (6.34)$$

where  $\delta(w)$  is the Dirac delta function. The total weighted contribution to the  $j^{\text{th}}$  bin is given by

$$p_j = \int_0^1 w \rho_j(w) dw \quad (6.35)$$

$$= \frac{1}{n_{\text{seed}}} \sum_i w_{ij} \quad (6.36)$$

with a standard deviation of

$$\sigma(p_j) = \sqrt{\int w^2 \rho_j(w) dw} \quad (6.37)$$

$$= \frac{1}{n_{\text{seed}}} \sqrt{\sum_i w_{ij}^2} \quad (6.38)$$

Substituting equation 6.33 into equation 6.37 yields

$$\sigma_{\text{seed}}(p_j) = \frac{1}{N_{\text{tot}}} \sqrt{\sum_i N_{ij}^2} \quad (6.39)$$

## 6.5.2 Smearing Statistics

A treatment of the statistical uncertainty arising from using a finite number of smears,  $N_{\text{smear}}$ , is once again established within [134, 136] and is summarised here. A statistical uncertainty arises from the application of a finite  $N_{\text{smear}}$  in the limit of large  $n_{\text{seed}}$ . Smearing the  $i^{\text{th}}$  seed event produces  $N_{ij}$  events in the  $j^{\text{th}}$  bin of a pseudo-data distribution

$$N_{ij} = N_{\text{smear}} w_{ij} \quad (6.40)$$

where  $w_{ij}$  is a weight associated with the pseudo-data event that enters the bin  $j$  due to the  $i^{\text{th}}$  seed event. As each smearing is independent of any other smearing in an event, the distribution of events is assumed to be Poissonian, with  $\sigma_{ij}(N_{ij}) = \sqrt{N_{ij}}$ . Considering all selected seed events, the variance of the number of pseudo-data events in histogram bin  $j$ ,  $N_j$ , is given by

$$\sigma_j^2(N_j) = \sum_i \sigma_{ij}^2(N_{ij}) = \sum_i N_{ij} \quad (6.41)$$

## The Jet Smearing Method

---

The standard deviation of  $N_j$  is normalised to the total number of events such that the uncertainty on the number of events in the  $j^{\text{th}}$  histogram bin of a normalised distribution is given by:

$$\sigma_{\text{smear}}(p_j) = \frac{1}{N_{\text{tot}}} \sqrt{\sum_i N_{ij}} \quad (6.42)$$

and setting  $N_{\text{smear}} \sim \mathcal{O}(1000)$  causes the statistical uncertainty associated with using finite smears to be negligible.

### 6.5.3 Total Statistical Uncertainty

The uncertainties arising from using a finite number of seed events and a finite number of smears in normalised distributions can be combined by summation of the variances in equations 6.39 and 6.42:

$$\sigma(p_j)_{\text{total stat.}}^2 = \sigma(p_j)_{\text{seed}}^2 + \sigma(p_j)_{\text{smear}}^2 \quad (6.43)$$

$$= \left( \frac{1}{N_{\text{tot}}^2} \sum_i N_{ij}^2 \right) + \left( \frac{1}{N_{\text{tot}}^2} \sum_i N_{ij} \right) \quad (6.44)$$

the full statistical uncertainty is therefore

$$\sigma(p_j)_{\text{total stat.}} = \frac{1}{N_{\text{tot}}} \sqrt{\sum_i N_{ij}(N_{ij} + 1)} \quad (6.45)$$

### 6.5.4 Seed Selection

A bias towards high leading jet  $p_T$  seed events was observed in the early stages of Run 2 when requirements were placed upon a  $E_T^{\text{miss}}$ -significance  $S$  defined as in equation 6.3 leading to the adoption of the definition of the variable shown in equation 6.4. Modifying the definition of the variable removed the large bias observed as shown in figure 6.7. However, to ensure that any uncertainty arising from the choice of seed selection was taken into account, the seed selection requirement was varied upwards and downwards in a *high* and *low* variation, representing an increase or decrease in the value of the seed selection requirement. This systematic uncertainty was considered

optional for analyses and was not applied in all instances of use of the jet smearing software.

### 6.5.5 Low-side Tail Shape Selection

Values of  $\Delta\sigma_{\text{tail}}^{\text{high}}$  and  $\Delta\sigma_{\text{tail}}^{\text{low}}$  were chosen to cover the entire range of statistical uncertainties of data points in figures 6.31 and 6.32 and to account for the differences observed in data/estimate agreement in  $R_2$  distributions due to the selected tail shape. In some cases a larger range is covered due to the non-continuous nature of the distribution due to highly prescaled events entering the low-side tail region with comparatively large statistical uncertainties. The values used for the high and low tail variations are shown in tables 6.12 and 6.13. Response maps were produced including the optimal, high and low tail modifications, from which an uncertainty was extracted from the difference in observed events between the high or low variation and the optimal value.

### 6.5.6 Gaussian Core Correction

In the event that corrections to the Gaussian core of the jet response are required, a systematic uncertainty is introduced by adding high and low variations of  $\sigma_{\text{correction}}(p_T)$ , defined in equation 6.13. Variations of  $\sigma_{\text{correction}}(p_T) \pm 0.05$  are used based on studies performed during Run 1 [136]. Gaussian core correction was observed to be of negligible importance during early Run 2, as discussed in section 6.4.1.2.

## 6.6 Origin of $E_T^{\text{miss}}$ in 0-lepton SUSY analyses

One of the central assumptions of the Jet Smearing technique is that the main source of fake  $E_T^{\text{miss}}$  in SUSY analyses searching for fully hadronic final states with high- $E_T^{\text{miss}}$  is from the mismeasurement of jets and from undetected particles arising from the decay of heavy flavour jets. Both cases are shown in figure 6.35 and are discussed in section 6.1.

This study was motivated by a concern that incorrectly applied event cleaning procedures such as the removal of jets originating from pile-up events and the removal

## The *Jet Smearing* Method

of jets failing requirements on JVT (discussed in section 5.1.2.2) could introduce a significant amount of  $E_T^{\text{miss}}$  in the final states of analyses.

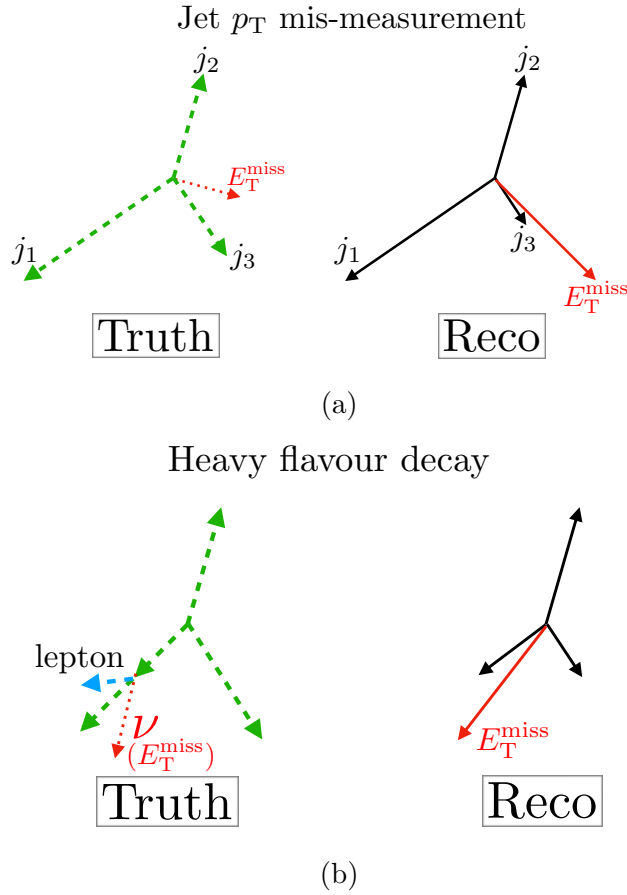


Fig. 6.35 Diagrams of the assumed dominant sources of fake  $E_T^{\text{miss}}$  in regions that the *JetSmearing* tool is designed for usage within. Mismeasurement of the  $p_T$  of one jet is shown in (a) although this may occur for multiple jets in an event. The decay of a heavy flavour jet is shown in (b), which can lead to increased  $E_T^{\text{miss}}$  if the decay products are not reconstructed in the detector. ‘Truth’ refers to particle-level Monte Carlo simulated events, while ‘Reco’ refers to the event as reconstructed by the ATLAS detector in data or MC simulated events.

### 6.6.1 Alternative $E_T^{\text{miss}}$ definitions

To probe the origin of the  $E_T^{\text{miss}}$  in kinematic regions in which the jet smearing methodology is commonly used, the standard  $E_T^{\text{miss}}$  calculation in equation 5.11 was modified with the reconstructed jet collection replaced by a collection of truth jets that could be topologically linked to reconstructed jets.

## 6.6 Origin of $E_T^{\text{miss}}$ in 0-lepton SUSY analyses

---

Truth and reconstructed jet matching in this analysis was intentionally similar to the method used in response map creation for the Jet Smearing software tool, described in section 6.2, to enable reliable extrapolation of any conclusions from this study to the Jet Smearing use case. The two step procedure for jet matching was as follows:

- Initially the truth jet was redefined to include any truth neutrinos and truth muons within  $\Delta R < 0.4$  of the truth jet by adding their four momenta. This step ensured that the truth jets considered mirrored reconstructed jets as much as possible. The addition of truth electron four momenta was not necessary as truth jets are constructed at the particle energy scale from any final-state particles with a lifetime  $c\tau > 10$  mm with the exclusion of any muons, neutrinos or pile-up activity [102].
- The truth jet is matched with a reconstructed jet if they are found within  $\Delta R < 0.3$  of one another, where  $\Delta R$  is defined in equation 3.7. Truth jets were discarded if multiple reconstructed jets were matched, such that the pair were uniquely associated.

Reconstructed  $E_T^{\text{miss}}$  (referred to as **Reco  $E_T^{\text{miss}}$** ) was then calculated per event with the contribution from reconstructed jets removed and replaced with the matched truth jet collection. The  $E_T^{\text{miss}}$  variable recalculated in this manner was termed **Reco  $E_T^{\text{miss}}$  TruthMatched Jets**.

Simplified  $E_T^{\text{miss}}$  variables were calculated using reconstructed jets. These variables were expected to produce a reduced contribution in the  $E_T^{\text{miss}}$  distribution tails due to fake- $E_T^{\text{miss}}$  when compared to the standard  $E_T^{\text{miss}}$  definition discussed in section 5.1.6. Simplified  $E_T^{\text{miss}}$  definitions were created using either the calorimeter or track-based soft term and were defined as follows:

- Remove jet JVT variable requirements
- Exclude electrons, photons and taus from the  $E_T^{\text{miss}}$  calculation, such that the  $E_T^{\text{miss}}$  is calculated with calorimeter energy deposits and muons
- Pile-up causes broadening of the core of the  $E_T^{\text{miss}}$  distribution, but does not contribute to the tails of the  $E_T^{\text{miss}}$  distribution and so effects due to pile-up removal of physics objects were not considered for simplified- $E_T^{\text{miss}}$  cases.

## The *Jet Smearing* Method

---

By considering all physics objects as either jets or muons, the introduction of  $E_T^{\text{miss}}$  via electron-jet overlap removal is avoided. In addition, the removal of the JVT variable on jets ensured that no fake  $E_T^{\text{miss}}$  was introduced through the removal of jets failing to meet this criterion. Direct comparisons of the  $E_T^{\text{miss}}$  built with both soft terms effectively shows the Run 1 scenario versus the Run 2 scenario and if any fake  $E_T^{\text{miss}}$  is introduced by using a track-based soft term.

### 6.6.2 Kinematic regions investigated

The regions used in this study were designed to be similar to kinematic regions used in the analyses where Jet Smearing is most useful — high  $E_T^{\text{miss}}$  regions with zero leptons and jets. Four regions were defined with a naming convention corresponding to the analysis pre-selection that inspired the region. The regions considered were inspired by the following analyses:

- *Multi- $b$  analysis*: a search for pair production of gluinos decaying to produce final states of  $b$ -jets and  $E_T^{\text{miss}}$  [139, 149]
- *Sbottom analysis*: the fully hadronic portion of a search for pair production of stop and sbottom squarks decaying to final states of  $b$ -tagged jets and  $E_T^{\text{miss}}$  [141]
- *Strong-0L analysis*: a search for pair production of squarks and gluinos decaying to fully hadronic final states of jets and  $E_T^{\text{miss}}$  [129]

A generic *inclusive* region with looser requirements than the analysis-specific regions was also included to illustrate the effects of event requirements on  $E_T^{\text{miss}}$ . Table 6.14 fully defines each region considered.  $N_{\text{jet}}$  refers to the number of fully calibrated anti- $k_t$  EMTopo jets with distance parameter  $\Delta R = 0.4$ ,  $|\eta| < 2.8$  and  $p_T \geq 20$  GeV passing quality requirements.  $N_{\text{jet}(35)}$  refers to the subset of  $N_{\text{jet}}$  where an additional  $p_T > 35$  GeV requirement is placed on jets. A veto is placed on muons and electrons passing `baseline` requirements (isolated with  $p_T > 7$  GeV,  $|\eta| < 2.7 (< 2.47)$  for muons (electrons)) and surviving the overlap removal procedure in all regions considered. Requirements were placed on reconstructed  $E_T^{\text{miss}}$  and not on the alternative  $E_T^{\text{miss}}$  variables detailed in section 6.6.1. Reconstructed and truth objects were all taken from PYTHIA 8 dijet MC.

## 6.6 Origin of $E_T^{\text{miss}}$ in 0-lepton SUSY analyses

Table 6.14 Event selections placed on reconstructed objects used to construct the kinematic regions used to determine  $E_T^{\text{miss}}$  origin. Null entries correspond to no requirement being placed on the corresponding variable.

Variable	Inclusive High-HT	Multib-like	Sbottom-like	Strong $0\ell$ -like
$N_{\text{leptons}}$	0	0	0	0
$N_{\text{b-jet}}$	—	$\geq 3$	2	—
$N_{\text{jet}}$	$\geq 2$	$\geq 4$	—	$\geq 2$
$N_{\text{jet}(35)}$	—	—	$\leq 4$	—
$p_T(j_1)$	—	—	$> 130 \text{ GeV}$	$> 200 \text{ GeV}$
$p_T(j_2)$	$> 50 \text{ GeV}$	—	—	—
$p_T(j_4)$	—	$> 50 \text{ GeV}$	$< 50 \text{ GeV}$	$> 50 \text{ GeV}$
$H_T$	$> 200 \text{ GeV}$	—	—	$> 200 \text{ GeV}$
$E_T^{\text{miss}}$	$\geq 200 \text{ GeV}$			
$\Delta\phi(j_{1-4}, E_T^{\text{miss}})_{\text{min}}$	—	—	—	$> 0.2$

### 6.6.3 Results

Distributions of  $\text{Reco } E_T^{\text{miss}}$   $\text{TruthMatched Jets}$  were plotted as a function of the  $\text{Reco } E_T^{\text{miss}}$  in figure 6.36. Events lying on or with  $y$ -values above the leading diagonal of this plot (where  $y = x$  and shown by a black line) were classified as potentially arising from incorrect jet removal (either from overlap removal or JVT jet removal). Events with large  $\text{Reco } E_T^{\text{miss}}$  and low  $\text{Reco } E_T^{\text{miss}}$   $\text{TruthMatched Jets}$  values were consistent with originating from jet mismeasurement or heavy flavour jet decay.

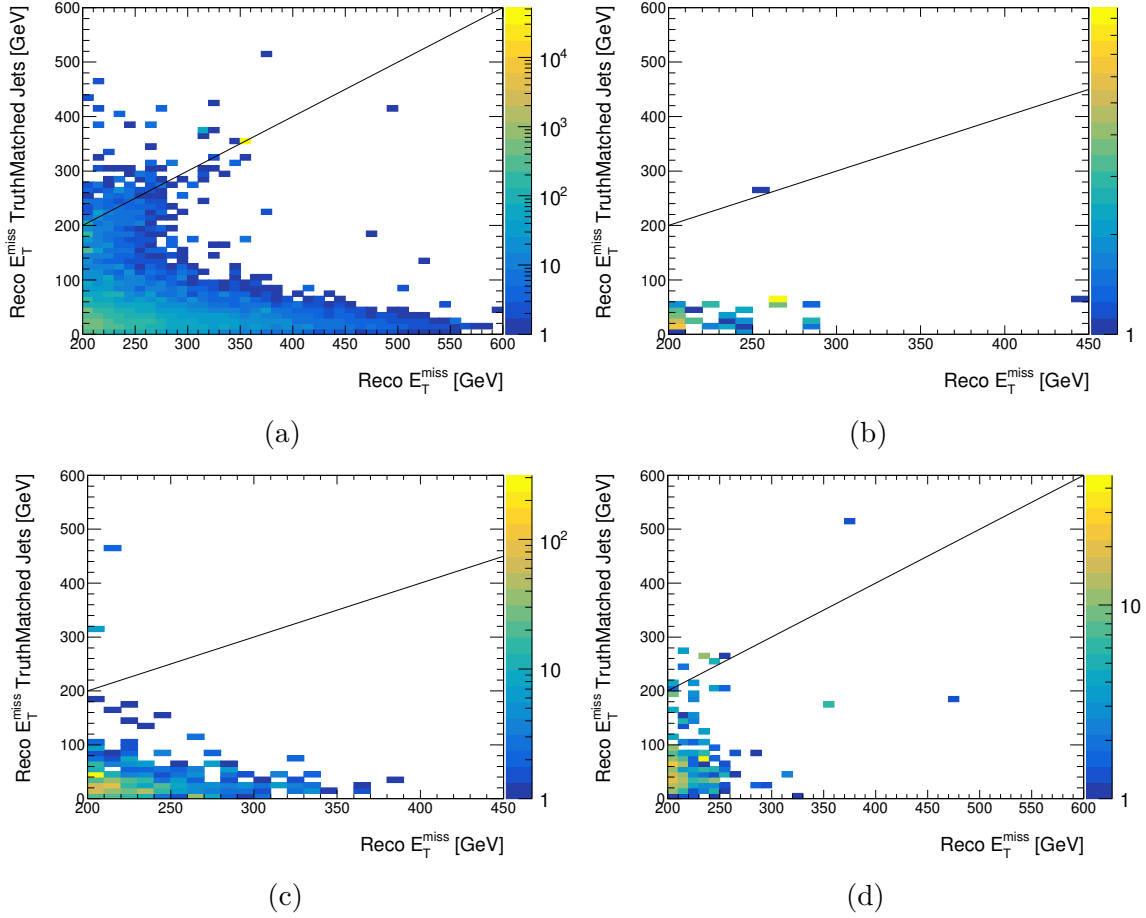


Fig. 6.36 2D plot showing reconstructed  $E_T^{\text{miss}}$  on the  $x$ -axis plotted against a modified version of the reconstructed  $E_T^{\text{miss}}$  on the  $y$ -axis. The modified reconstructed  $E_T^{\text{miss}}$  was recalculated by replacing the reconstructed jet collection with truth jets. Truth jets in this case include any truth muons and neutrinos within  $\Delta R < 0.4$  of the truth jet. Truth jets were only used in the case that they were within  $\Delta R < 0.3$  of exactly one reconstructed jet in the event. Truth jets within  $\Delta R < 0.3$  of multiple reconstructed jets were discounted. Figure (a) shows the **Inclusive High-HT** region, (b) shows the **Multib-like** region, (c) shows the **Sbottom-like** region and (d) shows the **Strong  $0\ell$ -like** kinematic region defined in table 6.14.

All regions show a large proportion of events with low **Reco  $E_T^{\text{miss}}$  TruthMatched Jets** and high reconstructed  $E_T^{\text{miss}}$  due to the mismeasurement of jet  $p_T$ . This effect is enhanced in figures 6.36b and 6.36c which require the presence of  $b$ -tagged jets, as these events can include additional  $E_T^{\text{miss}}$  from the decay of heavy flavour jets.

Distributions of the reconstructed  $E_T^{\text{miss}}$  are also compared with the simplified  $E_T^{\text{miss}}$  (described in section 6.6.1) in figure 6.37.

## 6.6 Origin of $E_T^{\text{miss}}$ in 0-lepton SUSY analyses

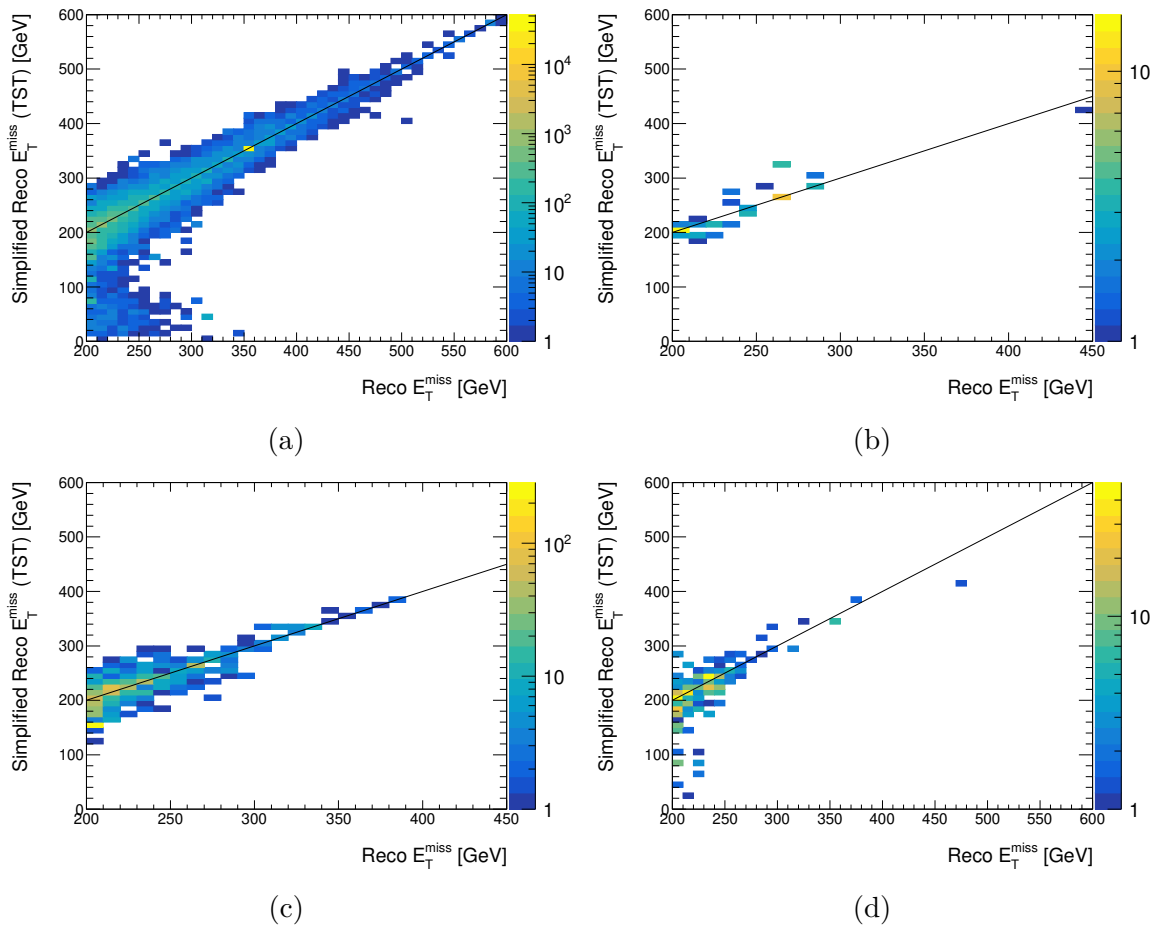


Fig. 6.37 2D plot showing reconstructed  $E_T^{\text{miss}}$  on the  $x$ -axis plotted against a simplified of the reconstructed  $E_T^{\text{miss}}$  on the  $y$ -axis defined in section 6.6.1. The simplified reconstructed  $E_T^{\text{miss}}$  is built using jets, muons and a track-based soft term with the omission of a JVT requirement on low- $p_T$  jets. Figure (a) shows the Inclusive High-HT region, (b) shows the Multib-like region, (c) shows the Sbottom-like region and (d) shows the Strong  $0\ell$ -like kinematic region defined in table 6.14.

This simplified  $E_T^{\text{miss}}$  is calculated using exclusively reconstructed jets and muons with a track-based soft term and omits any removal of jets failing a JVT requirement. Both effects serve to eliminate any potential incorrect removal of jets (and introduction of  $E_T^{\text{miss}}$ ) due to electron-jet overlap removal and JVT-jet removal. The observed presence of a majority of events on the leading diagonal in figure 6.37 in this case shows a jet-dominated definition of  $E_T^{\text{miss}}$  matching the original definition which takes into account all reconstructed physics objects and includes the removal of jets failing to meet JVT requirements. The equivalence of the two variables in the kinematic regions investigated can be interpreted as the result of the dominant source of fake

## The Jet Smearing Method

$E_T^{\text{miss}}$  introduced in the event being due to the mismeasurement of jets or the decay of heavy flavour jets.

The effect of the introduction of a track-based soft term in the  $E_T^{\text{miss}}$  definition for Run 2 as opposed to a cell-based soft term (as used for Run 1) is shown for all regions in figure 6.38.

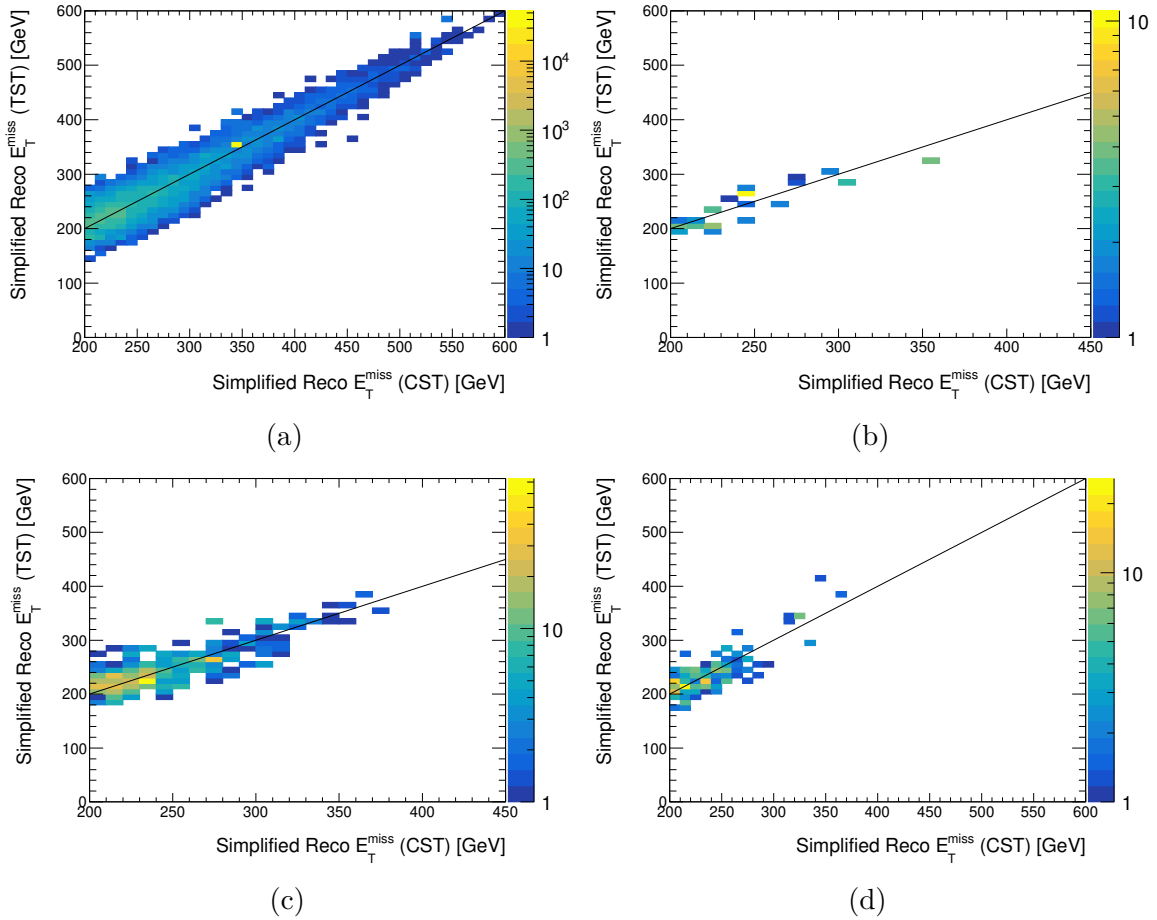


Fig. 6.38 2D plot comparing two simplified  $E_T^{\text{miss}}$  definitions described in section 6.6.1. The simplified reconstructed  $E_T^{\text{miss}}$  is built using jets, muons and a track-based (cell-based) soft term TST (CST) with the omission of a JVT requirement on low- $p_T$  jets. Figure (a) shows the **Inclusive High-HT** region, (b) shows the **Multib-like** region, (c) shows the **Sbottom-like** region and (d) shows the **Strong  $0\ell$ -like** kinematic region defined in table 6.14.

Any significant deviation from the leading diagonal would identify an introduction of  $E_T^{\text{miss}}$  due to the change in definition of the soft term between the two simplified  $E_T^{\text{miss}}$  definitions. In all regions there is very little difference between the two  $E_T^{\text{miss}}$  def-

initions, and so it could not be concluded that the move to a track based soft term was responsible for the introduction of significant  $E_T^{\text{miss}}$  within the regions in which Jet Smearing is designed for use.

### 6.6.4 Conclusion

An investigation into the origin of  $E_T^{\text{miss}}$  within several kinematic regions suitable for the Jet Smearing methodology was presented. Jet Smearing has historically assumed that the dominant source of  $E_T^{\text{miss}}$  within fully hadronic and high- $E_T^{\text{miss}}$  final states is due to the mismeasurement of jets in addition to the decay of heavy flavour jets. The results presented in section 6.6 confirm this assumption. Figure 6.38 demonstrates that no significant  $E_T^{\text{miss}}$  is introduced through the use of a track based soft term in  $E_T^{\text{miss}}$  definitions. Additionally, figure 6.37 confirms that no significant  $E_T^{\text{miss}}$  is introduced through the application of electron-jet overlap removal or the removal of jets failing to meet JVT requirements in the specific kinematic regions considered.

## 6.7 Summary

This chapter introduced the Jet Smearing method for estimation of the QCD multijet background in searches for new physics. SUSY analyses discussed in the following chapters used the Jet Smearing method to estimate the multijet background in dedicated control regions before extrapolating their estimate to regions enriched in signal events. Dijet  $\phi$  corrections were provided to analyses for use with 2015 and 2016 data, along with suggested systematic variations of the seed event selection variable  $S$ . Response maps with a modified low-side tail and high/low systematic variations were made available to analyses, but their successful performance could not be sufficiently verified in time for the analyses to include them in their estimate.

Section 6.2 described the jet response construction procedure. Section 6.3 described the process of defining a seed selection to select well-measured events on which Jet Smearing was performed to produce collections of pseudo-data. Section 6.4 described the dedicated calibration analyses that correct the initial MC-derived jet response to model the behaviour of data events. Section 6.5 considered the statistical and systematic

## The *Jet Smearing* Method

---

uncertainties that arise from using the Jet Smearing technique and discussed the ways in which they are taken into consideration.

Finally, section 6.6 explored the origin of missing transverse momentum in the kinematic regions for which jet smearing was designed to operate within, testing a central assumption of the technique.

# Chapter 7

## Implementation of Jet Smearing in ATLAS SUSY Searches

This chapter describes two searches for supersymmetry using data recorded in 2015 and 2016. The first analysis, referred to in this chapter as the ‘Strong-0 $\ell$ ’ analysis, searched for the strong production of supersymmetry with pair production of squarks and gluinos decaying to final states of 2-6 jets,  $E_T^{\text{miss}}$  and an absence of electrons and muons. While this analysis reported its findings at various stages throughout the ongoing Run 2 data taking campaign, this chapter will focus on the analysis published in December 2017 using the 36.1 fb $^{-1}$  dataset [129], expanding upon the previously published analysis using 3.5 fb $^{-1}$  of  $\sqrt{s} = 13$  TeV data [150]. The Strong-0 $\ell$  analysis contains two sub-analyses. The author’s contribution to the development and calibration of the Jet Smearing software package targeted the sub-analysis using the effective mass  $m_{\text{eff}}$  as a discriminating variable used to construct signal regions. The Strong-0 $\ell$  analysis discussed in this chapter refers solely to this area of the analysis and represents the benchmark analysis for which the Jet Smearing technique, discussed in chapter 6, was calibrated to data. As a member of the analysis team, the author worked closely with the analysis to provide input files and calibrations with which the multijet background estimate was generated in the control, validation and signal regions of the analysis.

The second analysis described in this chapter is referred to as the ‘Sbottom’ analysis and searches for the direct production of the supersymmetric partners of the  $b$  and  $t$  quarks, the  $\tilde{b}$  and  $\tilde{t}$  squarks, with one final detected state consisting of 2  $b$ -tagged jets

and  $E_T^{\text{miss}}$  within the detector [141]. The author worked on this analysis to provide an estimate of the multijet contribution to events in dedicated control regions using the Jet Smearing software tool along with providing calibrations of the input jet responses to data for the analysis.

### 7.1 Analysis Motivation

The Strong- $0\ell$  analysis searches for the decay products of strongly produced SUSY particle pairs assuming conservation of  $R$ -parity, discussed in section 2.4, in which the LSP  $\tilde{\chi}_1^0$  is stable and presents itself as  $E_T^{\text{miss}}$  in the detector. The analysis takes advantage of a theoretically large strong SUSY production cross section (see figure 2.10) and searches for the decay products of gluinos and mass degenerate first and second generation squarks. Events containing electrons and muons are rejected in order to suppress  $E_T^{\text{miss}}$  from leptonic decays of  $W$  bosons which contain neutrinos.

In the event that the supersymmetric partners of the  $t$  and  $b$  quarks are the only SUSY particles for which production at the LHC is possible, searches for the production of  $\tilde{b}_1$  and  $\tilde{t}_1$ , the lightest mass eigenstates of  $\tilde{b}_{L,R}$  and  $\tilde{t}_{L,R}$ , decaying to final states of  $b$ -tagged jets in addition to significant  $E_T^{\text{miss}}$  are well motivated. All other quarks are assumed to be significantly more massive in this scenario and inaccessible at  $\sqrt{s} = 13$  TeV. The lightest mass eigenstates  $\tilde{b}_1$  and  $\tilde{t}_1$  are referred to as  $\tilde{b}$  and  $\tilde{t}$  throughout this chapter.

### 7.2 Discriminating Variables

In the analyses considered in this chapter, key variables are formed using reconstructed and calibrated physics objects introduced in section 5.1 to construct kinematic regions used to enhance the presence of background-like events (in the case of background estimation) and signal-like events (for a discovery or exclusion of a physics process with some limit). The variables described in this section are used by one or both of the analyses described in this chapter.

### 7.2.1 Simple Variables

- $p_T(j_i)$  —  $p_T$  of the  $i^{\text{th}}$  jet in the event, sorted in descending  $p_T$ . The leading jet,  $j_1$ , is defined as the hardest jet in the event.
- $N_X$  — Number of physics objects of type  $X$  present in the event such as  $N_{\text{jet}}$  and  $N_{b\text{-jet}}$ .
- $H_T$  — Scalar sum of jet  $p_T$  in the event

$$H_T = \sum^{n_{\text{jet}}} p_T(j_i) \quad (7.1)$$

where  $n_{\text{jet}}$  is defined per analysis and may not include all jets in an event.

- $E_T^{\text{miss}}$  — Discussed in section 5.1.6,  $E_T^{\text{miss}}$  is a key variable in searches for  $R$ -parity conserving SUSY, where signatures of large  $E_T^{\text{miss}}$  are expected in the final state due to invisible stable SUSY particles escaping the detector.
- $\sum E_T$  — Scalar sum of the transverse energy  $E_T$  in an event.
- $E_T^{\text{miss}}$ -significance,  $S$  — Defined as

$$S = \frac{E_T^{\text{miss}}}{\sqrt{X}} \quad (7.2)$$

where  $X$  can be the variable  $\sum E_T$  or  $H_T$ . A variant of this variable is used to define events with well-measured jets to be passed to the Jet Smearing tool, discussed in chapter 6.

### 7.2.2 Leading Dijet Invariant Mass $m_{jj}$

The invariant mass of the highest  $p_T$  jet pair is used to reduce contamination from the  $t\bar{t}$  process in events where one or more of the jets is identified as a  $b$ -jet. In the case where both leading jets are identified as  $b$ -jets, the variable is referred to as  $m_{bb}$ .

### 7.2.3 Effective Mass $m_{\text{eff}}$

The effective mass  $m_{\text{eff}}$  [151] is defined as the scalar sum of jet  $p_T$  and  $E_T^{\text{miss}}$  in an event

$$m_{\text{eff}} = \sum (p_T^{\text{jet}}) + E_T^{\text{miss}} \quad (7.3)$$

and is related to the mass of the pair of SUSY particles produced within the detector. It is used to discriminate between signal-like and background like events in SUSY searches where mismeasured jets generate  $E_T^{\text{miss}}$ . Larger  $m_{\text{eff}}$  is expected in SUSY events due to the decay of the LSP pair resulting in significant  $E_T^{\text{miss}}$  in addition to several high momentum jets from the decay of the produced SUSY particles. Conversely, multijet background events are, in general, expected to be associated with lower effective masses [151] due to the lack of genuine  $E_T^{\text{miss}}$  in these events. Minimum requirements on  $N_j$ -dependent effective mass are therefore used in conjunction with  $E_T^{\text{miss}}$  requirements to heavily suppress the multijet background. Variants of this discriminating variable include  $m_{\text{eff}}(N_j)$  and  $m_{\text{eff}}(\text{incl.})$ , denoting the use of the  $N$  highest  $p_T$  jets or all jets in an event passing a minimum  $p_T$  threshold, respectively. The use of  $m_{\text{eff}}(\text{incl.})$  further suppresses SM backgrounds due to their typically low multiplicity of high momentum jets. The  $m_{\text{eff}}(\text{incl.})$  distribution in simulated SUSY signal events is observed to peak at higher values than the predicted SM background in figure 7.6.

### 7.2.4 $\frac{E_T^{\text{miss}}}{m_{\text{eff}}(N_j)}$ and $\frac{E_T^{\text{miss}}}{\sqrt{H_T}}$

Requirements on  $E_T^{\text{miss}}/m_{\text{eff}}$  and  $E_T^{\text{miss}}/\sqrt{H_T}$  use ratios of the correlated variables discussed previously to further separate SUSY signal from multijet events. Events with significant  $E_T^{\text{miss}}$  resulting from SUSY particle production typically have a lower  $\sqrt{H_T}$  than events with similar  $E_T^{\text{miss}}$  from multijet production, as significant  $E_T^{\text{miss}}$  in multijet events arises from the mismeasurement of one or more high- $p_T$  jets. Additionally, for the same value of  $m_{\text{eff}}$  SUSY events are expected to generally have higher  $E_T^{\text{miss}}$  than multijet events. Both analyses discussed in this chapter place minimum requirements on such variables [129, 141].

### 7.2.5 Azimuthal Separation Between Jets and $E_T^{\text{miss}}$

The minimum angular requirement in  $\Delta\phi$  between the jets and  $\vec{E}_T^{\text{miss}}$  present in the event is used to reduce the presence of multijet background events. Multijet background events typically have  $E_T^{\text{miss}}$  aligned with one of the jets in the event due to jet  $p_T$  mismeasurement in the kinematic regions considered by both analyses. Placing high minimum requirements on this angle, for example  $\Delta\phi(\text{jet}_{1,2,(3)}, \vec{E}_T^{\text{miss}})_{\text{min}} > 0.4$  (defined with the two or three highest  $p_T$  jets), is observed to reduce multijet background contamination in the kinematic regions of analyses. If a jet is mismeasured and undergoes a downward  $p_T$  fluctuation, the fake source of  $E_T^{\text{miss}}$  generated will be aligned with the jet, giving small values of this variable.

### 7.2.6 Aplanarity

Aplanarity [152, 153] uses the event shape to differentiate background-like events from signal-like events. The jet sphericity tensor [152] is defined as

$$S^{\alpha\beta} = \frac{\sum_i p_i^\alpha p_i^\beta}{\sum_i |\vec{p}_i|^2} \quad (7.4)$$

where  $i$  refers to a calorimeter energy cluster and  $\alpha$  and  $\beta$  refer to the components of the jet momentum in  $x, y$  and  $z$  measured in each calorimeter cluster, considered in the rest frame of the jet. Eigenvalues  $\lambda_1, \lambda_2$  and  $\lambda_3$  are determined from  $S^{\alpha\beta}$ , where  $\lambda_1 \geq \lambda_2 \geq \lambda_3$  and  $\lambda_1 + \lambda_2 + \lambda_3 = 1$ . Aplanarity is then defined as

$$Ap = \frac{3\lambda_3}{2} \quad (7.5)$$

and is bounded by the range  $0 \leq Ap \leq 0.5$ . Events with energy clusters distributed isotropically have  $Ap = 0.5$ . Highly directional distributions of energy clusters in the event have values of  $Ap = 0$  and correspond to more signal-like events. Placing minimum requirements on the aplanarity further removes background-like events from the kinematic regions in the Strong- $0\ell$  analysis.

### 7.2.7 Leading Dijet $p_T$ Asymmetry $\mathcal{A}$

The dijet  $p_T$  asymmetry  $\mathcal{A}$  is defined as

$$\mathcal{A} = \frac{p_T(j_1) - p_T(j_2)}{p_T(j_1) + p_T(j_2)} \quad (7.6)$$

and is used when  $\Delta m(\tilde{b}, \tilde{\chi}_1^0) < 20$  GeV to select events with a high  $p_T$  ISR jet in the Sbottom analysis.

### 7.2.8 Minimum Mass of a Lepton and $b$ -Jet Pair, $m_{b\ell}^{\min}$

The minimum mass of a lepton and  $b$ -tagged jet pair  $m_{b\ell}^{\min}$  is defined as

$$m_{b\ell}^{\min} = \min_{i=1,2}(m_{\ell b_i}) \quad (7.7)$$

where  $i = 1, 2$  denotes the highest and second-highest  $p_T$   $b$ -jet in the event. This variable is used to enhance the presence of single-top events in the Sbottom analysis.

### 7.2.9 Transverse Mass $m_T$

The transverse mass  $m_T$  is defined for an event in the sbottom analysis, discussed in section 7.5, as

$$m_T = \sqrt{2p_T^\ell E_T^{\text{miss}} - 2\vec{p}_T^\ell \cdot \vec{p}_T^{\text{miss}}} \quad (7.8)$$

and is used to select  $t\bar{t}$  and  $W$  + jets events for estimation of  $t\bar{t}$  and  $W$  + jets backgrounds in the zero-lepton channel of the Sbottom analysis.

### 7.2.10 Contraverse Mass $m_{CT}$

The contraverse mass  $m_{CT}$  [154] provides a measure of the mass of a pair of particles produced in the detector which decay semi-invisibly, with some of their decay products escaping the detector environment without detection. For a pair of identical massive

particles decaying into two visible and two invisible particles, the contranverse mass is defined as

$$m_{\text{CT}}^2(v_1, v_2) = [E_{\text{T}}(v_1) + E_{\text{T}}(v_2)]^2 - [\vec{p}_{\text{T}}(v_1) - \vec{p}_{\text{T}}(v_2)]^2 \quad (7.9)$$

$$= m^2(v_1 + m^2(v_2) + 2[E_{\text{T}}(v_1)E_{\text{T}}(v_2) + \vec{p}_{\text{T}}(v_1) \cdot \vec{p}_{\text{T}}(v_2)]) \quad (7.10)$$

where  $v_1$  and  $v_2$  are the visible particles produced in the decay. The variable takes its maximum value when

$$m_{\text{CT}}^{\text{max}} = \frac{m_i^2 - m_X^2}{m_i} \quad (7.11)$$

where  $i$  is the heavy pair produced particle that goes on to decay and  $X$  refers to the invisible decay product of  $i$ . This variable is relied upon in the sbottom analysis to reduce the contribution of the SM background resulting from top quark production when  $i = t$ ,  $X = W$  and  $m_{\text{CT}}^{\text{max}} = 135$  GeV. In the context of the kinematic regions of the Sbottom analysis targeting the pair production of  $\tilde{b}$  squarks, the visible particles are the  $b$ -tagged jets while the invisible particles are pairs of the LSP  $\tilde{\chi}_1^0$ .

### 7.2.11 $m_T^{\text{min}}(\text{jet}_{1-4}, E_T^{\text{miss}})$

The minimum transverse mass, calculated with any of the four highest- $p_{\text{T}}$  jets in the event and the event  $E_T^{\text{miss}}$ . This variable is used to reduce the  $t\bar{t}$  background contribution in Sbottom analysis kinematic regions searching for small mass differences between the  $\tilde{b}$  and the  $\tilde{\chi}_1^0$ . In such events, the lepton from the semi-leptonic decay of  $t\bar{t}$  fails to be identified as a lepton and is instead identified as  $E_T^{\text{miss}}$ .

## 7.3 General SUSY Analysis Strategy

SUSY analyses use simulated MC events or data-driven methods to estimate major SM backgrounds in *signal regions* (SRs), kinematic regions constructed using discriminating variables to enhance the presence of signal-like events while concurrently rejecting SM background processes. To ensure the correct modelling of the SM background in SRs, dedicated *control regions* (CRs) use kinematic regions that enhance the presence of

## Implementation of Jet Smearing in ATLAS SUSY Searches

background-like events for a given SM process while minimising contamination from signal-like events. The background estimation is normalised to data in CRs before extrapolation of the estimate to the SR. CRs are designed to be kinematically similar but orthogonal to the SRs such that they represent statistically independent sets of data from the SRs and minimise the systematic uncertainties associated with the background estimation extrapolation. Analyses additionally use *validation regions* (VRs), regions kinematically between the CR and SR, to confirm the validity of the background estimate. After the background estimate from the CR is successfully validated in the VR, it can be extrapolated to the SR. At this stage, the background estimate can be compared with data for the first time in the SR. This process is referred to as *unblinding* and is used to avoid biasing the final result. Figure 7.1 gives an overview of the process.

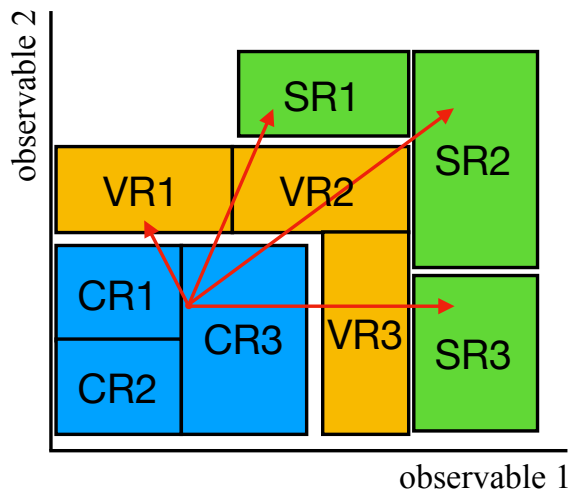


Fig. 7.1 Representation of a typical SUSY analysis strategy with control, validation and signal regions. Background estimates are extrapolated from control regions to signal regions after verification of background modelling in the intermediate validation regions. Figure adapted from [155].

The number of background events from a particular SM process appearing in a SR is estimated [155] with

$$N_{\text{process}}(\text{SR est.}) = N_{\text{process}}(\text{CR obs.}) \times \left[ \frac{\text{MC}_{\text{process}}(\text{SR raw})}{\text{MC}_{\text{process}}(\text{CR raw})} \right] \quad (7.12)$$

where for a given SM process  $N_{\text{process}}(\text{SR est.})$  is the estimated number of background events in the SR,  $N_{\text{process}}(\text{CR obs.})$  is the number of data events observed within the

CR  $MC_{\text{process}}(\text{CR}(\text{SR}) \text{ raw})$  is the background estimate in the CR (SR) from simulated MC or an equivalent data-driven background estimate before normalisation to data is applied. The ratio of observed data events within a CR to the number of predicted events for a particular SM background is treated as a scale factor for the relevant process. The ratio within the square brackets of equation 7.12 is referred to as the *transfer factor* (TF) between the CR and SR. Systematic uncertainties arising from the extrapolation of the background estimate between CR and SR mostly cancel if the regions are sufficiently kinematically similar.

### 7.3.1 Statistical Interpretation

SUSY analyses generally aim for the discovery of an excess of events above the SM background in one or more SR, with the assumption that any SUSY signal would appear only in the SR and not in any CR. Statistical tests are performed on the observed event yields in SRs to determine the significance of any excess over the predicted background. In the event of the absence of new physics, exclusion limits for the masses of new particles or parameters of a BSM theory are determined.

In the event of the discovery of new physics, the expected number of events  $\lambda$  in a SR is expressed as

$$\lambda(\text{SR}) = s \times \mu_s + b_{\text{SM}} \quad (7.13)$$

where  $s$  is the number of signal events,  $\mu_s$  is the signal strength of the BSM model under consideration and  $b_{\text{SM}}$  is the contribution from SM background events in all processes considered by the analysis. The signal strength  $\mu_s$  is assigned  $\mu_s = 1$  in the case that the signal strength is exactly that of the proposed BSM theory and  $\mu_s = 0$  in the case where no BSM signal events are observed in the SR, consistent with a background-only hypothesis.

Statistical tests are performed for several scenarios with ‘background-only’, ‘discovery’ and ‘exclusion’ fits using the HistFitter software package [155]. Background-only fits concentrate on the CRs where it is assumed there is no signal contamination. This fit generates a normalisation factor  $\mu$  between the MC simulated background in the CR and the number of observed events and is employed to determine the number of

expected background events in each SR and VR. The number of observed events in SRs are then compared with the expected SM background before determining the statistical significance of any observed excess in data above the SM background. Using the assumption that a discovery can only be claimed if there is an observed excess of events with respect to the SM, a signal is observed if  $\mu_s > 0$ . The  $\mu_s = 0$  hypothesis is therefore tested and if rejected a signal discovery is made.

Downward fluctuations of  $\mu_s$  cannot be said to exclude the signal model tested, but rather point to issues with the quality of the SM background estimation. In the event of an excess of observed events over the background-only hypothesis, the significance of the excess is investigated.

The significance  $Z$  is defined such that a Gaussian distributed observable (such as particle mass,  $E_T^{\text{miss}}$  and so on) that is observed  $Z$  standard deviations above the mean of the distribution has a probability  $p$  of the upward fluctuation being due to background-only effects. It is generally accepted within the field of particle physics that a discovery must reject the background-only hypothesis with a one-sided significance of  $Z \geq 5$ , equivalent to the probability of the excess occurring due to an upward fluctuation of the background of  $P = 2.87 \times 10^{-7}$  [156]. In the event that no discovery is made, exclusion limits are set at the 95% confidence level (CL) (a  $p$ -value of 0.05) both for specific SUSY models and independently of the chosen model using the  $CL_s$  prescription [157], where

$$CL_s \approx P(n_{s+b} \leq n_{\text{obs}}) / P(n_b \leq n_{\text{obs}}) \quad (7.14)$$

approximately defines the confidence level of the exclusion limit.

## 7.4 Strong SUSY Production Resulting in 2-6 Jets and $E_T^{\text{miss}}$

The large production cross-section associated with the strong production of supersymmetry (see figure 2.10) motivates searches for the pair production of squarks and gluinos, decaying directly or with intermediate steps to the LSP  $\tilde{\chi}_1^0$ , which appears in the detector as  $E_T^{\text{miss}}$ .

## 7.4 Strong SUSY Production Resulting in 2-6 Jets and $E_T^{\text{miss}}$

As discussed in section 2.5, this analysis assumes that the supersymmetric partners of the left and right handed first and second generation squarks mix to form mass eigenstates  $\tilde{q}_{1,2}$ , with third generation squarks considered too massive for production at the LHC.

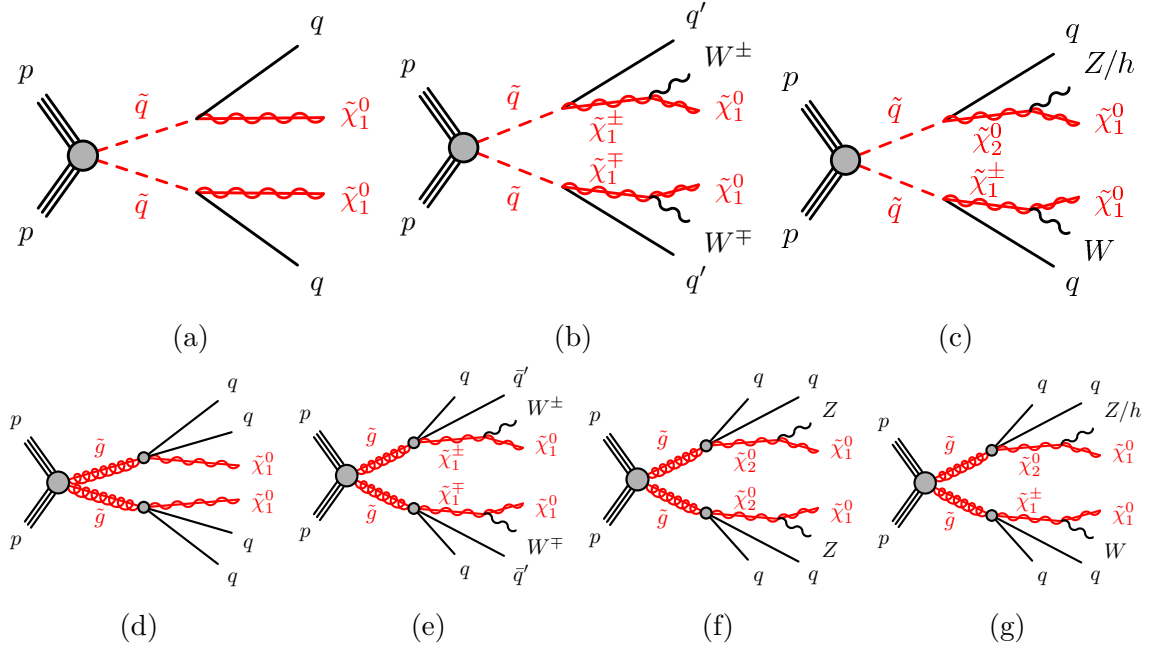


Fig. 7.2 Pair production of squarks and gluinos with subsequent decays in the simplified models considered in the analysis. Squarks are pair produced in the scenarios shown by (a), (b) and (c), with (a) showing the direct decay of the squarks to jets and the LSP. Scenarios (b) and (c) show the potential decay via an intermediate chargino  $\tilde{\chi}_1^\pm$  or heavier neutralino  $\tilde{\chi}_2^0$ , resulting in the production of  $W, Z$  and  $h$  bosons along with jets and the LSP. Gluino production is shown through scenarios (d)-(g) for direct decays to the LSP and for decays via intermediate charginos or heavier neutralinos. Figures from [129].

The analysis considers simplified models [158, 159] that target the direct production of pairs of squarks or pairs of gluinos with subsequent decays to  $\tilde{\chi}_1^0$  shown in figure 7.2. Such simplified models were the focus of previous analyses [150] and their reanalysis with a higher luminosity dataset was driven by this convention. The simplified models introduce a small number of BSM particles and assume that, in the case of squark production, the gluino is too massive for production at the LHC. In the case of gluino pair production, the squark mass is then assumed to be too large for production at the LHC. In this way the heavier of the squark or gluino is effectively decoupled and its mass arbitrarily assigned the value of 450 TeV [129]. Squark pair

## Implementation of Jet Smearing in ATLAS SUSY Searches

---

production is shown by figures 7.2a – 7.2c. Squark production is followed by either the direct decay of the squark to a quark (observed as a jet in the detector) and the lightest neutralino  $\tilde{\chi}_1^0$  through  $\tilde{q} \rightarrow q\tilde{\chi}_1^0$  or a decay via an intermediate SUSY particle. The lightest neutralino is considered the LSP in this analysis. Squarks decaying via an intermediate chargino  $\tilde{q} \rightarrow q\tilde{\chi}_1^\pm$ ,  $\tilde{\chi}_1^\pm \rightarrow W^\pm\tilde{\chi}_1^0$  can result in higher jet multiplicities in the final states due to the decay of the  $W$ . Squarks decaying through an intermediate heavier neutralino  $\tilde{q} \rightarrow q\tilde{\chi}_2^0$ ,  $q\tilde{\chi}_2^0 \rightarrow Z/h$  result in the production of  $Z$  and  $h$  bosons, which can decay to produce higher jet multiplicity final states. The analysis includes a veto on reconstructed electrons and muons in the SRs. Gluino production is considered in a similar manner: either a direct decay to the LSP via  $\tilde{g} \rightarrow qq\tilde{\chi}_1^0$  producing detected final states with 4 jets and  $E_T^{\text{miss}}$ , or decay via an intermediate chargino or heavier neutralino resulting in 5 and 6 jet final states through the production and decay of  $W, Z$  and  $h$  bosons.

Additional simplified models inspired by the MSSM [160, 161] with additional constraints on the number of free parameters imposed by experiment and theory are considered to target the inclusive production of squarks and gluinos, in which the production of squark-gluino pairs is possible. Such models assume that gluinos,  $\tilde{\chi}_1^0$  and the first- and second-generation squarks are the only SUSY particles with masses low enough for production at the LHC and are additionally simplified by assuming  $\tilde{\chi}_1^0$  to be purely bino-like. The decay of the SUSY particle then proceeds either directly to  $\tilde{\chi}_1^0$  or via a squark or gluino if kinematically possible [129].

The analysis defines SRs using MC simulated SUSY signal samples generated with the MG5\_aMCNLO event generator [162], using the NNPDF2.3LO PDF set [76] with interfaced with PYTHIA8 [75] using the A14 parameter set. SRs are optimised for maximum expected discovery sensitivity against the SM background using MC simulated signal events. Two key discriminating variables used by the analysis are the number of jets  $N_j$  and  $m_{\text{eff}}$  [151].

### 7.4.1 Event Selection and Signal Regions

The analysis considers calibrated objects as defined in section 5.1. Events are required to include a primary vertex with a minimum of two associated tracks with  $p_T > 400$  MeV. In the event of multiple candidate primary vertices, the vertex with the largest scalar sum of associated track transverse momenta is selected.

## 7.4 Strong SUSY Production Resulting in 2-6 Jets and $E_T^{\text{miss}}$

---

The analysis considers calibrated anti- $k_t$  jets (see section 5.1.2) with a radius parameter  $\Delta R = 0.4$  (defined in equation 3.7),  $p_T > 20$  GeV and  $|\eta| < 2.8$ , where  $\Delta R$  is defined in equation 3.7. Jets originating from  $b$  quarks are identified using the MV2c10 algorithm detailed in section 5.1.3 using an operating point providing an average of 77% efficiency in  $b$ -jet identification. Any  $b$ -tagged jets with  $p_T > 50$  GeV and  $|\eta| < 2.5$  are considered by the analysis. Any event is rejected by the analysis if it contains a jet meeting the **LooseBad** criteria. Alternatively, if one of the two highest  $p_T$  jets with  $p_T > 100$  GeV in an event meet the **TightBad** criteria, the event is rejected. Both criteria are detailed in section 5.1.2. Jets with  $p_T < 60$  GeV are required to have a JVT variable (see section 5.1.2)  $JVT > 0.59$  to reduce contamination from jets originating from pile-up.

Electrons and muons are collectively referred to as ‘leptons’ in the analysis, which excludes  $\tau$ -leptons from this definition. Muons are rejected if they have  $p_T > 7$  GeV and  $|\eta| < 2.7$ , while electrons with  $p_T > 7$  GeV and  $|\eta| < 2.47$  are rejected. Calibrated, isolated photons are considered by the analysis if they have  $p_T > 150$  GeV,  $|\eta| < 2.37$  and are not within  $\Delta R < 0.4$  of an electron or muon. Kinematic regions used for background estimation may not use a lepton veto, instead requiring leptons to pass an additional set of requirements such that they are deemed ‘high-purity’. High-purity muons are required to have  $p_T > 27$  GeV,  $|\eta| < 2.4$  and be well isolated. High-purity electrons must be well isolated, satisfy the ‘Tight’ criteria defined in section 5.1.4.1 and have  $p_T > 27$  GeV. The complete definition of high purity leptons is available in [129].

After meeting the above requirements, overlapping physics objects are resolved with an overlap removal procedure discussed in section 5.1.7. Physics objects surviving the overlap removal procedure are used to calculate the  $E_T^{\text{miss}}$  in the event, in addition to a track-based soft term (discussed in section 5.1.6) accounting for the energy in the event that is not identified with any reconstructed object.

The analysis defines 24 inclusive SRs to target squark and gluino production and their subsequent decays using a selection of the discriminating variables described in section 7.2. Most significantly, signal regions are defined by the number of jets and the requirement on  $m_{\text{eff}}(\text{incl.})$ . Squark production and direct decay to  $\tilde{\chi}_1^0$  and jets is targeted by considering events with at least 2-3 jets in eight distinct SRs, while gluino production with direct decay to jets and  $\tilde{\chi}_1^0$  is considered in seven SRs requiring at least four or five jets. Decay to  $\tilde{\chi}_1^0$  via an intermediate SUSY particle (‘one-step’ decays) is considered by nine SRs that target both squark and gluino pair production.

Two SRs targeting the one-step decay scenario use large-radius jets and target both squark and gluino production with subsequent decay via an intermediate  $\tilde{\chi}_1^\pm$  or  $\tilde{\chi}_2^0$  before eventual decay to the LSP, for cases where the intermediate SUSY particle has a similar mass to the produced squark or gluino. Large radius jets are constructed with the jet reclustering technique [163] by using the standard calibrated anti- $k_t$  jets with  $\Delta R = 0.4$  and  $p_T > 25$  GeV as inputs to an anti- $k_t$  algorithm with a radius parameter set to  $\Delta R = 1.0$  defined in equation 3.7. Signal regions have the naming convention of the value of  $N_j$  followed by the  $m_{\text{eff}}(\text{incl.})$  requirement placed on the region. Tables in appendices B.1–B.4 show the complete set of requirements that characterise all 24 signal regions.

### 7.4.2 Background Estimation

The analysis uses dedicated CRs to produce an estimate of the most significant SM backgrounds, before extrapolating the estimate to the orthogonal SRs. The most significant SM background encountered in the SRs of the analysis is  $Z(\rightarrow \nu\nu) + \text{jets}$ , which presents a significant source of  $E_T^{\text{miss}}$ . Other major backgrounds considered by the analysis include the production of  $W(\rightarrow \ell\nu) + \text{jets}$ , single top quark and  $t\bar{t}$  production.

A  $\gamma + \text{jets}$  region is used to estimate the  $Z(\rightarrow \nu\nu) + \text{jets}$  background in SRs. Photons with  $p_T > 150$  GeV are selected and considered as invisible particles when calculating the  $E_T^{\text{miss}}$  to mirror the  $Z \rightarrow \nu\nu$  decay.

$W + \text{jet}$  production predominantly concerns the fully hadronic decay of the  $W$  to a  $\tau$  and a neutrino (with subsequent hadronic decay of the  $\tau$ ) but can also include leptonic  $W$  decays where the electron or muon fails to be identified in event reconstruction. The  $W$  CR targets  $W(\rightarrow \ell\nu) + \text{jet}$  events using high-purity leptons (defined in section 7.4.1) while rejecting events including  $b$ -tagged jets. An additional requirement is placed on the transverse mass of the combination of  $E_T^{\text{miss}}$  and the lepton selected in the event, where the lepton is treated as a jet with equivalent transverse momentum to model hadronic  $\tau$  decay.

## 7.4 Strong SUSY Production Resulting in 2-6 Jets and $E_T^{\text{miss}}$

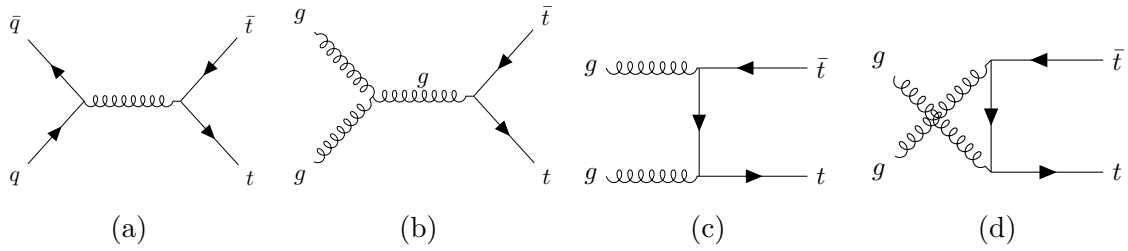


Fig. 7.3 Leading order  $t\bar{t}$  production processes at the LHC.

Top quark backgrounds result in the production of a single top quark or a pair, followed by subsequent decay to a  $W$  and a  $b$ -tagged jet. Figure 7.3 shows the processes by which pairs of top quarks are produced in the LHC to leading order. The  $W$  then decays, potentially producing jets and  $E_T^{\text{miss}}$  in the final state. Events where the  $W$  boson decays into a muon or electron are removed with the lepton veto. Top quark decays where both  $W$  bosons decay directly to jets are suppressed with the same variables used to suppress the multijet contribution to SRs. Semi-leptonic decays of top quark pairs  $t\bar{t} \rightarrow b\bar{b}\tau\nu qq$  followed by the hadronic decay of the  $\tau$  can potentially result in fully hadronic final states with significant  $E_T^{\text{miss}}$ . The background contribution in the SR from this process is constrained through the use of a dedicated CR which uses a similar event selection to the  $W$  region, but exclusively selects events with  $b$ -jets and  $30 \text{ GeV} < m_T(\ell, E_T^{\text{miss}}) < 100 \text{ GeV}$  to target events with semi-leptonic top decays and remove any contribution from signal events.

Multijet production is considered in dedicated CRs, but minimised in SRs through the use of discriminating variables discussed in section 7.2, particularly  $\Delta\phi(\text{jet}, \vec{E}_T^{\text{miss}})_{\text{min}}$  and  $\frac{E_T^{\text{miss}}}{m_{\text{eff}}(N_j)}$ . This background causes the introduction of fake  $E_T^{\text{miss}}$  due to jet mismeasurement or misidentification, in addition to a source of genuine  $E_T^{\text{miss}}$  through the decay of heavy flavour jets to neutrinos. Jet smearing, introduced in chapter 6, is used to generate the pseudo-data collections that are normalised to data in the dedicated multijet CRs described in appendix B.

The background estimate for the production and subsequent decay of  $WW$ ,  $WZ$ , or  $ZZ$  does not use the CR/SR approach, instead an estimate is taken directly from Sherpa 2.2.1 [22] MC simulated events, normalised by cross-section calculated at NLO in  $\alpha_S$ . The CRs used by the analysis are shown in table 7.1 for each SR, providing a total of 96 distinct CRs used by the analysis. Any jet  $p_T$ ,  $m_{\text{eff}}(\text{incl.})$  and multiplicity requirements used by the CRs mirror those of the SR they are assigned to. Both the top and  $W$

## Implementation of Jet Smearing in ATLAS SUSY Searches

CRs remove the SR requirements on  $|\eta(\text{jet})|$ ,  $\Delta\phi(\text{jet}, \vec{E}_T^{\text{miss}})_{\text{min}}$  and aplanarity. CRs designed for SRs requiring  $m_{\text{eff}}(\text{incl.}) > 2200$  GeV remove the requirements on  $\frac{E_T^{\text{miss}}}{m_{\text{eff}}(N_j)}$  to increase the number of events entering the CRs.

Table 7.1 Dedicated control regions used to estimate significant SM backgrounds in each signal region used by the analysis [129].

CR	SR process	CR process	Requirements
CR $\gamma$	$Z(\rightarrow \nu\nu) + \text{jets}$	$\gamma + \text{jets}$	Isolated photon, $p_T(\gamma) > 150$ GeV
CRW	$W(\rightarrow \ell\nu) + \text{jets}$	$W(\rightarrow \ell\nu) + \text{jets}$	$30 \text{ GeV} < m_T(\ell, E_T^{\text{miss}}) < 100 \text{ GeV}$ & $b$ -veto
CRT	$t\bar{t}$ & single top	$t\bar{t} \rightarrow b\bar{b}qql\nu$	$30 \text{ GeV} < m_T(\ell, E_T^{\text{miss}}) < 100 \text{ GeV}$ & $b$ -tag
CRQ	Multijets	Multijets	Inverted $\Delta\phi(\text{jet}, \vec{E}_T^{\text{miss}})_{\text{min}}$ and $\frac{E_T^{\text{miss}}}{m_{\text{eff}}(N_j)}$ (or $\frac{E_T^{\text{miss}}}{\sqrt{H_T}}$ )

The CRs, defined through the requirements placed on events, are designed to be kinematically similar to the SRs, such that the theoretical uncertainties associated with the extrapolation of the background estimate in the CR to the SR are minimised. Transfer factors (TFs) (discussed in section 7.3 and defined in equation 7.12) are used for each CR to estimate the number of SM background events appearing in each SR. TFs are then used in likelihood fits to obtain the background estimate in the SR.

### 7.4.2.1 Multijet background

The multijet background in the analysis was estimated using the Jet Smearing technique. Seed events were selected with the use of single jet triggers with thresholds of 15, 25, 60, 110, 150, 200, 260, 320, 360 and 400 GeV in  $p_T$  and an additional higher  $p_T$  requirement was placed on jets passing each trigger to ensure that the trigger was operating with 100% efficiency. A requirement of  $0.5 \text{ GeV}^{1/2}$  was placed on the  $E_T^{\text{miss}}$ -significance, which used the definition given in equation 6.4 with  $M = 8$  GeV. The requirement was relaxed by  $0.1 \text{ GeV}^{1/2}$  for each additional  $b$ -tagged jet present in the event. Pseudo-data distributions were generated using the jet response measured with MC simulated dijet events modelling the pile-up distribution observed in 2015 and 2016 data following corrections to the pseudo-data jet- $\phi$  distribution. No corrections to the tail of the jet response were made available at the time of publication of this analysis. Distributions of pseudo-data were normalised to data in a dedicated CR ‘CRQ’, defined in table 7.1, for each SR used in the analysis to provide an estimate for the number of multijet

## 7.4 Strong SUSY Production Resulting in 2-6 Jets and $E_T^{\text{miss}}$

---

events entering each SR. The predicted and observed event yield for multijet control regions in a selection of SRs is shown in figures 7.4 and 7.5. A conservative systematic uncertainty of 100% was applied to the estimate in all cases and is observed to largely provide good modelling of the data distributions in CRs.

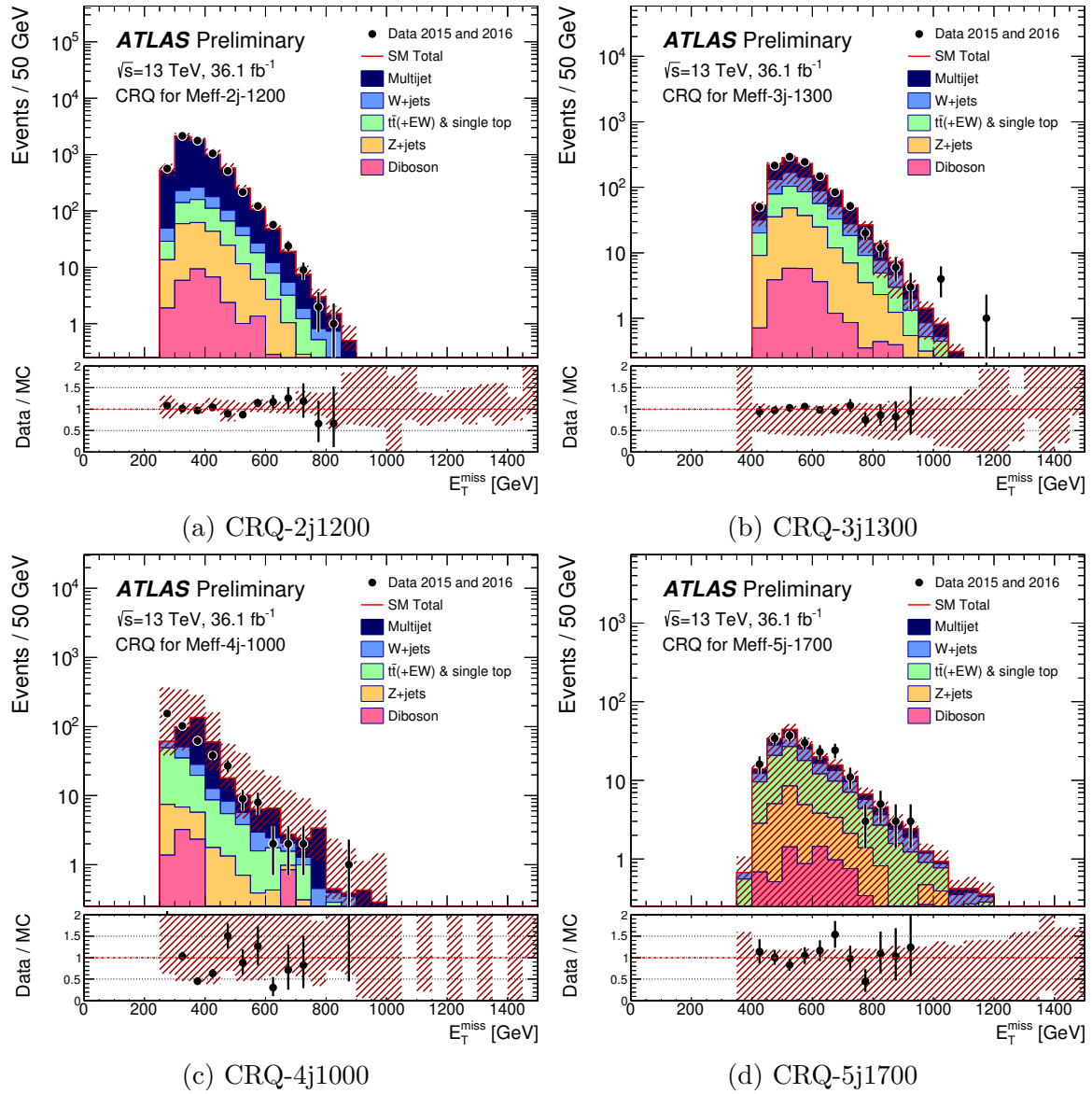


Fig. 7.4 Distributions of  $E_T^{\text{miss}}$  in a selection of the multijet control regions studied in the analysis using  $36.1 \text{ fb}^{-1}$  of  $\sqrt{s} = 13 \text{ TeV}$  data. Each control region is associated with a particular signal region, defined in tables B.1–B.4. Observed data is shown by black points. Background predictions for SM production of  $W$ +jets (light blue),  $t\bar{t}$  and single top quark (green),  $Z$ +jets (yellow) and diboson (pink) are normalised to process cross-section and integrated luminosity, while the pseudo-data distribution used to estimate the multijet background is normalised to data and is shown in dark blue. The red hatched band shows the combined statistical and systematic uncertainties on the estimate. Figures from [164].

## 7.4 Strong SUSY Production Resulting in 2-6 Jets and $E_T^{\text{miss}}$

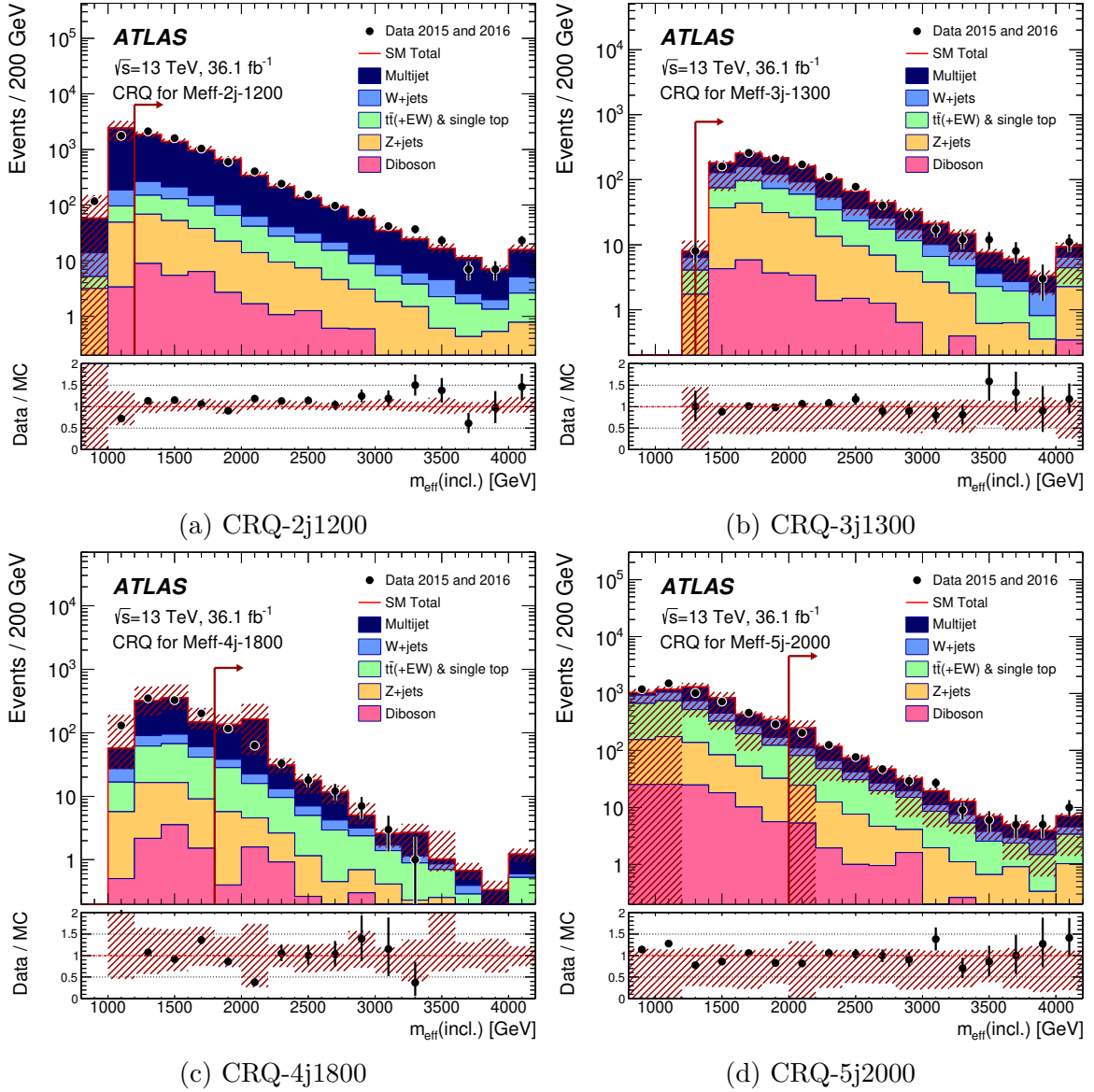


Fig. 7.5 Distributions of  $m_{\text{eff}}(\text{incl.})$  in a selection of the multijet control regions studied in the analysis using  $36.1 \text{ fb}^{-1}$  of  $\sqrt{s} = 13 \text{ TeV}$  data. Each control region is associated with a particular signal region, defined in tables B.1–B.4. Red arrows within the figures denote the requirement on  $m_{\text{eff}}(\text{incl.})$  for the particular region. Observed data is shown by black points. Background predictions for SM production of  $W$ +jets (light blue),  $t\bar{t}$  and single top quark (green),  $Z$ +jets (yellow) and diboson (pink) are normalised to process cross-section and integrated luminosity, while the pseudo-data distribution used to estimate the multijet background is normalised to data and is shown in dark blue. The final bin in each figure has an increased number of predicted and observed events with respect to nearby bins as it includes overflow events. The red hatched band shows the combined statistical and systematic uncertainties on the estimate. Figures from [165].

### 7.4.3 Results

Due to the high rejection of multijet events in all SRs used by the analysis, the multijet contribution was observed to be negligible. Figure 7.6 shows the distribution of the  $m_{\text{eff}}(\text{incl.})$  variable within the signal region requiring six or more jets and  $m_{\text{eff}}(\text{incl.}) > 2600$  GeV, with the  $m_{\text{eff}}(\text{incl.})$  requirement denoted by the red arrow.

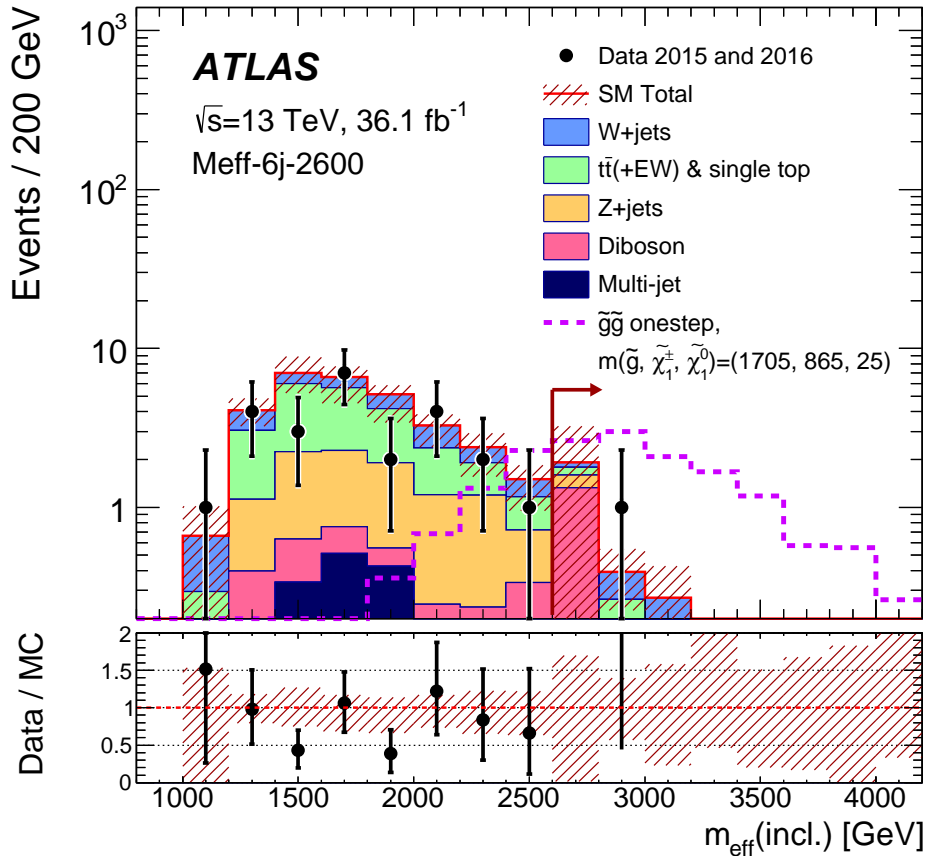


Fig. 7.6 Distribution of  $m_{\text{eff}}(\text{incl.})$  in the Strong- $0\ell$  signal region requiring 6 or more jets and  $m_{\text{eff}}(\text{incl.}) > 2600$  GeV, shown by the red arrow. Observed data are shown by black points. Estimated SM background contributions are shown for  $W$ +jets,  $t\bar{t}$  and single top production,  $Z$ +jets, diboson production and multijet production by the light blue, green, orange, pink and dark blue histograms, respectively. The distribution of simulated signal events due to the decay of pair produced gluinos to  $\tilde{\chi}_1^0$  with  $m_{\tilde{g}} = 1705$  GeV and  $m_{\tilde{\chi}_1^0} = 25$  GeV is shown by the dashed pink line. Red hatched bands denote the combined systematic and statistical uncertainties. Figure from [129].

Table 7.2 shows the number of events expected and observed in a selection of the signal regions investigated. The uncertainty from the Jet Smearing technique was

## 7.4 Strong SUSY Production Resulting in 2-6 Jets and $E_T^{\text{miss}}$

---

found to have a negligible contribution to the uncertainty of a majority of signal regions [129].

Table 7.2 Number of observed and expected events with uncertainties in a selection of signal regions investigated in the analysis. The multijet estimate is derived using the Jet Smearing technique. Values taken from [129].

Signal Region	2j-1200	3j-1300	4j-1800	5j-2000	6j-2600
Events Observed	611	429	55	59	1
Total Expected	$526 \pm 31$	$390 \pm 29$	$49 \pm 7$	$65 \pm 7$	$2.2 \pm 1.4$
Multijet Expected	$6 \pm 6$	$1.4 \pm 1.4$	$0.10 \pm 0.10$	$0.09 \pm 0.09$	$0.06 \pm 0.06$

The number of data events entering each SR is compared with the expected events due to the SM background in figure 7.7. The number of expected background events is determined through extrapolation of an estimate in the CR associated with the relevant background process for each SR, discussed in section 7.3.1. No significant excess of events is observed above the predicted SM background in any SR – the largest excesses are observed in the 2j-1200 and 2j-2100 regions and correspond to a significance of  $2.0\sigma$  [129].

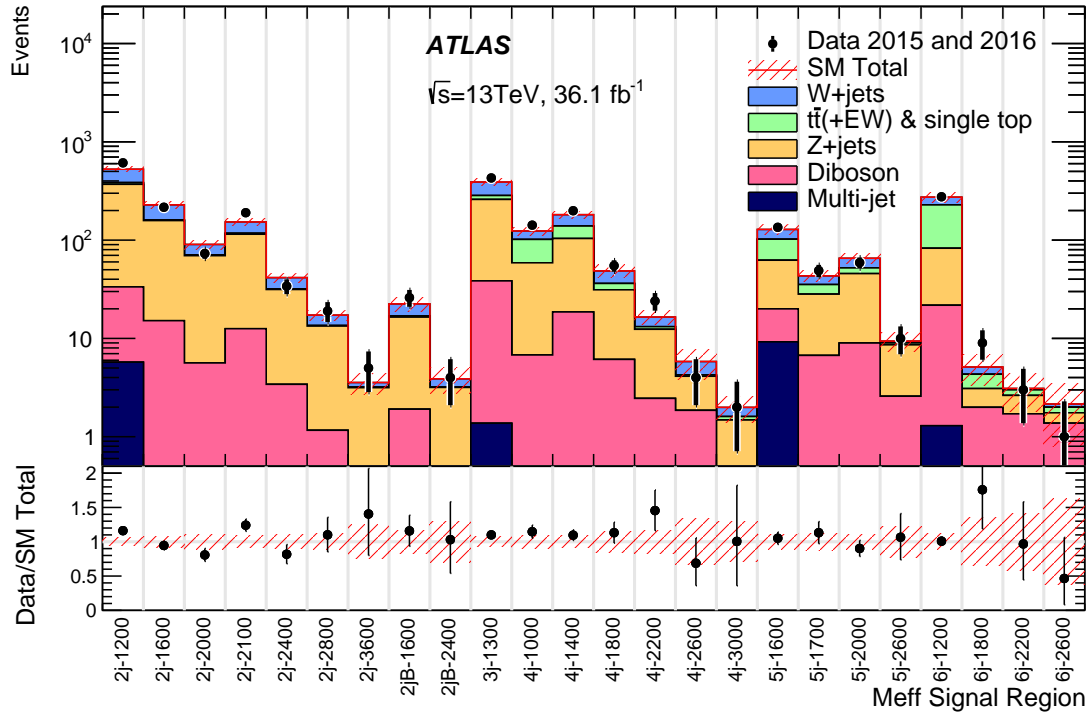


Fig. 7.7 Observed event yields in all SRs and the expected number of events due to SM background processes, derived from a background-only fit. The hatched error bands show the combined statistical and systematic uncertainty associated with the background estimate in each SR. A ratio of observed data events to expected background events is shown in the bottom of the figure. Figure from [129].

On confirming the absence of a SUSY discovery, exclusion limits are placed on the masses of the first and second generation squarks, gluino and  $\tilde{\chi}_1^0$  at the 95% confidence level. Figures 7.8 and 7.9 show the expected and observed exclusion limits for the simplified model of pair production of squarks (gluinos) with direct decay to a quark (a pair of quarks) and the LSP  $\tilde{\chi}_1^0$ .

## 7.4 Strong SUSY Production Resulting in 2-6 Jets and $E_T^{\text{miss}}$

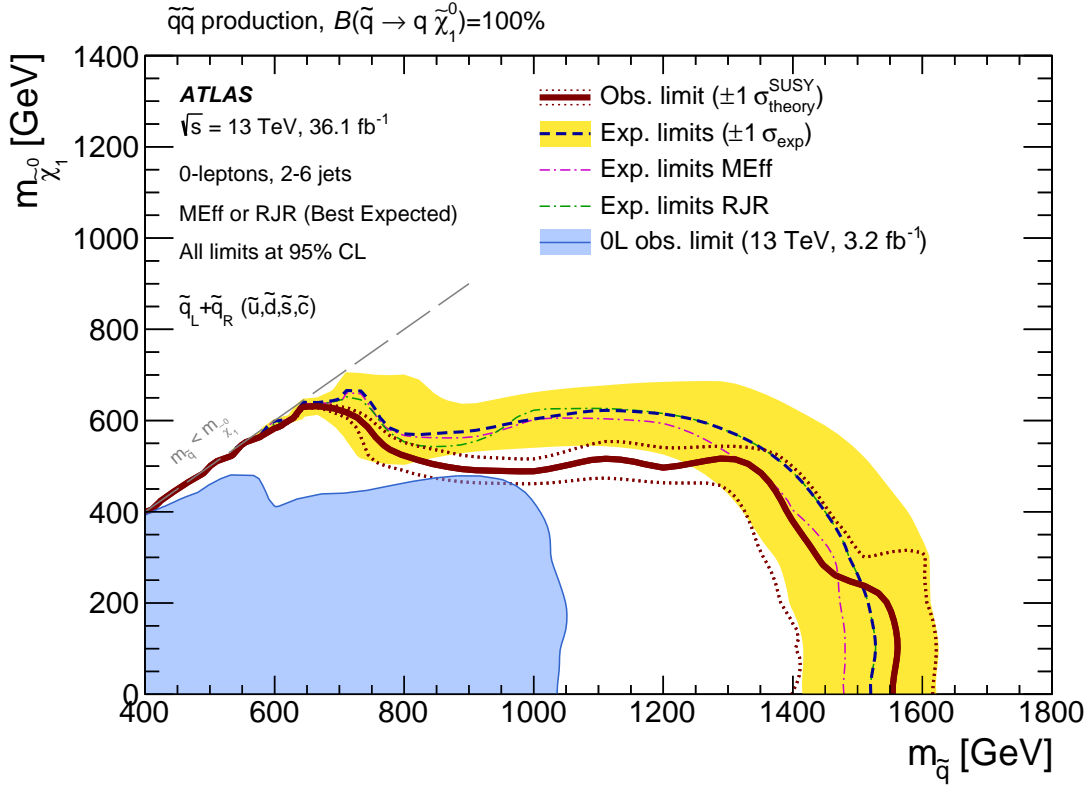


Fig. 7.8 Exclusion limits for SUSY particle masses at the 95% confidence level (CL) derived with  $36.1 \text{ fb}^{-1}$  of  $\sqrt{s} = 13 \text{ TeV}$  data for the direct production of pairs of first and second generation squarks in the case where gluinos are too massive for LHC production. In this model, squarks decay directly to a quark and the LSP  $\tilde{\chi}_1^0$  with a branching ratio of 100%. The exclusion limit is presented as a function of the masses of squarks and the  $\tilde{\chi}_1^0$  mass. The pink dashed line shows the contribution to the expected exclusion limits from the sub-analysis using  $m_{\text{eff}}(\text{incl.})$  as a discriminating variable, the limit from the other analysis not discussed in this chapter is shown by the green dashed line. Combined expected exclusion limits from both sub-analyses are shown by the dashed blue line. The yellow error band surrounding the expected exclusion limit shows the  $1\sigma$  uncertainty on the expected exclusion limit. The observed exclusion limit from a combination of the analyses is shown by the dark red line, with the associated  $1\sigma$  uncertainty shown by the dashed dark red line and arising from variations of the theoretical signal process cross-section. The previously excluded region of phase-space from the analysis using  $3.2 \text{ fb}^{-1}$  of data at  $\sqrt{s} = 13 \text{ TeV}$  is shown by the shaded blue area. Figure from [129].

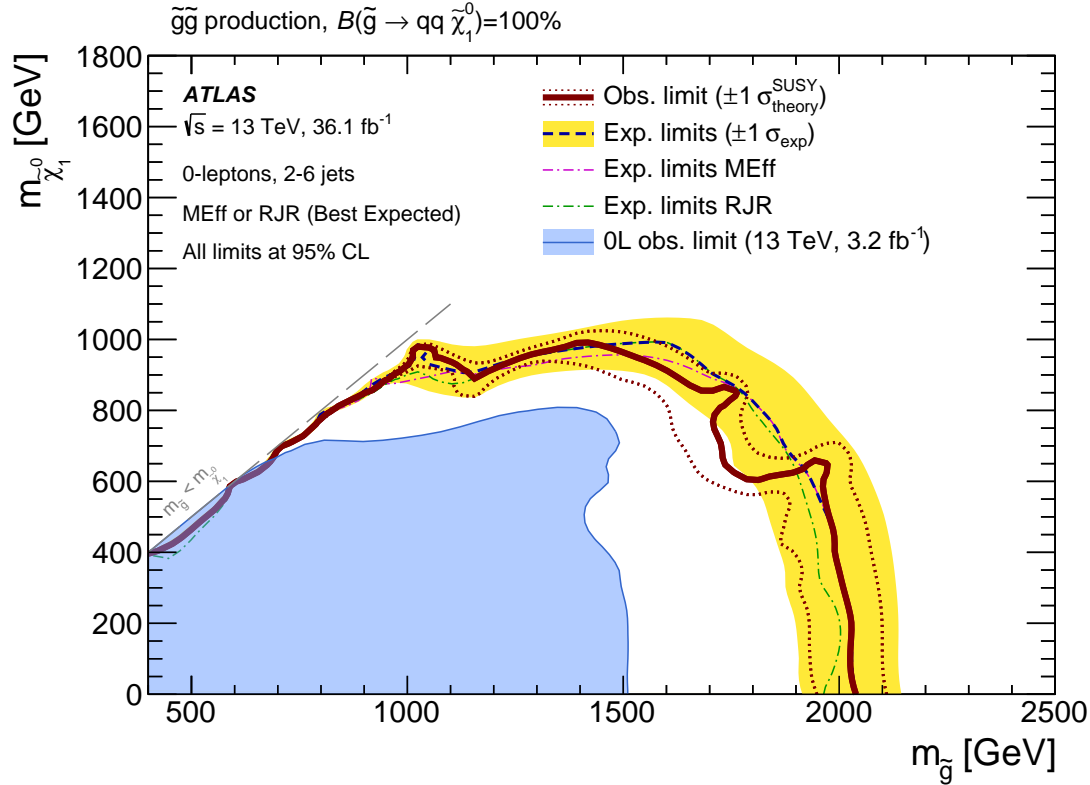


Fig. 7.9 Exclusion limits for SUSY particle masses at the 95% confidence level (CL) derived with  $36.1 \text{ fb}^{-1}$  of  $\sqrt{s} = 13 \text{ TeV}$  data for the direct production of pairs of gluinos in the case where first and second generation squarks are too massive for LHC production. In this model gluinos decay directly to a pair of quarks and a  $\tilde{\chi}_1^0$  with a branching ratio of 100%. The exclusion limit is presented as a function of the masses of gluinos and the  $\tilde{\chi}_1^0$  mass. The pink dashed line shows the contribution to the expected exclusion limits from the sub-analysis using  $m_{\text{eff}}$  (incl.) as a discriminating variable, the limit from the other analysis not discussed in this chapter is shown by the green dashed line. Combined expected exclusion limits from both sub-analyses are shown by the dashed blue line. The yellow error band surrounding the expected exclusion limit shows the  $1\sigma$  uncertainty on the expected exclusion limit. The observed exclusion limit from a combination of the analyses is shown by the dark red line, with the associated  $1\sigma$  uncertainty shown by the dashed dark red line and arising from variations of signal process cross-section. The previously excluded region of phase-space from the analysis using  $3.2 \text{ fb}^{-1}$  of data at  $\sqrt{s} = 13 \text{ TeV}$  is shown by the shaded blue area. Figure from [129].

Assuming a massless  $\tilde{\chi}_1^0$ , first and second generation squarks are excluded up to 1.55 TeV, while under the same assumption gluino masses up to 2.03 TeV are excluded under this simplified model. The previously established exclusion limits for these simplified

scenarios are shown in shaded blue and are vastly expanded upon with this set of results.

## 7.5 Third Generation SUSY Production Resulting in $b$ -Jets and $E_T^{\text{miss}}$

The sbottom analysis [141] employed simplified MSSM-inspired models to search for the production of  $\tilde{b}$  with a direct decay  $\tilde{b} \rightarrow b\tilde{\chi}_1^0$  with a 100% branching ratio, in addition to the process in which a  $\tilde{b}$  ( $\tilde{t}$ ) is produced, with subsequent decay either directly to the LSP via  $\tilde{b} \rightarrow b\tilde{\chi}_1^0$  ( $\tilde{t} \rightarrow t\tilde{\chi}_1^0$ ) or through a decay via an intermediate chargino  $\tilde{b} \rightarrow t\tilde{\chi}_1^\pm$ ,  $\tilde{\chi}_1^\pm \rightarrow W\tilde{\chi}_1^0$  ( $\tilde{t} \rightarrow b\tilde{\chi}_1^\pm$ ,  $\tilde{\chi}_1^\pm \rightarrow W\tilde{\chi}_1^0$ ). The indirect decay assumes that the mass difference between  $\tilde{\chi}_1^\pm$  and  $\tilde{\chi}_1^0$  is small enough that other decay products resulting from the associated off-shell  $W$  in the decay are not reconstructed in the detector due to their low momentum. Either indirect decay is assumed to occur with a 50% probability. Both scenarios are shown in figure 7.10.

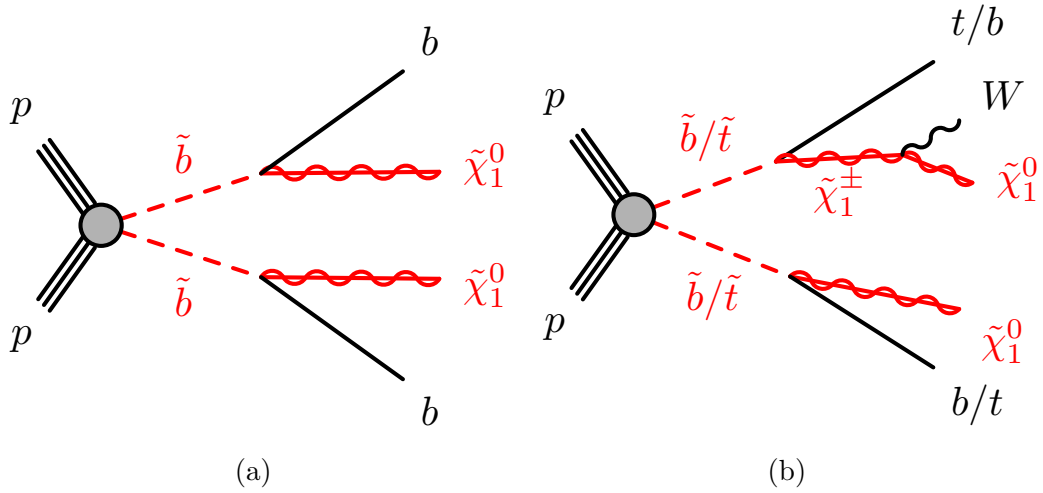


Fig. 7.10 Simplified SUSY signal models considered by the sbottom analysis. (a) Pair production of  $\tilde{b}$  with a direct decay  $\tilde{b} \rightarrow b\tilde{\chi}_1^0$  with a 100% branching ratio. (b) Pair production of  $\tilde{b}$  ( $\tilde{t}$ ), decaying either directly to the LSP via  $\tilde{b} \rightarrow b\tilde{\chi}_1^0$  ( $\tilde{t} \rightarrow t\tilde{\chi}_1^0$ ) or via an intermediate chargino  $\tilde{b} \rightarrow t\tilde{\chi}_1^\pm$ ,  $\tilde{\chi}_1^\pm \rightarrow W\tilde{\chi}_1^0$  ( $\tilde{t} \rightarrow b\tilde{\chi}_1^\pm$ ,  $\tilde{\chi}_1^\pm \rightarrow W\tilde{\chi}_1^0$ ) where  $\Delta m(\tilde{\chi}_1^\pm, \tilde{\chi}_1^0)$  is sufficiently small that the  $W$  is not reconstructed by the detector due to its low momentum. A 50% probability is assumed for either decay process. Figures from [141].

Figure 7.10a represents a fully hadronic final state, while figure 7.10b can result in fully hadronic final states if the hadronic decay of the  $t$  is considered, however an additional final state including one lepton is available via the semi-leptonic decay of the  $t$ .

The analysis defines SRs using MC simulated SUSY signal samples generated with the MADGRAPH5\_aMCNLO event generator [162], using the NNPDF2.3LO PDF set [76] with parton showering, hadronisation and underlying event modelled by PYTHIA 8 [75] with the A14 parameter set.

SRs targeting hadronic final states with the complete absence of reconstructed electrons or muons form a portion of the analysis referred to as the ‘zero-lepton channel’, on which this section of the chapter will focus. SRs and associated CRs searching for final states including leptons in this analysis (referred to as the 1-lepton channel) will not be discussed in detail in this chapter, although it should be noted that the results from these SRs are considered in addition to the fully hadronic SRs in the exclusion limits on the masses of third generation squarks presented in this section.

This analysis uses the  $\Delta\phi(\text{jet}, \vec{E}_T^{\text{miss}})_{\text{min}}$ ,  $H_T$  and  $m_{\text{eff}}$  (alone and in combination with  $E_T^{\text{miss}}$ ) discriminating variables discussed in section 7.2 in addition to several variables specific to this analysis to define kinematic control and SRs for the ‘zero-lepton’ channel of the analysis. The  $H_T$  variable used in this analysis is labelled  $H_{T4}$  and is constructed by summing the transverse momenta of the fourth highest- $p_T$  jet and all lower- $p_T$  jets within the event.

### 7.5.1 Event Selection and Signal Regions

This section will describe the overall requirements placed on the physics objects considered in the analysis before discussing the specific requirements placed on events that define the SRs for the zero-lepton channel of the analysis.

#### 7.5.1.1 Object Definitions

‘Baseline’ and ‘signal’ physics objects are defined in the analysis using the calibrated reconstructed objects detailed in section 5.1 and largely mirror the definitions provided in section 7.4.1.

## 7.5 Third Generation SUSY Production Resulting in $b$ -Jets and $E_T^{\text{miss}}$

---

Jets are considered ‘baseline’ by the analysis if they possess  $p_T > 20$  GeV and  $|\eta| < 2.8$ . A subset of the baseline jets, ‘signal’ jets, is created using baseline jets that survive the overlap removal procedure described in section 5.1.7 and have  $p_T > 35$  GeV. The identification of  $b$ -tagged jets is performed using the MV2c10 algorithm detailed in section 5.1.3 set to the working point corresponding to an average 77%  $b$ -tagging efficiency as a function of jet  $p_T$ .

Reconstructed electrons are required to satisfy the ‘loose’ criteria (discussed in section 5.1.4.1) with  $p_T > 10$  GeV and  $|\eta| < 2.47$ . Muons are required to satisfy the ‘medium’ criteria (see section 5.1.5), have  $p_T > 10$  GeV and  $|\eta| < 2.5$ , with a transverse (longitudinal) impact parameter greater than 0.2 mm (1 mm). The zero-lepton channel of the analysis places a veto upon baseline leptons that survive the overlap removal procedure in all SRs. Where leptons are used to define CRs for background estimation, leptons are required to additionally have  $p_T > 27$  GeV and are termed ‘signal’ leptons. To ensure signal leptons are isolated from  $b$ -jets originating from the semi-leptonic decay of  $t$  quarks, signal leptons must be isolated from physics objects within  $\max(0.2, 10 \text{ GeV}/p_T^\ell)$  as the separation between leptons and  $b$ -jets originating from this process decreases with increasing  $t$  quark  $p_T$  [141]. Signal electrons must additionally satisfy the ‘tight’ criteria.

Reconstructed photons are used to define CRs in this analysis and are required to have  $p_T > 10$  GeV,  $|\eta| < 2.37$  and satisfy the ‘tight’ criteria to be considered ‘baseline’. Signal photons are required to have  $p_T > 145$  GeV to ensure 100% efficiency of the photon trigger used to define a CR used to estimate the Z+jets background.

Missing transverse momentum is constructed as discussed in section 7.4.1 with the omission of reconstructed photons.

### 7.5.1.2 Signal Region Construction

Three classifications of signal regions are employed, labelled SRA, SRB and SRC, and are defined by decreasing  $\Delta m(\tilde{b}, \tilde{\chi}_1^0)$  as shown in figure 7.11.

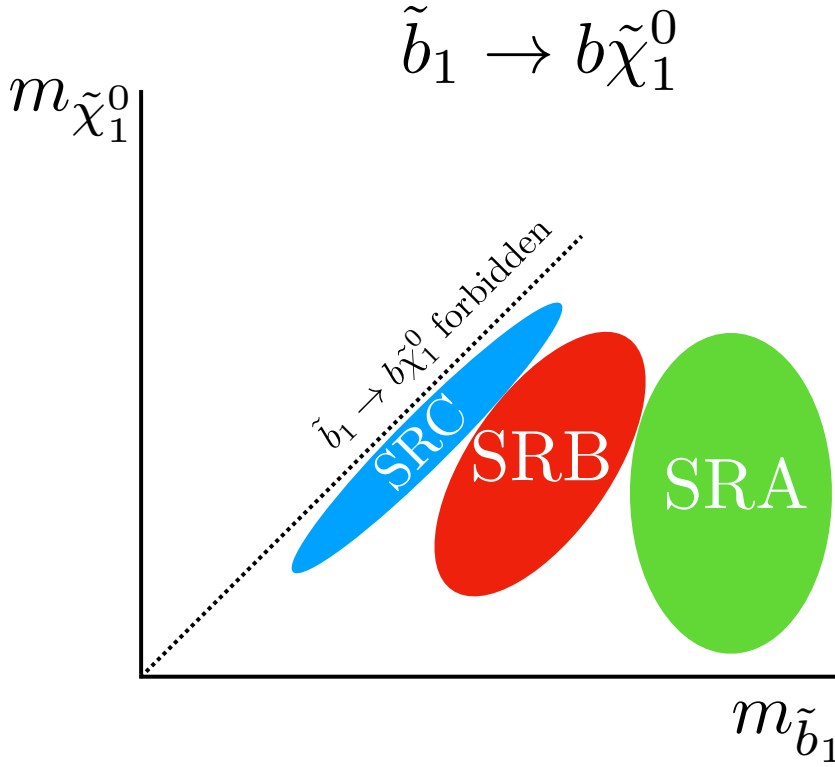


Fig. 7.11 Overview of the regions of  $m_{\tilde{\chi}_1^0}$ — $m_{\tilde{b}_1}$  phase space targeted by the three general classes of signal region utilised in the zero-lepton channel of the sbottom analysis searching for the process  $\tilde{b} \rightarrow b\tilde{\chi}_1^0$ . SRA targets a mass difference of  $> 250$  GeV between the  $\tilde{b}$  and  $\tilde{\chi}_1^0$ . SRB targets the intermediate region of  $50 \text{ GeV} < \Delta m(\tilde{b}, \tilde{\chi}_1^0) < 250$  GeV. Finally, SRC targets the compressed region where  $\Delta m(\tilde{b}, \tilde{\chi}_1^0) < 50$  GeV.

Five SRs are employed by the analysis based on the three targeted regions of the  $m_{\tilde{\chi}_1^0}$ — $m_{\tilde{b}}$  phase space shown in figure 7.11. The SRA region shown in figure 7.11 is divided into three separate regions by varying the requirement on the  $m_{\text{CT}}$  variable defined in equation 7.9. All signal regions used in the analysis are fully defined in table 7.3.

## 7.5 Third Generation SUSY Production Resulting in $b$ -Jets and $E_T^{\text{miss}}$

Table 7.3 Signal regions constructed for the zero-lepton channel of the sbottom analysis [141], characterised by the mass difference between the  $\tilde{b}$  and  $\tilde{\chi}_1^0$ . SRA targets scenarios with high  $\Delta m(\tilde{b}, \tilde{\chi}_1^0)$ , SRC targets a low  $\Delta m(\tilde{b}, \tilde{\chi}_1^0)$ , while SRB targets the intermediate region. SRA is further divided into three regions by varying requirements on the  $m_{\text{CT}}$  variable.

Requirement	SRA-350	SRA-450	SRA-550	SRB	SRC
Baseline lepton veto					
$N_{\text{jets}}(p_{\text{T}} > 35 \text{ GeV})$	2-4	2-4	2-4	2-4	—
$N_{\text{jets}}(p_{\text{T}} > 20 \text{ GeV})$	—	—	—	—	2-5
$b$ -jets	$j_{1,2}$	$j_{1,2}$	$j_{1,2}$	any 2	$j_2$ and one of $j_{3-5}$
$p_{\text{T}}(j_1)$ [GeV]	$> 130$	$> 130$	$> 130$	$> 50$	$> 500$
$p_{\text{T}}(j_2)$ [GeV]	$> 50$	$> 50$	$> 50$	$> 50$	$> 20$
$p_{\text{T}}(j_4)$ [GeV]	$< 50$	$< 50$	$< 50$	—	—
$H_{\text{T}4}$ [GeV]	—	—	—	—	$< 70$
$E_T^{\text{miss}}$ [GeV]	$> 250$	$> 250$	$> 250$	$> 250$	$> 500$
$\frac{E_T^{\text{miss}}}{m_{\text{eff}}}$	$> 0.25$	$> 0.25$	$> 0.25$	—	—
$\Delta\phi(\text{jet}_{1-4}, \vec{E}_T^{\text{miss}})_{\text{min}}$	$> 0.4$	$> 0.4$	$> 0.4$	$> 0.4$	—
$\Delta\phi(\text{jet}_{1-2}, \vec{E}_T^{\text{miss}})_{\text{min}}$	—	—	—	—	$> 0.2$
$\Delta\phi(b_1, \vec{E}_T^{\text{miss}})$	—	—	—	$< 2.0$	—
$\Delta\phi(b_2, \vec{E}_T^{\text{miss}})$	—	—	—	$< 2.5$	—
$\Delta\phi(j_1, \vec{E}_T^{\text{miss}})$	—	—	—	—	$> 2.5$
$m_{jj}$ [GeV]	—	—	—	—	$> 200$
$m_{\text{CT}}$ [GeV]	$> 350$	$> 450$	$> 550$	—	—
$m_T^{\text{min}}(\text{jet}_{1-4}, E_T^{\text{miss}})$ [GeV]	—	—	—	$> 250$	—
$m_{\text{eff}}$ [GeV]	—	—	—	—	$> 1300$
$\mathcal{A}$	—	—	—	—	$> 0.8$

SRA, sensitive to the largest mass differences between the  $\tilde{b}$  and  $\tilde{\chi}_1^0$ , requires  $\Delta m(\tilde{b}, \tilde{\chi}_1^0) > 250 \text{ GeV}$ . SRA targets events with high  $E_T^{\text{miss}}$  and two  $b$ -jets and is further divided into three regions with increasing  $m_{\text{CT}}$  requirement, denoted ‘SRA-X’ where X represents the value of  $m_{\text{CT}}$  in GeV.

## Implementation of Jet Smearing in ATLAS SUSY Searches

---

SRB targets the intermediate region in figure 7.11 of  $50 \text{ GeV} < \Delta m(\tilde{b}, \tilde{\chi}_1^0) < 250 \text{ GeV}$ . In this region, the  $m_T^{\min}(\text{jet}_{1-4}, E_T^{\text{miss}})$  variable is heavily relied upon to reduce the  $t\bar{t}$  background by selecting  $m_T^{\min}(\text{jet}_{1-4}, E_T^{\text{miss}}) > 250 \text{ GeV}$ . Requiring a maximum of four jets removes contributions from hadronic  $t$ -decays and the multijet background. The  $Z + \text{jets}$  background contribution is minimised by requiring that  $|\Delta\phi(b_1, \vec{E}_T^{\text{miss}})| < 2.0$  and  $|\Delta\phi(b_2, \vec{E}_T^{\text{miss}})| < 2.5$  (where  $b_1$  and  $b_2$  are the two leading  $b$ -jets in the event).

SRC targets the ‘compressed’ case of  $\Delta m(\tilde{b}, \tilde{\chi}_1^0) < 50 \text{ GeV}$ , where due to the small mass difference between the produced  $\tilde{b}$  and  $\tilde{\chi}_1^0$  any final state with two  $b$ -tagged jets, zero leptons and significant  $E_T^{\text{miss}}$  from  $\tilde{\chi}_1^0$  is difficult to obtain. To mitigate this difficulty, SRC targets the production of a  $\tilde{b}$  pair in association with a high  $p_T$  non- $b$ -tagged jet arising from ISR. The produced  $\tilde{b}$  pair then receives a boost in momentum from recoil against the ISR jet before decaying to a similar mass  $\tilde{\chi}_1^0$  and a soft  $b$ -jet likely aligned with the now significant  $E_T^{\text{miss}}$  in the event. Additional requirements of a high  $p_T$  leading jet with  $p_T > 500 \text{ GeV}$ ,  $E_T^{\text{miss}} > 500 \text{ GeV}$  and  $\Delta\phi(j_1, E_T^{\text{miss}}) > 2.5$  are placed to reduce the potentially large background arising from  $t\bar{t}$  and  $W + \text{jets}$  production. Requirements on the minimum  $\Delta\phi$  between jets and  $E_T^{\text{miss}}$  in the event are relaxed for this signal region with respect to others in the analysis as the soft  $b$ -jets in the event are likely to be aligned with  $E_T^{\text{miss}}$  [141]. To mitigate the potential introduction of a large multijet background in SRC due to this, stringent requirements were placed on the asymmetry variable defined in equation 7.6. As the choice of relaxed minimum  $\Delta\phi$  between jets and  $E_T^{\text{miss}}$  in the event may introduce an additional contribution from the multijet background to the SR, the derivation of an estimate of this background with the Jet Smearing technique was prioritised.

In general, analyses place stringent requirements on  $\Delta\phi(\text{jet}, \vec{E}_T^{\text{miss}})_{\min}$  to reduce the multijet background contribution in SRs. SRC places a low requirement on the angular distribution of the leading two  $b$ -jets and  $\vec{E}_T^{\text{miss}}$  to consider events where the  $b$ -jets are of a lower momentum. As lowering this requirement would cause a higher acceptance of multijet events, accurate estimation of the multijet background was expected to be of a higher priority for this region than others in the analysis. The  $H_{T4}$  variable refers to the summed  $p_T$  of the fourth-highest momentum jet in the event and all lower momentum jets in the event, reducing the contribution of high jet multiplicity events in the SR.

## 7.5.2 Background Estimation

A set of dedicated kinematic regions were constructed for each major background in all signal regions, enriched in the relevant SM background process. The predicted observed number of events from either MC simulated events or data driven predictions is normalised to the observed data event yields in each region. The background estimate in each CR is extrapolated to the corresponding SR. This section will focus exclusively on the techniques for background estimation in the zero-lepton channel of the analysis, although the corresponding description of the background estimation used for the one-lepton channel of the analysis is available in [141].

The constructed regions targeting major non-QCD backgrounds in the SRA, SRB and SRC regions are defined in appendix C. Major backgrounds are largely characterised by  $Z$ +jet events, single  $t$ ,  $t\bar{t}$  pair production, the associated production of a  $t\bar{t}$  pair with a  $W$  or  $Z$  boson (denoted by  $t\bar{t}V$ ) and  $W$ +jet events. The production of a  $Z$  boson decaying to a neutrino-antineutrino pair in addition to  $b$ -quarks is the dominant background in all signal regions of the zero-lepton channel of the analysis and is estimated using same-flavour opposite-sign (SFOS) pairs of leptons with an invariant mass in the range 76-106 GeV [141].

### 7.5.2.1 Multijet Background Estimation

The contribution from multijet events was estimated using the Jet Smearing technique introduced in chapter 6. For the purposes of generating an estimate of the expected number of multijet events in the SRs, a dedicated CR was established for each SR targeting multijet events. VRs were constructed between control and SRs to ensure adequate background estimation [141].

A collection of pseudo-data was generated by selecting seed events with  $E_T^{\text{miss}}$  significance  $S$  as defined in equation 6.4 with  $M = 8$  GeV and relaxed requirements on this variable depending upon the number of  $b$ -tagged jets in the event. Additionally, systematic variations were constructed to loosen or tighten the requirement on  $S$  to take into consideration the systematic uncertainty associated with the choice of seed events as described in section 6.5.4. The nominal and systematic variations of  $S$  are shown in table 7.4. The multijet estimate derived from the use of the jet smearing technique has an additional conservative 30% systematic uncertainty added in quadrature. Requirements

## Implementation of Jet Smearing in ATLAS SUSY Searches

---

were also placed upon the value of  $E_T^{\text{miss}}/\langle p_T \rangle$ , where  $\langle p_T \rangle$  considers all selected jets within seed events. Lowering the requirement on this variable increases the presence of well-measured dijet-like topologies and its use was inspired by the dijet balance analysis discussed in section 6.4.1.

Table 7.4 Nominal and systematic variations of the seed selection requirements used to generate collections of pseudo-data with the Jet Smearing technique. Collections of pseudo-data are then used in place of MC simulated events to normalise the background estimate to observed data yields in dedicated control regions.

Seed Selection	$S$ [ $\text{GeV}^{1/2}$ ]	$E_T^{\text{miss}}/\langle p_T \rangle$
$S_{\text{nominal}}$	$< (0.2 + 0.01 \times N_{b\text{-jet}})$	$< 0.2$
$S_{\text{up}}$	$< (0.6 + 0.2 \times N_{b\text{-jet}})$	—
$S_{\text{down}}$	$< 0.1$	$< 0.07$

Three CRs, shown in table 7.5, were constructed to provide an estimate of the multijet contribution in each of the three categories of signal region, denoted CRqX where ‘X’ refers to the class of SR (A, B or C).

## 7.5 Third Generation SUSY Production Resulting in $b$ -Jets and $E_T^{\text{miss}}$

Table 7.5 Selection requirements used to define the QCD control regions in the zero-lepton channel of the sbottom analysis [141].

Requirement	CRqA	CRqB	CRqC
$N_{\text{leptons}}$ (baseline)	0	0	0
$N_{\text{photons}}$	—	0	—
$N_{\text{jets}}(p_T > 35 \text{ GeV})$	2-4	2-4	—
$N_{\text{jets}}(p_T > 20 \text{ GeV})$	—	—	2-5
$N_{b\text{-jets}}$	2	2	2
$b$ -jets	$j_1$ and $j_2$	—	$j_2$ and one of $j_{3-5}$
$E_T^{\text{miss}}$ [GeV]	$> 250$	$> 250$	[250 – 500]
$m_{\text{eff}}$ [GeV]	—	—	$> 1300$
$E_T^{\text{miss}}/m_{\text{eff}}$	$< 0.25$	—	—
$m_{jj}$ [GeV]	$> 200$	—	$> 200$
$p_T(j_1)$ [GeV]	$> 130$	$> 50$	$> 500$
$p_T(j_2)$ [GeV]	$> 50$	$> 50$	—
$p_T(j_4)$ [GeV]	$< 50$	—	$< 50$
$p_T(b_2)$ [GeV]	—	$> 35$	—
$H_{T4}$ [GeV]	—	—	$< 70$
$\Delta\phi(\text{jet}_{1-4}, \vec{E}_T^{\text{miss}})_{\text{min}}$	$< 0.4$	$< 0.1$	—
$\Delta\phi(\text{jet}_{1-2}, \vec{E}_T^{\text{miss}})_{\text{min}}$	—	—	$< 0.1$
$\Delta\phi(b_1, \vec{E}_T^{\text{miss}})$	—	$< 2.0$	—
$\Delta\phi(b_2, \vec{E}_T^{\text{miss}})$	—	$< 2.5$	—
$\Delta\phi(j_1, \vec{E}_T^{\text{miss}})$	—	—	$> 2.5$
$\mathcal{A}$	—	—	$< 0.8$

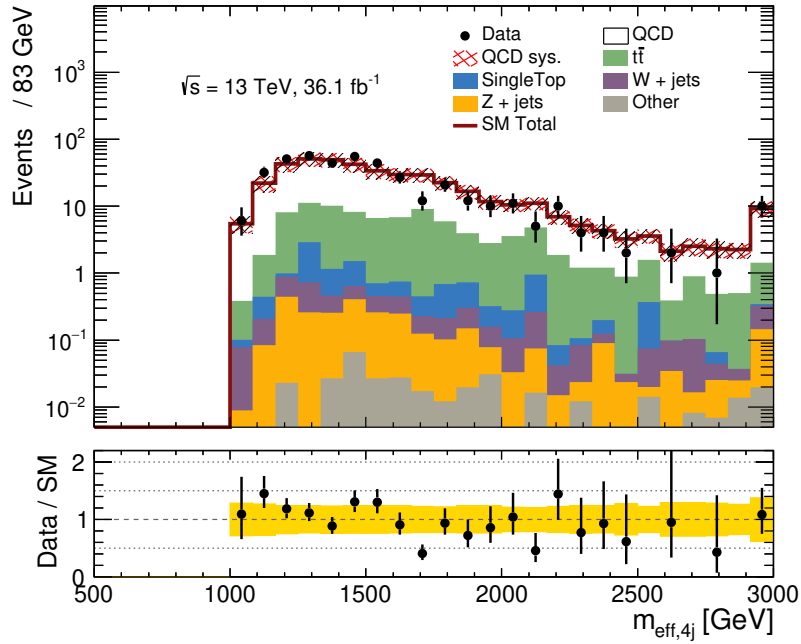
## Implementation of Jet Smearing in ATLAS SUSY Searches

---

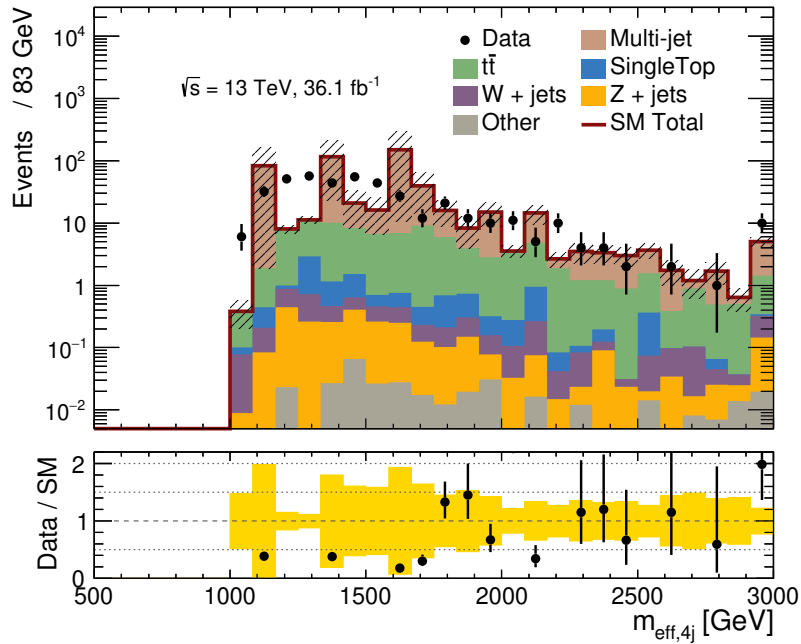
Generally, the multijet CRs used by the analysis are defined by inverting the requirement on key variables that reject multijet background events in the SRs. CRqA is constructed by inverting the requirements on  $\Delta\phi(\text{jet}_{1-4}, \vec{E}_T^{\text{miss}})_{\text{min}}$  and  $E_T^{\text{miss}}/m_{\text{eff}}$  while removing any requirement on the  $m_{\text{CT}}$  variable. Requiring low  $\Delta\phi(\text{jet}_{1-4}, \vec{E}_T^{\text{miss}})_{\text{min}}$  increases the number of multijet events and the likelihood that at least one of the jets in the event is associated with the  $E_T^{\text{miss}}$ . CRqB mirrors the selection requirements of SRB while inverting the  $\Delta\phi(\text{jet}_{1-4}, \vec{E}_T^{\text{miss}})_{\text{min}}$  requirement and removing the  $m_T^{\text{min}}(\text{jet}_{1-4}, E_T^{\text{miss}})$  requirement to increase the number of events in the CR. CRqC inverts the requirement on  $\Delta\phi(\text{jet}_{1-2}, \vec{E}_T^{\text{miss}})_{\text{min}}$ . The multijet background estimate for the SRC region was considered to be of particular importance as the region uses a relaxed requirement on  $\Delta\phi(\text{jet}_{1-2}, \vec{E}_T^{\text{miss}})_{\text{min}}$  with respect to other SRs, leading to potentially significant contamination of the SR by multijet events. The selection requirements defining all multijet CRs are provided in table 7.5.

Multijet background estimates derived from the Jet Smearing technique were directly compared with the number of multijet events predicted by dijet MC simulated events. All other background processes in the CRqX SRs were estimated using MC simulated events. The estimated SM background is shown by the coloured histograms in the following figures. In the case of the  $t\bar{t}$  estimate, events resulting from all  $t\bar{t}$  decays except fully hadronic decays are shown. Figures 7.12, 7.14 and 7.16 show the estimated and observed distributions of the  $m_{\text{eff}}$  variable in each CR, constructed using the four highest- $p_T$  jets in the event, for both cases. Figures 7.13, 7.15 and 7.17 compare the distributions of  $\Delta\phi(j_1, \vec{E}_T^{\text{miss}})$  for both cases. Uncertainties are shown within the yellow bands in all figures. Multijet estimates derived from the Jet Smearing technique in figures 7.12a–7.17a show the combined statistical uncertainty and systematic uncertainties arising from variation of the seed selection variable in addition to a 30% uncertainty. Multijet estimates using dijet MC simulated events in place of pseudo-data in figures 7.12b–7.17b show the statistical uncertainty only.

## 7.5 Third Generation SUSY Production Resulting in $b$ -Jets and $E_T^{\text{miss}}$

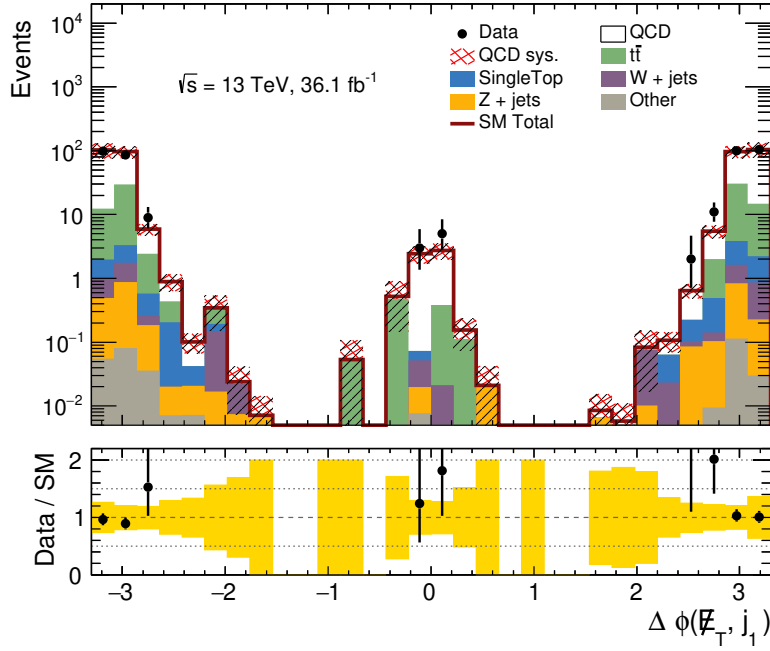


(a)

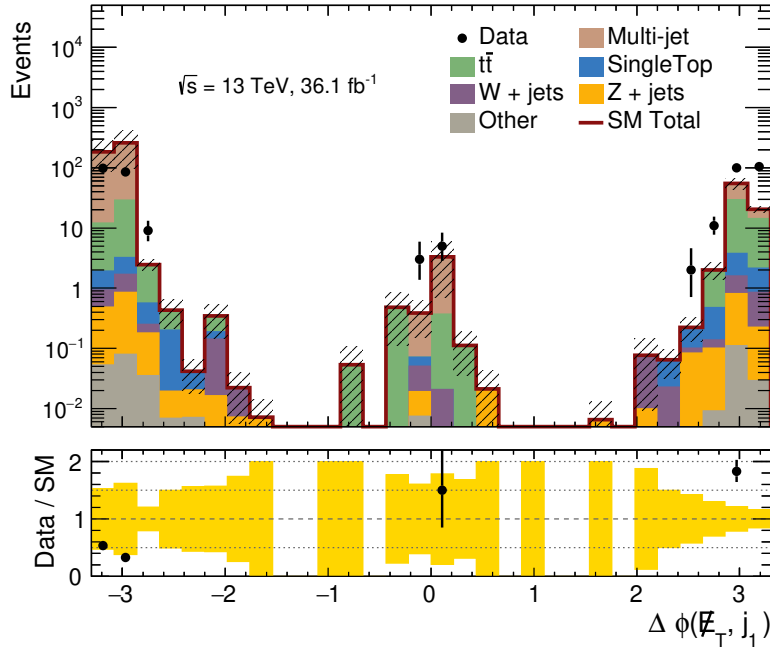


(b)

Fig. 7.12 Comparison of the  $m_{\text{eff}}(N_j)$  variable distribution with  $N = 4$  in the QCD control region for the SRA regions, with multijet events derived from (a) Jet Smearing and (b) dijet MC events. The white distribution in (a) represents the collection of pseudo-data generated with the Jet Smearing technique. The yellow band in (a) shows the combined statistical and systematic uncertainty. In (b) the yellow band represents the statistical uncertainty only. Pseudo-data jet  $\phi$  distributions have been calibrated to data.



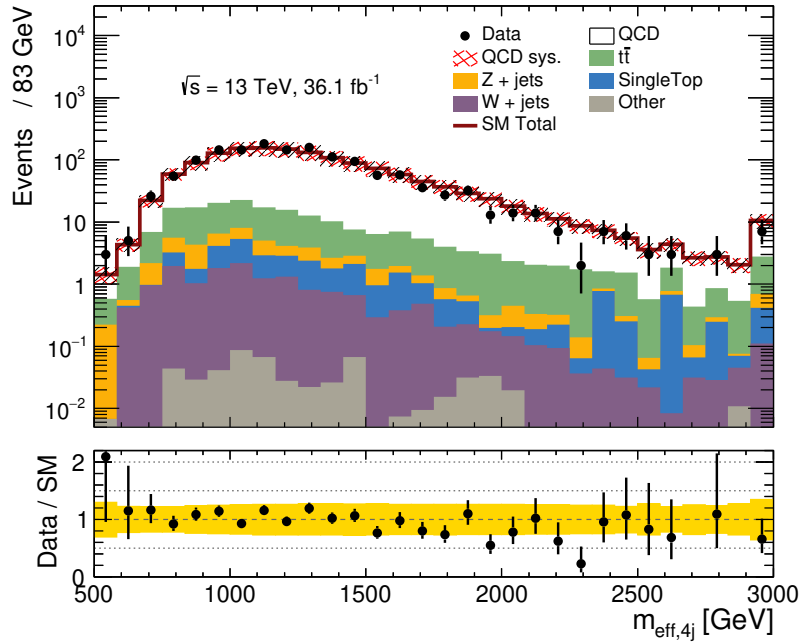
(a)



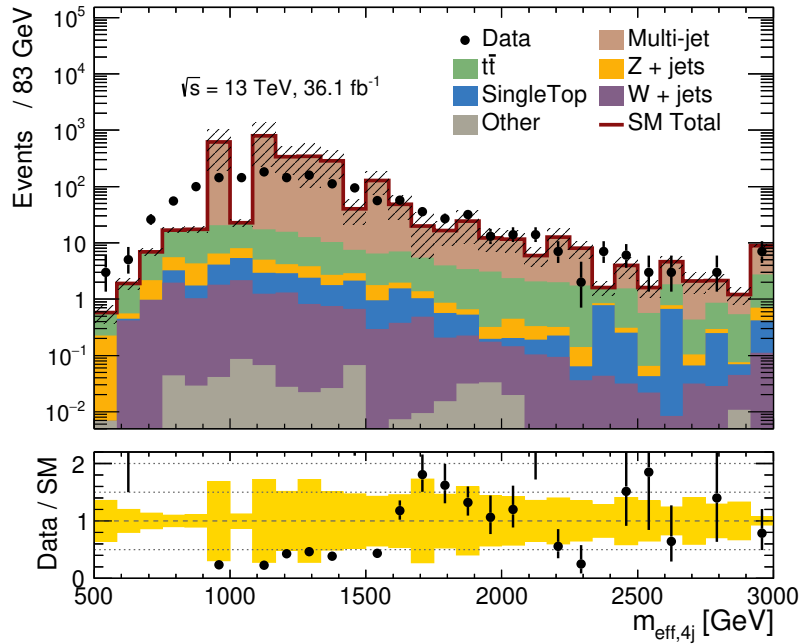
(b)

Fig. 7.13 Comparison of the  $\Delta\phi(j_1, \vec{E}_T^{\text{miss}})$  variable distribution in the QCD control region for SRA, with multijet events derived from (a) Jet Smearing and (b) dijet MC events. The white distribution in (a) represents the collection of pseudo-data generated with the Jet Smearing technique. The yellow band in (a) shows the combined statistical and systematic uncertainty. In (b) the yellow band represents the statistical uncertainty only. Pseudo-data jet  $\phi$  distributions have been calibrated to data.

## 7.5 Third Generation SUSY Production Resulting in $b$ -Jets and $E_T^{\text{miss}}$

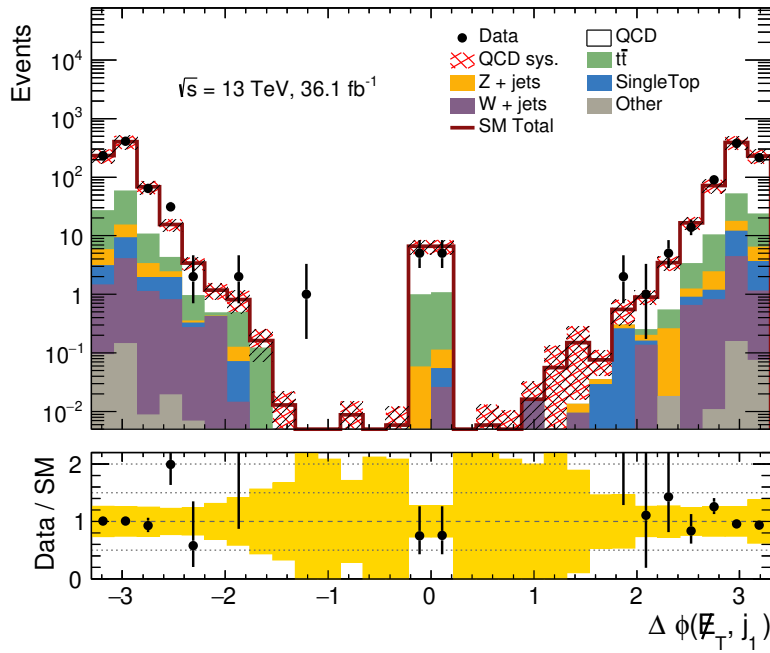


(a)

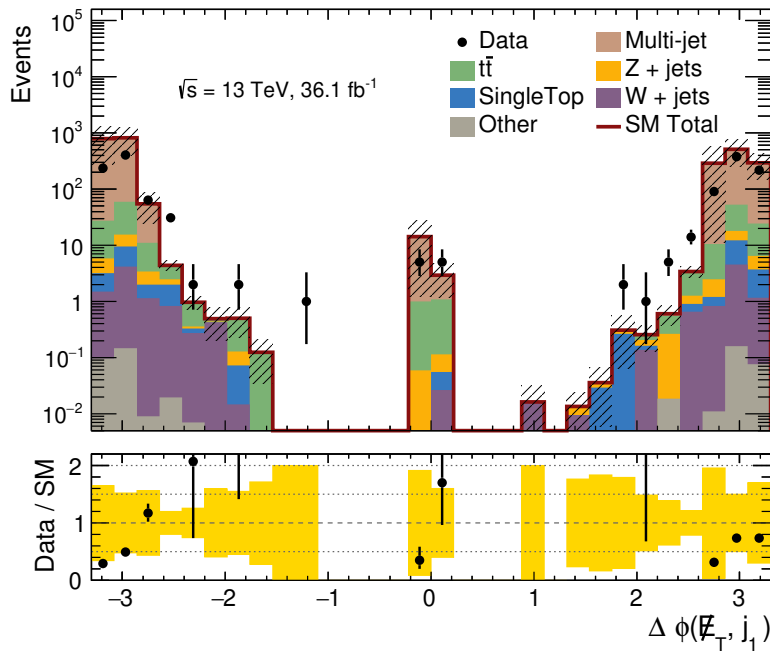


(b)

Fig. 7.14 Comparison of the  $m_{\text{eff}}(N_j)$  variable distribution with  $N = 4$  in the QCD control region for the SRB region, with multijet events derived from (a) Jet Smearing and (b) dijet MC events. The white distribution in (a) represents the collection of pseudo-data generated with the Jet Smearing technique. The yellow band in (a) shows the combined statistical and systematic uncertainty. In (b) the yellow band represents the statistical uncertainty only. Pseudo-data jet  $\phi$  distributions have been calibrated to data.



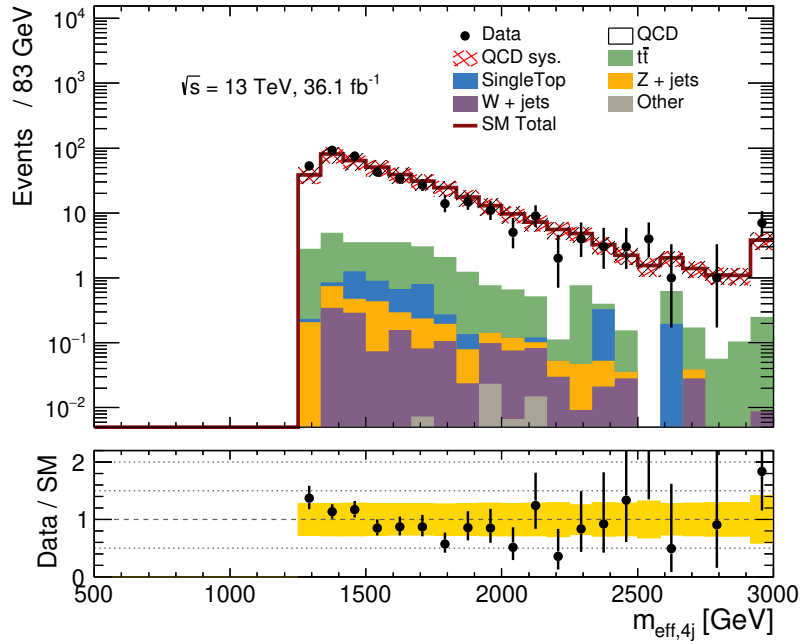
(a)



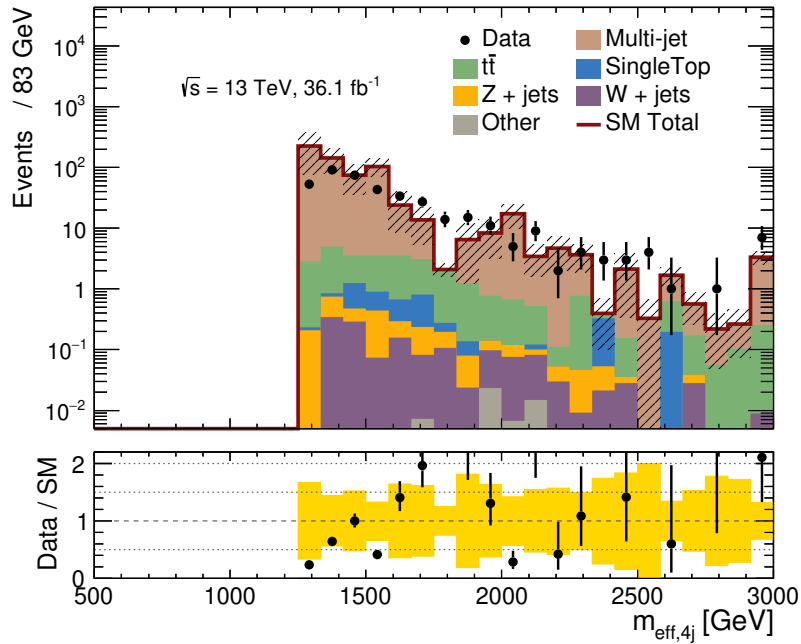
(b)

Fig. 7.15 Comparison of the  $\Delta\phi(j_1, \vec{E}_T^{\text{miss}})$  variable distribution in the QCD control region for SRB, with multijet events derived from (a) Jet Smearing and (b) dijet MC events. The white distribution in (a) represents the collection of pseudo-data generated with the Jet Smearing technique. The yellow band in (a) shows the combined statistical and systematic uncertainty. In (b) the yellow band represents the statistical uncertainty only. Pseudo-data jet  $\phi$  distributions have been calibrated to data.

## 7.5 Third Generation SUSY Production Resulting in $b$ -Jets and $E_T^{\text{miss}}$

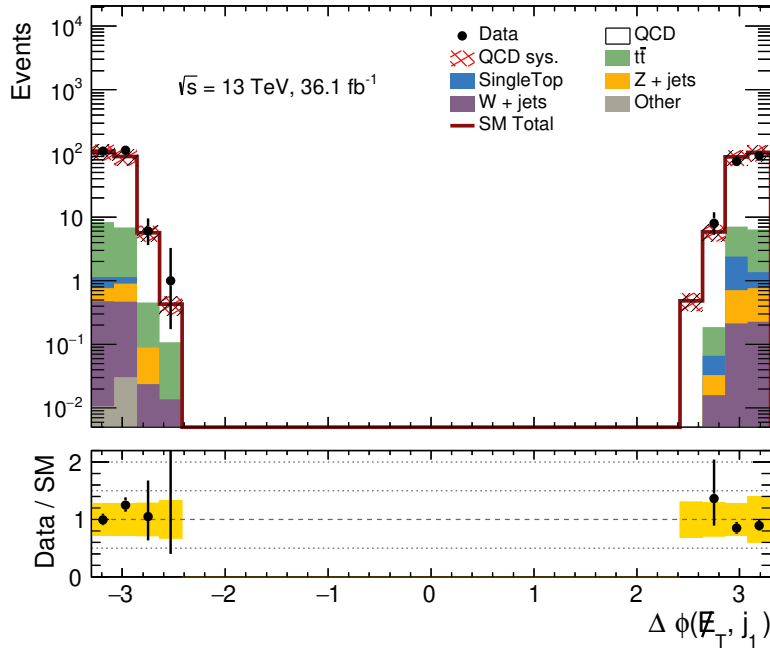


(a)

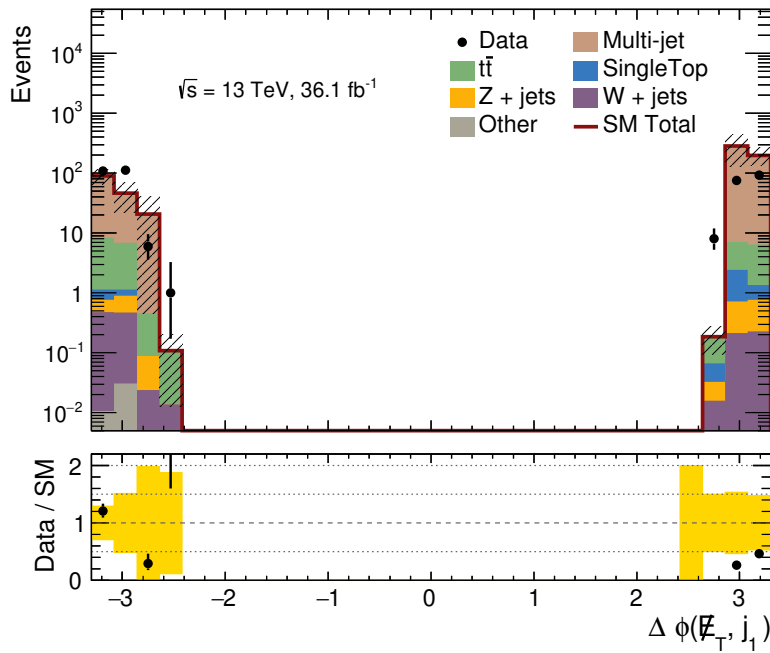


(b)

Fig. 7.16 Comparison of the  $m_{\text{eff}}(N_j)$  variable distribution with  $N = 4$  in the QCD control region for SRC, with multijet events derived from (a) Jet Smearing and (b) dijet MC events. The white distribution in (a) represents the collection of pseudo-data generated with the Jet Smearing technique. The yellow band in (a) shows the combined statistical and systematic uncertainty. In (b) the yellow band represents the statistical uncertainty only. Pseudo-data jet  $\phi$  distributions have been calibrated to data.



(a)



(b)

Fig. 7.17 Comparison of the  $\Delta\phi(j_1, \vec{E}_T^{\text{miss}})$  variable distribution in the QCD control region for SRC, with multijet events derived from (a) Jet Smearing and (b) dijet MC events. The white distribution in (a) represents the collection of pseudo-data generated with the Jet Smearing technique. The yellow band in (a) shows the combined statistical and systematic uncertainty. In (b) the yellow band represents the statistical uncertainty only. Pseudo-data jet  $\phi$  distributions have been calibrated to data.

## 7.5 Third Generation SUSY Production Resulting in $b$ -Jets and $E_T^{\text{miss}}$

---

Pseudo-data underwent additional  $\phi$ -smearing (discussed in section 6.4.2) to ensure correct modelling of the jet- $\phi$  resolution in data. Corrections to the Gaussian core of the jet response were calculated with the dijet-balance analysis (section 6.4.1), although they were found to be of negligible importance at the time the analysis was performed. Corrections to the tail of the jet response were also not available at the time of the analysis and so are not shown in figures 7.12–7.17. In all cases the background estimate derived from the data-driven Jet Smearing technique is shown to produce a significantly improved data-estimate agreement with respect to that derived from MC-simulated events, highlighting the power of the Jet Smearing technique and its applicability within this analysis.

### 7.5.3 Results

After extrapolation of the estimate to SRs, the multijet background was found to be negligible in all regions investigated, with the large associated uncertainty having minimal impact on the total SM background estimate. The observed and expected number of events for each signal region is shown in table 7.6, with the number of expected multijet events highlighted.

Table 7.6 Number of observed and expected events with uncertainties in a selection of signal regions investigated in the analysis. Values taken from [166] and [141].

Signal Region	SRA350	SRA450	SRA550	SRB	SRC
Events Observed	81	24	10	45	7
Total Expected	$70 \pm 13$	$22 \pm 5$	$7.2 \pm 1.5$	$37 \pm 7$	$5.5 \pm 1.5$
Multijet Expected	$0.02 \pm 0.01$	$0.01 \pm 0.01$	$0.00 \pm 0.00$	$0.11 \pm 0.07$	$0.02 \pm 0.01$

No significant excess of events above the SM background was observed in any of the signal regions considered by the analysis. Figure 7.18 shows the expected and observed number of events for each signal region, with the relative excess or deficit of observed events compared to the background estimate shown in the lower panel. Backgrounds from multijet, diboson and rare events are combined in figure 7.18 where they are labelled as ‘others’. Diboson events do not account for more than 9.45% of the

## Implementation of Jet Smearing in ATLAS SUSY Searches

background prediction in any signal region of the zero lepton channel of the analysis discussed in this chapter [166].

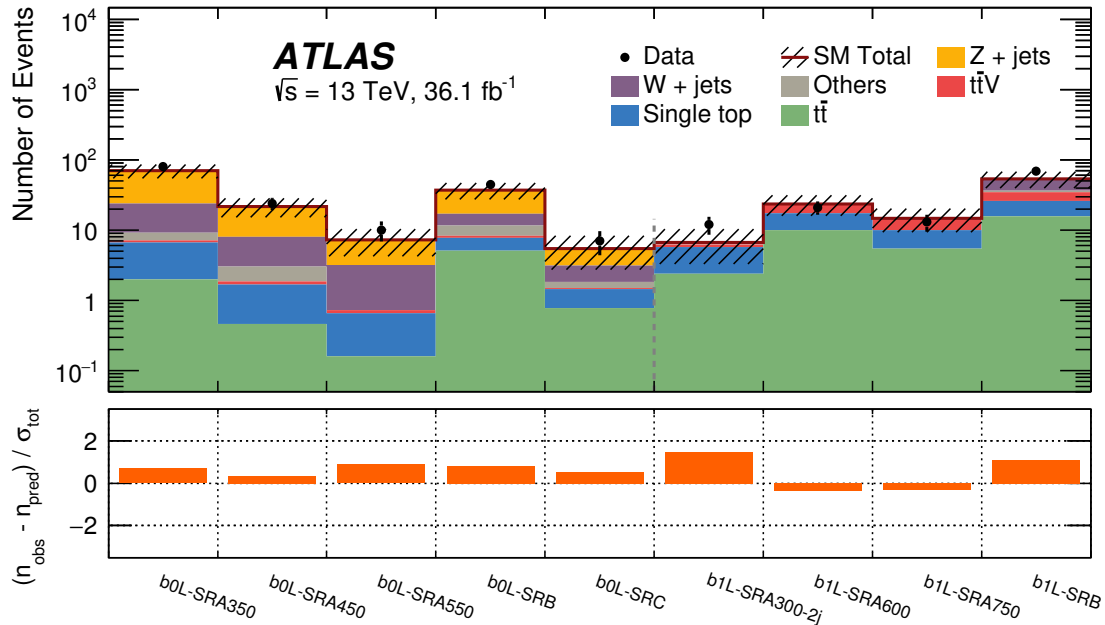


Fig. 7.18 Observed and expected events in each signal region of the sbottom analysis. Estimates of the expected number of background events are normalised to observed data in the control regions of the analysis and extrapolated with a background-only likelihood fit to the signal regions. Significant backgrounds are plotted separately, while minimal backgrounds from diboson, multijet and rare events are labelled ‘others’ and plotted in grey. The total uncertainty on the background estimate is shown by the hatched band and the pull is shown in the lower panel. Figure from [141].

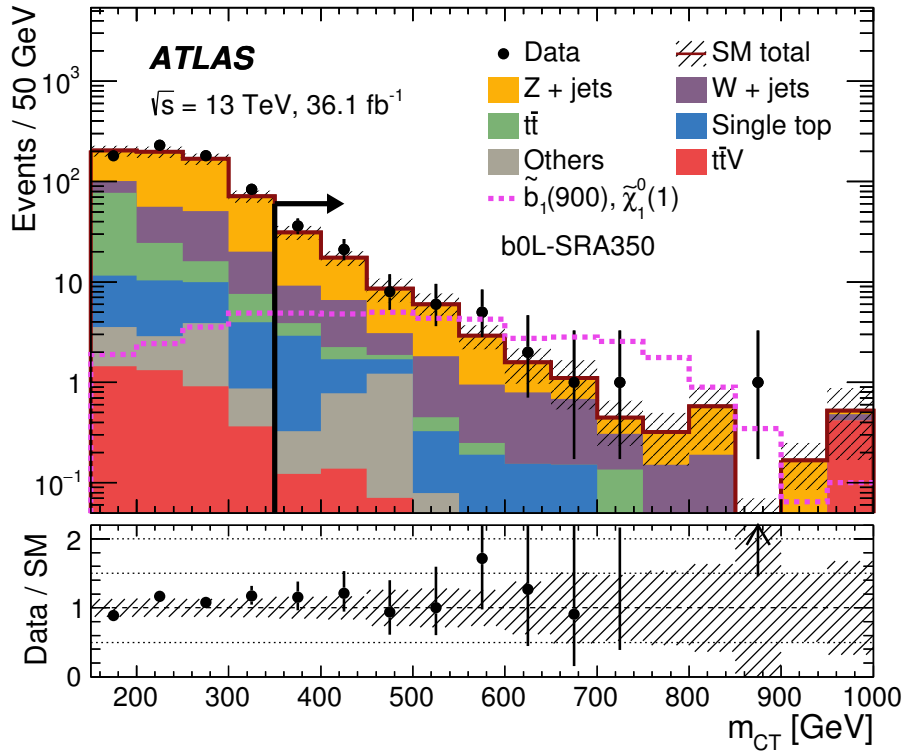


Fig. 7.19 Distributions of the  $m_{CT}$  variable in the SRA-350 signal region using  $36.1 \text{ fb}^{-1}$  of  $\sqrt{s} = 13 \text{ TeV}$  data, where all requirements defined in table 7.3 are applied except the  $m_{CT}$  selection itself, which is shown by the black arrow. Standard model background predictions are shown with coloured histograms, data is shown by black points and a simulated signal sample where  $[m_{\tilde{b}} = 900 \text{ GeV}, m_{\tilde{\chi}_1^0} = 1 \text{ GeV}]$  is shown by the dashed pink line. Figure from [141].

The potential separation of the simulated signal and background in SRA-350 using the  $m_{CT}$  variable defined in equation 7.9 is shown in figure 7.19, where the signal region is shown to the right of the arrow. The simulated signal sample shown is for the specific scenario with  $\tilde{b}$  and  $\tilde{\chi}_1^0$  masses, in GeV, shown in the figure. Observed data is shown in the signal region in black points and fails to show an excess above the SM in the SR.

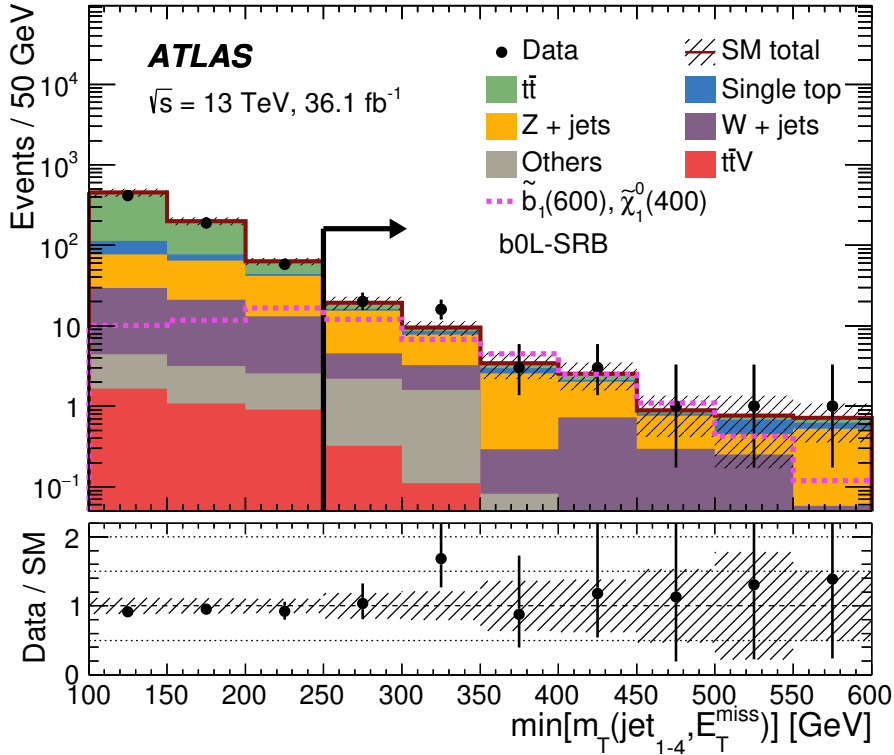


Fig. 7.20 Distributions of the  $m_T^{\min}(\text{jet}_{1-4}, E_T^{\text{miss}})$  variable defined in section 7.2.11 within the SRB signal region using  $36.1 \text{ fb}^{-1}$  of  $\sqrt{s} = 13 \text{ TeV}$  data, where all requirements defined in table 7.3 are applied except the  $m_T^{\min}(\text{jet}_{1-4}, E_T^{\text{miss}})$  selection itself, which is shown by the black arrow. Standard model background predictions are shown with coloured histograms, data is shown by black points and a simulated signal sample where  $[m_{\tilde{b}} = 600 \text{ GeV}, m_{\tilde{\chi}_1^0} = 400 \text{ GeV}]$  is shown by the dashed pink line. Figure from [141].

Figure 7.20 shows the potential separation between a simulated signal and the SM background provided by the  $m_T^{\min}(\text{jet}_{1-4}, E_T^{\text{miss}})$  variable defined in section 7.2.11, where the signal region is shown to the right of the arrow and is fully defined in table 7.3. The simulated signal sample shown is for the specific scenario with  $\tilde{b}$  and  $\tilde{\chi}_1^0$  masses, in GeV, shown in the figure. Observed data is shown in the signal region in black points and fails to show an excess above the SM in the SR.

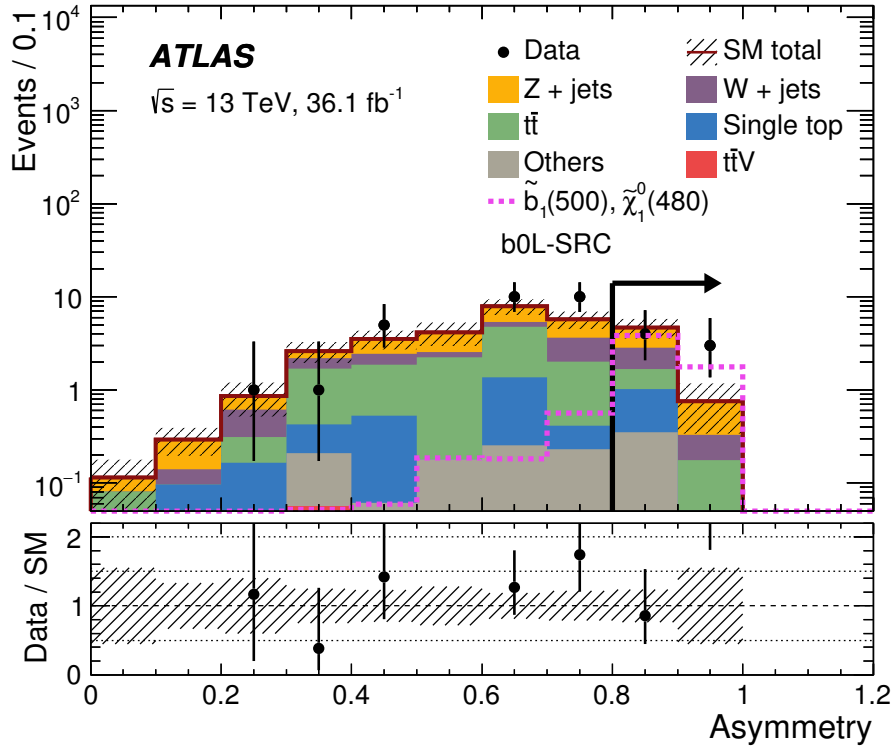


Fig. 7.21 Distributions of the asymmetry variable defined in equation 7.6 within the SRC signal region using  $36.1 \text{ fb}^{-1}$  of  $\sqrt{s} = 13 \text{ TeV}$  data, where all requirements defined in table 7.3 are applied except the selection on asymmetry itself, which is shown by the black arrow. Standard model background predictions are shown with coloured histograms, data is shown by black points and a simulated signal sample where  $[m_{\tilde{b}} = 500 \text{ GeV}, m_{\tilde{\chi}_1^0} = 480 \text{ GeV}]$  is shown by the dashed pink line. Figure from [141].

The potential separation between a simulated signal and the SM background in SRC provided by the asymmetry variable defined in equation 7.6 is shown in figure 7.21 where the signal region is shown to the right of the arrow and is fully defined in table 7.3. The simulated signal sample shown is for the specific scenario with  $\tilde{b}$  and  $\tilde{\chi}_1^0$  masses, in GeV, shown in the figure. Observed data is shown in the signal region in black points and fails to show an excess above the SM in the SR.

The absence of a discovery lead to the setting of exclusion limits of  $\tilde{b}_1$  and  $\tilde{\chi}_1^0$  masses at the 95% confidence level. Figures 7.22 and 7.23 show the exclusion limits obtained for two SUSY production scenarios in the  $m_{\tilde{b}_1} - m_{\tilde{\chi}_1^0}$  plane. The scenario shown in figure 7.22 tested by the zero-lepton channel of this analysis corresponds to  $\tilde{b}_1$  production

## Implementation of Jet Smearing in ATLAS SUSY Searches

with subsequent prompt decay via  $\tilde{b}_1 \rightarrow b\tilde{\chi}_1^0$ , while another scenario shown in figure 7.23 combines the zero-lepton and one-lepton channels of the analysis to consider the processes  $\tilde{b}_1 \rightarrow b\tilde{\chi}_1^0$  and  $\tilde{b}_1 \rightarrow t\tilde{\chi}_1^\pm$  occurring with an equal probability for each decay and assumes  $\Delta m(\tilde{\chi}_1^\pm, \tilde{\chi}_1^0) \sim 1$  GeV.

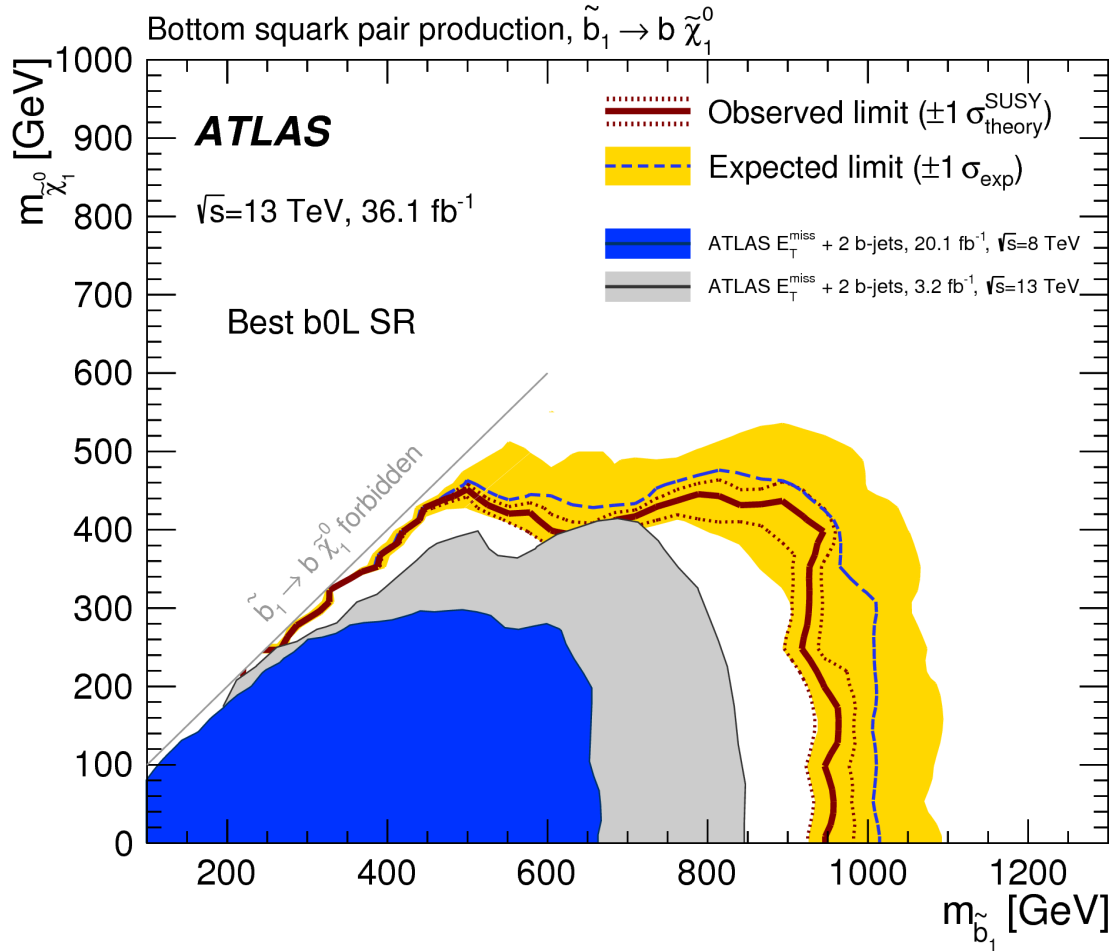


Fig. 7.22 Observed and expected exclusion limits at the 95% confidence level in the  $m_{\tilde{b}_1} - m_{\tilde{\chi}_1^0}$  plane for  $\tilde{b}_1$  production and subsequent decay via  $\tilde{b}_1 \rightarrow b\tilde{\chi}_1^0$  with a branching ratio of 100%. Exclusion limits from previous ATLAS searches are shown by the shaded blue and grey areas. Expected exclusion limits are shown by a dashed blue line, with a yellow band showing the  $\pm 1\sigma$  uncertainty on this value at each point. Limits derived from observed data are shown by the solid dark brown line, with dotted brown lines showing the  $\pm 1\sigma$  variation of the theoretical uncertainty on the cross-section of SUSY production process. The boundary of the kinematically forbidden region where  $\tilde{\chi}_1^0$  is more massive than  $\tilde{b}$  is shown by the diagonal grey line. Figure from [141].

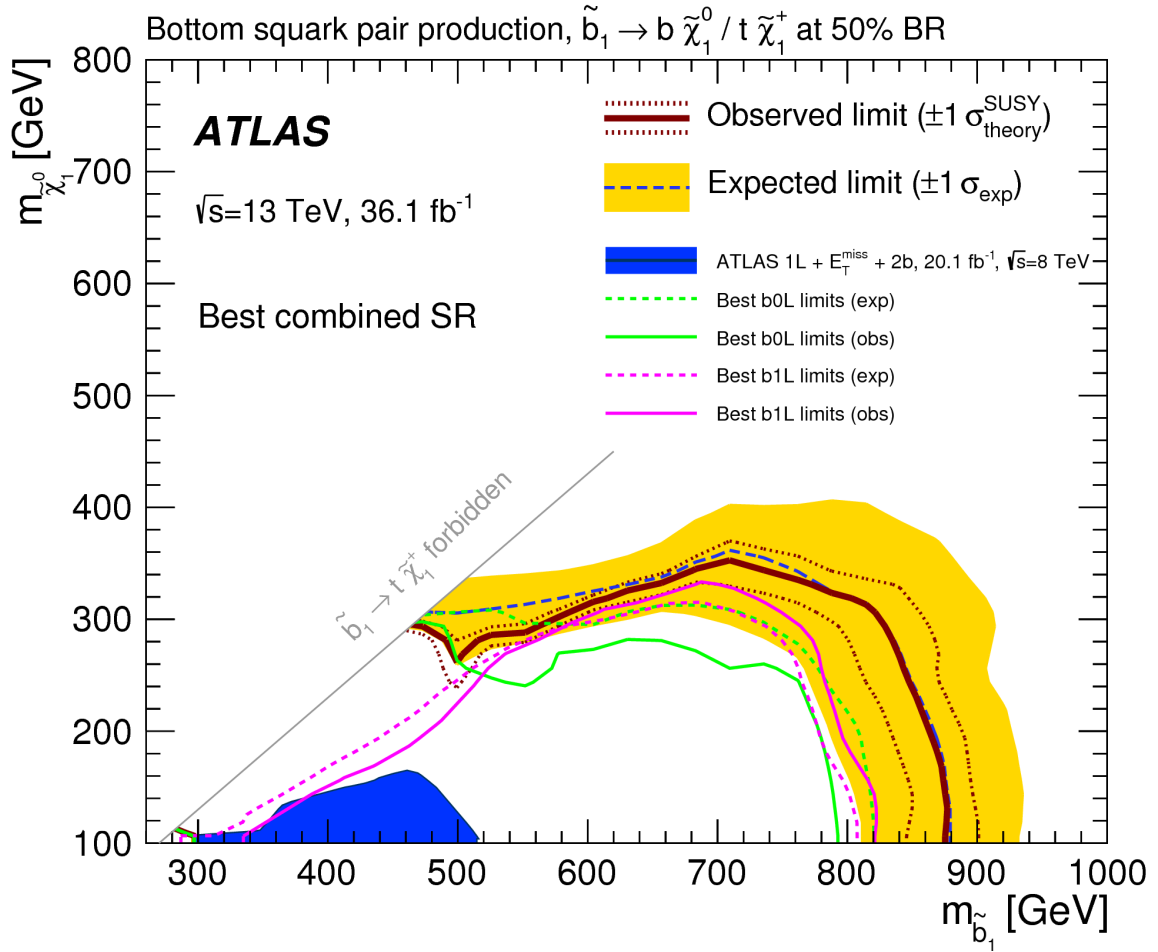


Fig. 7.23 Observed and expected exclusion limits at the 95% confidence level in the  $m_{\tilde{b}_1} - m_{\tilde{\chi}_1^0}$  plane for  $\tilde{b}_1$  production and subsequent decay via  $\tilde{b}_1 \rightarrow b \tilde{\chi}_1^0$  or  $\tilde{b}_1 \rightarrow t \tilde{\chi}_1^\pm$  with a branching ratio of 50% for each process. Exclusion limits from a previous ATLAS search is shown by the shaded blue area. The observed (expected) limits from the zero and one lepton channels of the analysis are shown by the green and pink solid (dashed) lines, respectively. Expected exclusion limits from a combination of both channels are shown by a dashed blue line, with a yellow band showing the  $\pm 1\sigma$  uncertainty on this value at each point. Observed exclusion limits from a combination of both channels are shown by the solid dark brown line, with dotted brown lines showing the  $\pm 1\sigma$  variation of the theoretical uncertainty on the cross-section of SUSY production process. The boundary of the kinematically forbidden region where  $\tilde{\chi}_1^0$  is more massive than  $\tilde{b}$  is shown by the diagonal grey line. Figure from [141].

The direct decay scenario probed by the zero-lepton channel of the analysis excludes  $\tilde{b}_1$  masses up to 950 GeV for  $m_{\tilde{\chi}_1^0} < 420$  GeV, while scenarios involving mixed decays of

either  $\tilde{b}_1 \rightarrow b\tilde{\chi}_1^0$  or  $\tilde{b}_1 \rightarrow t\tilde{\chi}_1^\pm$  with equal probability exclude  $\tilde{b}_1$  masses up to 860 GeV for  $m_{\tilde{\chi}_1^0} < 250$  GeV [141].

## 7.6 Revised Multijet Estimate Uncertainty

After normalising the Jet Smearing derived multijet estimate in the CRs to the observed data, the estimated number of multijet events was extrapolated to the SR associated with each CR and was found to be negligible in all SRs. The multijet background estimate used in this analysis was generated using the Jet Smearing technique detailed in chapter 6 with corrections to the  $\phi$  distribution of pseudo-data jets derived in section 6.4.1.2. However, no corrections were applied to the Gaussian core due to the good agreement between pseudo-data and data in the asymmetry variable observed in figure 6.13. Corrections to the non-Gaussian tails of the jet response were not utilised by the analysis due to time constraints. Systematic uncertainties for the method were generated by either increasing or decreasing the kinematic requirements for events to be categorised as *seed* events as discussed in section 7.5.2.1 in addition to a conservative 30% systematic added in quadrature to the final uncertainty. This method omitted other sources of statistical uncertainty generated by the jet smearing technique.

After re-optimisation of several elements of the jet response calibration procedure discussed in section 6.4, the multijet estimate in this analysis was re-examined. Corrections to the Gaussian core were rederived and are discussed in section 6.4.1.2. As with the 2015 dataset, corrections to the Gaussian core of the jet response of *b*-veto events were observed to have a minimal impact. However, the increase in luminosity between the two sets of corrections allowed the *b*-tagged case to be explicitly treated and a set of corrections obtained. In both cases the procedure of fitting a Gaussian function to the data and pseudo-data asymmetry distributions was re-optimised to reduce the uncertainties associated with each correction parameter in equation 6.10. The list of parameters obtained from the fitting procedure is shown in table 6.4. Additionally, the calibration to the  $\phi$  distribution of pseudo-data events was rederived for the increased luminosity dataset as discussed in section 6.4.2.2. This set of corrections represented the first and only set of corrections to the  $\phi$  distribution of *b*-tagged pseudo-data events ever applied to ATLAS data. Corrections to the non-Gaussian tails of the jet response were generated and are discussed at length in section 6.4.3. These corrections

## 7.6 Revised Multijet Estimate Uncertainty

---

were made available as a set of jet response maps featuring an optimal non-Gaussian tail calibration in addition to a high and low systematic variation on the correction, accounting for the uncertainty in the estimation of the optimal correction. The systematic variations were interpreted as a weight, extracted from the systematic variation response maps during the application of the Jet Smearing technique and applied in the calculation of the total uncertainty in the analysis.

### 7.6.1 Multijet Contribution in SRC CRs

Updated estimates of the number of multijet events in SRC were generated by normalising the pseudo-data collection in a dedicated control region as described in section 7.5.2.1 and shown for several key variables in figures 7.24–7.27. The multijet estimate in table 7.8 labelled ‘Analysis’ (figure (a) in the following figures) considers a systematic variation on the seed event selection in addition to a flat 30% uncertainty and mirrors the approach taken by the original analysis. The nominal and high/low seed variations considered in this study were made less stringent than those used in the original analysis and are shown in table 7.7.

Table 7.7 Nominal and systematic variations of the seed selection requirements used to generate collections of pseudo-data in the revised calculation of the multijet estimate uncertainty.

Seed Selection	$S$ [GeV <sup>1/2</sup> ]	$E_T^{\text{miss}} / \langle p_T \rangle$
$S_{\text{nominal}}$	$< (0.3 + 0.01 \times N_{b\text{-jet}})$	—
$S_{\text{up}}$	$< (0.6 + 0.2 \times N_{b\text{-jet}})$	—
$S_{\text{down}}$	$< (0.2 + 0.01 \times N_{b\text{-jet}})$	$< 0.2$

The multijet estimate labelled as ‘Full’ (figure (b) in the following figures) in table 7.8 considers systematic uncertainties arising from corrections to the Gaussian core and non-Gaussian tails of the jet response in addition to statistical uncertainties from the number of applications of the smearing procedure and selected seed events, all of which are discussed in section 6.5. As the ‘Full’ case does not vary the choice of seed selection, the source of systematic uncertainty described in section 6.5.4 is not applied in this case.

## Implementation of Jet Smearing in ATLAS SUSY Searches

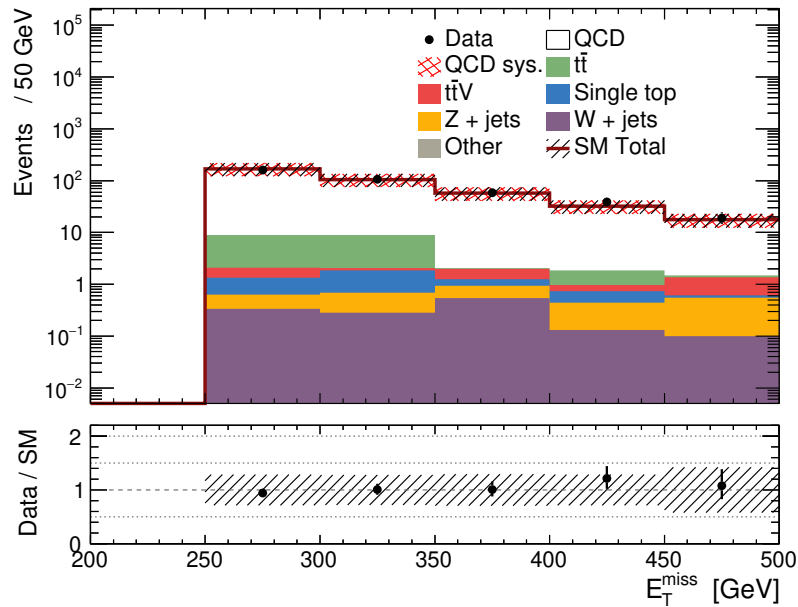
---

In both cases the multijet estimate is generated using a calibrated jet response containing corrections to the Gaussian core, pseudo-data  $\phi$  distributions and non-Gaussian tails detailed in sections 6.4.1.2, 6.4.2.2 and 6.4.3.3. Table 7.8 details the statistics located in the QCD control region targeting SRC. No contamination of signal events from an appropriate simulated signal sample with  $m_{\tilde{t}} = 500$  GeV and  $m_{\tilde{\chi}_1^0} = 480$  GeV were observed in SRC.

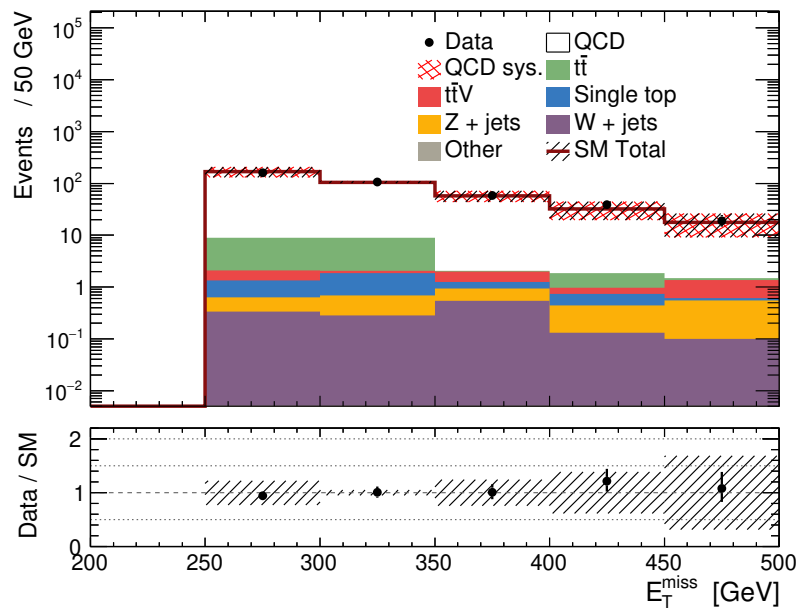
Table 7.8 The number of multijet events expected in the QCD control region for SRC, with the total estimate from MC and Jet Smearing and the number of observed data events provided. Uncertainties on the QCD estimate generated using the technique used by the analysis are labelled “Analysis”, whereas the uncertainties generated from all sources considered by the Jet Smearing technique are labelled “Full”.

Events	CRC-QCD	
	Analysis	Full
Observed Data	$382.00 \pm 19.54$	$382.00 \pm 19.54$
Total Background Estimate	$382.00 \pm 107.80$	$382.00 \pm 6.22$
QCD	$358.74 \pm 107.64$	$358.74 \pm 2.04$
$t\bar{t}$	$14.77 \pm 5.71$	$14.77 \pm 5.71$
$t\bar{t}V$	$2.68 \pm 1.07$	$2.68 \pm 1.07$
Single top	$2.56 \pm 0.81$	$2.56 \pm 0.81$
$Z$ + jets	$1.85 \pm 0.24$	$1.85 \pm 0.24$
$W$ + jets	$1.39 \pm 0.29$	$1.39 \pm 0.29$
Other	$0.00 \pm 0.00$	$0.00 \pm 0.00$

## 7.6 Revised Multijet Estimate Uncertainty

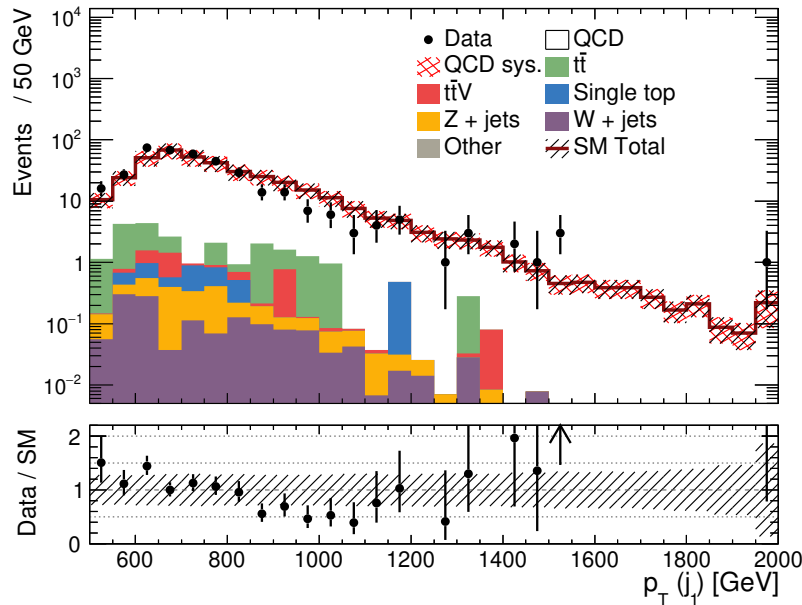


(a)

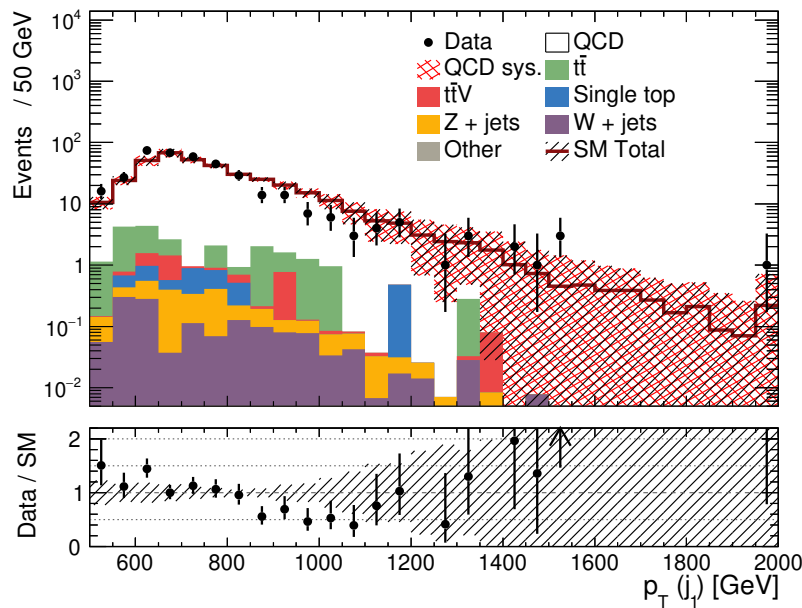


(b)

Fig. 7.24 Comparison of the  $E_T^{\text{miss}}$  distribution in the QCD control region for SRC with a multijet estimate from the fully calibrated jet smearing method. The uncertainty associated with multijet events is shown by the hatched band and is derived from the statistical uncertainty in addition to (a) the variation of seed selection in addition to a 30% uncertainty as within the original analysis and (b) from calibration to the Gaussian core, non-Gaussian tails and additional statistical uncertainties described in section 6.5. The white distribution represents the collection of pseudo-data generated with the Jet Smearing technique.



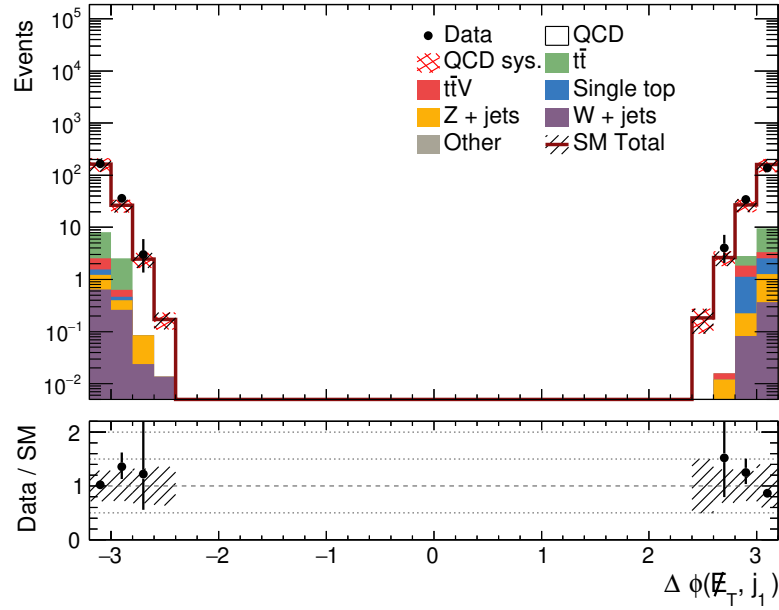
(a)



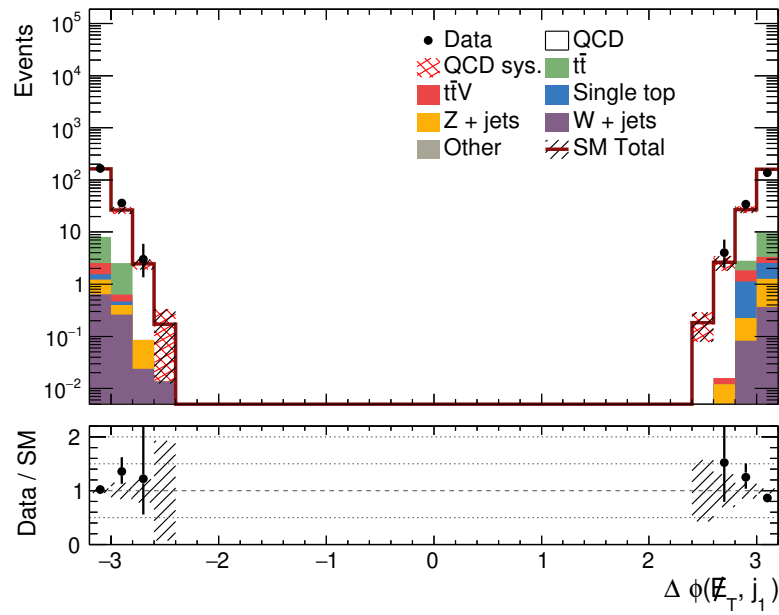
(b)

Fig. 7.25 Comparison of the  $p_T(j_1)$  distribution in the QCD control region for SRC with a multijet estimate from the fully calibrated jet smearing method. The uncertainty associated with multijet events is shown by the hatched band and is derived from the statistical uncertainty in addition to (a) the variation of seed selection in addition to a 30% uncertainty as within the original analysis and (b) from all other sources described in section 6.5. The white distribution represents the collection of pseudo-data generated with the Jet Smearing technique.

## 7.6 Revised Multijet Estimate Uncertainty

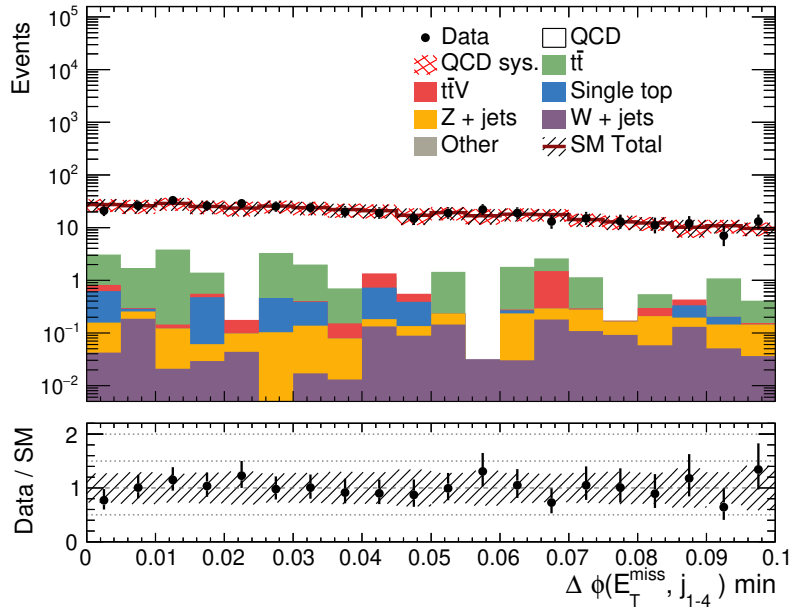


(a)

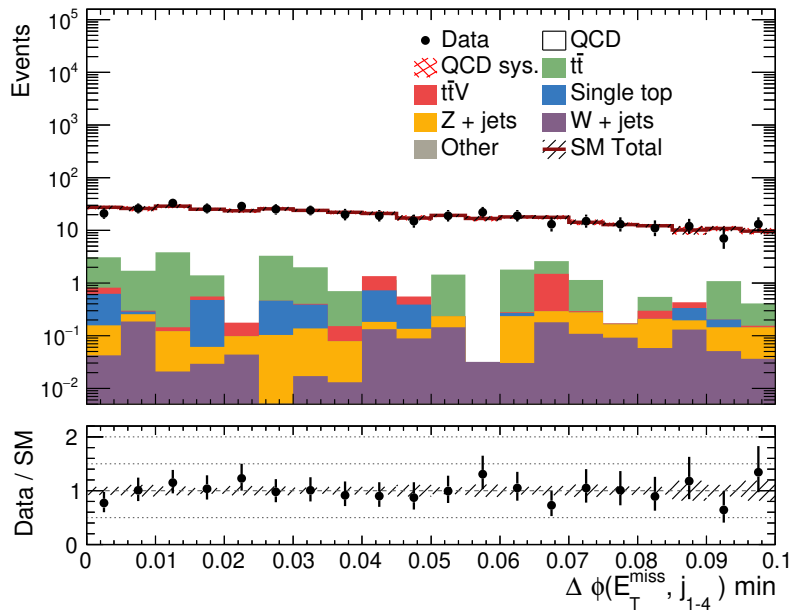


(b)

Fig. 7.26 Comparison of the  $\Delta\phi(j_1, \vec{E}_T^{\text{miss}})$  distribution in the QCD control region for SRC with a multijet estimate from the fully calibrated jet smearing method. The uncertainty associated with multijet events is shown by the hatched band and is derived from the statistical uncertainty in addition to (a) the variation of seed selection in addition to a 30% uncertainty as within the original analysis and (b) from all other sources described in section 6.5. The white distribution represents the collection of pseudo-data generated with the Jet Smearing technique.



(a)



(b)

Fig. 7.27 Comparison of the  $\Delta\phi(j_{1-4}, \vec{E}_T^{\text{miss}})_{\text{min}}$  distribution in the QCD control region for SRC with a multijet estimate from the fully calibrated jet smearing method. The uncertainty associated with multijet events is shown by the hatched band and is derived from the statistical uncertainty in addition to (a) the variation of seed selection in addition to a 30% uncertainty as within the original analysis and (b) from all other sources described in section 6.5. The white distribution represents the collection of pseudo-data generated with the Jet Smearing technique.

## 7.6 Revised Multijet Estimate Uncertainty

---

The uncertainties derived from the sources considered in section 6.5, with the omission of the variation of the seed selection variable, are observed to be significantly greater than those considered by the analysis at high values of  $p_T$ , while the opposite is true at lower  $p_T$ . Good agreement is observed between data and the SM estimate for  $E_T^{\text{miss}}$  and the  $\Delta\phi(j_{1-4}, \vec{E}_T^{\text{miss}})_{\text{min}}$  variable used by the analysis to reject multijet events in signal regions. The multijet estimate is then extrapolated to SRC after normalisation in the CR.

### 7.6.2 Event Yields in SRC

The multijet estimate presented in table 7.9 represents an update to both the multijet estimate and associated uncertainty in SRC with respect to those presented in table 7.6. Expected signal events for SRC are shown and are derived from a simulated signal sample where  $m_{\tilde{t}} = 500$  GeV and  $m_{\tilde{\chi}_1^0} = 400$  GeV, with masses chosen based on the observed exclusion limit shown in figure 7.22.

Table 7.9 The number of multijet events expected in SRC of the sbottom analysis, with the total estimate from MC and the number of observed data events provided. Uncertainties on the QCD estimate generated using the technique used by the analysis are labelled “Analysis”, whereas the uncertainties generated from all sources considered by the Jet Smearing technique are labelled “Full”.

Events	SRC	
	Analysis	Full
Observed Data	7	7
Total Background Estimate	$5.64 \pm 1.16$	$5.64 \pm 2.82$
Multijet	$0.18 \pm 0.07$	$0.18 \pm 2.57$
Expected signal	11.65	

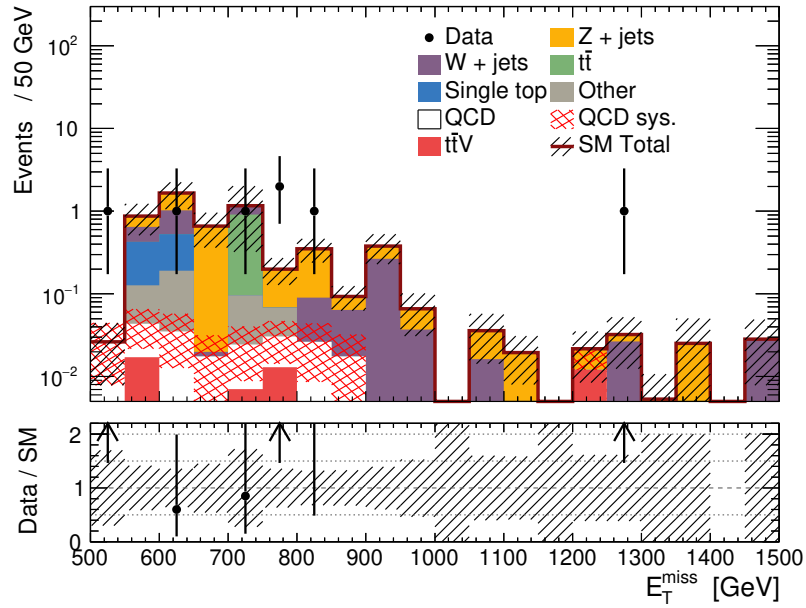
The number of estimated multijet events is increased in both cases with respect to the original estimate for SRC shown in table 7.6. The background fitting procedure was not performed in this comparison as this study aimed to directly compare the multijet estimate and associated uncertainty, which was not considered by the background fit

## Implementation of Jet Smearing in ATLAS SUSY Searches

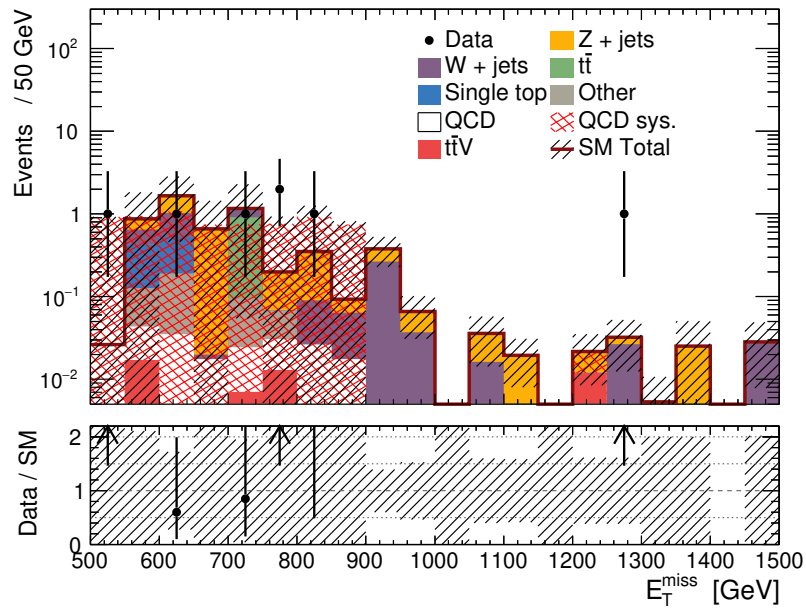
---

in the original analysis. Other SM background estimates are generated by scaling the estimate provided by MC simulated events to the result of the background fit obtained by the analysis. The uncertainty associated with the multijet estimate is greatly increased when considering the range of uncertainties introduced by the jet smearing technique in section 6.5, further reducing the significance of the already statistically insignificant observed excess of data over the estimated SM background in SRC. The effect of using the full set of uncertainties associated with the Jet Smearing technique in SRC of the sbottom analysis is directly compared with the uncertainties considered by the original analysis in figures 7.28–7.30.

## 7.6 Revised Multijet Estimate Uncertainty

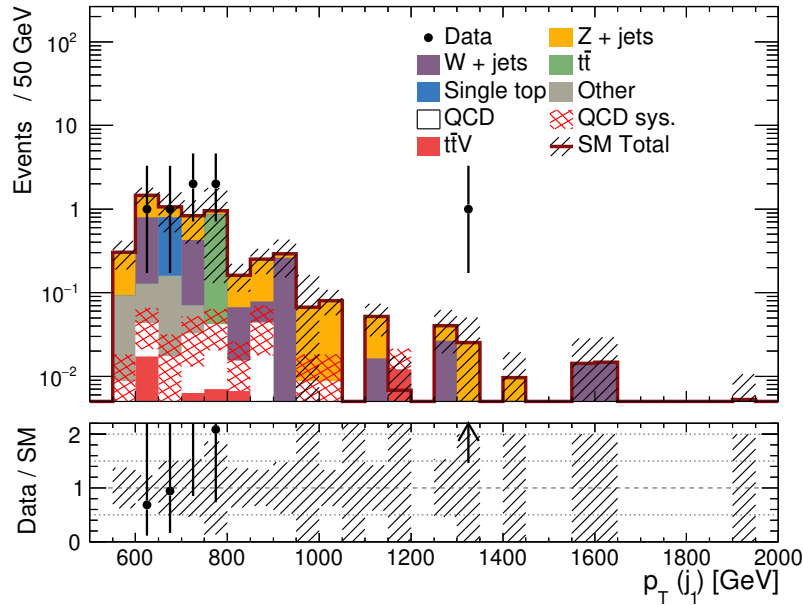


(a)

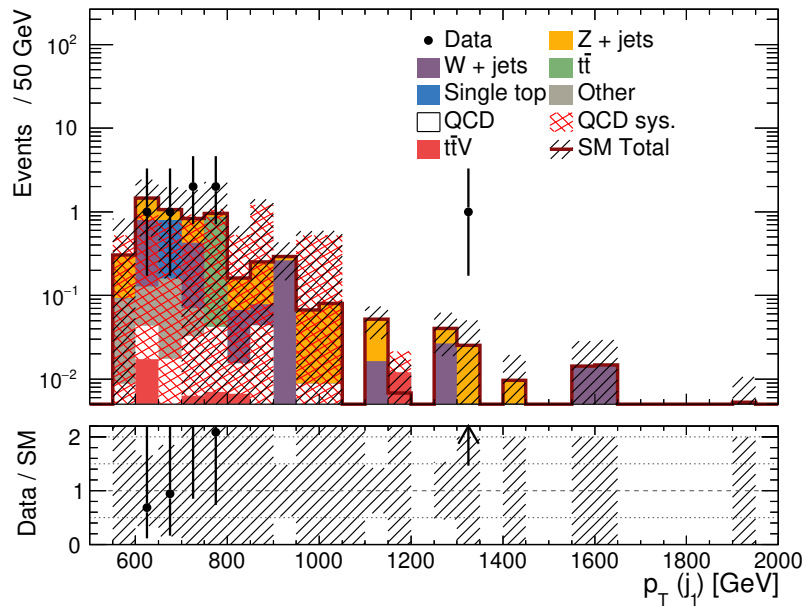


(b)

Fig. 7.28 Comparison of the  $E_T^{\text{miss}}$  distribution in SRC with a multijet estimate from the fully calibrated jet smearing method. The uncertainty associated with multijet events is shown by the red hatched band and is derived from the statistical uncertainty in addition to (a) the variation of seed selection and additional 30% uncertainty as within the original analysis and (b) from all other sources described in section 6.5. The white distribution represents the collection of pseudo-data generated with the Jet Smearing technique.



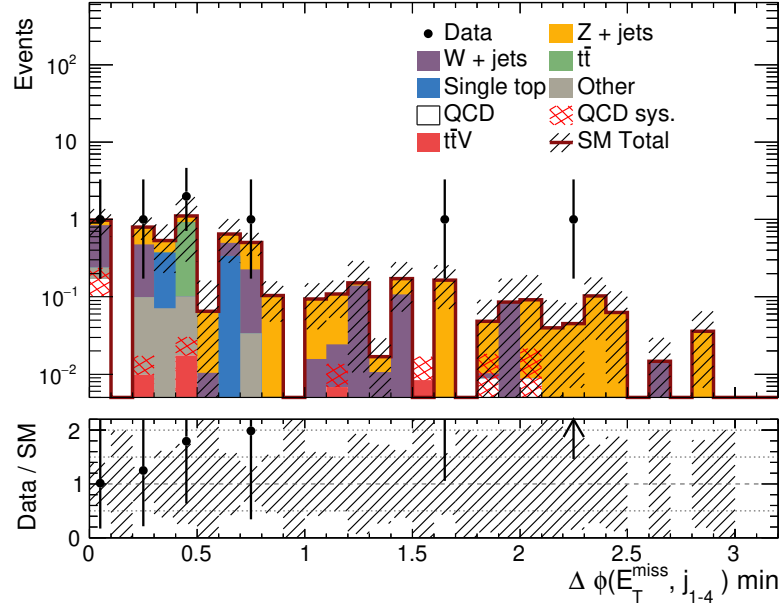
(a)



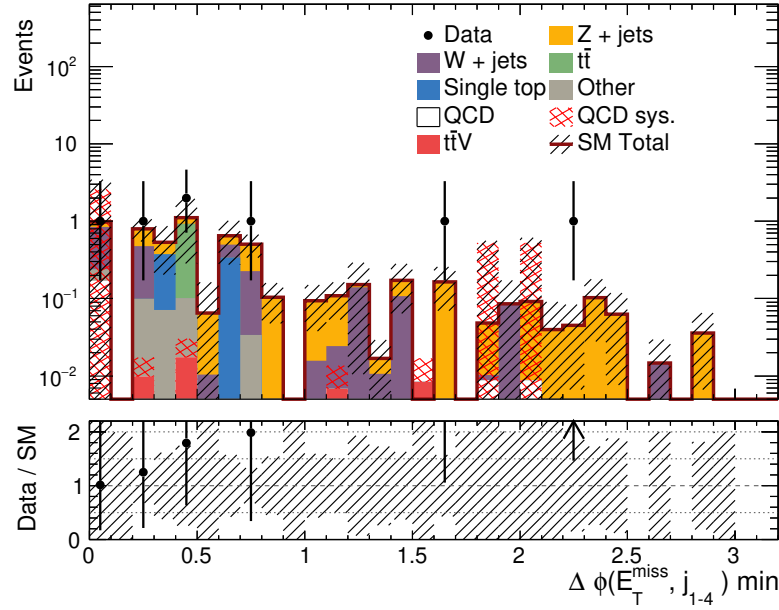
(b)

Fig. 7.29 Comparison of the  $p_T(j_1)$  distribution in SRC with a multijet estimate from the fully calibrated jet smearing method. The uncertainty associated with multijet events is shown by the red hatched band and is derived from the statistical uncertainty in addition to (a) the variation of seed selection and additional 30% uncertainty as within the original analysis and (b) from all other sources described in section 6.5. The white distribution represents the collection of pseudo-data generated with the Jet Smearing technique.

## 7.6 Revised Multijet Estimate Uncertainty



(a)



(b)

Fig. 7.30 Comparison of the  $\Delta\phi(j_{1-4}, \vec{E}_T^{\text{miss}})_{\text{min}}$  distribution in SRC with a multijet estimate from the fully calibrated jet smearing method. The uncertainty associated with multijet events is shown by the red hatched band and is derived from the statistical uncertainty in addition to (a) the variation of seed selection and additional 30% uncertainty as within the original analysis and (b) from all other sources described in section 6.5. The white distribution represents the collection of pseudo-data generated with the Jet Smearing technique.

Figures 7.28 and 7.29 both clearly show the increase in the uncertainty associated with the multijet estimate when using the sources of uncertainty considered in section 6.5 (with the omission of the seed variation uncertainty) with respect to the uncertainties derived from a variation of seed event selection in addition to a uniformly applied 30% uncertainty. Figure 7.30 shows the expected and observed  $\Delta\phi(j_{1-4}, \vec{E}_T^{\text{miss}})_{\text{min}}$  distribution in SRC. At low values of  $\Delta\phi(j_{1-4}, \vec{E}_T^{\text{miss}})_{\text{min}} < 0.2$ , associated with multijet events, the uncertainty of the estimate is significantly increased. The use of the uncertainties discussed in section 6.5 does not result in the increased significance of excess data events but instead reduces the already low significance of the excess in observed events above the expected SM background.

## 7.7 Summary

This chapter presented the general SUSY search strategy with the ATLAS detector and introduced two well-motivated analyses searching for evidence of strong and third generation SUSY production using  $36.1 \text{ fb}^{-1}$  of  $\sqrt{s} = 13 \text{ TeV}$  data. No significant excess of data above the SM prediction was observed in either analysis. Both analyses set exclusion limits on the masses of produced SUSY particles, which were greatly increased with respect to Run 1 limits.

Both analyses utilise the Jet Smearing technique, discussed in chapter 6, to generate an estimate of the QCD multijet background. The impact of the of the Jet Smearing multijet estimate with  $\phi$  calibration is investigated in both analyses and directly compared to the estimate provided by dijet MC simulated events in section 7.5.2.1.

Finally, section 7.6 shows the effect of the fully calibrated jet smearing method on the analysis searching for evidence of third generation SUSY production. The fully calibrated jet smearing estimate includes all sources of uncertainty discussed in 6.5 and is compared to the uncertainty applied to the estimate in the original analysis.

# Chapter 8

## Conclusions

This thesis presented an overview of the theoretical framework developed by physicists to attempt to describe matter and its fundamental interactions. The Standard Model is thought to have been ‘completed’ with the joint discovery of the Higgs boson at the LHC by the ATLAS and CMS experiments in 2012. Several shortcomings of the Standard Model were highlighted, the presence of which prompts theories for new physics to expand upon the Standard Model. Supersymmetry is a class of theoretical extensions to the Standard Model primarily motivated by providing an elegant solution to the hierarchy problem but that may also be able to describe the nature of the abundant dark matter in our universe.

The ATLAS detector, located on the LHC ring at CERN, plays host to a number of physics analyses searching for evidence of the production of particles not consistent with the Standard Model. A large portion of these analyses are specifically looking for evidence of the production and decay of supersymmetric particles.

Chapter 3 provided a description of the components of the ATLAS detector and their mode of operation. Radiation damage due to the proton-proton collisions occurring within the detector may prove to be a source of serious concerns in the years to come; to this end the effects of collision-induced radiation damage in the ATLAS silicon strip SCT are examined in chapter 4. The procedures utilised by analyses to identify and calibrate particles in an unambiguous fashion from the signals measured by the ATLAS detector are presented in chapter 5.

## Conclusions

---

A data-driven technique for the estimation of the QCD multijet background is presented in chapter 6. Multijet production has a high cross section at the LHC and is poorly modelled by Monte Carlo simulated events. Without careful understanding of this background by SUSY analyses, kinematic regions designed to enhance the presence of signal-like events may have high levels of QCD multijet contamination. The continuing development of the software implementation of this technique and its calibration for use within  $\sqrt{s} = 13$  TeV analyses has formed the bulk of the work performed by the author over the course of the PhD.

Finally, chapter 7 represents two of the most recent SUSY search results obtained from the ATLAS detector, analysing the  $36.1 \text{ fb}^{-1}$  of LHC data collected in 2015 and 2016 at a centre-of-mass collision energy of  $\sqrt{s} = 13$  TeV. No evidence of the production of SUSY particles was obtained through either analysis. In the absence of such a discovery, the results of both analyses were used to set relevant lower bounds on the potential masses of the supersymmetric particles considered.

Despite the lack of forthcoming evidence of the production of BSM particles at the LHC, hope remains for future analyses using a rapidly growing  $\sqrt{s} = 13$  TeV data collection that will be used to improve background estimation techniques enabling the analysis of signal regions constructed using increasingly restrictive requirements. An upcoming high luminosity upgrade aims to enable the delivery of  $3000 \text{ fb}^{-1}$  [167] by 2035 at a centre-of-mass collision energy of  $\sqrt{s} = 14$  TeV, enhancing the potential production rate of rare processes and providing an unprecedented opportunity for the discovery of BSM physics. Continued searches for evidence of SUSY particle production may lead to a discovery, but equally as significantly scientifically, they may lead to the exclusion of a vast range of particle masses, requiring a reassessment of long held theoretical motivations.

# References

- [1] ATLAS Collaboration. “The ATLAS Experiment at the CERN Large Hadron Collider”. In: *JINST* 3 (2008), S08003.
- [2] CMS Collaboration. “The CMS experiment at the CERN LHC”. In: *Journal of Instrumentation* 3.08 (2008), S08004.
- [3] ATLAS Collaboration. “Observation of a new particle in the search for the Standard Model Higgs boson with the ATLAS detector at the LHC”. In: *Physics Letters B* 716.1 (2012), pp. 1–29. URL: <http://www.sciencedirect.com/science/article/pii/S037026931200857X>.
- [4] CMS Collaboration. “Observation of a new boson at a mass of 125 GeV with the CMS experiment at the LHC”. In: *Physics Letters B* 716.1 (2012), pp. 30–61. URL: <http://www.sciencedirect.com/science/article/pii/S0370269312008581>.
- [5] M. Tanabashi et al. (Particle Data Group). “Review of Particle Physics”. In: *Phys. Rev. D* 98, 030001 (2018).
- [6] Otto Eberhardt et al. “Impact of a Higgs Boson at a Mass of 126 GeV on the Standard Model with Three and Four Fermion Generations”. In: *Phys. Rev. Lett.* 109 (24 Dec. 2012), p. 241802. URL: <https://link.aps.org/doi/10.1103/PhysRevLett.109.241802>.
- [7] D. DeCamp et al. “Determination of the number of light neutrino species”. In: *Physics Letters B* 231.4 (1989), pp. 519–529. URL: <http://www.sciencedirect.com/science/article/pii/0370269389907041>.
- [8] David Griffiths. *Introduction to Elementary Particles*. John Wiley & Sons, 2008.
- [9] Antonio Pich. “The Standard Model of Electroweak Interactions”. In: *Proceedings, High-energy Physics. Proceedings, 18th European School (ESHEP 2010): Raseborg, Finland, June 20 - July 3, 2010*. 2012, pp. 1–50. arXiv: 1201.0537 [hep-ph]. URL: <https://inspirehep.net/record/1083304/files/arXiv:1201.0537.pdf>.
- [10] Mark Thomson. *Modern particle physics*. Cambridge University Press, 2013.
- [11] Steven Weinberg. “A Model of Leptons”. In: *Phys. Rev. Lett.* 19 (21 Nov. 1967), pp. 1264–1266. URL: <https://link.aps.org/doi/10.1103/PhysRevLett.19.1264>.
- [12] Abdus Salam. “Weak and Electromagnetic Interactions”. In: *Conf. Proc. C* 680519 (1968), pp. 367–377.

## References

---

- [13] ATLAS Collaboration. *Determination of the strong coupling constant  $\alpha_s$  from transverse energy-energy correlations in multijet events at  $\sqrt{s} = 8$  TeV using the ATLAS detector*. Tech. rep. CERN-EP-2017-093. July 2017. URL: <http://cds.cern.ch/record/2273893>.
- [14] Vladimir Naumovich Gribov and Lev N Lipatov. “Deep inelastic ep scattering in perturbation theory”. In: *Sov. J. Nucl. Phys.* 15.IPTI-381-71 (1972), pp. 781–807.
- [15] L. N. Lipatov. “The parton model and perturbation theory”. In: *Sov. J. Nucl. Phys.* 20 (1975). [*Yad. Fiz.*20,181(1974)], pp. 94–102.
- [16] Guido Altarelli and Giorgio Parisi. “Asymptotic freedom in parton language”. In: *Nuclear Physics B* 126.2 (1977), pp. 298–318.
- [17] Yuri L Dokshitzer. “Calculation of the structure functions for deep inelastic scattering and e+ e- annihilation by perturbation theory in quantum chromodynamics”. In: *Zh. Eksp. Teor. Fiz* 73 (1977), p. 1216.
- [18] A. D. Martin et al. “Parton distributions for the LHC”. In: *Eur. Phys. J.* C63 (2009), pp. 189–285. arXiv: 0901.0002 [[hep-ph](#)].
- [19] Ahmed Ali and Gustav Kramer. “Jets and QCD: A Historical Review of the Discovery of the Quark and Gluon Jets and its Impact on QCD”. In: *Eur. Phys. J.* H36 (2011), pp. 245–326. arXiv: 1012.2288 [[hep-ph](#)].
- [20] Matteo Cacciari, Gavin P. Salam, and Gregory Soyez. “The Anti-k(t) jet clustering algorithm”. In: *JHEP* 04 (2008), p. 063. arXiv: 0802.1189 [[hep-ph](#)].
- [21] ATLAS Collaboration. “Measurement of inclusive jet and dijet cross-sections in proton-proton collisions at  $\sqrt{s} = 13$  TeV with the ATLAS detector”. In: *Journal of High Energy Physics* 2018.5 (May 2018), p. 195.
- [22] T. Gleisberg et al. “Event generation with SHERPA 1.1”. In: *JHEP* 02 (2009), p. 007. arXiv: 0811.4622 [[hep-ph](#)].
- [23] Vera C Rubin, W Kent Ford Jr, and Norbert Thonnard. “Rotational properties of 21 SC galaxies with a large range of luminosities and radii, from NGC 4605/R= 4kpc/to UGC 2885/R= 122 kpc”. In: *The Astrophysical Journal* 238 (1980), pp. 471–487.
- [24] Stephen P. Martin. “A Supersymmetry primer”. In: *Adv.Ser.Direct.High Energy Phys.* 21 (2010), pp. 1–153. arXiv: [hep-ph/9709356](#) [[hep-ph](#)].
- [25] N. Sakai. “Naturalness in supersymmetric GUTS”. In: *Zeitschrift für Physik C Particles and Fields* 11.2 (June 1981), pp. 153–157. URL: <https://doi.org/10.1007/BF01573998>.
- [26] S. Dimopoulos, S. Raby, and Frank Wilczek. “Supersymmetry and the scale of unification”. In: *Phys. Rev. D* 24 (6 Sept. 1981), pp. 1681–1683. URL: <https://link.aps.org/doi/10.1103/PhysRevD.24.1681>.
- [27] L.E. Ibáñez and G.G. Ross. “Low-energy predictions in supersymmetric grand unified theories”. In: *Physics Letters B* 105.6 (1981), pp. 439–442. URL: <http://www.sciencedirect.com/science/article/pii/0370269381912004>.
- [28] Savas Dimopoulos and Howard Georgi. “Softly Broken Supersymmetry and SU(5)”. In: *Nucl. Phys.* B193 (1981), pp. 150–162.

- 
- [29] Yu. A. Golfand and E. P. Likhtman. “Extension of the Algebra of Poincare Group Generators and Violation of p Invariance”. In: *JETP Lett.* 13 (1971). [Pisma Zh. Eksp. Teor. Fiz.13,452(1971)], pp. 323–326.
- [30] D.V. Volkov and V.P. Akulov. “Is the neutrino a goldstone particle?” In: *Physics Letters B* 46.1 (1973), pp. 109–110. URL: <http://www.sciencedirect.com/science/article/pii/0370269373904905>.
- [31] J. Wess and B. Zumino. “Supergauge Transformations in Four-Dimensions”. In: *Nucl. Phys.* B70 (1974), pp. 39–50.
- [32] J. Wess and B. Zumino. “Supergauge Invariant Extension of Quantum Electrodynamics”. In: *Nucl. Phys.* B78 (1974), p. 1.
- [33] S. Ferrara and B. Zumino. “Supergauge Invariant Yang-Mills Theories”. In: *Nucl. Phys.* B79 (1974), p. 413.
- [34] Abdus Salam and J. A. Strathdee. “Supersymmetry and Nonabelian Gauges”. In: *Phys. Lett.* 51B (1974), pp. 353–355.
- [35] Glennys R. Farrar and Pierre Fayet. “Phenomenology of the Production, Decay, and Detection of New Hadronic States Associated with Supersymmetry”. In: *Phys. Lett.* 76B (1978), pp. 575–579.
- [36] Jonathan L. Feng. “Naturalness and the Status of Supersymmetry”. In: *Ann. Rev. Nucl. Part. Sci.* 63 (2013), pp. 351–382. arXiv: 1302.6587 [hep-ph].
- [37] P. Fayet. “Supersymmetry and weak, electromagnetic and strong interactions”. In: *Physics Letters B* 64.2 (1976), pp. 159–162. URL: <http://www.sciencedirect.com/science/article/pii/0370269376903191>.
- [38] P. Fayet. “Spontaneously broken supersymmetric theories of weak, electromagnetic and strong interactions”. In: *Physics Letters B* 69.4 (1977), pp. 489–494. URL: <http://www.sciencedirect.com/science/article/pii/0370269377908528>.
- [39] Christoph Borschensky et al. “Squark and gluino production cross sections in pp collisions at  $\sqrt{s} = 13, 14, 33$  and 100 TeV”. In: *Eur. Phys. J.* C74.12 (2014), p. 3174. arXiv: 1407.5066 [hep-ph].
- [40] D. R. Tovey. “Inclusive SUSY searches and measurements at ATLAS”. In: *EPJ direct* 4.1 (Dec. 2002), pp. 1–24.
- [41] ATLAS Collaboration. “Summary of the searches for squarks and gluinos using  $\sqrt{s} = 8$  TeV pp collisions with the ATLAS experiment at the LHC”. In: *JHEP* 10 (2015), p. 054. arXiv: 1507.05525 [hep-ex].
- [42] CMS Collaboration. *Summary of comparison plots in simplified models spectra for the 8TeV dataset*. <https://twiki.cern.ch/twiki/bin/view/CMSPublic/SUSYSMSSummaryPlots8TeV> [Accessed: November 2017]. 2016.
- [43] A. A. Sokolov and I. M. Ternov. “Synchrotron radiation”. In: *Soviet Physics Journal* 10.10 (Oct. 1967), pp. 39–47. URL: <https://doi.org/10.1007/BF00820300>.
- [44] Lyndon Evans and Philip Bryant. “LHC Machine”. In: *Journal of Instrumentation* 3.08 (2008), S08001. URL: <http://stacks.iop.org/1748-0221/3/i=08/a=S08001>.
- [45] J Campbell et al. *MCFM - Monte Carlo for FeMtobarn processes*. 2018. URL: <https://mcfm.fnal.gov/> (visited on 06/12/2018).

## References

---

- [46] Lyndon Evans and Philip Bryant. “LHC Machine”. In: *JINST* 3 (2008), S08001.
- [47] Christiane Lefèvre. “The CERN accelerator complex. Complexe des accélérateurs du CERN”. Dec. 2008. URL: <https://cds.cern.ch/record/1260465>.
- [48] M Benedikt et al. “LHC Design Report, volume III, The LHC injector chain”. In: *CERN, Geneva* (2004).
- [49] ALICE Collaboration. “The ALICE experiment at the CERN LHC”. In: *Journal of Instrumentation* 3.08 (2008), S08002. URL: <http://stacks.iop.org/1748-0221/3/i=08/a=S08002>.
- [50] LHCb Collaboration. “The LHCb Detector at the LHC”. In: *Journal of Instrumentation* 3.08 (2008), S08005. URL: <http://stacks.iop.org/1748-0221/3/i=08/a=S08005>.
- [51] LEP Working Group for Higgs Boson Searches. “Search for the Standard Model Higgs boson at LEP”. In: *Physics Letters B* 565 (2003), pp. 61–75. URL: <http://www.sciencedirect.com/science/article/pii/S0370269303006142>.
- [52] ATLAS Collaboration. “The ATLAS Inner Detector commissioning and calibration”. In: *The European Physical Journal C* 70.3 (Dec. 2010), pp. 787–821. URL: <https://doi.org/10.1140/epjc/s10052-010-1366-7>.
- [53] Karolos Potamianos. “The upgraded Pixel detector and the commissioning of the Inner Detector tracking of the ATLAS experiment for Run-2 at the Large Hadron Collider”. In: *PoS EPS-HEP2015* (2015), p. 261. arXiv: 1608.07850 [physics.ins-det].
- [54] M Capeans et al. *ATLAS Insertable B-Layer Technical Design Report*. Tech. rep. CERN-LHCC-2010-013. ATLAS-TDR-19. Sept. 2010. URL: <https://cds.cern.ch/record/1291633>.
- [55] G. Apollinari et al. “High Luminosity Large Hadron Collider HL-LHC”. In: *CERN Yellow Report* 5 (2015), pp. 1–19. arXiv: 1705.08830 [physics.acc-ph].
- [56] A. La Rosa and on behalf of ATLAS collaboration. “The ATLAS Insertable B-Layer: from construction to operation”. In: *Journal of Instrumentation* 11.12 (2016), p. C12036. URL: <http://stacks.iop.org/1748-0221/11/i=12/a=C12036>.
- [57] ATLAS Collaboration. “ATLAS pixel detector electronics and sensors”. In: *Journal of Instrumentation* 3.07 (2008), P07007. URL: <http://stacks.iop.org/1748-0221/3/i=07/a=P07007>.
- [58] ATLAS Collaboration. “Operation and performance of the ATLAS semiconductor tracker”. In: *Journal of Instrumentation* 9.08 (2014), P08009.
- [59] *ATLAS inner detector: Technical Design Report, 1*. Technical Design Report ATLAS. Geneva: CERN, 1997. URL: <https://cds.cern.ch/record/331063>.
- [60] J R Pater. “The ATLAS SemiConductor Tracker operation and performance”. In: *Journal of Instrumentation* 7.04 (2012), p. C04001. URL: <http://stacks.iop.org/1748-0221/7/i=04/a=C04001>.
- [61] ATLAS collaboration and others. “Operation and performance of the ATLAS semiconductor tracker”. In: *Journal of Instrumentation* 9.08 (2014), P08009.

- [62] A Ahmad et al. “The silicon microstrip sensors of the ATLAS semiconductor tracker”. In: *Nuclear Instruments and Methods in Physics Research Section A: Accelerators, Spectrometers, Detectors and Associated Equipment* 578.1 (2007), pp. 98–118.
- [63] William R Leo. *Techniques for Nuclear and Particle Physics Experiments: A How-To Approach*. Springer Science & Business Media, 1994.
- [64] ATLAS Collaboration. “The ATLAS Transition Radiation Tracker (TRT) proportional drift tube: Design and performance”. In: *Journal of Instrumentation* 3.02 (2008), P02013.
- [65] E. Hines. “Performance of Particle Identification with the ATLAS Transition Radiation Tracker”. In: *Particles and fields. Proceedings, Meeting of the Division of the American Physical Society, DPF 2011, Providence, USA, August 9-13, 2011*. 2011. arXiv: 1109.5925 [physics.ins-det]. URL: <https://inspirehep.net/record/929696/files/arXiv:1109.5925.pdf>.
- [66] A. Andronic and J.P. Wessels. “Transition radiation detectors”. In: *Nuclear Instruments and Methods in Physics Research Section A: Accelerators, Spectrometers, Detectors and Associated Equipment* 666 (2012). *Advanced Instrumentation*, pp. 130–147. URL: <http://www.sciencedirect.com/science/article/pii/S0168900211018134>.
- [67] Christian W Fabjan and Fabiola Gianotti. “Calorimetry for particle physics”. In: *Reviews of Modern Physics* 75.4 (2003), p. 1243.
- [68] ATLAS Collaboration. *ATLAS muon spectrometer: Technical design report*. Tech. rep. 1997.
- [69] Aranzazu Ruiz-Martinez and ATLAS Collaboration. *The Run-2 ATLAS Trigger System*. Tech. rep. ATL-DAQ-PROC-2016-003. Geneva: CERN, Feb. 2016. URL: <https://cds.cern.ch/record/2133909>.
- [70] Joao Pequeno. “Event Cross Section in a computer generated image of the ATLAS detector.” Mar. 2008. URL: <https://cds.cern.ch/record/1096081>.
- [71] ATLAS Collaboration. *LuminosityPublicResultsRun2*. <https://twiki.cern.ch/twiki/bin/view/AtlasPublic/LuminosityPublicResultsRun2> [Accessed: November 2017]. 2017.
- [72] Zachary Marshall and the Atlas Collaboration. “Simulation of Pile-up in the ATLAS Experiment”. In: *Journal of Physics: Conference Series* 513.2 (2014), p. 022024. URL: <http://stacks.iop.org/1742-6596/513/i=2/a=022024>.
- [73] ATLAS Collaboration. “The ATLAS Simulation Infrastructure”. In: *The European Physical Journal C* 70.3 (Dec. 2010), pp. 823–874. URL: <https://doi.org/10.1140/epjc/s10052-010-1429-9>.
- [74] Torbjorn Sjostrand, Stephen Mrenna, and Peter Z. Skands. “A Brief Introduction to PYTHIA 8.1”. In: *Comput. Phys. Commun.* 178 (2008), pp. 852–867. arXiv: 0710.3820 [hep-ph].
- [75] *Summary of ATLAS Pythia 8 tunes*. Tech. rep. ATL-PHYS-PUB-2012-003. Geneva: CERN, Aug. 2012. URL: <https://cds.cern.ch/record/1474107>.

## References

---

- [76] Stefano Carrazza, Stefano Forte, and Juan Rojo. “Parton Distributions and Event Generators”. In: *Proceedings, 43rd International Symposium on Multiparticle Dynamics (ISMD 13)*. 2013, pp. 89–96. arXiv: 1311.5887 [hep-ph]. URL: <https://inspirehep.net/record/1266070/files/arXiv:1311.5887.pdf>.
- [77] Stefan Höche. “Introduction to parton-shower event generators”. In: *Proceedings, Theoretical Advanced Study Institute in Elementary Particle Physics: Journeys Through the Precision Frontier: Amplitudes for Colliders (TASI 2014): Boulder, Colorado, June 2-27, 2014*. 2015, pp. 235–295. arXiv: 1411.4085 [hep-ph]. URL: <https://inspirehep.net/record/1328513/files/arXiv:1411.4085.pdf>.
- [78] S. Agostinelli et al. “Geant4 — a simulation toolkit”. In: *Nuclear Instruments and Methods in Physics Research Section A: Accelerators, Spectrometers, Detectors and Associated Equipment* 506.3 (2003), pp. 250–303. URL: <http://www.sciencedirect.com/science/article/pii/S0168900203013688>.
- [79] ATLAS Collaboration. *The simulation principle and performance of the ATLAS fast calorimeter simulation FastCaloSim*. Tech. rep. ATL-PHYS-PUB-2010-013. Geneva: CERN, Oct. 2010. URL: <https://cds.cern.ch/record/1300517>.
- [80] Michael Moll. “Radiation damage in silicon particle detectors”. PhD thesis. University of Hamburg, 1999. URL: <https://mmoll.web.cern.ch/mmoll/thesis>.
- [81] G Lindström et al. In: *Nuclear Instruments and Methods in Physics Research Section A: Accelerators, Spectrometers, Detectors and Associated Equipment* 466.2 (2001), pp. 308–326.
- [82] Olaf Krasel. “Charge collection in irradiated silicon detectors”. PhD thesis. Universität Dortmund, 2004.
- [83] Robert Harper. “Radiation Damage studies of the silicon microstrip detectors and finding an intermediate mass Higgs Boson at ATLAS”. PhD thesis. Sheffield U., 2001.
- [84] Angela Vasilescu. *The NIEL scaling hypothesis applied to neutron spectra of irradiation facilities and in the ATLAS and CMS SCT*. Tech. rep. 1997, pp. 97–2.
- [85] A Abdesselam et al. “The barrel modules of the ATLAS semiconductor tracker”. In: *Nuclear Instruments and Methods in Physics Research Section A: Accelerators, Spectrometers, Detectors and Associated Equipment* 568.2 (2006), pp. 642–671.
- [86] G. Lutz. “A simplistic model for reverse annealing in irradiated silicon”. In: *Nuclear Instruments and Methods in Physics Research Section B: Beam Interactions with Materials and Atoms* 95.1 (1995), pp. 41–49. URL: <http://www.sciencedirect.com/science/article/pii/0168583X94003203>.
- [87] A. Koutoulaki. “The ITk Strip Tracker for the phase-II upgrade of the ATLAS detector of the HL-LHC”. In: *Journal of Instrumentation* 12.04 (2017), p. C04022. URL: <http://stacks.iop.org/1748-0221/12/i=04/a=C04022>.
- [88] ATLAS Collaboration. Private communication - agreed between ATLAS TC and CERN RP. 2016.
- [89] Lamont, Mike. ICHEP 2016, Chicago. 2016. URL: <https://indico.cern.ch/event/432527/contributions/2255495/attachments/1321399/1981784/LHC-performance-ICHEP16.pdf>.

- 
- [90] Paul Miyagawa. *RadiationBackgroundSimulationsPhase0*. 2015. URL: <https://twiki.cern.ch/twiki/bin/view/Atlas/RadiationBackgroundSimulationsPhase0> (visited on 04/25/2016).
- [91] ATLAS Collaboration. *Hit Efficiency, leakage currents, noise and detector status at start of 2016*. Publicly available plots of SCT Hit Efficiency, leakage currents, noise and detector status at start of 2016. May 2016. URL: <https://atlas.web.cern.ch/Atlas/GROUPS/PHYSICS/PLOTS/SCT-2016-001/>.
- [92] R Bates et al. *Reassessment of cooling requirements for the ATLAS barrel SCT*. Tech. rep. ATL-COM-INDET-2009-093. Geneva: CERN, Dec. 2009. URL: <https://cds.cern.ch/record/1229424>.
- [93] ATLAS Collaboration. *ATLAS inner detector: Technical design report. Vol. 2*. Apr. 1997.
- [94] Taka Kondo. *SCTIVScan*. 2018. URL: <https://twiki.cern.ch/twiki/bin/view/Atlas/SctIVScan> (visited on 05/20/2018).
- [95] ATLAS Collaboration. “Performance of the ATLAS track reconstruction algorithms in dense environments in LHC Run 2”. In: *The European Physical Journal C* 77.10 (Oct. 2017), p. 673. URL: <https://doi.org/10.1140/epjc/s10052-017-5225-7>.
- [96] T. Cornelissen et al. *Concepts, Design and Implementation of the ATLAS New Tracking (NEWT)*. Tech. rep. 2007.
- [97] V Lacuesta. “Track and vertex reconstruction in the ATLAS experiment”. In: *Journal of Instrumentation* 8.02 (2013), p. C02035. URL: <http://stacks.iop.org/1748-0221/8/i=02/a=C02035>.
- [98] Gavin P Salam. “Towards jetography”. In: *The European Physical Journal C* 67.3-4 (2010), pp. 637–686.
- [99] Bora Isildak. “Measurement of the differential dijet production cross section in proton-proton collisions at  $\sqrt{s} = 7$  tev”. PhD thesis. Bogazici U., 2011. arXiv: 1308.6064 [hep-ex]. URL: <http://inspirehep.net/record/1251416/files/arXiv:1308.6064.pdf>.
- [100] ATLAS Collaboration. “Topological cell clustering in the ATLAS calorimeters and its performance in LHC Run 1”. In: *Eur. Phys. J. C* 77 (2017), p. 490. arXiv: 1603.02934 [hep-ex].
- [101] A. Hrynevich. “ATLAS jet and missing energy reconstruction, calibration and performance in LHC Run-2”. In: *Journal of Instrumentation* 12.06 (2017), p. C06038. URL: <http://stacks.iop.org/1748-0221/12/i=06/a=C06038>.
- [102] ATLAS Collaboration. “Jet energy scale measurements and their systematic uncertainties in proton-proton collisions at  $\sqrt{s} = 13$  TeV with the ATLAS detector”. In: *Phys. Rev. D* 96.7 (2017), p. 072002. arXiv: 1703.09665 [hep-ex].
- [103] ATLAS Collaboration. “Jet energy scale measurements and their systematic uncertainties in proton-proton collisions at  $\sqrt{s} = 13$  TeV with the ATLAS detector”. In: *Phys. Rev. D* 96.7 (2017), p. 072002. arXiv: 1703.09665 [hep-ex].
- [104] ATLAS Collaboration. “Jet energy measurement and its systematic uncertainty in proton-proton collisions at  $\sqrt{s} = 7$  TeV with the ATLAS detector”. In: *Eur. Phys. J. C* 75 (2015), p. 17. arXiv: 1406.0076 [hep-ex].

## References

---

- [105] ATLAS Collaboration. “Performance of pile-up mitigation techniques for jets in  $pp$  collisions at  $\sqrt{s} = 8$  TeV using the ATLAS detector”. In: *Eur. Phys. J. C* 76.11 (2016), p. 581. arXiv: 1510.03823 [hep-ex].
- [106] ATLAS Collaboration. *Jet global sequential corrections with the ATLAS detector in proton-proton collisions at  $\sqrt{s} = 8$  TeV*. Tech. rep. ATLAS-CONF-2015-002. Geneva: CERN, Mar. 2015. URL: <http://cds.cern.ch/record/2001682>.
- [107] ATLAS Collaboration. *Selection of jets produced in 13 TeV proton-proton collisions with the ATLAS detector*. Tech. rep. ATLAS-CONF-2015-029. Geneva: CERN, July 2015. URL: <http://cds.cern.ch/record/2037702>.
- [108] ATLAS Collaboration. “Characterisation and mitigation of beam-induced backgrounds observed in the ATLAS detector during the 2011 proton-proton run”. In: *JINST* 8 (2013), P07004. arXiv: 1303.0223 [hep-ex].
- [109] *Tagging and suppression of pileup jets with the ATLAS detector*. Tech. rep. ATLAS-CONF-2014-018. Geneva: CERN, May 2014. URL: <https://cds.cern.ch/record/1700870>.
- [110] *Performance of the ATLAS Secondary Vertex  $b$ -tagging Algorithm in 7 TeV Collision Data*. Tech. rep. ATLAS-CONF-2010-042. Geneva: CERN, July 2010. URL: <https://cds.cern.ch/record/1277682>.
- [111] *Optimisation of the ATLAS  $b$ -tagging performance for the 2016 LHC Run*. Tech. rep. ATL-PHYS-PUB-2016-012. Geneva: CERN, June 2016. URL: <https://cds.cern.ch/record/2160731>.
- [112] *Commissioning of the ATLAS high-performance  $b$ -tagging algorithms in the 7 TeV collision data*. Tech. rep. ATLAS-CONF-2011-102. Geneva: CERN, July 2011. URL: <https://cds.cern.ch/record/1369219>.
- [113] G Piacquadio and C Weiser. “A new inclusive secondary vertex algorithm for  $b$ -jet tagging in ATLAS”. In: *Journal of Physics: Conference Series* 119.3 (2008), p. 032032. URL: <http://stacks.iop.org/1742-6596/119/i=3/a=032032>.
- [114] A. Hoecker et al. “TMVA - Toolkit for Multivariate Data Analysis”. In: *ArXiv Physics e-prints* (Mar. 2007). eprint: physics/0703039.
- [115] ATLAS Collaboration. “Measurements of  $b$ -jet tagging efficiency with the ATLAS detector using  $t\bar{t}$  events at  $\sqrt{s} = 13$  TeV”. In: (2018). arXiv: 1805.01845 [hep-ex].
- [116] ATLAS collaboration. *Calibration of  $b$ -tagging using dileptonic top pair events in a combinatorial likelihood approach with the ATLAS experiment*. Tech. rep. 2014.
- [117] W Lampl et al. *Calorimeter Clustering Algorithms: Description and Performance*. Tech. rep. ATL-LARG-PUB-2008-002. ATL-COM-LARG-2008-003. CERN, Apr. 2008. URL: <https://cds.cern.ch/record/1099735>.
- [118] *Electron efficiency measurements with the ATLAS detector using the 2015 LHC proton-proton collision data*. Tech. rep. ATLAS-CONF-2016-024. Geneva: CERN, June 2016. URL: <https://cds.cern.ch/record/2157687>.
- [119] *Electron and photon energy calibration with the ATLAS detector using data collected in 2015 at  $\sqrt{s} = 13$  TeV*. Tech. rep. ATL-PHYS-PUB-2016-015. Geneva: CERN, Aug. 2016. URL: <https://cds.cern.ch/record/2203514>.

- 
- [120] Thijs G. Cornelissen et al. “The global  $\chi^2$  track fitter in ATLAS”. In: *J. Phys. Conf. Ser.* 119 (2008), p. 032013.
- [121] ATLAS Collaboration. “Measurement of the photon identification efficiencies with the ATLAS detector using LHC Run-1 data”. In: *Eur. Phys. J. C* 76.12 (2016), p. 666. arXiv: 1606.01813 [hep-ex].
- [122] *Photon identification in 2015 ATLAS data*. Tech. rep. ATL-PHYS-PUB-2016-014. Geneva: CERN, Aug. 2016. URL: <https://cds.cern.ch/record/2203125>.
- [123] ATLAS Collaboration. “Muon reconstruction performance of the ATLAS detector in proton–proton collision data at  $\sqrt{s} = 13$  TeV”. In: *Eur. Phys. J. C* 76.5 (2016), p. 292. arXiv: 1603.05598 [hep-ex].
- [124] ATLAS Collaboration. *ATLAS Muon Combined Performance with the full 2016 dataset*. <https://atlas.web.cern.ch/Atlas/GROUPS/PHYSICS/PLOTS/MUON-2017-001/> [Accessed: January 2018]. 2017.
- [125] ATLAS Collaboration. “Performance of algorithms that reconstruct missing transverse momentum in  $\sqrt{s} = 8$  TeV proton–proton collisions in the ATLAS detector”. In: *The European Physical Journal C* 77.4 (Apr. 2017), p. 241. URL: <https://doi.org/10.1140/epjc/s10052-017-4780-2>.
- [126] *Performance of missing transverse momentum reconstruction for the ATLAS detector in the first proton-proton collisions at  $\sqrt{s} = 13$  TeV*. Tech. rep. ATL-PHYS-PUB-2015-027. Geneva: CERN, July 2015. URL: <https://cds.cern.ch/record/2037904>.
- [127] ATLAS Collaboration. “Performance of missing transverse momentum reconstruction with the ATLAS detector using proton–proton collisions at  $\sqrt{s} = 13$  TeV”. In: *The European Physical Journal C* 78.11 (Nov. 2018), p. 903. URL: <https://doi.org/10.1140/epjc/s10052-018-6288-9>.
- [128] ATLAS Collaboration. *Missing transverse energy performance in 2017 data*. <https://atlas.web.cern.ch/Atlas/GROUPS/PHYSICS/PLOTS/JETM-2017-011/> [Accessed: January 2018]. 2017.
- [129] ATLAS Collaboration. “Search for squarks and gluinos in final states with jets and missing transverse momentum using  $36 \text{ fb}^{-1}$  of  $\sqrt{s} = 13$  TeV  $pp$  collision data with the ATLAS detector”. In: *Phys. Rev. D* 97 (11 June 2018), p. 112001. URL: <https://link.aps.org/doi/10.1103/PhysRevD.97.112001>.
- [130] ATLAS Collaboration. *JES Public Plots for Moriond 2017*. <https://atlas.web.cern.ch/Atlas/GROUPS/PHYSICS/PLOTS/JETM-2017-003/> [Accessed: January 2018]. 2017.
- [131] Steven Schramm et al. *A method for the construction of strongly reduced representations of ATLAS experimental uncertainties and the application thereof to the jet energy scale*. Tech. rep. ATL-COM-PHYS-2015-374. Geneva: CERN, May 2015. URL: <https://cds.cern.ch/record/2014656>.
- [132] ATLAS Collaboration. “Jet energy resolution in proton-proton collisions at  $\sqrt{s} = 7$  TeV recorded in 2010 with the ATLAS detector”. In: *Eur. Phys. J. C* 73.3 (2013), p. 2306. arXiv: 1210.6210 [hep-ex].

## References

---

- [133] ATLAS Collaboration. “Improved luminosity determination in pp collisions at  $\sqrt{s} = 7$  TeV using the ATLAS detector at the LHC”. In: *Eur. Phys. J. C* 73.8 (2013), p. 2518. arXiv: 1302.4393 [hep-ex].
- [134] Robert Duxfield. “Background Control in Inclusive Supersymmetry Searches and Offline Reconstruction at ATLAS”. PhD thesis. University of Sheffield, Aug. 2008.
- [135] Simon Owen. “Multijet Background Estimation for Supersymmetry Searches Using the ATLAS Detector at the Large Hadron Collider”. PhD thesis. University of Sheffield, Aug. 2012. URL: <http://etheses.whiterose.ac.uk/id/eprint/2854>.
- [136] Gareth Thomas Fletcher. “Multijet Background Estimation For SUSY Searches And Particle Flow Offline Reconstruction Using The ATLAS Detector At The LHC”. Presented 01 Jun 2015. PhD thesis. University of Sheffield, Mar. 2015. URL: <https://cds.cern.ch/record/2054397>.
- [137] ATLAS Collaboration. “Search for squarks and gluinos with the ATLAS detector in final states with jets and missing transverse momentum using  $4.7 \text{ fb}^{-1}$  of  $\sqrt{s}=7$  TeV proton-proton collision data”. In: *Phys. Rev. D* 87 (1 Jan. 2013), p. 012008. URL: <http://link.aps.org/doi/10.1103/PhysRevD.87.012008>.
- [138] Calum Michael Macdonald. “Searches for supersymmetry in final states containing b-tagged jets with the ATLAS detector”. PhD thesis. University of Sheffield, Aug. 2017. URL: <http://etheses.whiterose.ac.uk/17990/>.
- [139] ATLAS Collaboration. “Search for Supersymmetry in final states with missing transverse momentum and multiple  $b$ -jets in proton–proton collisions at  $\sqrt{s} = 13$  TeV with the ATLAS detector”. In: *Journal of High Energy Physics* 2018.6 (June 2018), p. 107. URL: [https://doi.org/10.1007/JHEP06\(2018\)107](https://doi.org/10.1007/JHEP06(2018)107).
- [140] ATLAS Collaboration. “Search for a scalar partner of the top quark in the jets plus missing transverse momentum final state at  $\sqrt{s}=13$  TeV with the ATLAS detector”. In: *JHEP* 12 (2017), p. 085. arXiv: 1709.04183 [hep-ex].
- [141] ATLAS Collaboration. “Search for supersymmetry in events with  $b$ -tagged jets and missing transverse momentum in  $pp$  collisions at  $\sqrt{s} = 13$  TeV with the ATLAS detector”. In: *JHEP* 11 (2017), p. 195. arXiv: 1708.09266 [hep-ex].
- [142] ATLAS Collaboration. “Search for squarks and gluinos in events with hadronically decaying tau leptons, jets and missing transverse momentum in proton–proton collisions at  $\sqrt{s} = 13$  TeV recorded with the ATLAS detector”. In: *Eur. Phys. J. C* 76.12 (2016), p. 683. arXiv: 1607.05979 [hep-ex].
- [143] ATLAS Collaboration. “Search for dark matter produced in association with bottom or top quarks in  $\sqrt{s} = 13$  TeV pp collisions with the ATLAS detector”. In: *Eur. Phys. J. C* 78.1 (2018), p. 18. arXiv: 1710.11412 [hep-ex].
- [144] ATLAS Collaboration. “Measurement of detector-corrected observables sensitive to the anomalous production of events with jets and large missing transverse momentum in  $pp$  collisions at  $\sqrt{s} = 13$  TeV using the ATLAS detector”. In: *Eur. Phys. J. C* 77.11 (2017), p. 765. arXiv: 1707.03263 [hep-ex].
- [145] ATLAS Collaboration. *JetEtmissMC15*. <https://twiki.cern.ch/twiki/bin/viewauth/AtlasProtected/JetEtmissMC15> [Accessed: February 2018]. 2017.

- 
- [146] Benjamin Nachman and Christopher G. Lester. “Significance variables”. In: *Phys. Rev. D* 88 (7 Oct. 2013), p. 075013. URL: <https://link.aps.org/doi/10.1103/PhysRevD.88.075013>.
- [147] Theodor Christian Herwig. *ATLAS jet trigger performance in 2016 data*. Tech. rep. ATL-DAQ-PROC-2016-020. Geneva: CERN, Nov. 2016. URL: <https://cds.cern.ch/record/2229226>.
- [148] Tomasz Skwarnicki. “A study of the radiative CASCADE transitions between the Upsilon-Prime and Upsilon resonances”. PhD thesis. Cracow, INP, 1986. URL: <http://www-library.desy.de/cgi-bin/showprep.pl?DESY-F31-86-02>.
- [149] ATLAS Collaboration. “Search for pair production of gluinos decaying via stop and sbottom in events with  $b$ -jets and large missing transverse momentum in  $pp$  collisions at  $\sqrt{s} = 13$  TeV with the ATLAS detector”. In: *Phys. Rev. D* 94.3 (2016), p. 032003. arXiv: 1605.09318 [hep-ex].
- [150] ATLAS Collaboration. “Search for squarks and gluinos in final states with jets and missing transverse momentum at  $\sqrt{s}=13$  TeV with the ATLAS detector”. In: *Eur. Phys. J. C* 76.7 (July 2016).
- [151] I. Hinchliffe et al. “Precision SUSY measurements at CERN LHC”. In: *Phys. Rev. D* 55 (9 May 1997), pp. 5520–5540. URL: <https://link.aps.org/doi/10.1103/PhysRevD.55.5520>.
- [152] James D. Bjorken and Stanley J. Brodsky. “Statistical Model for Electron-Positron Annihilation into Hadrons”. In: *Phys. Rev. D* 1 (5 Mar. 1970), pp. 1416–1420. URL: <https://link.aps.org/doi/10.1103/PhysRevD.1.1416>.
- [153] Chunhui Chen. “New approach to identifying boosted hadronically decaying particles using jet substructure in its center-of-mass frame”. In: *Phys. Rev. D* 85 (3 Feb. 2012), p. 034007. URL: <https://link.aps.org/doi/10.1103/PhysRevD.85.034007>.
- [154] Daniel R. Tovey. “On measuring the masses of pair-produced semi-invisibly decaying particles at hadron colliders”. In: *JHEP* 04 (2008), p. 034. arXiv: 0802.2879 [hep-ph].
- [155] M. Baak et al. “HistFitter software framework for statistical data analysis”. In: *Eur. Phys. J. C* 75 (2015), p. 153. arXiv: 1410.1280 [hep-ex].
- [156] Glen Cowan et al. “Asymptotic formulae for likelihood-based tests of new physics”. In: *Eur. Phys. J. C* 71 (2011). [Erratum: *Eur. Phys. J. C* 73,2501(2013)], p. 1554. arXiv: 1007.1727 [physics.data-an].
- [157] A L Read. “Presentation of search results: the  $CL_s$  technique”. In: *Journal of Physics G: Nuclear and Particle Physics* 28.10 (2002), p. 2693. URL: <http://stacks.iop.org/0954-3899/28/i=10/a=313>.
- [158] Johan Alwall, Philip Schuster, and Natalia Toro. “Simplified Models for a First Characterization of New Physics at the LHC”. In: *Phys. Rev. D* 79 (2009), p. 075020. arXiv: 0810.3921 [hep-ph].
- [159] Daniele Alves. “Simplified Models for LHC New Physics Searches”. In: *J. Phys. G* 39 (2012). Ed. by Nima Arkani-Hamed et al., p. 105005. arXiv: 1105.2838 [hep-ph].

## References

---

- [160] A. Djouadi et al. “The Minimal supersymmetric standard model: Group summary report”. In: *GDR (Groupement De Recherche) - Supersymetrie Montpellier, France, April 15-17, 1998*. 1998. arXiv: hep-ph/9901246 [hep-ph].
- [161] Carola F. Berger et al. “Supersymmetry Without Prejudice”. In: *JHEP* 02 (2009), p. 023. arXiv: 0812.0980 [hep-ph].
- [162] J. Alwall et al. “The automated computation of tree-level and next-to-leading order differential cross sections, and their matching to parton shower simulations”. In: *JHEP* 07 (2014), p. 079. arXiv: 1405.0301 [hep-ph].
- [163] Benjamin Nachman et al. “Jets from Jets: Re-clustering as a tool for large radius jet reconstruction and grooming at the LHC”. In: *JHEP* 02 (2015), p. 075. arXiv: 1407.2922 [hep-ph].
- [164] Baptiste Abeloos et al. *Search for squarks and gluinos with the ATLAS detector in final states with jets and missing transverse momentum at  $\sqrt{s}=13$  TeV: supporting documentation for Moriond 2017*. Tech. rep. ATL-COM-PHYS-2016-1518. ATLAS Internal note. Geneva: CERN, Oct. 2016. URL: <https://cds.cern.ch/record/2228000>.
- [165] ATLAS Collaboration. *Search for squarks and gluinos in final states with jets and missing transverse momentum using  $36\text{ fb}^{-1}$  of  $\sqrt{s} = 13$  TeV pp collision data with the ATLAS detector*. <https://atlas.web.cern.ch/Atlas/GROUPS/PHYSICS/PAPERS/SUSY-2016-07/> [Accessed: April 2018]. 2017.
- [166] Davide Costanzo et al. *Search for stop and sbottom pair production with the ATLAS detector in final states with b-jets and  $E_T^{\text{miss}}$  in pp collisions at  $\sqrt{s} = 13$  TeV*. Tech. rep. ATL-COM-PHYS-2016-1697. ATLAS Internal note. Geneva: CERN, Nov. 2016. URL: <https://cds.cern.ch/record/2234855>.
- [167] “Physics at a High-Luminosity LHC with ATLAS”. In: *Proceedings, 2013 Community Summer Study on the Future of U.S. Particle Physics: Snowmass on the Mississippi (CSS2013): Minneapolis, MN, USA, July 29-August 6, 2013*. 2013. arXiv: 1307.7292 [hep-ex]. URL: <https://inspirehep.net/record/1245017/files/arXiv:1307.7292.pdf>.
- [168] Taka Kondo. *SCTRadDamageTools*. 2016. URL: <https://twiki.cern.ch/twiki/bin/view/Atlas/SCTRadDamageTools> (visited on 04/25/2016).
- [169] Taka Kondo. *Harper Model*. 2015. URL: [https://twiki.cern.ch/twiki/pub/Atlas/SCTRadDamageTools/Harper\\_model.pdf](https://twiki.cern.ch/twiki/pub/Atlas/SCTRadDamageTools/Harper_model.pdf) (visited on 07/24/2018).
- [170] A Chilingarov. “Temperature dependence of the current generated in Si bulk”. In: *Journal of Instrumentation* 8.10 (2013), P10003.
- [171] A Chilingarov et al. “Radiation studies and operational projections for silicon in the ATLAS inner detector”. In: *Nuclear Instruments and Methods in Physics Research Section A: Accelerators, Spectrometers, Detectors and Associated Equipment* 360.1 (1995), 432–437, Table 2.

# Appendix A

## Radiation Damage Estimation

The depletion voltage and leakage current evolution models used to generate estimates in chapter 4 are presented in this appendix.

### Hamburg Model for Depletion Voltage Evolution

The Hamburg model [80, 81, 168] describes the evolution of depletion voltage due to NIEL radiation via the change of  $N_{\text{eff}}$ . It includes terms for each factor contributing to the change in effective doping concentration, namely the removal of donors and creation of stable acceptors, the creation of unstable acceptors, and a term for reverse annealing which is differentiated from *beneficial* annealing as it serves to raise the depletion voltage rather than lowering it after type inversion.

A complete list of the parameters of the model is given below:

$$N_{\text{eff}}\left(\Phi_{eq}, t(T_a)\right) = N_{\text{eff},0} - \Delta N_{\text{eff}}\left(\Phi_{eq}, t(T_a)\right) \quad (\text{A.1})$$

$$\Delta N_{\text{eff}}(\Phi, t) = N_C(\Phi) + N_a(\Phi, t(T_a)) + N_Y(\Phi, t(T_a)) \quad (\text{A.2})$$

## Radiation Damage Estimation

---

Table A.1 Hamburg Depletion Voltage Model Parameters

Parameter	Value
Donor Removal and Stable Acceptors	$N_C(\Phi) = N_{C0}(1 - e^{-c\Phi}) + g_C\Phi$
Unstable Acceptor	$N_a(\Phi, t, T) = g_a\Phi \exp\left\{-\Theta(T)_a \cdot \frac{t}{\tau_a}\right\}$
$\Theta(T)_a$	$\exp\left\{\frac{E_a}{k_B} \left[\frac{1}{T_R} - \frac{1}{T}\right]\right\}$
Reverse Annealing	$N_Y(\Phi, t, T) = g_y\Phi \left(1 - \frac{1}{(1+\Theta(T)_y t/\tau_y)}\right)$
$\Theta(T)_y$	$\exp\left\{\frac{E_y}{k_B} [1/T_R - 1/T]\right\}$
$N_{C0}$	$0.70(\pm 10\%) \times N_{\text{eff},0}$
$c$	$0.075(\pm 10\%) \text{ cm}^{-1}/N_{C0}$
$g_a$	$(0.018 \pm 0.0014) \text{ cm}^{-1}$
$\tau_a$	$2.29(\pm 10\%) \text{ days}$
$T_R$	$20^\circ\text{C}$
$E_a$	$(1.09 \pm 0.03) \text{ eV}$
$g_C$	$(0.017 \pm 0.0005) \text{ cm}^{-1}$
$g_y$	$(0.059 \pm 0.001) \text{ cm}^{-1}$
$\tau_y$	$480(\pm 10\%) \text{ days at } 20^\circ\text{C}$
$E_y$	$(1.33 \pm 0.03) \text{ eV}$
$N_{\text{eff},0}$	$(1.105 \pm 0.16) \times 10^{12} \text{ cm}^{-3}$

Uncertainties of  $\pm 10\%$  are added to the time constants and are not included in the original formulation of the model.  $N_{\text{eff},0}$  corresponds to the initial full depletion voltage of  $(70 \pm 10) \text{ V}$  for the SCT sensors [62]. In addition, the bulk thickness is set to  $(0.0285 \pm 0.0015) \text{ cm}$ , the errors of sensor temperatures are set to  $\pm 1^\circ\text{C}$ . All errors are assumed to be independent with no correlations among parameters. The errors of the

---

FLUKA simulation for NIEL per luminosity are not available and were not included in the error estimation.

## Hamburg-Dortmund Leakage Current Model

The Hamburg-Dortmund model [80–82, 168] can be used for leakage current prediction by using the coefficient  $\alpha$  [82]. The factors of  $\frac{1}{2}$  in equation A.10 are introduced to model the effects of uniform radiation during each time period, rather than a single dose of radiation at the beginning of the period. The  $J$  values of current per unit volume given correspond to the end of each time period [168], and are split into the exponential and logarithmic components as defined in equation A.4. The function  $\Theta(T_a)$  enables varying annealing temperatures to be considered within the model.

$$I_{\text{leak}} = \alpha(t) \cdot \Phi_{\text{eq}} \cdot V \quad (\text{A.3})$$

$$\alpha(t) = \alpha_I \cdot \exp\left(-\frac{t}{\tau_I}\right) + \alpha_0^* - \beta \cdot \ln\left(\Theta(T_a) \frac{t}{t_0}\right) \quad (\text{A.4})$$

$$\Theta(T_a) = \exp\left[-\frac{E_I^*}{k_B} \left(\frac{1}{T_a} - \frac{1}{T_{\text{ref}}}\right)\right] \quad (\text{A.5})$$

$$\frac{1}{\tau_I} = k_{0I} \cdot \exp\left(-\frac{E_I}{k_B T_a}\right) \quad (\text{A.6})$$

$$J_i = J_i^{\text{exp}} + J_i^{\text{log}} \quad (\text{A.7})$$

$$J_k^{\text{exp}}(t_k) = \alpha_I \sum_{i=1}^k \Phi_i^{\text{eff}} \exp\left[-\left(\frac{t_{i+1}}{\tau_I(T_{i+1})} + \dots + \frac{t_k}{\tau_I(T_k)}\right)\right] \quad (\text{A.8})$$

where  $\Phi_i^{\text{eff}} = \Phi_i \frac{\tau_I(T_i)}{t_i} \left[1 - \exp\left(-\frac{t_i}{\tau_I(T_i)}\right)\right]$

$$\begin{aligned} J_k^{\text{exp}}(t_k) = & \alpha_I \cdot \left[ \Phi_1^{\text{eff}} \exp\left[-\left(\frac{t_2}{\tau_I(T_2)} + \frac{t_3}{\tau_I(T_3)} + \dots + \frac{t_k}{\tau_I(T_k)}\right)\right] \right. \\ & \left. + \dots + \Phi_{k-1}^{\text{eff}} \exp\left(-\frac{t_k}{\tau_I(T_k)}\right) + \Phi_k^{\text{eff}} \right] \quad (\text{A.9}) \end{aligned}$$

$$\begin{aligned}
 J_k^{\log} &= \sum_{i=1}^k \Phi_i \left[ \alpha_0^* - \beta \cdot \ln \left( \frac{t_{i,j}^{\log}}{t_0} \right) \right] \\
 &= \alpha_0^* \{ \Phi_1 + \dots + \Phi_k \} - \beta \left\{ \Phi_1 \ln \left[ \left( \frac{t_1 \Theta(T_1)}{2} + t_2 \Theta(T_2) + \dots + t_k \Theta(T_k) \right) / t_0 \right] \right. \\
 &\quad \left. + \dots + \Phi_k \ln \left[ \left( \frac{t_k \Theta(T_k)}{2} \right) / t_0 \right] \right\} \tag{A.10}
 \end{aligned}$$

A full list of parameters is given in Table A.2.

Table A.2 Hamburg-Dortmund Leakage Current Model Parameters

Parameter	Value
$\alpha_I$	$(1.23 \pm 0.06) \cdot 10^{-17}$ A/cm
$\alpha_0^*$	$7.07(\pm 10\%) \cdot 10^{-17}$ A/cm
$\beta$	$3.29(\pm 10\%) \cdot 10^{-18}$ A/cm
$E_I$	$(1.11 \pm 0.05)$ eV
$E_I^*$	$(1.30 \pm 0.14)$ eV
$T_{\text{ref}}$	21 °C
$t_0$	1 min
$k_{0I}$	$1.2_{-1.0}^{+5.3} \cdot 10^{13}$ s <sup>-1</sup>

## Sheffield-Harper Model for Leakage Current Estimation

The Sheffield-Harper model [83, 168] allows for the leakage current to be estimated while taking into account annealing. The parameters of the model are listed below for completeness.

$$I_n(T_{\text{ref}}) \equiv \alpha \sum_{i=1}^n g_{n,i} \delta \Phi_i^{\text{eq}} \tag{A.11}$$

$$g_{n,i} \equiv \sum_{k=1}^5 \left\{ A_k \frac{\tau_k}{\Theta_A(T_i) \delta t_i} \left[ 1 - \exp \left( \frac{-\Theta_A(T_i) \delta t_i}{\tau_k} \right) \right] \exp \left( -\frac{1}{\tau_k} \sum_{j=i+1}^n \Theta_A(T_j) \delta t_j \right) \right\} \tag{A.12}$$

---


$$\Theta_A(T) = \exp\left(\frac{E_I}{k_B} \left[ \frac{1}{T_{\text{ref}}} - \frac{1}{T} \right]\right) \quad (\text{A.13})$$

where  $\alpha(-7^\circ\text{C}) = (7.00 \pm 0.2) \times 10^{-18} \text{ A cm}^{-1}$  is a current-related damage constant at  $-7^\circ\text{C}$  recalculated [169] due to the increase of the temperature-dependent band gap in SCT sensors to  $E_g = 1.21 \text{ eV}$  [170] and  $E_I = 1.09 \pm 0.14 \text{ eV}$  [171]. The Arrhenius function  $\Theta_A(T)$  is used to scale the annealing time for temperatures other than the reference temperature.

The values of  $\tau_k$  at 293 K and  $A_k$  are given in table A.3.

Table A.3 Values of  $\tau_k$  at 293 K

$k$	$\tau_k$ [minutes]	$A_k$
1	$(1.2 \pm 0.2) \times 10^6$	$0.42 \pm 0.11$
2	$(4.1 \pm 0.6) \times 10^4$	$0.10 \pm 0.01$
3	$(3.7 \pm 0.3) \times 10^3$	$0.23 \pm 0.02$
4	$124 \pm 2.5$	$0.21 \pm 0.02$
5	$8 \pm 5$	$0.04 \pm 0.03$



# Appendix B

## Strong SUSY Production Analysis Signal Regions

The signal regions for the analysis described in section 7.4 are presented below.

Table B.1 Two and three jet signal regions targeting squark pair production and subsequent direct decay to jets and  $\tilde{\chi}_1^0$  shown in figure 7.2a. Signal regions are named using the convention of the minimum number of jets considered followed by the  $m_{\text{eff}}(\text{incl.})$  requirement. Values from [129].

Squark SRs	2j-1200	2j-1600	2j-2000	2j-2400	2j-2800	2j-3600	2j2100	3j-1300
$E_T^{\text{miss}} [\text{GeV}] >$	250	250	250	250	250	250	250	250
$p_T(j_1) [\text{GeV}] >$	250	300	350	350	350	350	600	700
$p_T(j_2) [\text{GeV}] >$	250	300	350	350	350	350	50	50
$p_T(j_3) [\text{GeV}] >$	—	—	—	—	—	—	—	50
$ \eta(j_{1,2})  <$	0.8	1.2	1.2	1.2	1.2	—	—	—
$\Delta\phi(\text{jet}_{1,2,(3)}, \vec{E}_T^{\text{miss}})_{\text{min}} >$	0.8	0.8	0.8	0.8	0.8	0.8	0.4	0.4
$\Delta\phi(\text{jet}_{i>3}, \vec{E}_T^{\text{miss}})_{\text{min}} >$	0.4	0.4	0.4	0.4	0.4	0.4	0.2	0.2
$\frac{E_T^{\text{miss}}}{\sqrt{H_T}} [\text{GeV}^{1/2}] >$	14	18	18	18	18	18	26	16
$m_{\text{eff}}(\text{incl.})[\text{GeV}] >$	1200	1600	2000	2400	2800	3600	2100	1300

## Strong SUSY Production Analysis Signal Regions

Table B.2 Four and five jet signal regions targeting gluino pair production and subsequent direct decay to jets and  $\tilde{\chi}_1^0$  shown in figure 7.2d. Signal regions are named using the convention of the minimum number of jets considered followed by the  $m_{\text{eff}}(\text{incl.})$  requirement. Values from [129].

Glucino SRs	4j-1000	4j-1400	4j-1800	4j-2200	4j-2600	4j-3000	5j-1700
$E_T^{\text{miss}} [\text{GeV}] >$	250	250	250	250	250	250	250
$p_T(j_1) [\text{GeV}] >$	200	200	200	200	200	200	700
$p_T(j_4) [\text{GeV}] >$	100	100	100	100	150	150	50
$p_T(j_5) [\text{GeV}] >$	—	—	—	—	—	—	50
$ \eta(j_{1,2,3,4})  <$	1.2	2.0	2.0	2.0	2.0	2.0	—
$\Delta\phi(\text{jet}_{1,2,(3)}, \vec{E}_T^{\text{miss}})_{\text{min}} >$	0.4	0.4	0.4	0.4	0.4	0.4	0.4
$\Delta\phi(\text{jet}_{i>3}, \vec{E}_T^{\text{miss}})_{\text{min}} >$	0.4	0.4	0.4	0.4	0.4	0.4	0.2
$\frac{E_T^{\text{miss}}}{m_{\text{eff}}(N_j)} >$	0.3	0.25	0.25	0.25	0.2	0.2	0.3
Aplanarity $>$	0.04	0.04	0.04	0.04	0.04	0.04	—
$m_{\text{eff}}(\text{incl.}) [\text{GeV}] >$	1000	1400	1800	2200	2600	3000	1700

Table B.3 Five and six jet signal regions targeting gluino or squark pair production decaying via an intermediate heavy SUSY particle  $\tilde{\chi}^\pm$  or  $\tilde{\chi}_2^0$  before subsequent decay to  $\tilde{\chi}_1^0$ . This scenario is displayed by figures 7.2b, 7.2c, 7.2e, 7.2f and 7.2g. Signal regions are named using the convention of the minimum number of jets considered followed by the  $m_{\text{eff}}(\text{incl.})$  requirement. Values from [129].

Glucino SRs	5j-1600	5j-2000	5j-2600	6j-1200	6j-1800	6j-2200	6j-2600
$E_T^{\text{miss}} [\text{GeV}] >$	250	250	250	250	250	250	250
$p_T(j_1) [\text{GeV}] >$	200	200	200	200	200	200	200
$p_T(j_6) [\text{GeV}] >$	50	50	50	50	100	100	100
$ \eta(j_{1-6})  <$	—	—	—	2.0	2.0	—	—
$\Delta\phi(\text{jet}_{1,2,(3)}, \vec{E}_T^{\text{miss}})_{\text{min}} >$	0.4	0.4	0.8	0.4	0.4	0.4	0.4
$\Delta\phi(\text{jet}_{i>3}, \vec{E}_T^{\text{miss}})_{\text{min}} >$	0.2	0.4	0.4	0.2	0.2	0.2	0.2
$\frac{E_T^{\text{miss}}}{m_{\text{eff}}(N_j)} >$	0.15	—	—	0.25	0.2	0.2	0.15
$\frac{E_T^{\text{miss}}}{\sqrt{H_T}} [\text{GeV}^{1/2}] >$	—	15	18	—	—	—	—
Aplanarity $>$	0.08	—	—	—	0.04	0.08	0.08
$m_{\text{eff}}(\text{incl.}) [\text{GeV}] >$	1600	2000	2600	1200	1800	2200	2600

Table B.4 Large R jet signal regions targeting squark and gluino production with a one-step decay via a heavier SUSY particle before eventual decay to  $\tilde{\chi}_1^0$  displayed by figures 7.2b, 7.2c, 7.2e, 7.2f and 7.2g. Signal regions are named using the convention of the minimum number of jets considered followed by the  $m_{\text{eff}}(\text{incl.})$  requirement. Values from [129].

Large-R jet SRs	2jB-1600	2jB-2400
$E_T^{\text{miss}} [\text{GeV}] >$	250	250
$p_T(\text{large R}j_1) [\text{GeV}] >$	200	200
$p_T(\text{large R}j_2) [\text{GeV}] >$	200	200
$m(\text{large R}j_1) [\text{GeV}] >$	[60, 110]	[60, 110]
$m(\text{large R}j_2) [\text{GeV}] >$	[60, 110]	[60, 110]
$\Delta\phi(\text{jet}_{1,2,(3)}, \vec{E}_T^{\text{miss}})_{\text{min}} >$	0.6	0.6
$\Delta\phi(\text{jet}_{i>3}, \vec{E}_T^{\text{miss}})_{\text{min}} >$	0.4	0.4
$\frac{E_T^{\text{miss}}}{\sqrt{H_T}} [\text{GeV}^{1/2}] >$	20	20
$m_{\text{eff}}(\text{incl.}) [\text{GeV}] >$	1600	2400



# Appendix C

## Sbottom SUSY Analysis Kinematic Regions

This appendix contains the definitions of the kinematic regions used within the sbottom analysis described in section 7.5.

Table C.1 Non-QCD multijet control regions constructed for the zero-lepton channel SRA and SRB regions of the *sbottom* analysis [141]. SFOS refers to same-flavour opposite-sign pairs of leptons (electrons or muons).

Requirement	CRzA	CRttA	CRstA	CRwA	CRzB	CRttB	CRwB
$N_{\text{leptons}}$	2 (SFOS)	1	1	1	2 (SFOS)	1	1
$p_T(\ell_1)$ [GeV]	> 90	> 27	> 27	> 27	> 27	> 27	> 27
$p_T(\ell_2)$ [GeV]	> 20	—	—	—	> 20	—	—
$m_{\ell\ell}$ [GeV]	[76-106]	—	—	—	[76-106]	—	—
$N_{\text{jets}}(p_T > 35 \text{ GeV})$	2-4	2-4	2-4	2-4	2-4	2-4	2-4
$p_T(j_1)$ [GeV]	> 50	> 130	—	> 130	> 50	> 50	> 50
$p_T(j_2)$ [GeV]	> 50	> 50	> 50	> 50	> 50	> 50	> 50
$p_T(j_4)$ [GeV]	< 50	< 50	< 50	< 50	—	—	—
$b$ -jets	$j_{1,2}$	$j_{1,2}$	$j_{1,2}$	$j_1$	any 2	any 2	any 2
$E_T^{\text{miss}}$ [GeV]	< 100	> 200	> 200	> 200	< 100	> 100	> 100
$E_T^{\text{miss,corr}}$ [GeV]	> 100	—	—	—	> 200	—	—
$\frac{E_T^{\text{miss}}}{m_{\text{eff}}}$	> 0.25	> 0.25	> 0.25	> 0.25	—	—	—
$\Delta\phi(\text{jet}_{1-4}, \vec{E}_T^{\text{miss}})_{\text{min}}$	—	> 0.4	> 0.4	> 0.4	> 0.4	> 0.4	> 0.4
$m_T$	—	—	—	> 30	—	> 30	> 30
$m_{bb}$ [GeV]	> 200	< 200	> 200	$m_{bj} > 200$	—	—	—
$m_{cT}$ [GeV]	> 250	> 250	> 250	> 250	—	—	—
$m_{b\ell}^{\text{min}}$ [GeV]	—	—	> 170	—	—	—	—
$m_T^{\text{min}}(\text{jet}_{1-4}, E_T^{\text{miss}})$ [GeV]	—	—	—	—	> 200	> 200	> 250
$\Delta\phi(b_1, \vec{E}_T^{\text{miss}})$	—	—	—	—	—	< 2.0	< 2.0
$\Delta\phi(b_2, \vec{E}_T^{\text{miss}})$	—	—	—	—	—	< 2.5	—

## Sbottom SUSY Analysis Kinematic Regions

---

Table C.2 Non-QCD multijet control regions constructed for the zero-lepton channel SRC signal region of the *sbottom* analysis [141].

Requirement	CRzC	CRttC	CRwC
$N_{\text{leptons}}$	2 (SFOS)	1	1
$p_T(\ell_1)$ [GeV]	$> 27$	$> 27$	$> 27$
$p_T(\ell_2)$ [GeV]	$> 20$	—	—
$m_{\ell\ell}$ [GeV]	[76-106]	—	—
$N_{\text{jets}}(p_T > 20 \text{ GeV})$	2-5	2-5	2-5
$p_T(j_1)$ [GeV]	$> 250$	$> 500$	$> 500$
$b$ -jets	$j_2$ and $j_3$ or $j_4$	$j_1$ and $j_3$ or $j_4$	$j_2$
$E_T^{\text{miss}}$ [GeV]	$< 100$	$> 100$	$> 100$
$E_T^{\text{miss,corr}}$ [GeV]	$> 200$	—	—
$m_T$	—	$> 30$	[30-120]
$m_{\text{eff}}$ [GeV]	$> 500$	$> 1300$	$> 500$
$m_{jj}$ [GeV]	$> 200$	$> 200$	$> 200$
$H_{T4}$ [GeV]	$< 70$	$< 70$	$< 70$
$\mathcal{A}$ [GeV]	$> 0.5$	$> 0.5$	$> 0.8$
$\Delta\phi(j_1, \vec{E}_T^{\text{miss}})$	$> 2.5$	$> 2.5$	$> 2.5$